

# **Imaging and characterization of angle-dependent seismic reflection data**

## **Proefschrift**

ter verkrijging van de graad van doctor  
aan de Technische Universiteit Delft,  
op gezag van de Rector Magnificus Prof. dr. ir. K. F. Wakker,  
in het openbaar te verdedigen ten overstaan van een commissie,  
door het College voor Promoties aangewezen  
op woensdag 17 juni 1998 te 10:30 uur

door

**Aart-Jan VAN WIJNGAARDEN**

natuurkundig ingenieur  
geboren te Dordrecht



Dit proefschrift is goedgekeurd door de promotor:  
Prof. dr. ir. A. J. Berkhou

Toegevoegd promotor:  
Dr. ir. C. P. A. Wapenaar

Samenstelling Promotiecommissie:

Rector Magnificus, voorzitter

Prof. dr. ir. A. J. Berkhou

*Technische Universiteit Delft, promotor*

Dr. ir. C. P. A. Wapenaar

*Technische Universiteit Delft, toegevoegd promotor*

Prof. dr. ir. J. T. Fokkema

*Technische Universiteit Delft*

Prof. ir. K. J. Weber

*Technische Universiteit Delft*

Prof. dr. J. C. Mondt

*Universiteit Utrecht*

Prof. dr. R. K. Snieder

*Universiteit Utrecht*

Dr. B. C. Scheffers

*TNO-NITG Delft*

ISBN 90-9011680-x

Copyright ©1998, by A. J. van Wijngaarden, Laboratory of Seismics and Acoustics, Faculty of Applied Physics, Delft University of Technology, Delft, The Netherlands.

All rights reserved. No part of this publication may be reproduced, stored in a retrieval system or transmitted in any form or by any means, electronic, mechanical, photocopying, recording or otherwise, without the prior written permission of the author.

#### SUPPORT

The research for this thesis has been financially supported by the DELPHI consortium.

Typesetting system:  $\text{\LaTeX} 2\epsilon$

Printed in The Netherlands by: Beeld en Grafisch Centrum, TU Delft.

#### COVER

*Wave field interference offshore Lofoten*

Aan Karin

en

aan Elise



# Contents

---

<b>Notation and Terminology</b>	<b>xiii</b>
<b>1 Use of amplitudes in seismic imaging and characterization</b>	<b>1</b>
1.1 Introduction into seismic exploration . . . . .	1
1.2 The seismic imaging process . . . . .	2
1.3 Use of angle-dependent reflectivity for seismic characterization . . . . .	4
1.4 Outline of thesis . . . . .	6
<b>2 Amplitude preserving imaging of angle-dependent reflection information</b>	<b>9</b>
2.1 Introduction . . . . .	9
2.2 The ‘WRW model’ in matrix notation . . . . .	10
2.3 Imaging by double focusing . . . . .	14
2.3.1 First focusing step in detection . . . . .	15
2.3.2 Second focusing in emission . . . . .	17
2.3.3 First focusing in emission . . . . .	21
2.3.4 Second focusing in detection . . . . .	22
2.3.5 Wave field extrapolation operator $\mathbf{W}$ . . . . .	23
2.4 The resolution of the focusing operators . . . . .	24
2.5 Numerical example double focusing . . . . .	26
2.6 The gridpoint gather . . . . .	30
2.6.1 Numerical examples for constructing the gridpoint gather . .	30
2.6.2 Field data example for constructing the gridpoint gather . .	33

2.7	The gridpoint gather in the Radon domain . . . . .	34
2.7.1	Derivation of reflection coefficients (RC function) via the Radon transform . . . . .	34
2.7.2	Numerical examples for the computation of the reflection coefficients . . . . .	37
2.7.3	Field data example for the computation of the reflection coefficients . . . . .	39
2.8	The influence of errors in the dip . . . . .	40
2.9	Determination of the local dip . . . . .	49
2.9.1	Numerical example for the determination of the local dip . . . . .	50
2.9.2	Field data example for the determination of the local dip . . . . .	50
2.10	The reflection coefficient gather . . . . .	51
2.10.1	Building the RC gather . . . . .	51
2.10.2	Removing noise and aliasing in the gridpoint domain . . . . .	54
<b>II</b>	<b>Multi component imaging of angle-dependent reflection information.</b>	<b>59</b>
II.1	Introduction . . . . .	59
II.2	General elastic forward modeling using the ‘WRW model’ . . . . .	60
II.3	Numerical multi component example for one layer model . . . . .	63
II.3.1	Numerical multi component example for multi layer model . . . . .	66
II.3.2	Forward modeling . . . . .	69
<b>3</b>	<b>Zoeppritz equations and interference effects</b>	<b>71</b>
3.1	Introduction . . . . .	71
3.2	The nonlinear reflection coefficient functions . . . . .	73
3.3	The linearized reflection coefficient functions . . . . .	74
3.3.1	The PP reflection coefficients . . . . .	74
3.3.2	The SS reflection coefficients . . . . .	74
3.3.3	The SP reflection coefficients . . . . .	75
3.3.4	The PS reflection coefficients . . . . .	76
3.3.5	Overview reflection coefficients p-dependency . . . . .	76
3.4	Numerical modeling of interfaces between two half spaces . . . . .	76

---

3.4.1	Modeling the response of an interface between two half spaces	77
3.4.2	Modeling the response of two interfaces between two identical half spaces	77
3.4.3	Modeling the response of four interfaces between two identical half spaces	84
3.4.4	Modeling the response of one interface between two different half spaces	93
3.5	Conclusions on numerical modeling of layers between half spaces	98
<b>III</b>	<b>Explicit nonlinear Knott-Zoeppritz equations.</b>	<b>101</b>
III.1	The non linear reflection coefficient functions	101
III.1.1	Explicit RC functions	102
<b>4</b>	<b>Compensation for <math>p</math>-dependent resolution</b>	<b>105</b>
4.1	Introduction	105
4.2	$P$ -dependent resolution	105
4.3	Transformation of the RC-gather to one scale	106
4.3.1	Constant velocity medium	106
4.3.2	Varying velocity medium	108
4.3.3	Transformation of angle gathers	111
4.4	Improving the resolution by deconvolution	112
4.4.1	Improving the resolution by deconvolution in the $p$ -domain	113
4.4.2	Improving the resolution by deconvolution in the angle-domain	115
4.5	Transformation of the RC-gather to ray parameter-scale cube	120
<b>5</b>	<b>Linear constrained elastic inversion</b>	<b>123</b>
5.1	Introduction	123
5.2	Weighted least-squares inversion	124
5.2.1	Seismic data	124
5.2.2	A priori data	125
5.2.3	Combination of seismic and a priori data	126
5.2.4	Maximum likelihood estimation	127
5.2.5	Singular value decomposition	127
5.3	Numerical and field data example	128

5.4	Influence of background velocity . . . . .	130
5.4.1	Numerical examples . . . . .	131
5.5	Type of norm and two versus three parameter inversion . . . . .	141
5.6	Use of multi mode PS, SP and SS data . . . . .	142
5.6.1	Use of $R_{PP}$ and $R_{SP}$ . . . . .	142
5.6.2	Use of $R_{PP}$ and $R_{SS}$ . . . . .	143
5.6.3	Numerical example multi mode inversion . . . . .	144
5.6.4	Use of AVO terms for lithology indication . . . . .	149
<b>6</b>	<b>Resolution and residue analysis</b>	<b>151</b>
6.1	The ZLF and residue analysis . . . . .	151
6.1.1	Local ZLF and residue analysis . . . . .	151
6.1.2	Global ZLF and residue analysis . . . . .	155
6.2	Estimation of covariance and standard deviations of estimated parameters . . . . .	158
6.2.1	Weighted least-squares inversion . . . . .	158
6.2.2	Result analysis using the SVD . . . . .	158
6.2.3	Influence of a priori information on inversion result . . . . .	161
6.3	Improving the inversion result . . . . .	162
6.3.1	Multi gather inversion . . . . .	163
6.3.2	Residual move-out correction . . . . .	165
<b>7</b>	<b>Lithology indicators</b>	<b>171</b>
7.1	Introduction . . . . .	171
7.2	Rock properties . . . . .	171
7.2.1	Velocity and elastic moduli . . . . .	172
7.2.2	$c_P - c_S$ relationships for single lithologies . . . . .	172
7.2.3	$c_P - c_S$ relationships for mixed lithologies . . . . .	173
7.3	Indicators . . . . .	175
7.3.1	Contrast deviation factor . . . . .	175
7.3.2	Anomaly indicator . . . . .	178
<b>8</b>	<b>Case study using a 2D marine data set from offshore Norway</b>	<b>181</b>

---

8.1	The SAGA 2D marine data set . . . . .	181
8.1.1	Geological description of the reservoir . . . . .	181
8.1.2	General processing sequence . . . . .	184
8.1.3	Estimated contrast sections . . . . .	188
8.1.4	Multi-gather inversion . . . . .	188
8.1.5	Residue analysis . . . . .	188
8.1.6	Modeling synthetic data at well . . . . .	196
8.1.7	Comparison of synthetic data and seismic data . . . . .	197
8.1.8	Influence of background velocity and $Q_{lithology}$ . . . . .	198
8.1.9	Direct Hydrocarbon Indicator . . . . .	201
8.1.10	Conclusions . . . . .	205
<b>9</b>	<b>Conclusions and remarks</b>	<b>207</b>
9.1	Preprocessing and imaging . . . . .	207
9.2	Inversion process and characterization . . . . .	208
9.3	Recommendations for future research . . . . .	209
<b>Bibliography</b>		<b>211</b>
<b>Author Index</b>		<b>215</b>
<b>Samenvatting</b>		<b>217</b>
<b>Summary</b>		<b>219</b>
<b>Curriculum vitae</b>		<b>221</b>
<b>Acknowledgment/Dankwoord</b>		<b>223</b>



# Notation and Terminology

Some definitions, notations, transformations and terminology used in this thesis, will be introduced below.

## Definitions

Any scalar function in the *space time* domain is denoted by a lower case symbol, e.g.  $p(x, t)$ . This function is written in terms of the spatial variable  $x$  and time  $t$ . The corresponding function in the *space frequency* domain or *wavenumber frequency* domain is denoted by the corresponding upper case symbol  $P(x, \omega)$  or  $P(k_x, \omega)$ . The corresponding function in the *Radon* domain is indicated with a tilde above the symbol,  $\tilde{P}(p, \omega)$ . Vector quantities are denoted with an arrow above the symbol, e.g.  $\vec{p}(x, t)$ . Matrices are denoted with a bold symbol, e.g.  $\mathbf{p}(x, t)$ .

The transpose of a vector (or matrix) is denoted with a superscript  $t$ , the complex conjugate with a superscript  $*$ .

## Transformations

The *forward* temporal Fourier transformation of a time dependent function is defined by

$$F(x, \omega) = \int_{-\infty}^{+\infty} f(x, t) \exp(-j\omega t) dt \quad (1)$$

and the *inverse* transformation is defined as

$$f(x, t) = \frac{1}{2\pi} \int_{-\infty}^{+\infty} F(x, \omega) \exp(j\omega t) d\omega. \quad (2)$$

Throughout this thesis only positive frequencies are considered, thus  $\omega \geq 0$ . The inverse temporal Fourier transformation can be reformulated as

$$f(x, t) = \frac{1}{\pi} \Re \left[ \int_0^{+\infty} F(x, \omega) \exp(j\omega t) d\omega \right]. \quad (3)$$

with  $\Re$  denoting the real part of the term between the brackets.

## Terminology

The new concepts used in the CFP approach has led to a number of new terms

which are explained below.

- **focusing operator**

Convolution operator working in the time domain on pre-stack seismic data. The operator represents the response of a point in the subsurface measured at the surface and works on the traces in a common detector gather or a common shot gather. Summation over the resulting traces in the gather defines one trace for a CFP gather.

- **focusing in detection**

Result of the focusing operator working on a common shot gather. The result can be interpreted as the measurement of an areal receiver positioned at the focus point in the subsurface, which is related to the focusing operator, and the source position of the used common shot gather.

- **focusing in emission**

Result of the focusing operator working on a common receiver gather. The result can be interpreted as the response of an areal source positioned at the focus point in the subsurface, which is related to the focusing operator, and the receiver position of the used common receiver gather.

- **common focus point (CFP) gather**

The multi-offset response of the subsurface due to a focusing areal source or receiver. For focusing in detection the measurements are generated by individual sources with different positions at the surface. For focusing in emission the response is registered by individual receivers with different positions at the surface.

- **gridpoint gather**

The output of the second focusing step in bifocal migration. It contains the grid point's reflectivity function at and around zero time (in the space-time domain). For a one-dimensional medium it equals the result of crosscorrelating a CFP gather with its time-reversed focusing operator. The gridpoint gather in the  $\tau - p$  domain contains the reflection coefficient function of the imaged gridpoint at  $\Delta\tau=0$ .

- **reflection coefficient (RC) gather**

Gather of reflection coefficient functions from subsurface gridpoints with the same lateral position. Note that a moveout corrected one-way image gather in the  $p - \tau$  domain.

# Chapter 1

## Use of amplitudes in seismic imaging and characterization

*This chapter starts with a description of the seismic exploration method. The use of amplitudes in seismic imaging and characterization is described and is placed in a historical context. Finally an outline of this thesis is given.*

### **1.1 Introduction into seismic exploration**

A steady increase of the energy demand in the world, causes a continuous search for new techniques to improve the hydrocarbon exploration, in terms of efficiency and effectiveness. The most powerful tool of the exploration geophysicist for discovering and characterizing natural resources, such as oil, coal and gas is the seismic exploration method. This method is an elastodynamic remote and global sensing technique and is based on measurements of the subsurface carried out at the surface of the earth. The detectors (or also called receivers) at the earth's surface measure the wave field originating from a source which is positioned at or close to the surface. In figure 1.1 two types of seismic experiments are shown: a marine acquisition and a land acquisition. In marine acquisition normally an air gun is used as source and hydrophones as receivers. In land acquisition dynamite or a seismic vibrator is used as source and geophones as receivers.

A part of the energy emitted by the source travels along the surface of the earth directly to the receivers. This wave is called the direct or surface wave. The surface wave contains information about the layers close to the surface of the earth and are not used in exploration seismics. Besides the surface wave the source also transmits waves into the subsurface, called body waves. Due to contrasts in the elastic parameters of the subsurface such a downward propagating wave gets reflected and propagates up towards the surface where it can be measured by the receivers. These reflected wave fields contain the information the exploration geophysicist is interested in.

The goal of the geophysicist is to derive from these reflections an accurate structural and lithological image of the subsurface of the earth. The technique to translate the measurements at the surface (called shot records) into a structural representation of the subsurface is called imaging or migration. For a good structural image a large number of shot records is needed, where for every shot record the source and receivers are placed at another position at the surface. By splitting up the images of the subsurface for different angles of illumination and reflection, angle-dependent information of the subsurface is obtained. This angle-dependent information is used for a lithological characterization of the earth. The characterization of the subsurface is verified once a borehole has been drilled and the logging tool has been lowered into the borehole to measure the subsurface parameters *locally* (as shown on the left in figure 1.1).

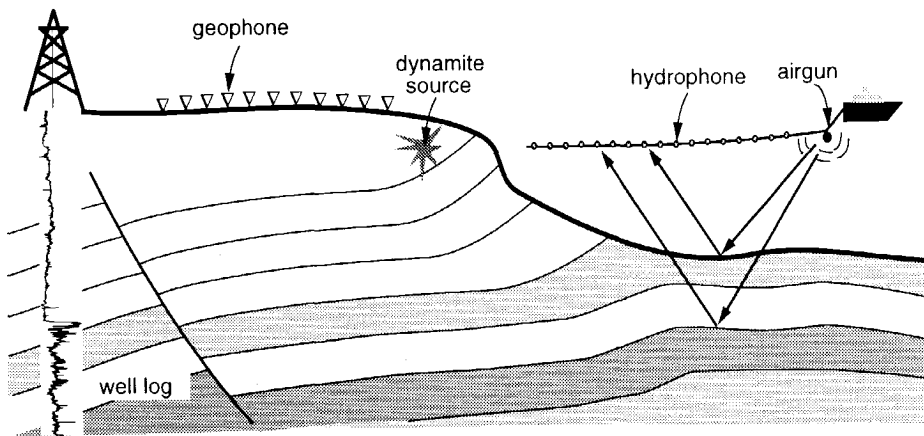


**Fig. 1.1** A schematic overview of the seismic acquisition for the land case (middle) and the marine case (right). At the left hand side a bore hole is shown with a well log measurement.

## 1.2 The seismic imaging process

On a conceptual level the seismic method can be represented by a set of operators related to the separate elements of the interaction of the elastodynamical waves with the earth. The operators of the conceptual model are shown in figure 1.2.

The quantity  $S(z_0)$  represents the source properties. The operator  $D^+(z_0)$  con-

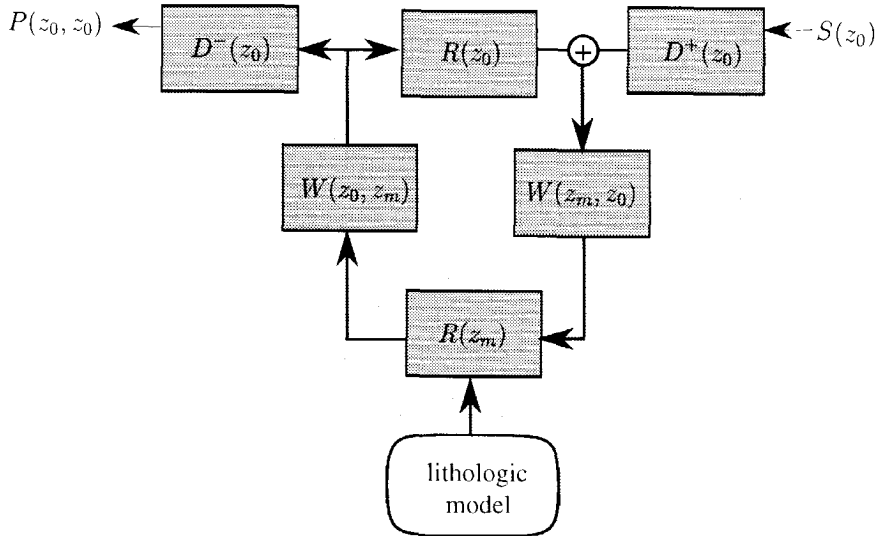


**Fig. 1.2** A conceptual overview of the seismic wave propagation. The link with the lithology is made by the reflection operator.

verts the source properties into a downgoing wave field. Furthermore, it can be used to represent the configuration (array) of the sources at or near the surface, the so-called acquisition source footprint. The propagation from the surface  $z_0$  down into the subsurface to depth level  $z_m$  is represented by the propagation operator  $W(z_m, z_0)$ . Reflection in the subsurface at a depth level  $z_m$  is described by the reflection operator  $R(z_m)$ . Note that this operator is related to changes in lithology. The propagation up to the surface is given by the propagation operator  $W(z_0, z_m)$ . The upgoing wave field at the surface is reflected into the earth again via a reflection at the surface. The reflection at the surface is represented by the operator  $R(z_0)$ , which converts upgoing wave fields into downgoing wave fields. These surface related multiple wave fields can be interpreted as secondary source wave fields. The measuring process at the surface is represented by the operator  $D^-(z_0)$ . It converts the upgoing wave fields, into the signals measured by a receiver.  $D^+(z_0)$  represents also the influence of the receiver configuration (array effects). Hence, the action of the operator  $D^-(z_0)$  yields the seismic reflection data  $P(z_0, z_0)$ .

The presented model is referred to as the WRW-model (Berkhout, 1982). It is a forward model, emphasizing the most relevant aspects of a seismic experiment.

Note that in the discrete description of the wave propagation all operators represent matrices.

To derive the structure and the material properties of the subsurface from the seismic reflection data, an inversion procedure is required. Generally, the process is split into two phases; the estimation of the reflection operator  $R$  and the inversion for lithologic parameters.

The aim of imaging is to estimate the reflection operator  $R(z_m)$ . This is done by eliminating first the effects of the surface related operators  $D^+(z_0)$  and  $D^-(z_0)$  (decomposition and elimination of the acquisition footprints) and  $R(z_0)$  (surface related multiple elimination), and secondly by removing the effects of the propagation operators  $W$  (inverse downward and upward extrapolation, after estimation of a propagation velocity or macro model). The imaging procedure reveals the structure of the earth in terms of the reflectivity operator  $R$ .

### **1.3 Use of angle-dependent reflectivity for seismic characterization**

The imaging is followed by lithologic inversion of the angle-dependent reflection operator  $R(z_m)$ . The aim of lithologic inversion is to estimate the material properties relevant for the recovery of the natural resources, such as the type of rock (lithology), its porosity, its porefill and its permeability. However, in practical situations this is not always possible and the inversion can be limited to indicators of transitions between several lithotypes, which are known to exist in the prospect.

The angle-dependent reflectivity of boundaries in the earth results in a changing reflection strength (i.e. amplitudes) as function of angle. In the early days of (quantitative) seismic amplitude analysis, amplitudes as function of offset were used (and without a proper migration algorithm). By varying the offset between the source and receiver in a seismic experiment, the response for different angles of illumination and reflection are measured and this is the basis for Amplitude-Versus-Offset (AVO) work.

The practical possibilities of AVO analysis as a lithology indicator were first pointed out by Koefoed (1955). The work on AVO increased tremendously after the publication of the work of Ostrander (1982, 1984). Ostrander showed that in the 'classical' case of a gas sand with an abnormally low Poisson's ratio embedded in sediments with a normal Poisson's ratio should result in a negative reflection coefficient with an increase in reflected P-wave energy with angle of incidence. These 'bright spots' were observed on conventional seismic data recorded over gas sands. This anomalous amplitude behaviour has been used as a direct hydrocarbon indicator (DHI) in

many areas. Later Rutherford and Williams (1989) defined three classes of AVO behaviour, based on their reflection coefficient for zero offset (angle=0°) and assuming a negative gradient for the AVO behaviour

- class I : a large positive reflection coefficient for zero offset
- class II : a small positive or negative reflection coefficient for zero offset
- class III : a large negative reflection coefficient for zero offset.

The amplitude behaviour of these three classes is shown in figure 1.3. The classical bright spot of Ostrander is an example of a class III type of AVO behaviour. Although the above mentioned classification is based on negative AVO gradients, also positive gradients are possible. These gradients correspond to other lithotypes, which also can result in bright spots.

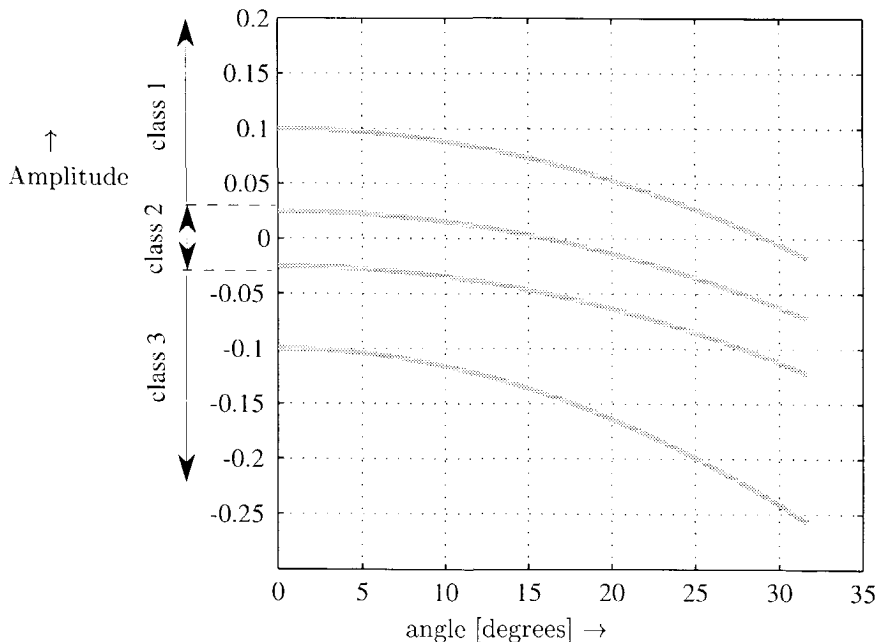


*Fig. 1.3 A schematic overview of the AVO classification of Rutherford (based on negative gradients for the AVO).*

This type of advanced lithologic characterization of the earth was developed at a time after the trend in the oil industry had shifted from a period of increasing the oil and gas production at almost any cost in the early 1980s to a cost-effective exploration in the 1990s. Reducing the risk in more complex and hostile environments

has become important. Therefore also the accuracy in the derived earth models is very important.

This resulted in more accurate (prestack) migration algorithms in the 1980s and 1990s for structural images of the earth, although most of the AVO analysis was done before migration. In this thesis a method for the amplitude analysis after (prestack) migration is discussed. The improved (lateral) resolution gives a more accurate amplitude behaviour which is used in the lithologic inversion step. Furthermore note that the underlying physical process is angle-dependent rather than offset-dependent. Therefore Amplitude-Versus-Angle (AVA) or Amplitude-Versus-rayParameter (AVP) analysis is more appropriate than AVO analysis.

#### 1.4 Outline of thesis

Chapter 2 describes an approach to amplitude preserving prestack imaging of angle-dependent reflectivity. The method is based on the use of common focus point technology (Berkhout, 1997a,b) (Thorbecke, 1997). The imaging or migration is explained as a double focusing process. By extending the structural imaging process (confocal migration for angle-averaged reflection reflectivity) into a *bifocal* process, the angle-dependent reflectivity of the subsurface is retrieved. In appendix II the bifocal migration scheme is shown for mode converted reflection data.

Chapter 3 and appendix III show the analytical expressions for angle-dependent reflection of elastodynamic waves at single boundaries. Both the full Knott-Zoeppritz equations are given as well as the linearized equations. The influence of a complex multi-layered earth on the seismic response is discussed and shown by a number of numerical experiments.

Chapter 4 introduces the concept of angle-dependent scale. The relation between the reflectivity on different scales (or resolutions) and compensation for the variance in scale in the imaged reflectivity are given.

Chapter 5 deals with the inversion of the imaged reflectivity for relative contrasts in elastic parameters. The inversion schemes for multi-mode data and the combinations of these results are discussed.

Chapter 6 shows the resolution and residue analysis for the inversion schemes discussed in chapter 5. Both local and global analyses are discussed. The influence of a velocity model on the inversion results is examined and finally tools for improving the inversion results are given.

Chapter 7 introduces the concept of Direct-Hydrocarbon-Indicators. First the basic principles of rockphysics are explained and several empirical relations are discussed. Finally the results of the inversion are used in this chapter to highlight specific lithologies in a global analysis.

Chapter 8 shows the results of the imaging and inversion algorithms on a 2D marine data set from the Norwegian part of the North Sea.



## Chapter 2

---

# Amplitude preserving imaging of angle-dependent reflection information

*This chapter describes the imaging of angle-dependent reflectivity. First the imaging in terms of double focusing is explained. This new bifocal imaging method will be introduced as an extension of the existing (confocal) imaging process with a new imaging principle. Next the influence of dip on the image is discussed, together with the dip estimation. This chapter deals primarily with the P-wave response in an elastic medium. Imaging of multi-component data will be described in appendix II.*

### 2.1 Introduction

In this chapter the bifocal imaging is used for the amplitude preserving estimation of angle-dependent reflectivity. This angle-dependent reflectivity will be used in the following chapters in the inversion for lithotypes. The imaging consists of a double focusing process. The first focusing step results in the *common focus point* (CFP) gather for a prespecified focus point in the subsurface. The CFP gather is interpreted as the response of an exploding reflector point. The second focusing step is performed for several lateral positions around the focus point and results in a *gridpoint gather*. The Radon transform translates the gridpoint gather into a *reflection coefficient* (RC)-gather which contains the bandlimited plane-wave reflection coefficients related to the focuspoint.

The numerical examples will include a horizontally layered medium and a dipping layer. The field data examples will be from a 2D dataset of the Haltenbanken area offshore Norway, which will be discussed in chapter 8. In figure 2.1, the two models for the numerical examples are shown. In figure 2.2, a part of the prestack migration is shown for the field data example.

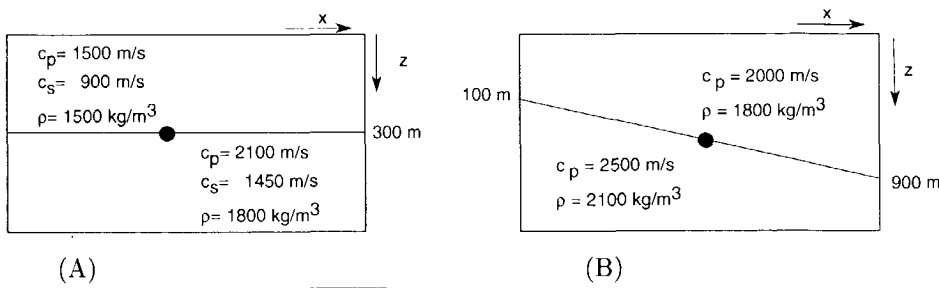


**Fig. 2.1** The models used in the numerical examples for a horizontal reflector (A) and dipping reflector (B).

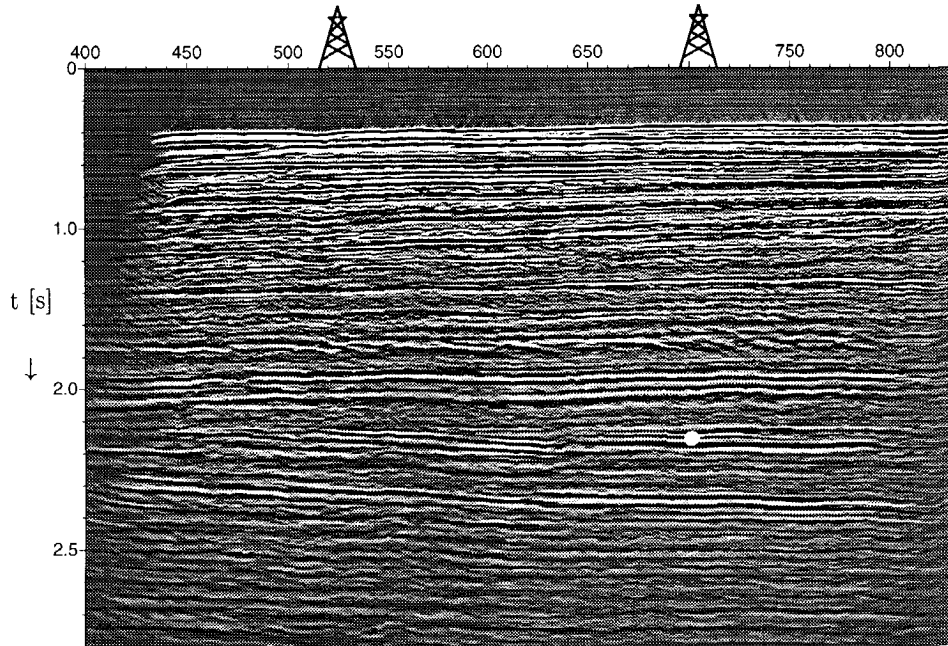


**Fig. 2.2** Prestack migration of a 2D marine dataset (courtesy SAGA Petroleum). The focus point at the target area is indicated with the white dot.

## 2.2 The 'WRW model' in matrix notation

The forward modeling of the primary reflection data in this thesis is based on the 'WRW model' (Berkhout, 1982) in matrix notation. For a more detailed discussion

of the matrix representation of seismic data and the matrix notation the reader is referred to Berkhouit (1982).

A short review of the one-way forward model is given below. All the matrices are formulated in the space-frequency domain (and refer to one Fourier component). Since the earth is assumed to be a linear time-invariant medium, it is allowed to represent the forward model by independent frequency components. The measured wave field represents a pressure field.

Matrices in the frequency domain are annotated as bold capitals, e.g.  $\mathbf{X}$ . The selected  $j^{th}$  column of this matrix is annotated as  $\vec{X}_j$  and the selected  $i^{th}$  row as  $\vec{X}_i^\dagger$ .

The WRW model is split up in matrices describing the physical processes of emission, downward propagation, reflection, upward propagation and detection. The operation of each process on the data will be a matrix multiplication of the operator matrix with the data matrix. Note that these multiplications become two-dimensional convolutions in the space-time domain. The elements of the WRW model are illustrated below using a simple subsurface model with one interface  $S_m$ .

### preprocessing

In this thesis the one-way description of primary reflection data is used. This means that a preprocessing step is needed to prepare the physically measured data for the imaging process. In the preprocessing step all surface-related effects, i.e. the surface multiples and surface waves, are removed (Verschuur, 1991). Also the direct wave is removed. A decomposition is performed on the data in such a way, that the source is a dipole, emitting only downgoing waves (P or S-waves) and the receivers are monopoles, measuring the upgoing wave field (P or S-waves) (Herrmann, 1992).

### emission

The source matrix  $\mathbf{S}^+(S_0)$  represents the sources (or source arrays) at the surface  $S_0$  used for seismic experiments. In this example only the PP data is discussed. This means a P-wave source, only PP reflection and detection of P-waves. The row index  $i$  of the matrix corresponds to the lateral position  $x_i$  at the surface and the  $j^{th}$  column  $\vec{S}_j^+(S_0)$  of  $\mathbf{S}^+(S_0)$  represents (one frequency component of) the downgoing source wave field along the surface  $S_0$  corresponding to the source (or source array) at position  $x_j$ . Note that the 'acquisition footprint' at the source side is captured in the source matrix  $\mathbf{S}^+(S_0)$ .

### downward propagation

The downward propagation from the surface  $S_0$  to interface  $S_m$  is represented by the matrix  $\mathbf{W}(S_m, S_0)$ . The index  $i$  of the row in the matrix corresponds to the position  $x_i$  at the interface  $S_m$  and the index  $j$  of the columns of the matrix corresponds to the position  $x_j$  at surface  $S_0$ . This means that the  $i^{th}$  row  $\vec{W}_i^\dagger(S_m, S_0)$  of  $\mathbf{W}(S_m, S_0)$  describes the forward propagation of a field at the surface  $S_0$  to  $x_i$  at interface  $S_m$ , as illustrated in figure 2.3A.

The downgoing incident field  $\vec{P}_j^+(S_m)$  at  $S_m$  due to one source at  $x_j$  is given by

the product of the propagation matrix with the source vector corresponding to the source at  $x_j$  (as illustrated in figure 2.3B)

$$\vec{P}_j^+(S_m) = \mathbf{W}(S_m, S_0) \vec{S}_j^+(S_0). \quad (2.1)$$

Note that a source  $\vec{S}_j^+(S_0)$  with structure  $(0, 0\dots 0, 1, 0\dots 0, 0)^T$  selects one column of the matrix  $\mathbf{W}(S_m, S_0)$ .

### reflection

The reflection at a boundary at  $S_m$  is represented by the matrix  $\mathbf{R}(S_m)$ . The matrix  $\mathbf{R}$  describes the reflection of a downgoing incident wave field. The column index  $j$  corresponds to the position of the incident field  $x_j$  at depth  $S_m$ , and the row index  $i$  corresponds to the position  $x_i$  of the reflected field at interface  $S_m$ . The upgoing reflected field  $\vec{P}_j^-(S_m)$  at depth  $S_m$  due to the source at the surface, as illustrated in figure 2.4A, is given by the reflection matrix  $\mathbf{R}(S_m)$  working on the incident field

$$\vec{P}_j^-(S_m) = \mathbf{R}(S_m) \mathbf{W}(S_m, S_0) \vec{S}_j^+(S_0). \quad (2.2)$$

Note that the  $j^{th}$  column of  $\mathbf{R}(S_m)$  corresponds to the reflected wave field at  $x_j$  at depth  $S_m$  due to the incident wave field  $\mathbf{W}(S_m, S_0) \vec{S}_j^+(S_0)$  at  $S_m$ .

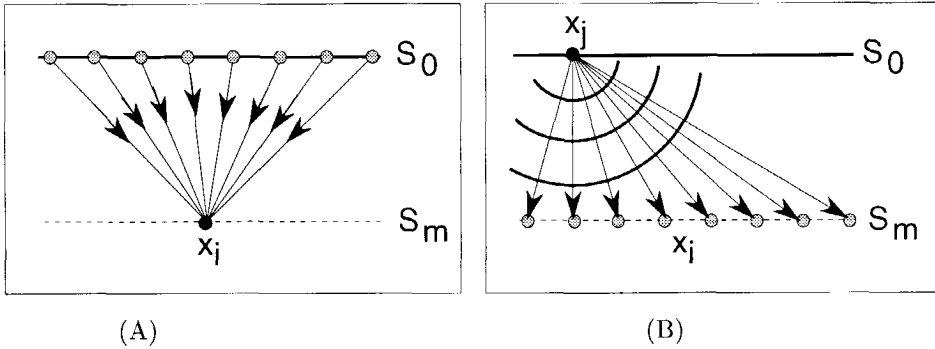


**Fig. 2.3** (A) The  $i^{th}$  row of the propagation matrix  $\mathbf{W}(S_m, S_0)$  and (B) the incident wave field  $\mathbf{W}(S_m, S_0) \vec{S}_j^+(S_0)$  at interface  $S_m$ .

### upward propagation

The upward propagation from interface  $S_m$  to  $S_0$  is represented by the matrix  $\mathbf{W}(S_0, S_m)$ . The column index  $j$  of the matrix corresponds to the positions  $x_j$  at  $S_m$  and the row index  $i$  of the matrix corresponds to the position  $x_i$  at the surface  $S_0$ . The upgoing wave field due to the source at the surface, as illustrated in figure 2.4B, is given by

$$\vec{P}_j^-(S_0) = \mathbf{W}(S_0, S_m) \mathbf{R}(S_m) \mathbf{W}(S_m, S_0) \vec{S}_j^+(S_0). \quad (2.3)$$

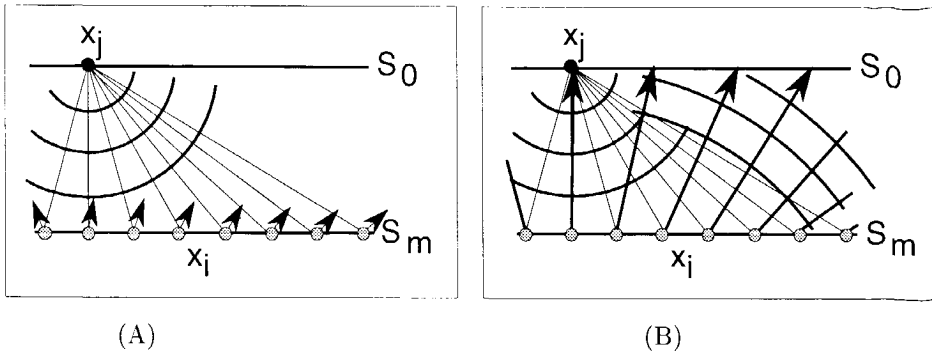


Fig. 2.4 (A) The reflected wave field just above the reflector and (B) the reflected wave field at the surface  $S_0$ .

### detection

If the upgoing wave field is measured by a receiver (array) with a certain directivity, then this (acquisition footprint at the receiver side) is represented by the matrix  $\mathbf{D}^-(S_0)$ . The measured wave field at the surface is now given by

$$\vec{P}_j^-(S_0) = \mathbf{D}^-(S_0) \mathbf{W}(S_0, S_m) \mathbf{R}(S_m) \mathbf{W}(S_m, S_0) \vec{S}_j^+(S_0). \quad (2.4)$$

The receivers described in this thesis are assumed to be monopoles, unless explicitly stated otherwise. In that situation the detector matrix can be written a (scaled) unit matrix  $\mathbf{D}^-(S_0) = D(\omega) \mathbf{I}$ ,  $D(\omega)$  being an frequency dependent scaling function. Equation 2.4 represents the primary response for one reflector at depth  $S_m$ . The primary response of a general multi-layered model is described by a summation over all boundaries  $m$

$$\vec{P}_j^-(S_0) = \mathbf{D}^-(S_0) \sum_m [ \mathbf{W}(S_0, S_m) \mathbf{R}(S_m) \mathbf{W}(S_m, S_0) ] \vec{S}_j^+(S_0), \quad (2.5)$$

as illustrated in the diagram in figure 2.5. The propagation through  $m$  layers from surface  $S_0$  to  $S_m$  is given by

$$\mathbf{W}(S_m, S_0) = \mathbf{W}(S_m, S_m - 1) \dots \mathbf{W}(S_2, S_1) \mathbf{W}(S_1, S_0). \quad (2.6)$$

The direct wave and the surface-related multiples are not included in equation 2.5. This is in agreement with the data used in this thesis. The data is assumed to be multiple-free after surface-related multiple elimination (Verschuur, 1991). In the previous example, only one source (array)  $\vec{S}_j^+(S_0)$  was used. If all shots of an acquisition are described,  $\vec{S}_j^+(S_0)$  should be replaced by a matrix  $\mathbf{S}^+(S_0)$ . The data matrix  $\mathbf{P}^-(S_0)$  describes the measured data for the complete acquisition:

$$\mathbf{P}^-(S_0) = \mathbf{D}^-(S_0) \sum_m [ \mathbf{W}(S_0, S_m) \mathbf{R}(S_m) \mathbf{W}(S_m, S_0) ] \mathbf{S}^+(S_0), \quad (2.7)$$

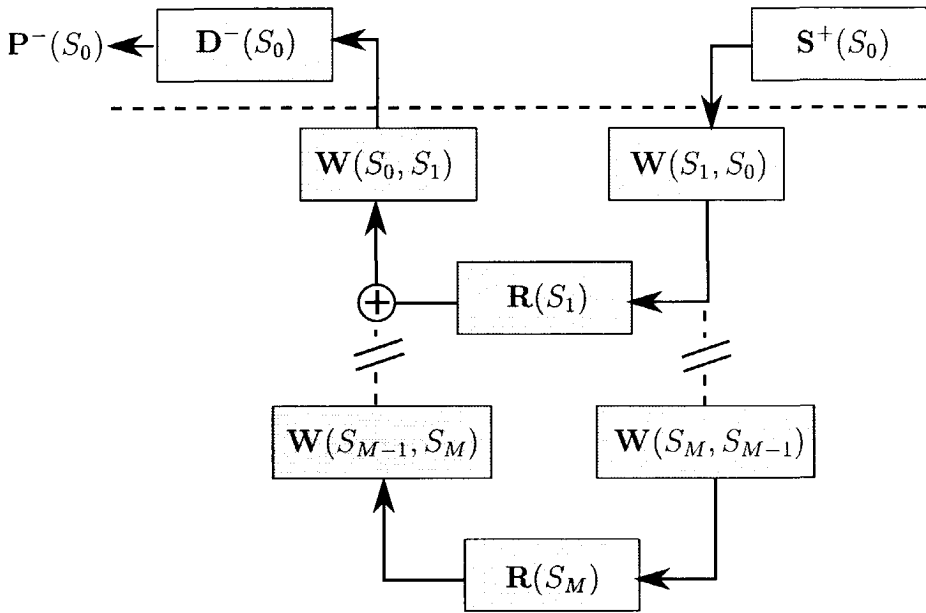


Fig. 2.5 The WRW scheme for one seismic experiment for  $M$  boundaries.

The structure of the modified equation 2.4 is shown in figure 2.6. (Here  $x_s$  and  $x_r$  indicate respectively the source and receiver coordinates.)

In the description above only the P-waves for an acoustic medium were discussed. In a full elastic medium not only P-waves, but also S-waves are present. Under the assumption that there are no conversions within layers, the WRW model can be extended to a full elastic description as discussed in appendix II. In this chapter the elastic PP-response is treated. The imaging of the other components (PS<sup>1</sup>, SP and SS) is described in appendix II.

### 2.3 Imaging by double focusing

The goal of amplitude preserving migration is to image the reflectivity matrix  $\mathbf{R}(S_m)$  at all interfaces  $S_m$  without distorting the amplitudes (Berkhout, 1997b). The starting point is the measured data  $\mathbf{P}^-(S_0)$ , which is described for a single layer model by  $\mathbf{D}^-(S_0)\mathbf{W}(S_0, S_m)\mathbf{R}(S_m)\mathbf{W}(S_m, S_0)\mathbf{S}^+(S_0)$ .

If the goal is to image  $\mathbf{R}(S_m)$ , then the upward propagation and detection signature  $\mathbf{D}^-(S_0)\mathbf{W}(S_0, S_m)$  has to be removed from the data  $\mathbf{P}^-(S_0)$  together with the downward propagation and source signature  $\mathbf{W}(S_m, S_0)\mathbf{S}^+(S_0)$ . These two processes are called the *focusing processes*.

<sup>1</sup>Here PS means S to P converted data

$$\begin{array}{c}
 x_s \rightarrow \\
 \left( \begin{array}{c} \bullet \\ \bullet \\ \bullet \\ \bullet \\ \bullet \end{array} \right) \\
 x_r \downarrow \left( \begin{array}{c} \bullet \\ \bullet \\ \bullet \\ \bullet \\ \bullet \end{array} \right) = \\
 \mathbf{P}^-(S_0)
 \end{array}$$
  

$$\begin{array}{ccccc}
 x''' \rightarrow & x'' \rightarrow & x' \rightarrow & x \rightarrow & x_s \rightarrow \\
 \left( \begin{array}{c} \bullet \\ \bullet \\ \bullet \\ \bullet \\ \bullet \end{array} \right) & \left( \begin{array}{c} \bullet \\ \bullet \\ \bullet \\ \bullet \\ \bullet \end{array} \right) & \left( \begin{array}{c} \bullet \\ \bullet \\ \bullet \\ \bullet \\ \bullet \end{array} \right) & \left( \begin{array}{c} \bullet \\ \bullet \\ \bullet \\ \bullet \\ \bullet \end{array} \right) & \left( \begin{array}{c} \bullet \\ \bullet \\ \bullet \\ \bullet \\ \bullet \end{array} \right) \\
 \downarrow & \downarrow & \downarrow & \downarrow & \downarrow \\
 \mathbf{D}^-(S_0) & \mathbf{W}(S_0, S_m) & \mathbf{R}(S_m) & \mathbf{W}(S_m, S_0) & \mathbf{S}^+(S_0)
 \end{array}$$

**Fig. 2.6** The general structure of the data matrix  $\mathbf{P}^-$  and the matrices in the WRW model. The scalars  $x_s$  and  $x_r$  denote the source respectively the receiver positions at  $S_0$ . The other scalars  $x'$  and  $x''$  denote the positions at the interface  $S_m$ .

If one side of the propagation (either upward or downward) has been removed from the data  $\mathbf{P}^-(S_0)$ , the generated ‘half-migrated’ data is called a *common focus point gathers* or in short a *CFP gathers* (Berkhout, 1997a) (Thorbecke, 1997).

The reflectivity matrix is computed by applying the second focusing step, i.e. removing the remaining propagation part in the CFP gather.

The first focusing process either removes the upward propagation or the downward propagation. In case the upward propagation is removed, we call this process *focusing in detection*. If the downward propagation is removed, we call this process *focusing in emission*.

The imaging process can start with focusing in *detection* (i.e. removing the upward propagation), followed by the second focusing step in *emission* (i.e. removing the downward propagation). These processes will be described in the following two sections. The imaging process can start with focusing in *emission*, followed by focusing in *detection*. This will be discussed in section 2.3.3 and 2.3.4. The two possible routes for double focusing are shown schematically in figure 2.8.

### 2.3.1 First focusing step in detection

In case we want to image the reflectivity of a point  $x_j$  on a boundary at  $S_m$  we start with equation 2.5 for the primary response in a multi-layered model. In the focusing in detection process, the receivers (of several shots gathers) are inversely

extrapolated into one focused receiver at the focus point  $x_j$  at interface  $S_m$  in the subsurface. The focusing operator  $\vec{F}_j^\dagger(S_m, S_0)$  for interface  $S_m$  is implicitly defined by

$$\vec{F}_j^\dagger(S_m, S_0) \mathbf{D}^-(S_0) \mathbf{W}(S_0, S_m) = \vec{I}_j^\dagger(S_m), \quad (2.8)$$

with  $\vec{I}_j^\dagger(S_m) = (0, 0, \dots, 0, 1, 0, \dots, 0)$ . Note that the focusing operator  $\vec{F}_j^\dagger(S_m, S_0)$  also compensates (in the ideal case) for the receiver directivity in  $\mathbf{D}^-(S_0)$ .

Applying this focusing operator to the data results in the CFP gather, given by

$$\begin{aligned} \vec{F}_j^\dagger(S_m, S_0) \mathbf{P}^-(S_0) = \\ \vec{P}_j^\dagger(S_m, S_0) = \vec{I}_j^\dagger(S_m) \mathbf{R}(S_m) \mathbf{W}(S_m, S_0) \mathbf{S}^+(S_0) + \\ \vec{I}_j^\dagger(S_m) \sum_{n|n \neq m} [\mathbf{W}(S_m, z_n) \mathbf{R}(z_n) \mathbf{W}(z_n, S_0)] \mathbf{S}^+(S_0). \end{aligned} \quad (2.9)$$

The first term is the response of the focus point, in which we are interested, and the second term equals the response of boundaries above and below the focus point. Note that the data vector  $\vec{P}_j^\dagger(S_m, S_0)$  still describes the upgoing wave field, but for notational convenience the minus sign has been omitted here.

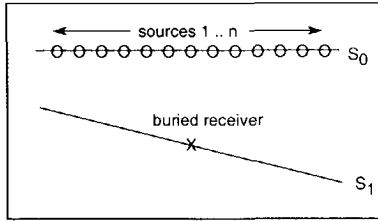


**Fig. 2.7** The interpretation of focusing in detection for a dipping layer.

The interpretation of the CFP gather after focusing in detection is interpreted as the response of the sources at the surface  $S_0$  measured just above the boundary  $S_1$ , without the direct or incident field. This is shown schematically in figure 2.7.

The focusing operator can also be defined in such a way, that the influence of the receiver (array) is not removed,

$$\vec{F}_j^\dagger(S_m, S_0) \mathbf{W}(S_0, S_m) = \vec{I}_j^\dagger(S_m). \quad (2.10)$$

Applying this focusing operator to the data results in the CFP gather, given by

$$\begin{aligned} \vec{F}_j^\dagger(S_m, S_0) \mathbf{P}^-(S_0) = \\ \vec{P}_j^\dagger(S_m, S_0) = \vec{D}_j^\dagger(S_m) \mathbf{R}(S_m) \mathbf{W}(S_m, S_0) \mathbf{S}^+(S_0) + \\ \vec{D}_j^\dagger(S_m) \sum_{n \neq m} [\mathbf{W}(S_m, z_n) \mathbf{R}(z_n) \mathbf{W}(z_n, S_0)] \mathbf{S}^+(S_0) \end{aligned} \quad (2.11)$$

with

$$\vec{D}_j^\dagger(S_m) \equiv \vec{F}_j^\dagger(S_m, S_0) \mathbf{D}^-(S_0) \mathbf{W}(S_0, S_m). \quad (2.12)$$

The vector  $\vec{D}_j^\dagger(S_m)$  shows the not-removed ‘acquisition footprint at the receiver side’ on the imaged reflectivity matrix  $\mathbf{R}(S_m)$ . If the matrix  $\mathbf{D}^-(S_0)$  at the surface equals an identity matrix  $\mathbf{I}$ , then  $\vec{D}_j^\dagger(S_m)$  equals  $\vec{I}_j^\dagger(S_m)$ , the ideal case, as shown in equation 2.9.

It is known that direct inversion of equation 2.10 is not stable, and it is common practice to use the modified matched inverse operators (Berkhout, 1982; Wapenaar and Berkhout, 1989) for the inverse extrapolation

$$\vec{F}_j^\dagger(S_m, S_0) = \vec{I}_j^\dagger(S_m) [\mathbf{W}(S_m, S_0)]^* = [\vec{W}_j^\dagger(S_m, S_0)]^*, \quad (2.13)$$

which approximates the least-squares solution for the matrix inversion (Berkhout, 1982).

In order to compute  $\vec{W}_j^\dagger(S_m, S_0)$  for one focus point we should compute the response of a monopole on  $S_m$ , measured at the surface  $S_0$  with dipole receivers. Also the responses of dipole sources at  $S_0$ , measured in the focus point with a monopole receiver, can be computed. This is what is modeled numerically: dipole sources at the surface and a monopole receiver at the focus point.

Note that since the conjugate of the forward-operator  $\vec{W}_j^\dagger(S_m, S_0)$  is used, the angle of the surface  $S_0$  must be taken into account (this is explained in more detail in section 2.3.5). Normally the surface is horizontal, so the dipoles are oriented vertically. This means that we do not need to include the local dip information in the CFP synthesis, as shown in figure 2.8.

### 2.3.2 Second focusing in emission

In the second focusing step we want to remove the propagation part that is left in the CFP gather in order to image  $\mathbf{R}(S_m)$ . This is done by extrapolation of the sources at the surface  $S_0$  into one source at the focuspoint  $x_j$  at interface  $S_m$ . The focusing operator  $\vec{F}_j(S_0, S_m)$  is defined by

$$\mathbf{W}(S_m, S_0) \mathbf{S}^+(S_0) \vec{F}_j(S_0, S_m) = \vec{I}_j(S_m), \quad (2.14)$$

with  $\vec{I}_j(S_m) = (0, 0, \dots, 0, 1, 0, \dots, 0)^T$ . Note that the focusing operator  $\vec{F}_j(S_0, S_m)$  also compensates (in the ideal case) for the source directivity in  $\mathbf{S}^+(S_0)$ .

Applying this focusing operator to the CFP gather (equation 2.9) results in one diagonal element  $R_{jj}$  from the reflectivity matrix  $\mathbf{R}(S_m)$  plus the responses from

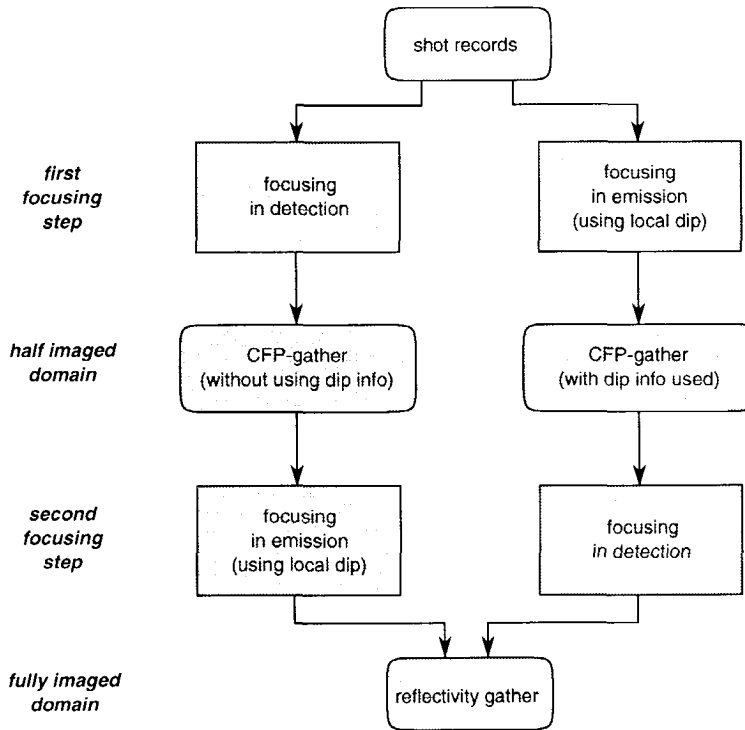


**Fig. 2.8** Overview of the two possible routes for imaging and the use of dip information in the focusing steps.

boundaries above and below the focus point, given by

$$\begin{aligned}
 \vec{P}_j^\dagger(S_m, S_0) \vec{F}_j(S_0, S_m) = \\
 P_{jj}(S_m, S_m) = R_{jj}(S_m) + \\
 \vec{I}_j^\dagger(S_m) \sum_{n|n \neq m} [\mathbf{W}(S_m, z_n) \mathbf{R}(z_n) \mathbf{W}(z_n, S_m)] \vec{I}_j(S_m), \quad (2.15)
 \end{aligned}$$

with

$$R_{jj}(S_m) = \vec{I}_j^\dagger(S_m) \mathbf{R}(S_m) \vec{I}_j(S_m). \quad (2.16)$$

The imaged element  $R_{jj}(S_m)$  of the reflectivity matrix is called the *confocal* imaged reflectivity. This is the reflectivity value that is used in normal prestack migration for a structural image. In section 2.7.1 it will be shown that this is an angle-averaged value of the angle-dependent reflection coefficient function.

For the imaging of the angle-dependent reflectivity at the focuspoint we need to image a full row  $\vec{R}_j^\dagger(S_m)$  of the reflectivity matrix (this will be discussed in more detail in section 2.7.1). This is accomplished by not only focusing into one source at  $x_i = x_j$  at interface  $S_m$ , but also into sources at  $x_i \neq x_j$  at interface  $S_m$ . The points  $x_i$  next to the focuspoint are called the bi-focuspoints.

For the imaging of the reflectivity  $\mathbf{R}(S_m)$  on a horizontal boundary, the bi-focuspoints are situated on a flat surface of equal depth. But in case of a dipping boundary the bi-focuspoints are situated on a dipping surface  $S_m$  as shown in figure 2.9.

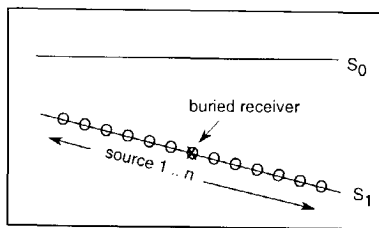


**Fig. 2.9** The interpretation of double focusing (the gridpoint gather). Clearly the bi-focuspoints are along the dipping interface  $S_1$ .

The focusing operator for a bi-focuspoint at  $(x_i, S_m)$  is given by

$$\mathbf{W}(S_m, S_0) \mathbf{S}^\dagger(S_0) \vec{F}_i(S_0, S_m) = \vec{I}_i(S_m). \quad (2.17)$$

Application of this focusing operator to the CFP gather results in one element  $R_{ji}$  from the reflectivity matrix  $\mathbf{R}(S_m)$  plus the response from boundaries above and below the focuspoint, given by

$$\begin{aligned} \vec{P}_j^\dagger(S_m, S_0) \vec{F}_i(S_0, S_m) = & \\ P_{ji}(S_m, S_m) = & R_{ji}(S_m) + \\ & \vec{I}_j^\dagger(S_m) \sum_{n|n \neq m} [\mathbf{W}(S_m, z_n) \mathbf{R}(z_n) \mathbf{W}(z_n, S_m)] \vec{I}_i(S_m). \end{aligned} \quad (2.18)$$

The imaged element  $R_{ji}(S_m)$  of the reflectivity matrix is called the *bifocal* imaged reflectivity. If the bifocal focusing step is repeated for a number of bi-focuspoints, then the double focused data, given by a row  $\vec{R}_j^\dagger(S_m)$  of the reflectivity matrix  $\mathbf{R}(S_m)$ , is obtained. This is called the *gridpoint* gather. This gather contains the angle-dependent reflectivity and will be discussed in detail in section 2.7.1.

The second focusing operator can also be defined in such a way, that the directivity of the source (array) is not removed,

$$\mathbf{W}(S_m, S_0) \vec{F}_i(S_0, S_m) = \vec{I}_i(S_m). \quad (2.19)$$

Application of this focusing operator to the CFP gather from equation 2.11 results in

$$\begin{aligned} \vec{P}_j^\dagger(S_m, S_0) \vec{F}_i(S_0, S_m) = \\ P_{ji}(S_m, S_m) = \vec{D}_j^\dagger(S_m) \mathbf{R}(S_m) \vec{S}_i(S_m) + \\ \vec{D}_j^\dagger(S_m) \sum_{n|n \neq m} [\mathbf{W}(S_m, z_n) \mathbf{R}(z_n) \mathbf{W}(z_n, S_m)] \vec{S}_i(S_m) \end{aligned} \quad (2.20)$$

with

$$\vec{S}_i(S_m) \equiv \mathbf{W}(S_m, S_0) \mathbf{S}(S_0) \vec{F}_i(S_0, S_m). \quad (2.21)$$

For  $j = i$  this is the *confocal* image. The extension to  $j = i$  and  $j \neq i$  is called the *bifocal* image. The influence of the unremoved ‘acquisition footprint’ on the imaged reflectivity matrix  $\mathbf{R}(S_m)$  is clear in this formulation. The vector  $\vec{S}_i(S_m)$  shows the not-removed ‘acquisition footprints at the source side’ and the vector  $\vec{D}_j^\dagger(S_m)$  shows the not-removed ‘acquisition footprints at the receiver side’. Note that if the matrix  $\mathbf{S}(S_m)$  equals an identity matrix  $\mathbf{I}$ , then  $\vec{S}_i(S_m) = \vec{I}_i(S_m)$ , the ideal case, as shown in equation 2.18.

It is known that direct inversion of equation 2.19 is not stable, and it is common practice to use the modified matched inverse operators for the inverse extrapolation,

$$\vec{F}_i(S_0, S_m) = [\mathbf{W}(S_0, S_m)]^* \vec{I}_i(S_m) = [\vec{W}_i(S_0, S_m)]^* \quad (2.22)$$

In order to compute  $\vec{W}_i(S_0, S_m)$  we should compute the response of a monopole on  $S_0$ , measured at the surface  $S_1$  with dipole receivers. We can also compute the responses of dipole sources at  $S_1$  (oriented  $\perp$  to  $S_1$ ), measured at the surface  $S_0$  with a monopole receiver.

This is what we model numerically. Note that the dip at the focuspoint is used for the modeling of the focusing operator, as indicated in the scheme in figure 2.8.

Note that in case of an horizontally layered 1D-medium, all the focusing operators (equation 2.17 and 2.19) for different bi-focuspoint are equal, but applied on shifted lateral positions. In case of a dip or any non-horizontally layered medium, for each bi-focuspoint (see figure 2.17) a different focusing operator should be used. The need for this depends of course on the complexity of the medium. The complexity can be split up in two parts: the local dip of the imaged reflector and the complexity of the overburden.

Due to the *local dip*, the bifocal points to the left and right of the focus point, are shifted up and downwards relative to the focus point (see figure 2.17). This means that even for an homogeneous upper layer, the second focusing operators have different ‘focus points in depth’. The influence of the dip is discussed in more

detail in section 2.8.

Due to a *complex overburden*, the bi-focus points to the left and to the right of the focus point can have different focusing operators, even for a horizontal reflector. In those cases where the overburden is not that complex the reflector can be assumed to be flat and one operator can be used in the second focusing step for all (bi)focuspoints (applied at shifted lateral positions).

### 2.3.3 First focusing in emission

In the previous two sections the prestack migration procedure started with focusing in detection, followed by focusing in emission. As shown in figure 2.8, the migration can also start with focusing in emission. The sources are inversely extrapolated into one focused source at the specified focuspoint  $(x_j, S_m)$  in the subsurface, analogous to the situation in the previous section. The definition of the focusing operator  $\vec{F}_j(S_m, S_0)$  is already given in equation 2.17. Note that in this focusing operator the local dip at the focuspoint is incorporated.

Application of this operator to the data results in the CFP gather, given by

$$\begin{aligned} \mathbf{P}^-(S_0) \vec{F}_j(S_0, S_m) = \\ \vec{F}_j(S_0, S_m) = \mathbf{D}^-(S_0) \mathbf{W}(S_0, S_m) \mathbf{R}(S_m) \vec{I}_j(S_m) + \\ \mathbf{D}^-(S_0) \sum_{n|n \neq m} [\mathbf{W}(S_0, z_n) \mathbf{R}(z_n) \mathbf{W}(z_n, S_m)] \vec{I}_j(S_m). \end{aligned} \quad (2.23)$$

The first term is the response of the focuspoint, the second term is the summation over the responses of all the boundaries above and below the focuspoint. The CFP gather is interpreted as the response of a source at  $(x_j, S_m)$  with the strength and characteristics of the reflectivity at  $(x_j, S_m)$ , measured at the surface  $S_0$ , as shown in figure 2.10. This CFP gather is very similar to the CFP gather in equation 2.9, but in the CFP gather (equation 2.23) the dip at the focuspoint is incorporated.

In case the source directivity is ignored in the focusing process, we can also use equation 2.19 for the definition of the focusing operator  $\vec{F}_j(S_0, S_m)$ . Application of this operator to the data, results in the CFP gather, given by

$$\begin{aligned} \mathbf{P}^-(S_0) \vec{F}_j(S_0, S_m) = \\ \vec{F}_j(S_0, S_m) = \mathbf{D}^-(S_0) \mathbf{W}(S_0, S_m) \mathbf{R}(S_m) \vec{S}_j(S_m) + \\ \mathbf{D}^-(S_0) \sum_{n|n \neq m} [\mathbf{W}(S_0, z_n) \mathbf{R}(z_n) \mathbf{W}(z_n, S_m)] \vec{S}_j(S_m), \end{aligned} \quad (2.24)$$

with  $\vec{S}_j(S_m)$  already defined in equation 2.21. This CFP gather still contains the 'acquisition footprint at the source side'.

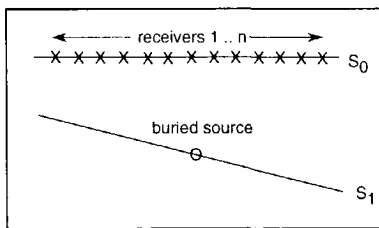


Fig. 2.10 The interpretation of focusing in emission for a dipping layer.

### 2.3.4 Second focusing in detection

In the second focusing step we want to image the scalar  $R_{ij}(S_m)$  of the reflectivity matrix by removing the propagation part that is left in the CFP gather. This is done by extrapolation of the receivers at the surface  $S_0$  into one receiver at  $(x_i, S_m)$ . The focusing operator  $\vec{F}_i^\dagger(S_0, S_m)$  is already defined in equation 2.8. Application of this focusing operator to the data, results in the gridpoint gather, defined by

$$\begin{aligned} \vec{F}_i^\dagger(S_0, S_m) \vec{P}_j(S_m, S_0) = \\ R_{ij}(S_m, S_m) = R_{ij}(S_m) + \\ \vec{I}_i^\dagger(S_m) \sum_{n|n \neq m} [\mathbf{W}(S_m, z_n) \mathbf{R}(z_n) \mathbf{W}(z_n, S_m)] \vec{I}_j(S_m). \end{aligned} \quad (2.25)$$

The imaged diagonal element  $R_{ij}(S_m)$  for  $i = j$  is the same *confocal* imaged reflectivity as shown in equation 2.15. Together with the imaged off-diagonal element  $R_{ij}(S_m)$  for  $i \neq j$  this is the *bifocal* imaged reflectivity as shown in equation 2.18. The gridpoint gather in equation 2.25 is interpreted as the response of a 'reflectivity source' on a boundary, measured by receivers along the same boundary as shown in figure 2.11. This gather contains the angle-dependent reflectivity and will be discussed in detail in section 2.7.1.

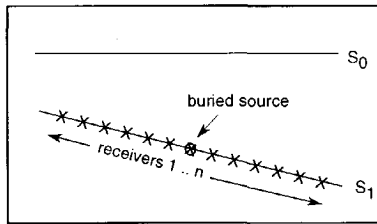


Fig. 2.11 The interpretation of double focusing (the gridpoint gather). Clearly the bifocuspoints are along the dipping interface  $S_1$ .

In case the receiver directivity is ignored in the focusing process, we can also use

equation 2.10 for the definition of the focusing operator  $\vec{F}(S_0, S_m)$ . Application of this operator to the CFP gather from equation 2.24 results in an image of the reflectivity, with the ‘acquisition footprint’ still present, given by

$$\begin{aligned} \vec{F}_i^\dagger(S_0, S_m) \vec{P}_j(S_m, S_0) = \\ P_{ij}(S_m, S_m) = \sum_i \vec{D}_i^\dagger(S_m) \mathbf{R}(S_m) \vec{S}_j(S_m) + \\ \vec{D}_i^\dagger(S_m) \sum_{n \neq m} [\mathbf{W}(S_m, z_n) \mathbf{R}(z_n) \mathbf{W}(z_n, S_m)] \vec{S}_j(S_m). \end{aligned} \quad (2.26)$$

As shown in figure 2.8 and discussed in the previous sections the first focusing step can be done both in detection as well as in emission. The advantage of first focusing in detection is however twofold. In the first place the shot record organization of seismic data makes it easier to focus in detection. Each shot record is transformed into one trace of the CFP gather. And secondly the CFP gathers can be constructed without knowledge of the local dip.

### 2.3.5 Wave field extrapolation operator $\mathbf{W}$

The forward extrapolation of an incident pressure field  $P^-$  at the surface  $S_0$  to a dipping interface  $S_1$  is shown schematically in figure 2.12(A) and is given by the product of the extrapolation operator  $\mathbf{W}(S_1, S_0)$  and the field  $\vec{P}^-(S_0)$

$$\vec{P}^-(S_1) = \mathbf{W}(S_1, S_0) \vec{P}^-(S_0). \quad (2.27)$$

The elements of the extrapolation operator are given by

$$W_{ij}(S_1, S_0) = \frac{1}{2\pi} \left[ \frac{1 + j\frac{\omega}{c} \Delta r_{ij}}{\Delta r_{ij}} \cos \phi_{ij} \right] \frac{e^{-j\frac{\omega}{c} \Delta r_{ij}}}{\Delta r_{ij}} \Delta x \Delta y. \quad (2.28)$$

The distance between the point  $\vec{x}_j$  on  $S_0$  and the point  $\vec{x}_i$  on  $S_1$  is given by the vector  $\Delta \vec{r}_{ij}$  with length  $\Delta r_{ij}$ . The angle  $\phi_{ij}$  between the normal at the surface  $S_0$  and the vector  $\Delta \vec{r}_{ij}$  as shown in figure 2.12(A) is defined by  $\cos \phi_{ij} = \vec{n}_0 \cdot \Delta \vec{r}_{ij} / \Delta r_{ij}$ .

In the 2-dimensional case the downward extrapolation matrix is given by

$$W_{ij}(S_1, S_0) = \sqrt{\frac{j\frac{\omega}{c}}{2\pi}} \frac{e^{-j\frac{\omega}{c} \Delta r_{ij}}}{\sqrt{\Delta r_{ij}}} \cos \phi_{ij} \Delta x. \quad (2.29)$$

for the far-field approximation ( $\frac{\omega}{c} \Delta r_{ij} \gg 1$ ).

The upward extrapolation of the reflected wave field from an interface  $S_1$  to a surface  $S_0$  in the 2-dimensional case is given by

$$W_{ij}(S_0, S_1) = \sqrt{\frac{j\frac{\omega}{c}}{2\pi}} \frac{e^{-j\frac{\omega}{c} \Delta r_{ji}}}{\sqrt{\Delta r_{ji}}} \cos \psi_{ji} \Delta x. \quad (2.30)$$

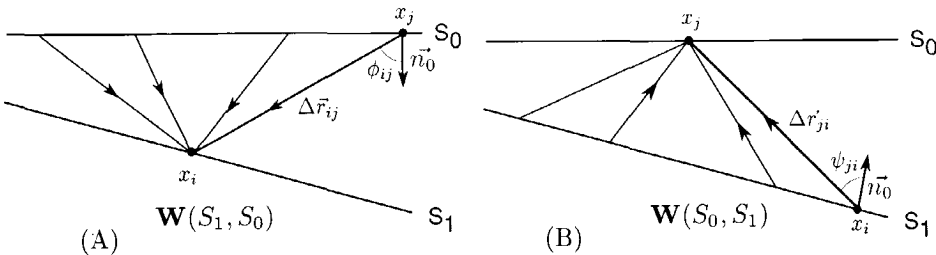


Fig. 2.12 (A) The downward extrapolation  $\mathbf{W}(S_1, S_0)$  and (B) upward extrapolation  $\mathbf{W}(S_0, S_1)$ .

The distance between the point  $x_i$  on  $S_1$  and the point  $x_j$  on  $S_0$  is given by the vector  $\Delta\vec{r}_{ji}$  with length  $\Delta r_{ji}$ . The angle  $\psi_{ji}$  between the normal at the surface  $S_1$  and the vector  $\Delta\vec{r}_{ji}$  as shown in figure 2.12(B) is defined by  $\cos\psi_{ji} = \vec{n}_1 \cdot \Delta\vec{r}_{ji} / \Delta r_{ji}$ . Note that the difference between  $\mathbf{W}(S_1, S_0)$  and  $\mathbf{W}(S_0, S_1)$  is given by the fact that the angle in the cosine term is taken relative to the normal  $\vec{n}_0$  at the surface  $S_0$  and to the normal  $\vec{n}_1$  at the surface  $S_1$  respectively.

## 2.4 The resolution of the focusing operators

The bifocal migration maps the measured data from the surface into the correct position in the subsurface, given a correct velocity model. The result is an image with maximum resolution. The resolution depends primarily on the surface acquisition configuration (for uncomplicated subsurface geometries). The acquisition configuration determines how well we can focus the energy at the focus point in the two focusing steps.

In this section a surface acquisition with a stationary receiver spread is discussed. The focusing property of this acquisition can be illustrated by showing the energy of the extrapolated wave field of the first focusing operator, as shown in figure 2.13. This focused volume is called the focusing beam. The beam is constructed by performing an inverse recursive depth extrapolation of the focusing operator through the model and calculating at every depth level the energy of the wave field as function of the lateral position. Note that for the construction of the beam only the focusing operator and a macro velocity model are needed. It is obvious that a long focusing operator (i.e. a long acquisition) will result in a sharp focused illumination of the focuspoint, as shown in figure 2.13(B). A short focusing operator will result in a diffuse illumination of the focuspoint, as shown in figure 2.13(A).

Note that the range of illumination angles is also related to length of the operator. A long operator gives a large range of illumination angles. If the focus point is

illuminated over a large range of angles, than the reflectivity can be imaged over a large range of angles, if the detection is also done over a large range of angles. This depends of course on the length of the second focusing operator (i.e. the acquisition). So if we can focus with a high resolution in the two focusing steps, this implicitly means that in the bifocal migration the angle-dependent reflectivity can be imaged over a large angle-range.

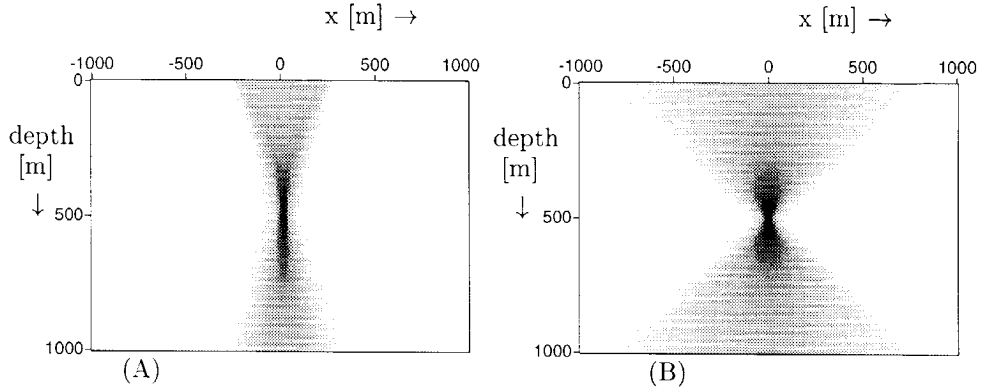


**Fig. 2.13** The focusing beams for a short (A) and long (B) focusing operator.

The influence of the acquisition on the imaging of the reflectivity is twofold. In the first place the directivity characteristics of the source and receiver (array) influence the imaged angle-dependent amplitudes. In the second place, the length of the acquisition is directly related to the range of angles over which the reflectivity can be imaged. As shown in equation 2.21, the focusing properties on the source side are described by the vector

$$\vec{S}_j(S_m) = \mathbf{W}(S_m, S_0) \mathbf{S}^\dagger(S_0) \vec{F}_j(S_0, S_m)$$

and the focusing properties on the receiver side are given by (equation 2.12)

$$\vec{D}_i^\dagger(S_m) = \vec{F}_i^\dagger(S_m, S_0) \mathbf{D}^\dagger(S_0) \mathbf{W}(S_0, S_m).$$

The combined influence on the imaged reflectivity is given by (equation 2.20):

$$\vec{D}_i^\dagger(S_m) \mathbf{R}(S_m) \vec{S}_j(S_m).$$

In equation 2.20 the vectors and 2-dimensional matrix are given in the frequency domain for one particular frequency. In order to relate this expression to the focusing beams in figure 2.13, equation 2.20 is transformed to the time domain via the inverse Fourier transform. In the time domain the vectors  $\vec{D}_i^\dagger(S_m; \omega_i)$  and  $\vec{S}_j(S_m; \omega_i)$  become matrices  $\mathbf{D}_i^\dagger(S_m; t)$  and  $\mathbf{S}_j(S_m; t)$ . The 2-dimensional matrix  $\mathbf{R}(S_m; \omega_i)$  becomes a 3-dimensional matrix  $\mathbf{R}(S_m; t)$  in the time domain. In the time domain the

matrix multiplications in equation 2.20 become convolutions.

Now for a (locally) lateral invariant reflector the order of the matrices  $\mathbf{D}_j^\dagger(S_m; t)$  and  $\mathbf{R}(S_m; t)$  in the convolution may be interchanged. The imaged reflectivity is then given by the convolution of the reflectivity matrix  $\mathbf{R}(S_m; t)$  and the matrix  $\mathbf{C}$ , which is the convolution in time of the focusing operators  $\mathbf{D}_j^\dagger(S_m; t)$  and  $\mathbf{S}_i(S_m; t)$ . At interface  $S_m$  the energy of these focusing operators is given in the focusing beams (figure 2.13). This means that for the structural image in the *confocal* migration the resolution at the focus point is given by the *product* of the two focusing beams (for emission and detection) at the focuspoint. For the angle-dependent image in the *bifocal* migration, for each trace of the gridpoint gather the resolution is given by the product of the two focusing beams for focusing in detection and focusing in emission at respectively the focuspoint and the bi-focuspoint; so the resolution of the imaged reflectivity at interface  $S_m$  is given by the lateral convolution of the two focusing beams.

## 2.5 Numerical example double focusing

In this section the focusing steps in the previous sections are illustrated with a numerical example. Although the WRW formulation is given in the frequency domain, in this example the displays are shown in time (after convolution with a ricker wavelet).

The model in Figure 2.1B is used for the numerical example (focus point at  $z=500$ m on the dipping interface). The (time-reversed) focusing operator for focusing in detection (equation 2.13) in the space-time domain and its amplitude distribution are shown in figure 2.14(A) and (C).

The operator is also transformed to the ray parameter-intercept time domain via the Radon transform. The operator and its amplitude distribution as a function of ray parameter  $p$  are shown in figure 2.14(B) and (D). The amplitude distributions are symmetrical around  $\Delta x_s = 0$  and  $p=0$ . Clearly the influence of the dip is not present in this operator.

The (time-reversed) focusing operator for focusing in emission (equation 2.22) in the space-time domain and its amplitude distribution are shown in figure 2.15(A) and (C). This operator is also transformed to the ray parameter-intercept time domain via the Radon transform. The operator and its amplitude distribution as a function of ray parameter  $p$  is shown in figure 2.15(B) and (D). The amplitude distributions are not symmetrical around  $\Delta x_s = 0$  and  $p=0$ . Due to the influence of the dip the amplitudes are shifted along the operator.

The CFP gather (equation 2.24) is made by focusing in emission (operator in figure 2.15). The operators, one shot record and the CFP gather are shown together in figure 2.20. The CFP gather is shown in more detail in figure 2.16(A). In this figure the head wave is only present at the left hand side due to limited length of the

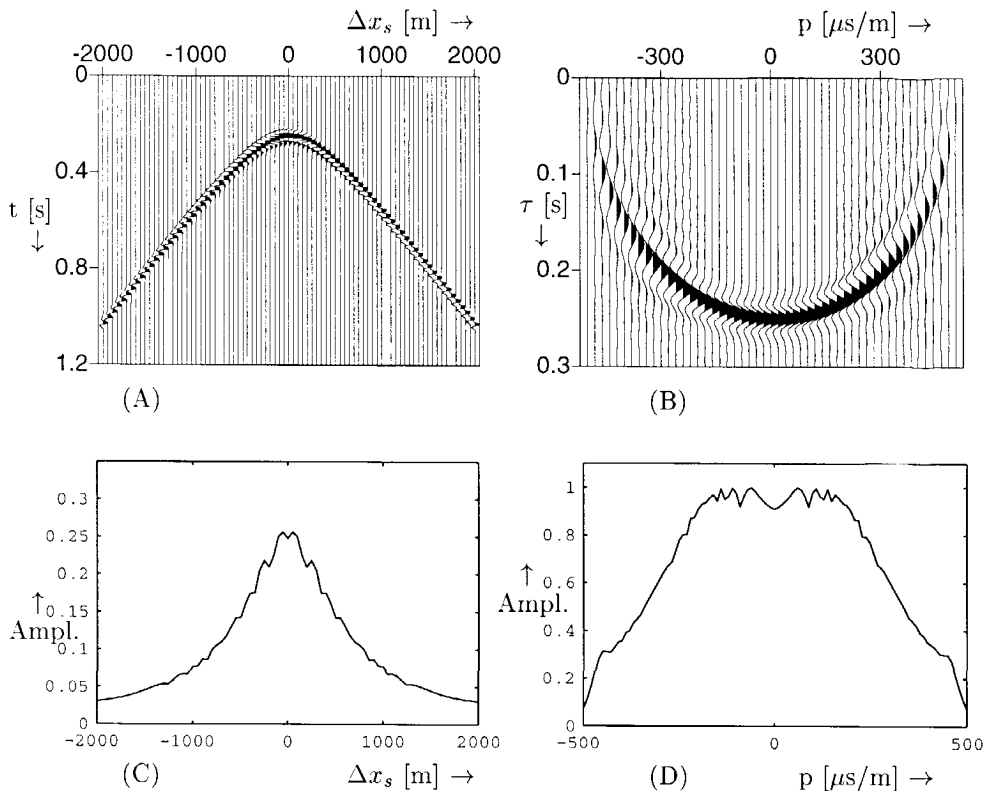


**Fig. 2.14** The (time-reversed) focusing operator (in detection) as function of offset (A) and ray parameter (B) and amplitude cross sections as function of offset (C) and ray parameter (D), for a dipping layer. Note that the dip has no influence on this operator and therefore the amplitudes around  $\Delta x_s = 0$  and  $p = 0$  are symmetric.

acquisition configuration. The CFP gather after Radon transform is shown in figure 2.16(B), and the amplitude distribution as a function of ray parameter  $p$  in 2.16(D). Note that the AVO response of the focuspoint (in CFP offset) is given by the ratio of the amplitudes in figures 2.16(C) and 2.15(C). The ratio of the amplitudes in figures 2.16(D) and 2.15(D) shows the reflectivity of the focuspoint as a function of ray parameter  $p$ .

In section 2.7 a more stable way for imaging the reflectivity as function of ray parameter  $p$  will be presented.

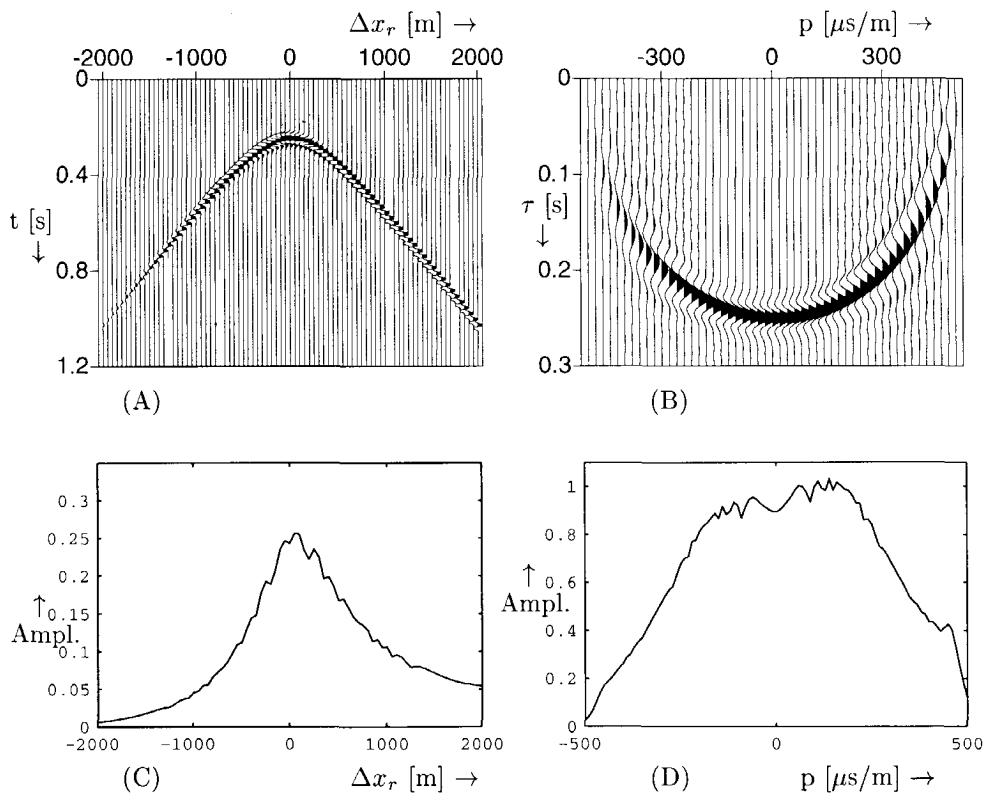


**Fig. 2.15** The (time-reversed) focusing operator (in emission) as function of offset (A) and ray parameter (B) and amplitude cross sections as function of offset (C) and ray parameter (D). Note that the amplitudes are not symmetrical around  $\Delta x_s = 0$  and  $p = 0$  due to the dip.

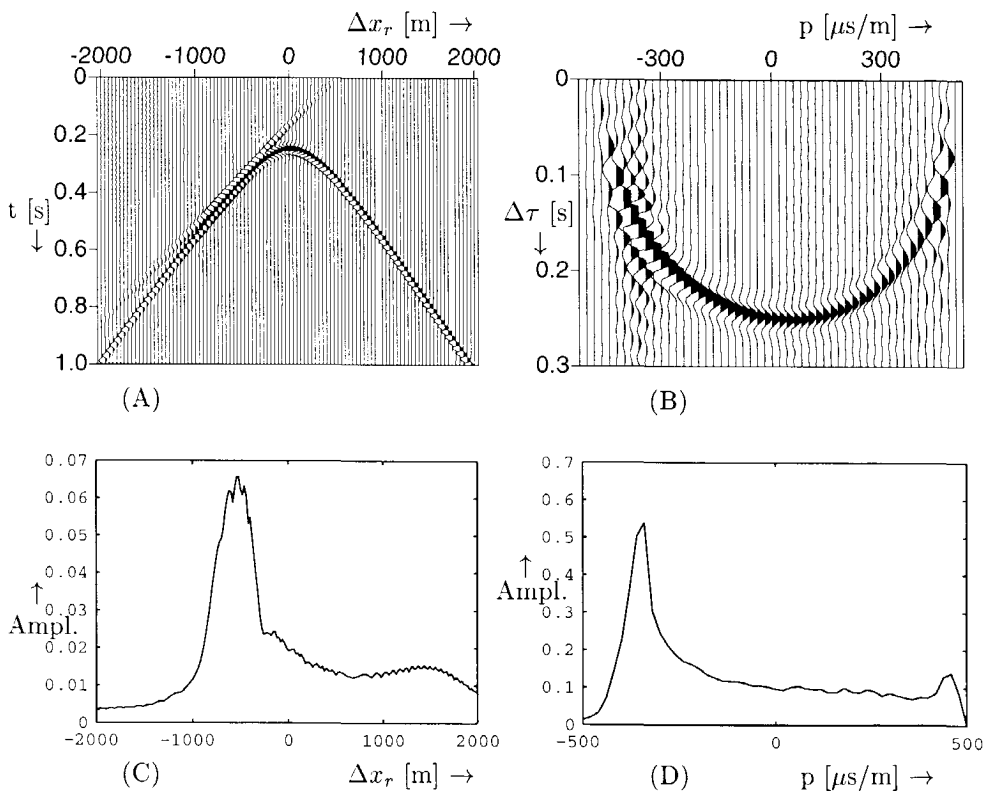


*Fig. 2.16* The CFP gather (after focusing in emission) as function of offset and ray parameter and amplitude cross sections as function of offset and ray parameter.

## 2.6 The gridpoint gather

The result of double focusing is called the gridpoint gather (as shown in section 2.3). The gather can be interpreted as the response of exploding 'reflectivity' sources on the reflector, measured by a receiver on the reflector, as shown in figure 2.17(A). This situation corresponds to the first focusing step in emission, followed by focusing in detection. The gridpoint gather can also be understood if we interchange the

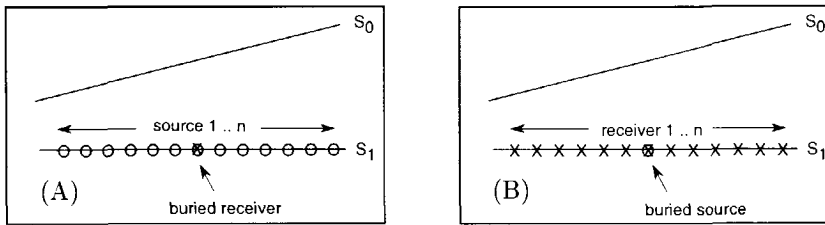


**Fig. 2.17** The interpretation of double focusing (the gridpoint gather). (A) The first focusing step in detection, followed by focusing in emission and (B) the first focusing step in emission, followed by focusing in detection.

sources and receivers in figure 2.17A into figure 2.17B. We have now one exploding 'reflectivity' source at the surface  $S_1$ . The response is measured with receivers along the surface. This situation corresponds to the first focusing step in detection, followed by focusing in emission.

Since the focused dipole sources on  $S_1$  are oriented perpendicular to  $S_1$ , the gridpoint is better illustrated if the subsurface is rotated such that  $S_1$  becomes horizontally as shown in figure 2.17. This configuration is already discussed by De Bruin (de Bruin, 1992, p. 53). Note that the direct wave is not present, but in case of a velocity contrast a head wave (indicating the critical angle) should be present.

### 2.6.1 Numerical examples for constructing the gridpoint gather

First the simple elastic model with one horizontal reflector (see figure 2.1A) is discussed. A focus point is defined on the reflector at 300m depth. A shot record is shown in figure 2.18, together with the (time reversed) first focusing operator (focusing in detection) and the resulting CFP gather. Note the head waves in the shot record and in the CFP response. For the homogeneous layer considered here, the focusing operators for focusing in emission and detection are the same. The gridpoint gather is constructed by application of the second focusing (in emission) operator (figure 2.18D) on the CFP gather (figure 2.18C) for a range of bi-focuspoints. The resulting gridpoint gather (in the time domain) is shown in figure 2.19.

Most of the energy in this gather is concentrated around the origin. The large crossing events indicate the limits of the lateral bandwidth. The other two linear events

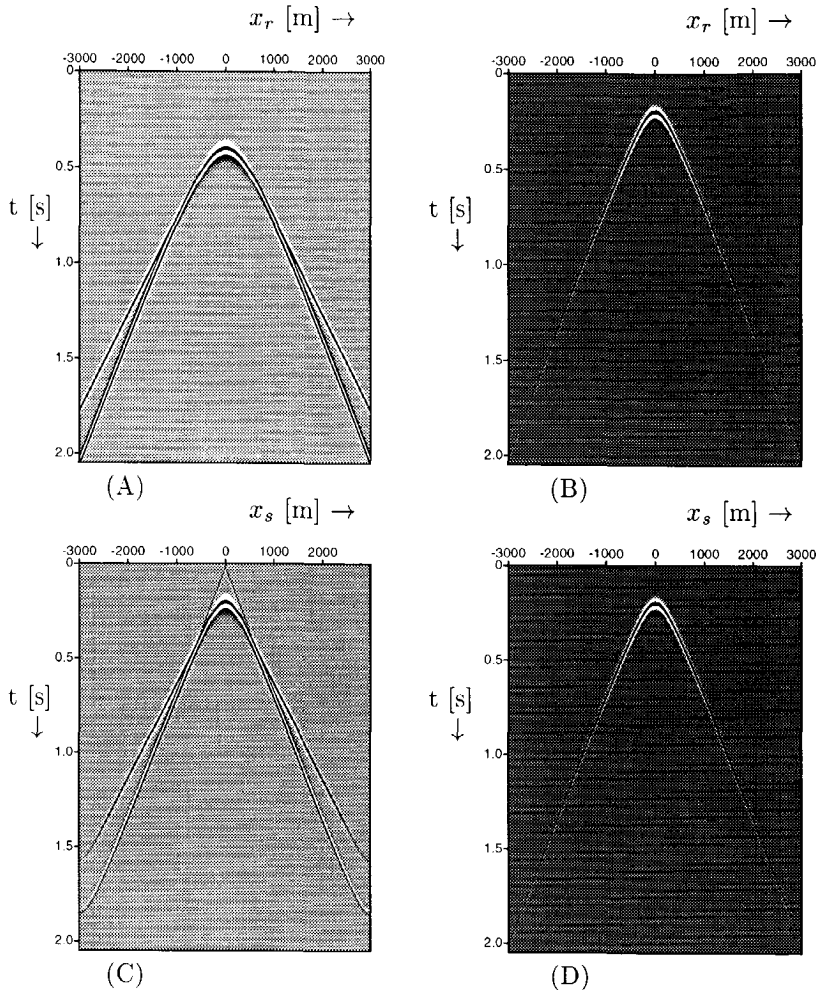


**Fig. 2.18** The shot record (A), (time reversed) first focusing operator (B), CFP gather (C) and (time reversed) second focusing operator (D) for a horizontal layer.

represent the head waves. Note that the two crossing events (indicating  $p_{min}$  and  $p_{max}$ ) divide the gridpoint gather in four triangles (indicated by A, B, C and D). The response of the focuspoint (given by the first term in equation 2.18) is within the left and right hand triangles A and B. The triangles C and D contain the responses of boundaries (if present) above and below the focuspoint (given by the first term in equation 2.18). The bandwidth limitation will be discussed in more detail in section 2.7.1.

In the second numerical example we use an acoustic model with a dipping reflector

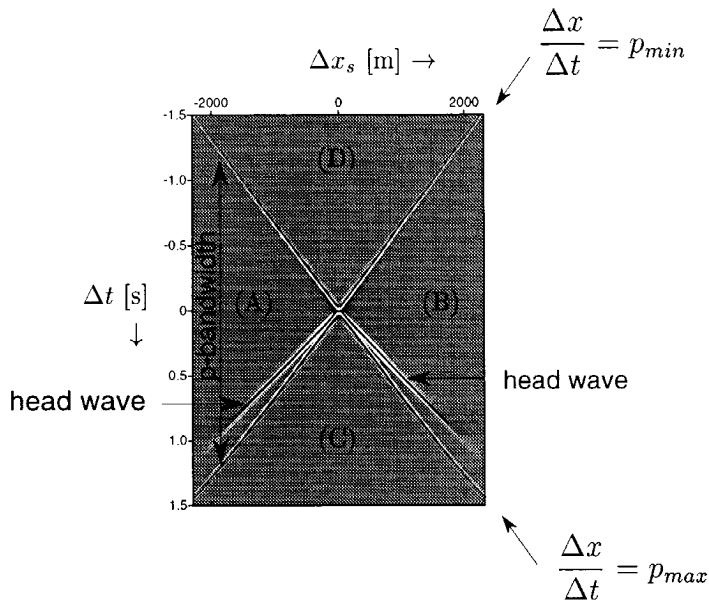


**Fig. 2.19** The gridpoint gather for a horizontal layer.

(see figure 2.1B). We define a focus point on the dipping reflector at 500m depth. The dip of the reflector is 11.3 degrees. A shot record is shown in figure 2.20, together with the (time reversed) first focusing operator (focusing in detection) and the resulting CFP gather. For the dipping layer considered here, the focusing operators for focusing in emission and detection are not the same. The gridpoint gather is constructed by application of the second focusing operator (in emission, figure 2.20D) on the CFP gather (figure 2.20C). The result is shown in figure 2.21. Due to the dip, for negative  $p$ -values there is a better illumination, since we used a fixed receiver spread acquisition centered around the midpoint at the surface above the focus point. This results in a non symmetrical gridpoint gather. At the left hand side of the gridpoint gather in figure 2.21 the head wave is clearly separated from the finite aperture cross. At the right hand side the head wave and finite aperture cross coincide. This means that on the right hand side the acquisition was not large enough to include the critical angle, whereas on the left hand side there is data beyond the critical angle. The bandwidth limitation will be discussed in more detail in section 2.7.1.

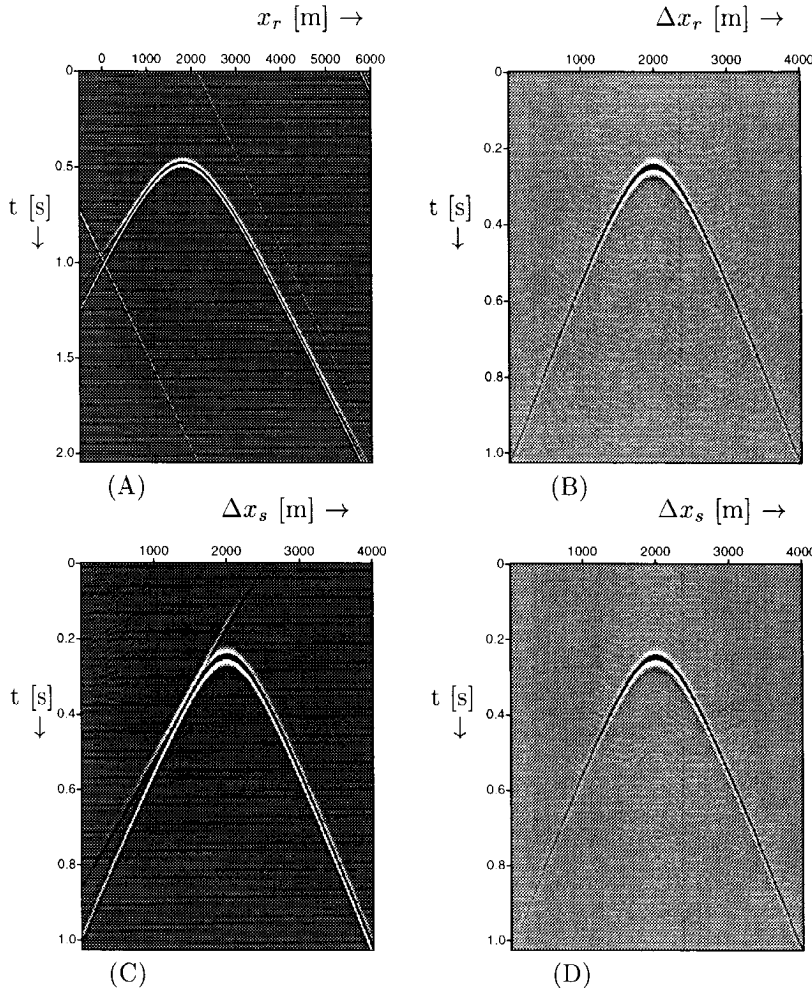


**Fig. 2.20** The shot record (A), (time reversed) first focusing operator (B), CFP gather (C) and (time reversed) second focusing operator (D) for a dipping layer. Note the difference between the focusing operators (B) and (D).

### 2.6.2 Field data example for constructing the gridpoint gather

In this example we use a marine dataset, as shown in figure 2.2. The focusing operator is shown in figure 2.22, with a shot and the CFP gather after focusing in emission. Reciprocity has been used to get a two sided CFP gather.

One (shifted) focusing operator is used for the second focusing step (assuming zero dip). The gridpoint gather is shown in figure 2.22D. Note that only for the cone centered around  $\Delta t=0$  the reflectivity is imaged correctly. The source and receiver directivities are not estimated or compensated for. Therefore the imaged data is

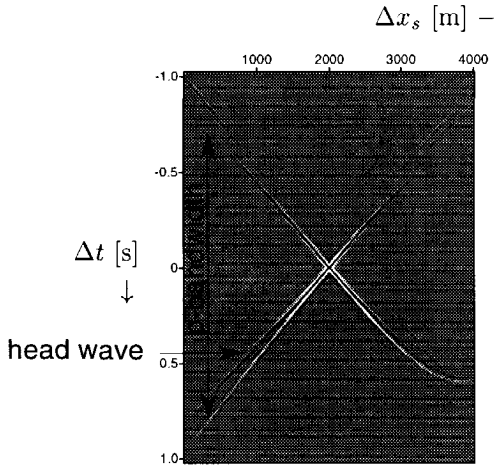


**Fig. 2.21** The gridpoint gather for a dipping layer.

given by

$$\vec{D}_i^\dagger(S_m) \mathbf{R}(S_m) \vec{S}_j(S_m) \quad (\forall i). \quad (2.31)$$

This means that by double focusing one row of the reflectivity matrix  $\mathbf{R}(S_m)$  is imaged, but the ‘footprints’ of the acquisition (vectors  $\vec{D}_i^\dagger(S_m)$  and  $\vec{S}_j(S_m)$ ) are ignored.

## 2.7 The gridpoint gather in the Radon domain

### 2.7.1 Derivation of reflection coefficients (RC function) via the Radon transform

The gridpoint gathers in the previous section showed the reflectivity in the space-time domain. In order to derive the reflection coefficients for plane-wave reflection, we apply a linear Radon transform to the gridpoint gather. The linear Radon transform in the space-frequency domain is given by

$$\tilde{R}(p, \omega; S_m) = \int_{-\infty}^{+\infty} R(x, \omega; S_m) e^{j\omega px} dx \quad (2.32)$$

and in the space-time domain by

$$\tilde{r}(p, \tau; S_m) = \int_{-\infty}^{+\infty} r(x, t + px; S_m) dx. \quad (2.33)$$

This can be explained with the aid of figure 2.23. Note that  $p$  is defined as the slowness along  $S_1$ . In figure 2.23A a number of downward focused sources and a

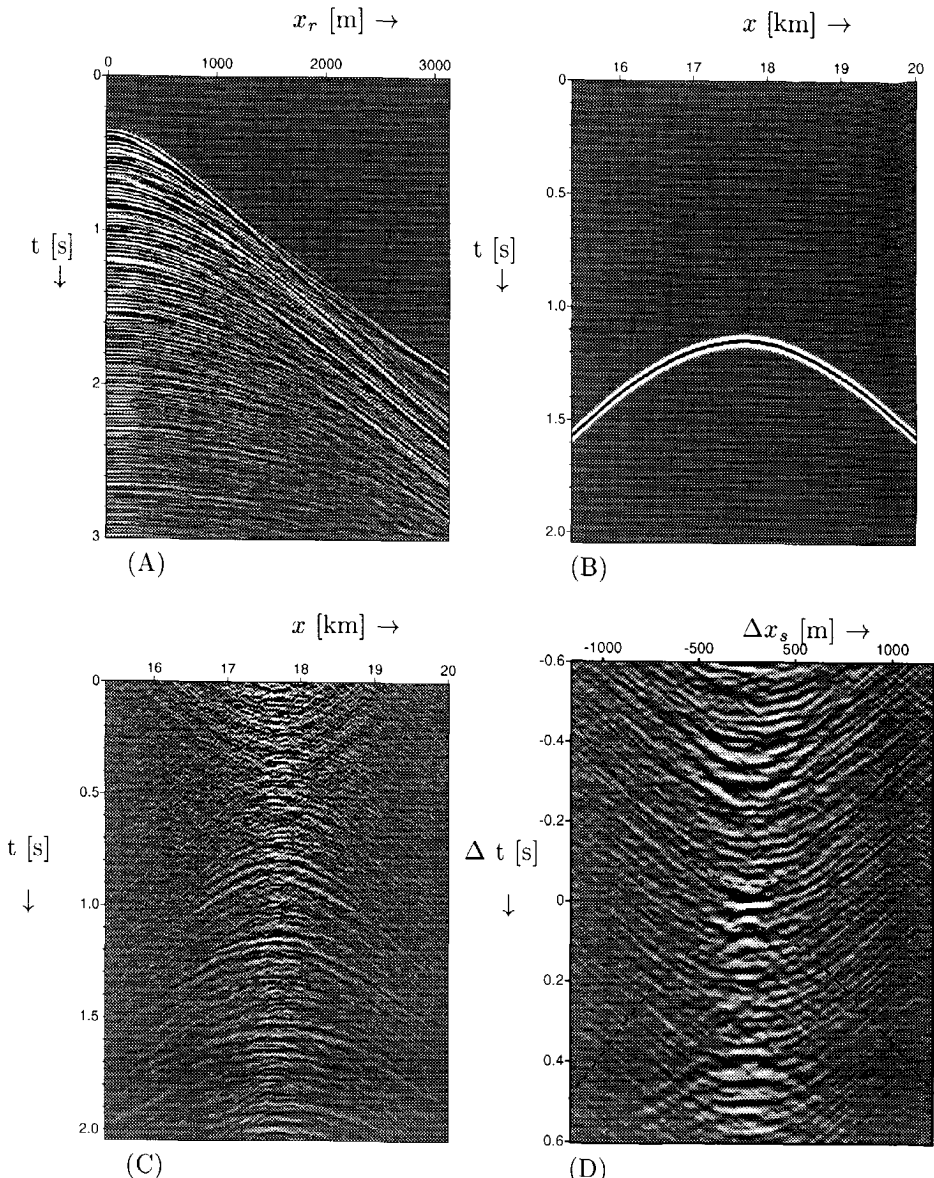


**Fig. 2.22** (A) The shot record and (B) the (time reversed) first focusing operator (B) for marine dataset. (C) The corresponding CFP gather and (D) the gridpoint gather. The area between the dashed lines indicates the response of the boundary with the focuspoint.

downward focused receiver along a reflector  $S_1$  are shown. If all the focused sources 'explode' at the same time, there is a *local* plane wave (with  $p=0$ ) illumination around

the receiver. The strength of the 'sources' is given by the local reflectivity. So the response measured in the receiver is the local plane-wave response for  $p=0$ .

This response is the same as adding all the responses of the different sources at time  $\Delta t=0$  in the gridpoint gather in figure 2.23D. Of course the largest contribution will be from the sources nearest to the receiver. Stacking along the line  $\Delta t=0$  in the gridpoint gather corresponds to the Radon transform for  $p=0$ . So for  $p=0$  the reflection coefficients correspond to the Radon transform of the gridpoint gather.

Note that due to the focusing in detection and emission we 'look' only *locally*. This means that due to the first focusing step, the receiver measures only the response in the narrow focusing beam. The focusing beam for the focusing in detection is schematically shown in the background of figure 2.23(A) and (B).

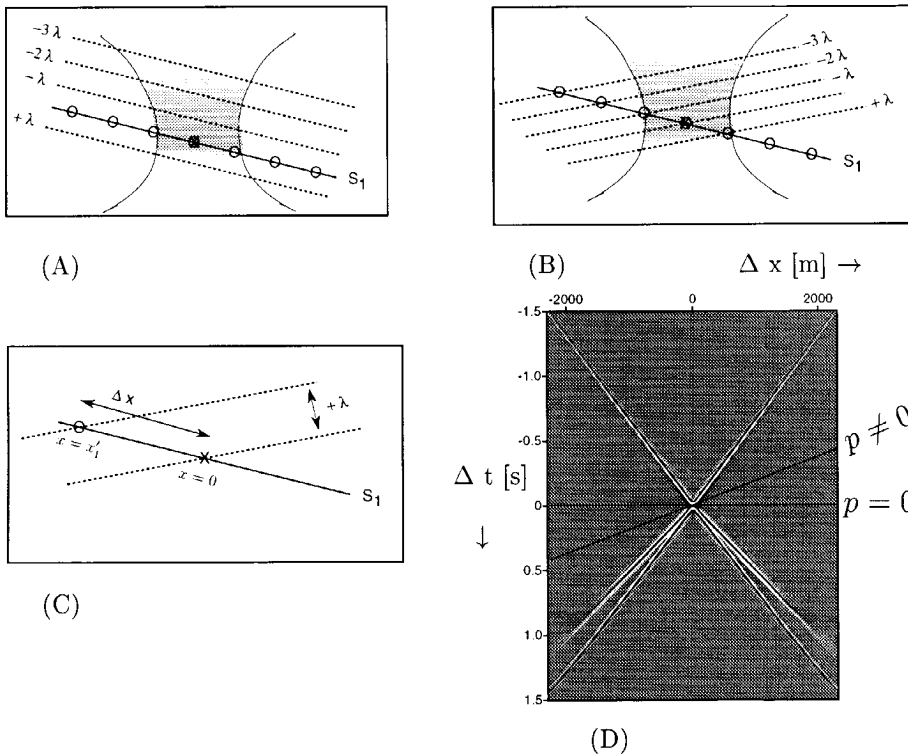


Fig. 2.23 Determination of reflection coefficients from the gridpoint gather via the Radon transform. Note that  $p$  is defined as the slowness along  $S_1$ .

If we would like to construct a *local* plane-wave illumination around the receiver with a certain angle  $\alpha$ , we would have to apply small time shifts to all the secondary sources. The secondary sources at  $x_n = n \times \Delta x$  should explode at a time delay of

$\Delta t_n = n \times T$  (with  $T = \frac{\Delta x \times \sin(\alpha)}{c} = p \times \Delta x$ ), as shown in figure 2.23B and 2.23C. In the gridpoint gather this means stacking along a line  $p = \Delta t / \Delta x$ . This corresponds to the Radon transform for this value of  $p$ . So the reflection coefficient function  $\tilde{r}(p)$  at the focus point corresponds to the local (discrete) linear Radon transform of the gridpoint gather,

$$\tilde{r}(p) = \sum_n \mathbf{r}(n\Delta x, \Delta\tau + p n\Delta x) \Delta x, \quad (2.34)$$

at  $\Delta\tau=0$ . Taking  $\Delta\tau=0$  in the gridpoint gather is an extension of the well-known ‘imaging principle’ (taking  $t=0$  in the confocal migration process, which equals the selection of data at  $t=0$  and  $\Delta x=0$  in the gridpoint gather).

The computation of the reflection coefficients can be done by

- extension of confocal migration to *bifocal* migration
- transformation of the gridpoint gather to the Radon domain
- extension of the imaging principle to taking  $\Delta\tau=0$

Note that the limits  $p_{min}$  and  $p_{max}$  of the imaged reflection coefficients are given by the acquisition. A large acquisition gives a well focused gridpoint gather in the space-time domain and a broad bandwidth in  $p$ .

If we look at the inverse Radon transform in the frequency domain, given by

$$R(\Delta x, \omega) = \frac{\omega}{2\pi} \int_{-\infty}^{+\infty} \tilde{R}(p, \omega) e^{-j\omega p \Delta x} dp, \quad (2.35)$$

it is interesting to look at the relationship between the confocal image ( $\Delta x=0$ ) and the  $p$ -dependent RC in the frequency domain

$$R(\Delta x = 0, \omega) = \frac{\omega}{2\pi} \int_{-\infty}^{+\infty} \tilde{R}(p, \omega) dp. \quad (2.36)$$

Note that the angle-averaged confocal result is a *weighted* summation over the  $p$ -dependent RC function, the weighting function being  $\frac{\omega}{2\pi}$ .

### 2.7.2 Numerical examples for the computation of the reflection coefficients

The Radon transform of the gridpoint gather in figure 2.19, is shown in figure 2.24A together with an amplitude cross section in figure B.

The RC gather (gather of RC functions for a range of focus points) shows clearly the phase shifts at  $p=\pm 500\mu\text{s}/\text{m}$  due to the critical angle in the elastic PP-reflection. Also in the amplitude cross plots these critical angles are present as sharp peaks. Beyond  $|p|=650\mu\text{s}/\text{m}$  the amplitude drops to zero. This corresponds to the largest angles used in the acquisition configuration.

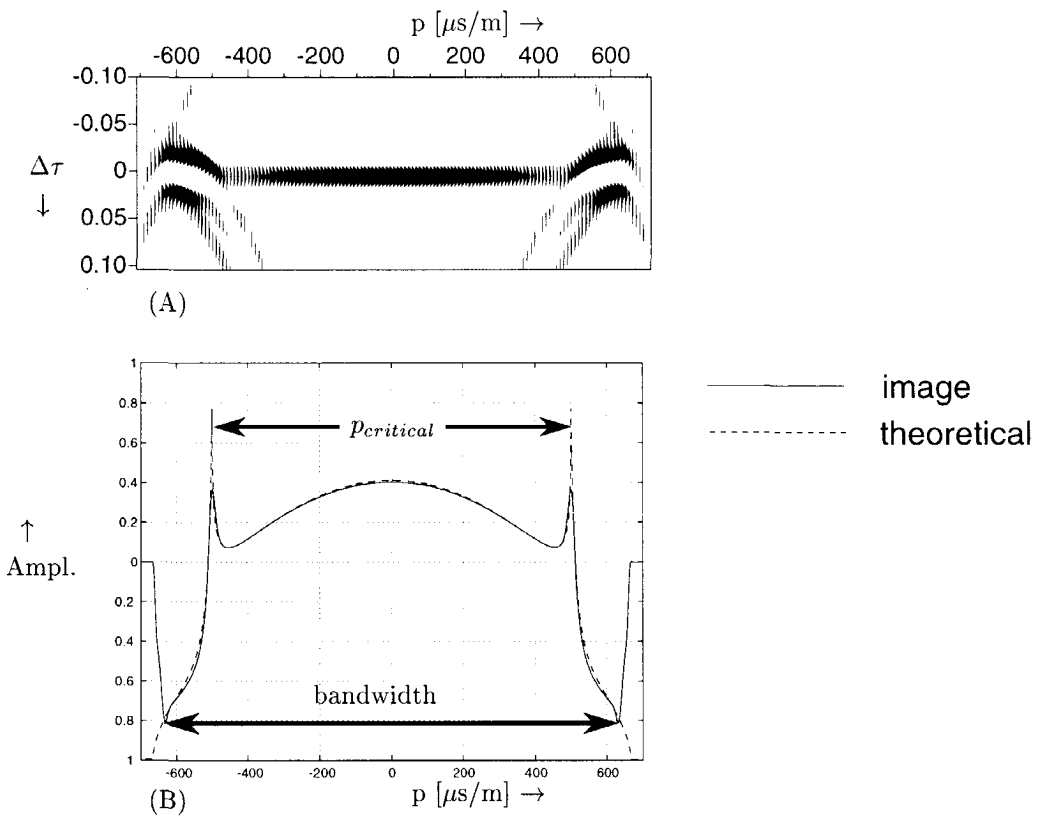


**Fig. 2.24** Reflection coefficients gather (A) and (B) amplitude cross section at  $\Delta\tau = 0$  for the horizontal elastic model. The dashed line indicates the real part of the analytical RC function

The Radon transform of the gridpoint gather in figure 2.21 (dipping reflector), is shown in figure 2.25A together with an amplitude cross section in figure B.

The RC gather also shows phase shifts at  $p = \pm 400 \mu\text{s}/\text{m}$  due to the critical angle in the acoustic PP-reflection. Also in the amplitude cross plots these critical angles are present as peaks. We used split-spread shots symmetrically divided around the midpoint at the surface above the focus point. Due to the dip the left hand side of the RC gather is better illuminated (negative  $p$ -values) than the right hand side. The amplitude cross section drops to zero below  $p = -480 \mu\text{s}/\text{m}$  at the left hand side, whereas the amplitudes drop to zero above  $p = 410 \mu\text{s}/\text{m}$  on the right hand side. Note that the  $p$ -values are defined relative to the dipping layer, and not relative to the subsurface. This means that the influence of the dip has been removed completely from the RC gather.

Note that the results shown in figure 2.25A and B for first focusing in detec-

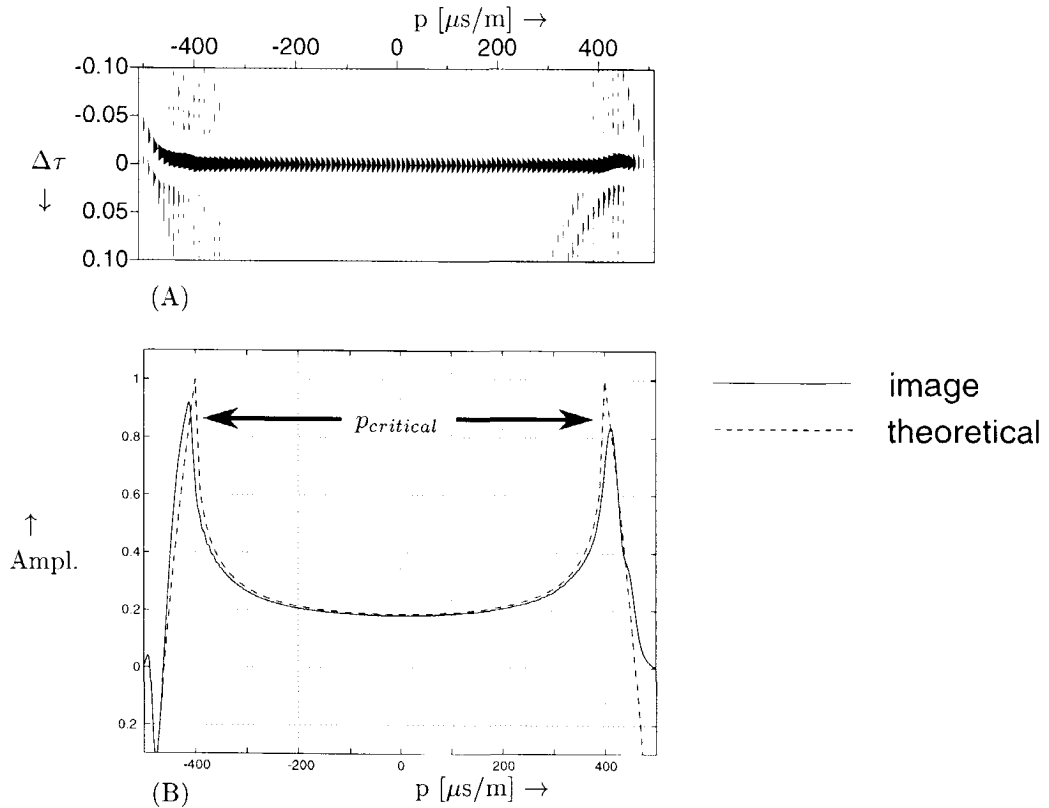


**Fig. 2.25** Reflection coefficients gather and amplitude cross section at  $\Delta\tau = 0$  for the dipping acoustic model. Note that the RC are not shifted by the dip. The dashed line indicates the real part of the analytical RC

tion followed by focusing in emission are the same as first focusing in emission and subsequently in detection.

The relation between the  $p$ -bandwidth in the gridpoint gather in the space-time domain and in the Radon domain is illustrated once more in figure 2.26. The figures (A) and (B) show a short and a long event in the time-ray parameter domain. The corresponding gathers in the time-space domain are shown in figure 2.26(C) and (D). The abrupt decay of the event in the time-rayparameter domain results in the crossing events in the gridpoint gather.

### 2.7.3 Field data example for the computation of the reflection coefficients

The Radon transform of the gridpoint gather in figure 2.22D, is shown in figure 2.27. Figure 2.27A shows the whole gather and figure 2.27B shows the data around  $\Delta\tau = 0$  in more detail. Note that the data at  $\Delta\tau = 0$  should be imaged correctly.

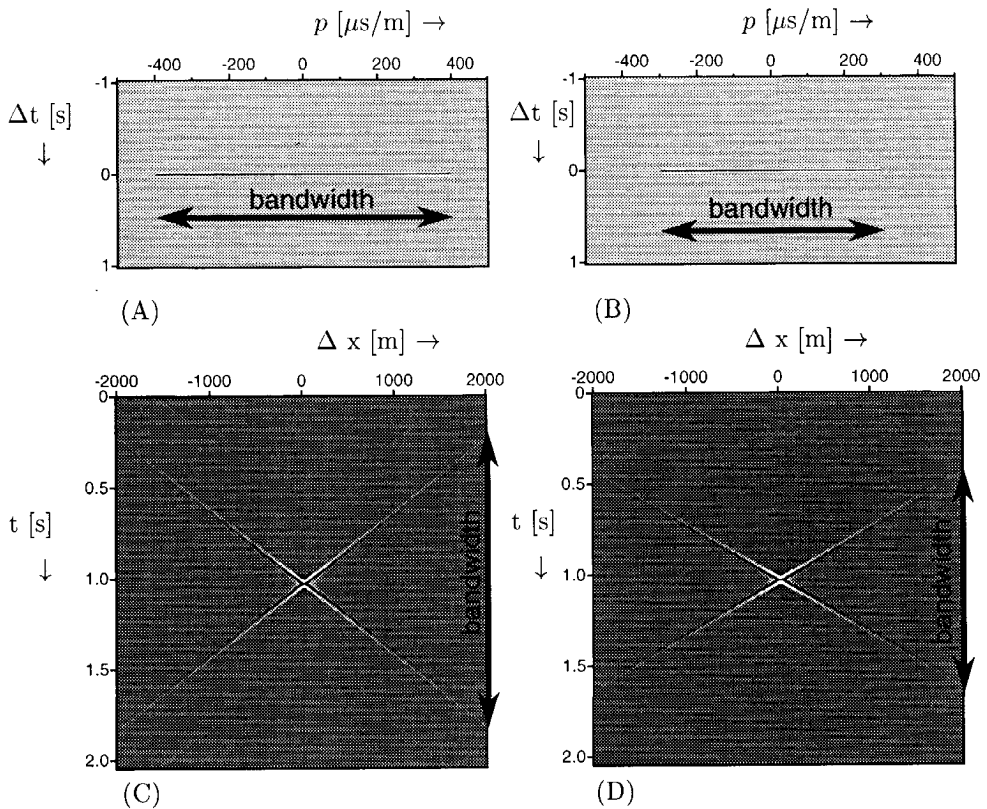


**Fig. 2.26** (A) An event in the time-ray parameter domain with a width of  $400 \mu\text{s}/\text{m}$  and (B) one with a width of  $300 \mu\text{s}/\text{m}$ . (C) and (D) show the corresponding inverse Radon transformed gathers in the time-space domain.

This shows clearly in figure 2.27A, where the data is aligned around  $\Delta\tau = 0$  and curved above and below.

## 2.8 The influence of errors in the dip

As shown in section 2.3, dip information is not needed for the focusing in detection. This means that ignoring the dip, or a wrong dip, will not influence the CFP gather after focusing in detection. For the focusing in emission on the other hand, the dip information is necessary. The dip is needed to compute the correct focusing operator because (1) we need to put the dipole source perpendicular to the interface and (2) we need to focus the secondary sources along the dipping interface (see figure 2.17) in order to remove the local dip in the migration process.

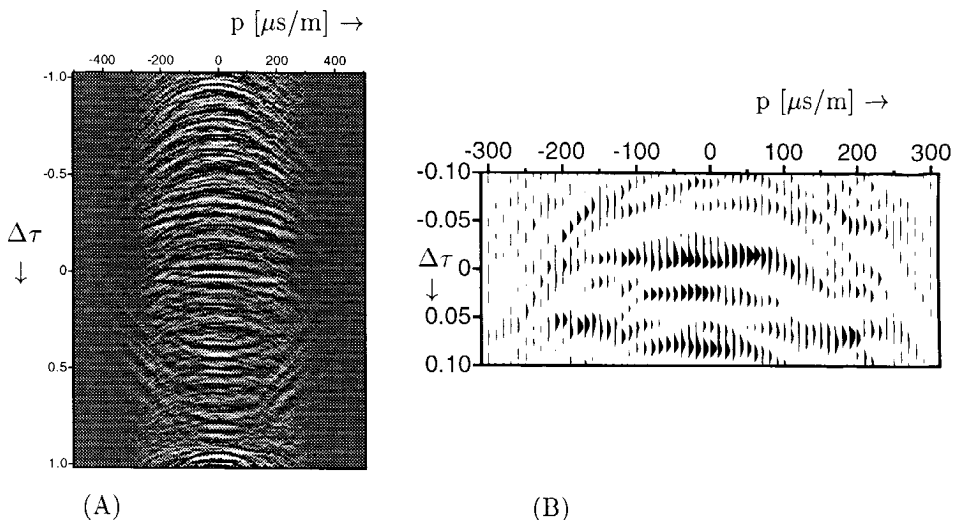


**Fig. 2.27** Reflection coefficients gather for the marine dataset. (B) shows an enlarged part of (A) around the focus point.

In this section the results are shown for ignoring the dip, compensating partially for the dip and taking the dip correctly into account. The four cases discussed are shown schematically in figure 2.28.

The model with a single dipping layer as shown in figure 2.1B is used. If the dip is ignored completely, one operator is used for focusing in detection and one for focusing in emission. This means in the second focusing step one operator is applied to the CFP gather a number of times, each time shifted laterally for another bifocus point (see section 2.3.2 page 20). The secondary sources will not be focused along the reflector, but along a horizontal plane through the focus point as shown in figure 2.28(A). The resulting gridpoint gather is shown in figure 2.29(A). Note that the gridpoint gather is rotated compared to figure 2.29(D) due to the dip.

The Radon transform of the gridpoint gather in figure 2.29A is shown in figure 2.30(B), together with the amplitude cross section at  $\Delta\tau = 0$  in 2.30(A). Due to the fact that we did not account for the dip, the imaged function is not symmetrical in  $p = 0$ . It appears as a shifted version of the theoretical function for the reflectivity. An approximate correction for this shift along the  $p$ -axis can be made by estimating the shift numerically in this example. The shift in  $p$ -values in figure 2.30(A) for the left critical angle is from  $p=340\mu\text{s}/\text{m}$  to  $p=400\mu\text{s}/\text{m}$ . Using a  $c_p=2000\text{m}/\text{s}$  this means a shift from  $42.8^\circ$  to  $51.3^\circ$ , or  $\Delta\alpha=10.3^\circ$ . The shift for the right critical angle is from  $53.1^\circ$  to  $65.3^\circ$ , or  $\Delta\alpha=12.2^\circ$ . The average  $\Delta\bar{\alpha}=11.3^\circ$  which is equal to the local dip.

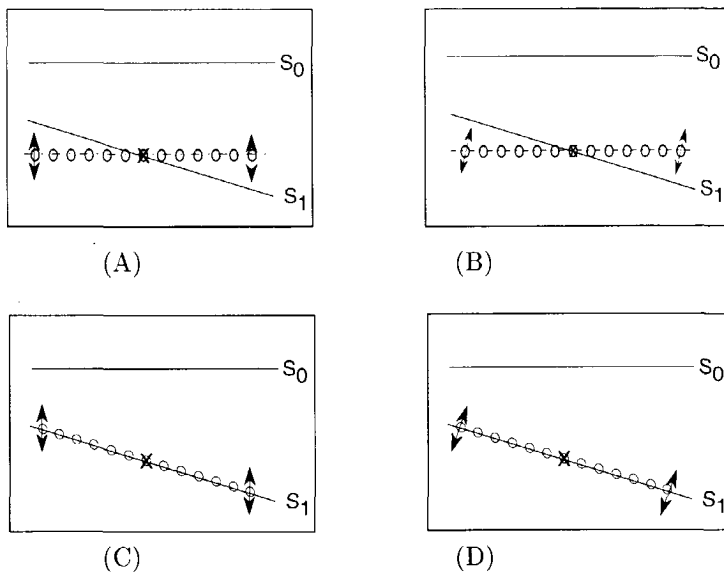


**Fig. 2.28** The four types of second focusing used for a dipping reflector. (A): Ignoring the dip completely. (B): including the dip in the second focusing operators, but only one operator (focusing along a flat line). (C): focusing along reflector without dip orientation in second focusing operator. (D): with the correct second focusing operators.

The result is shown in figure 2.30C. We still make a small error, since we approximate the focusing operator for a deeper/shallower focus point by a time shifted one for the focus point above/below and we did not use the correct orientation for the dipole in the focusing operator.

If we use the dip for the orientation of the dipole in the second focusing operator for the correct confocal illumination, we image the correct reflectivity for the structural image (confocal migration). But if this operator is repeatedly applied on the CFP gather (each time laterally shifted, see section 2.3.2 page 20) then the bifocal imaging is done along a horizontal plane through the focus point as shown in figure 2.28B. The imaged gridpoint gather is shown in 2.29B.

The Radon transform of the gridpoint gather in figure 2.29B is shown in figure 2.31B, together with the amplitude cross section at  $\Delta\tau = 0$  in 2.31A. Due to the fact that the focusing is done along the reflector, although the correct dipole orientation is used, there is a shift in p-values and incorrect amplitudes near the critical angles.

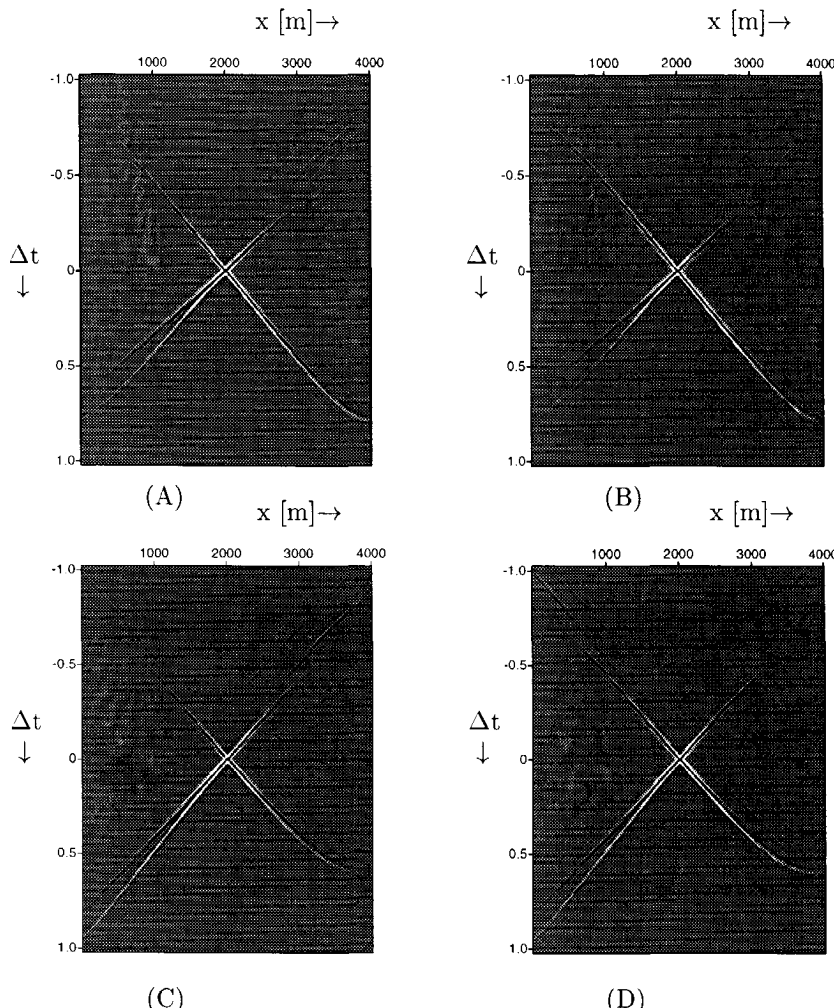


**Fig. 2.29** The gridpoint gathers for a dipping layer using the second focusing as shown in figure 2.28. (A): Ignoring the dip completely. (B): including the dip in the second focusing operators, but only one (shifted) operator (focusing along a flat line). (C): focusing along reflector without dip orientation in second focusing operator (focusing along the interface). (D): with the correct second focusing operators. The Radon transforms of A, B, C and D are shown in the figure 2.30, 2.31, 2.32 and 2.25.

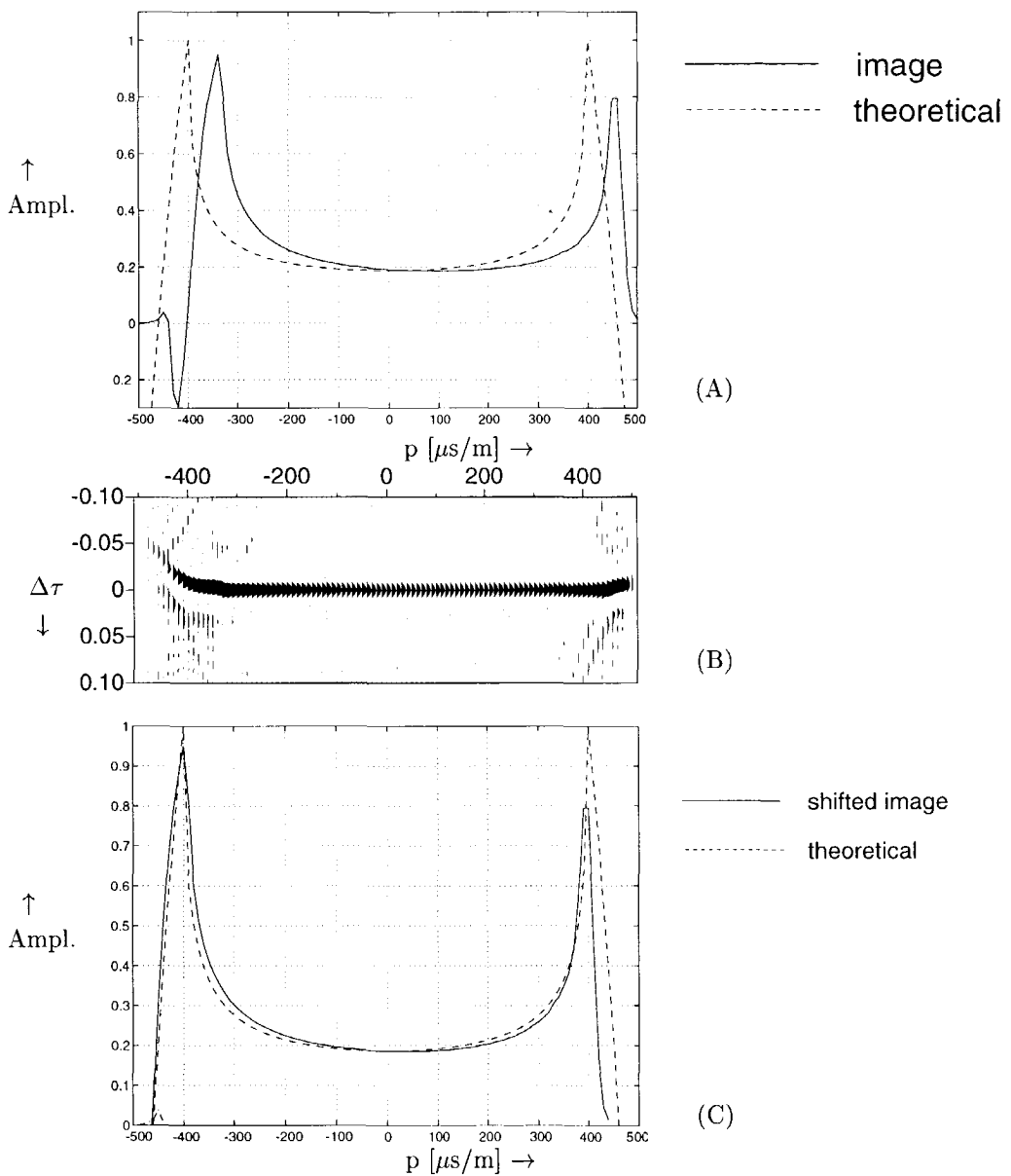


**Fig. 2.30** Reflection coefficients gather (B) and amplitude cross section at  $\Delta\tau = 0$  (A), in case we ignore the dip completely. The dashed line indicates the real part of the analytical RC (C) The amplitude cross sections after a shift over an angle, which is equal to the local dip of the imaged reflector. Note that the shifted imaged RC still differ from the analytical.

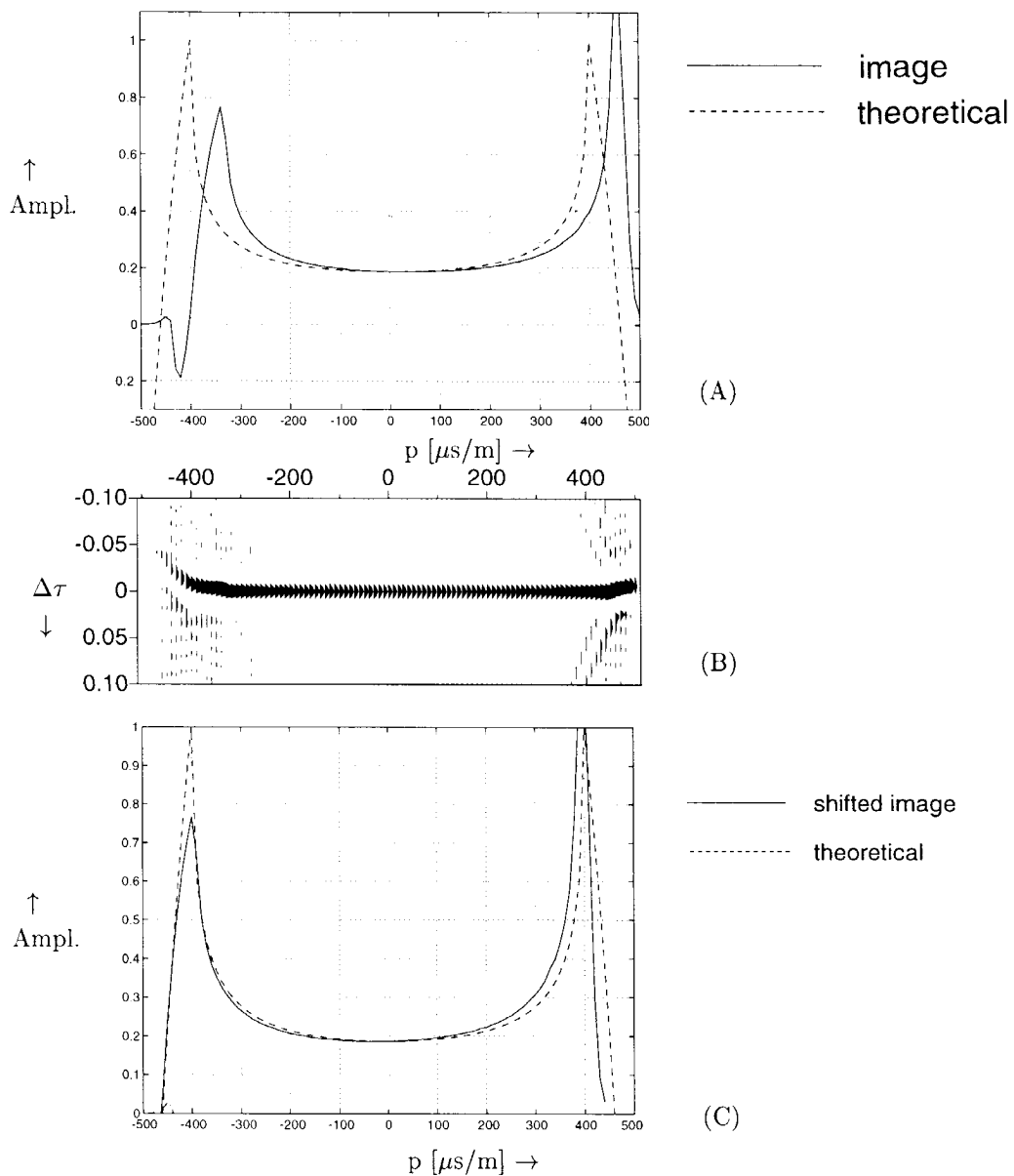


**Fig. 2.31** Reflection coefficients gather and amplitude cross section at  $\Delta\tau = 0$ , in case the dip is incorporated in the dipole orientation, but the second focusing step is done along a horizontal plane. The dashed line indicates the real part of the analytical RC (C) The amplitude cross sections after a shift over an angle, which is equal to the local dip of the imaged reflector.

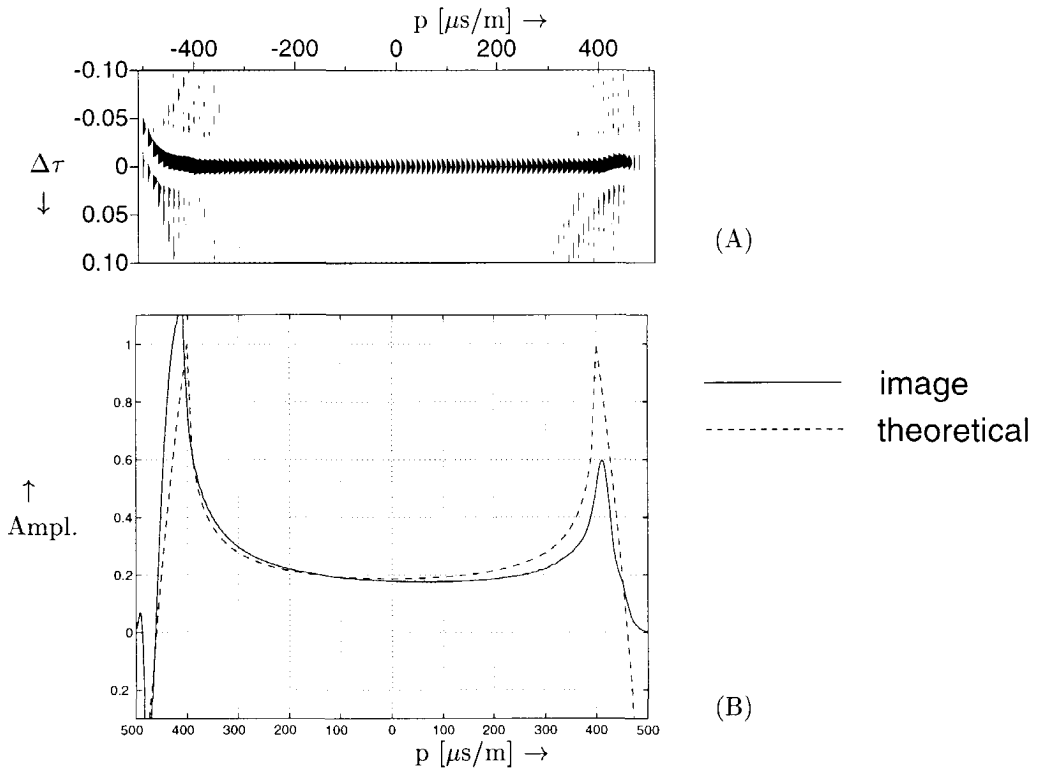


**Fig. 2.32** Reflection coefficients gather and amplitude cross section at  $\Delta\tau = 0$ , in case the dip is not incorporated in the dipole orientation, but the second focusing is done along the reflector. The dashed line indicates the real part of the analytical RC. Note that the imaged RC is not shifted in  $p$  compared with the analytical, but the amplitudes differ significantly.

An approximate correction for this shift along the  $p$ -axis can be made again by estimating the shift numerically in this example. The result is shown in figure 2.31C. Since the amplitudes at the critical angles are even worse than without any dip correction, one may conclude that in this example the two errors we make in ignoring the dip completely, cancel each other partly.

If the dip orientation is ignored, but the imaging in the second focusing is done along the reflector, as shown in figure 2.28(C), the gridpoint gather as shown in figure 2.29(C) is computed. The corresponding RC gather with amplitude cross section are shown in figure 2.32 (A) and (B). The amplitude cross section is not shifted from the analytical RC function, but there is a significant difference in amplitudes due to the fact that the dip is not included in the second focusing operators.

The correct gridpoint gather (using correct dipole orientation and a set of second

focusing operators along the dipping interface, as shown in figure 2.28D) is shown as a reference in 2.29D.

This is of course the best result for the RC gather, which is shown in figure 2.25. Using no information on the dip during the imaging, as shown in figure 2.28(A) is (in this example) better than using the dip information partly, as shown in figure 2.28(B) and (C). If the dip is not removed in the imaging step, than before using the RC data in the inversion with a shift in  $p$  (which corresponds to the angle of the local dip) the dip influence can be removed approximately.

Finally the same example as given in figure 2.29(A), where the dip was ignored in the imaging, has been repeated, but now with a dip varying from  $0^\circ$ , via  $5^\circ$  and  $10^\circ$  to  $20^\circ$ .

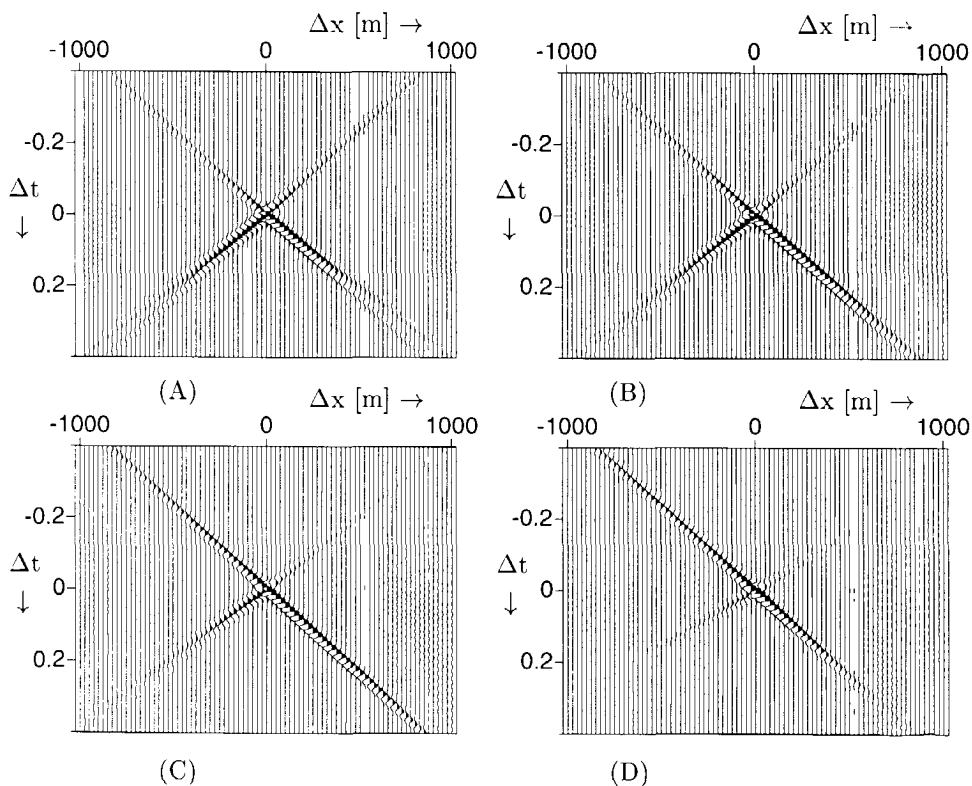


**Fig. 2.33** Four gridpoint gathers corresponding to a focus point on a reflector at 500m depth with a dip from  $0^\circ$ ,  $5^\circ$ ,  $10^\circ$  and  $20^\circ$ .

The focus point is located on the reflector at a depth of 500m. A moving spread acquisition has been used with a shot range from -2000m to +2000m and with a spread length of  $\pm 3000$ m. In the  $10^\circ$  and  $20^\circ$  case the shot range and receiver range was limited to -2500m and -1400m due to the fact that the dipping layer hits the surface at these offsets.

The change in the gridpoint gathers due to the increasing dip is shown in figure 2.33(A)-(D). Although the acquisition at the surface is fixed, the reflection angles at the reflector differ due to the dip. This can be seen in the corresponding gridpoint gathers in the Radon domain which are shown in figure 2.34 and the amplitude cross sections in figure 2.35. The response seems to shift to the right.

In order to compensate for the dip the following two steps should be followed:

- the surface acquisition should be adjusted in order to illuminate and detect with the optimal angle range
- the imaging (second focusing step) should be done along the interface in order to get the correct local reflectivity of the gridpoint.

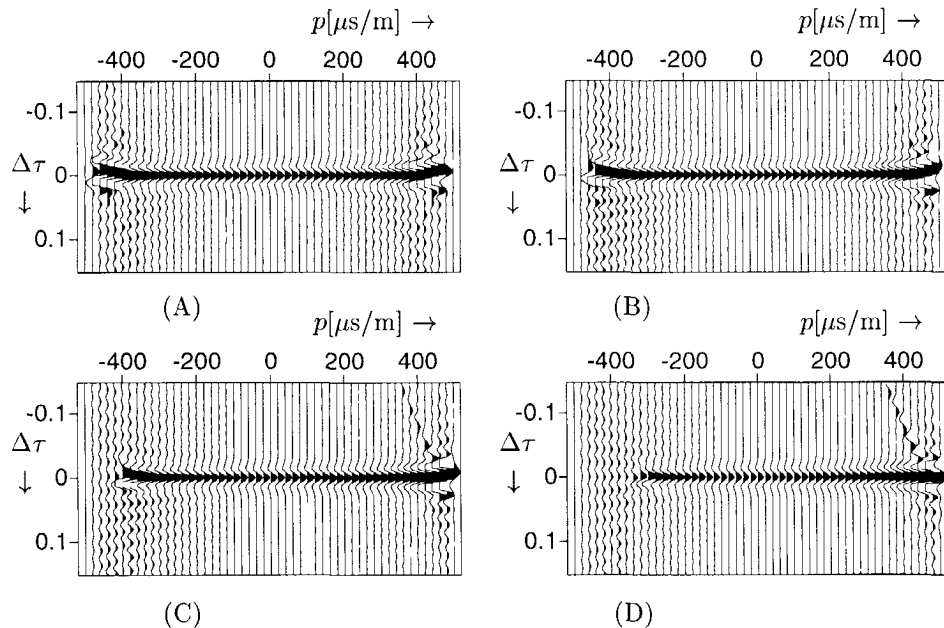


**Fig. 2.34** Four gridpoint gathers in the Radon domain corresponding to the gridpoint gathers in figure 2.33.

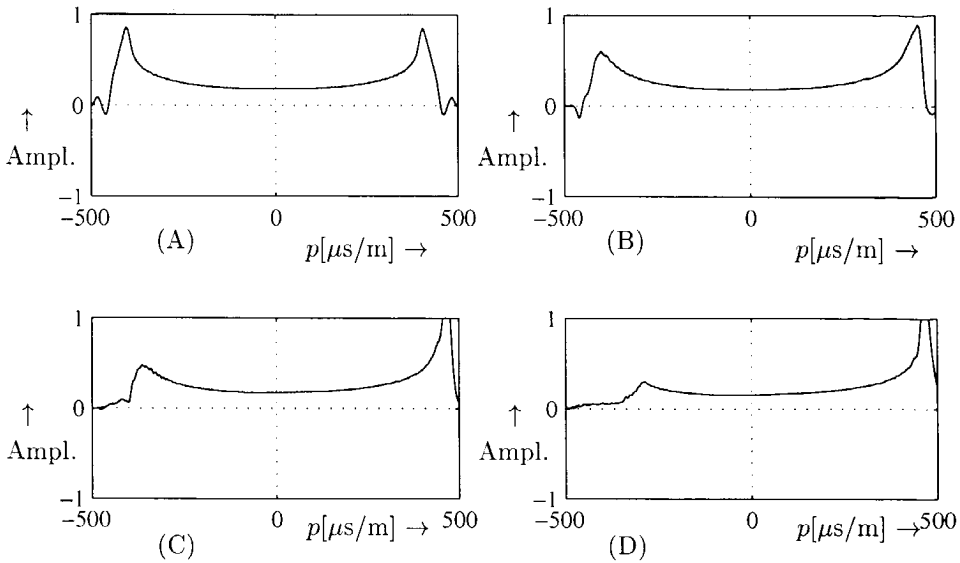


Fig. 2.35 Four amplitude cross sections of the gridpoint gathers in the Radon domain shown in figure 2.34.

## 2.9 Determination of the local dip

The local dip can be estimated by the cross correlation of CFP gathers. Consider the situation shown in figure 2.36. Around the dipping event  $S_1$  we choose 2 focus points at a lateral distance  $\Delta x$ . These are indicated by A and B. These focus points can be above, below or on the reflector, as long as they are focused at the same depth (same focusing operator, only shifted  $\Delta x$ ).

If we choose the focus point A above the interface, the CFP gather will be equal in travel times to the response of a secondary source at  $A'$ , which is the mirror image of A in the dipping reflector. The same reasoning can be used for focus point B and  $B'$ . The first focusing operators and the corresponding CFP responses are shown in figure 2.37. The difference in one-way time  $\Delta t$  between the CFP-responses is related to the difference in depth of the two mirror sources  $A'$  and  $B'$ ,

$$\Delta t = \Delta z / c. \quad (2.37)$$

We know that the lateral distance between the two mirror sources equals the lateral distance  $\Delta x$  between the focus points A and B. This means that the hypotenuse of the dashed triangle in figure 2.36 equals  $\Delta x$ . The vertical side of the dashed triangle is given by  $\Delta t c = \Delta z$ . The angle  $2\phi$  equals 2 times the dip of the reflector. This

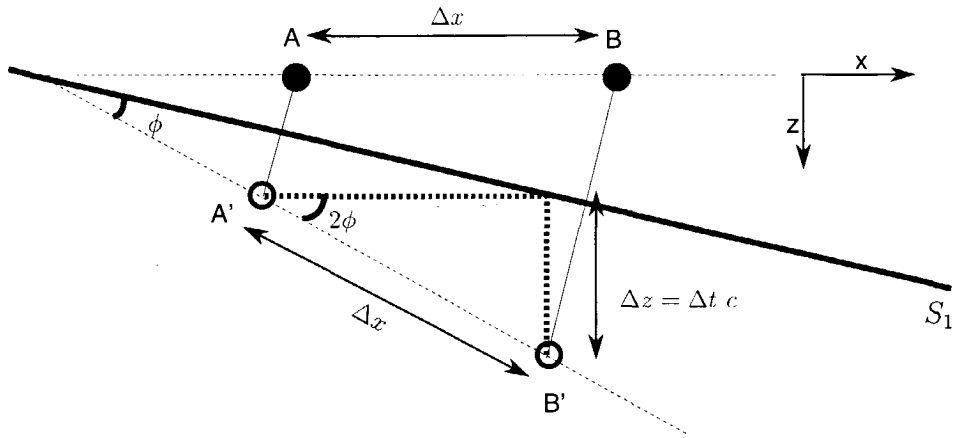


Fig. 2.36 The configuration for the two focus points used in the dip determination.

means that the angle can be computed, if  $\Delta t$  and  $c$  are known, by

$$\sin(2\phi) = c \Delta t / \Delta x = \Delta z / \Delta x. \quad (2.38)$$

The time shift  $\Delta t$  can be estimated by finding the maximum in the cross correlation of the CFP gathers belonging to the focus points A and B. We should use only a relative small area around the apex (small offsets  $\Delta x$  in the CFP gather), because we are interested in the shift of the apex. The large offsets in the CFP gather can not be used here. The same procedure can be used if the focus point A is shifted to the left, so on or below the reflector  $S_1$ .

### 2.9.1 Numerical example for the determination of the local dip

In this example we use again model B in figure 2.1. We choose focus points at 500m depth 120m and 240m to the right of the reflector at 500m. The CFP-responses together with the travel time curves for the focusing operators are shown in figure 2.37. We use only the area around the apex of the CFP-response, since we are interested in the shift of the apex. The cross correlation of these CFP gathers is shown in figure 2.38. The maximum is found at  $\Delta t = 0.022$ . The offset  $\Delta x$  was chosen as 120m. This means  $p = \Delta t / \Delta x = 1.8 \times 10^{-4}$ . With  $c = 2000$  m/s this gives an angle of  $\phi = 11^\circ \pm 1.0^\circ$ . This corresponds well with the  $11.3^\circ$  dip of the model.

### 2.9.2 Field data example for the determination of the local dip

We use the marine dataset as shown in figure 2.2. We choose 2 focus points with a lateral distance of 200m. The CFP-responses are shown in figure 2.39. The cross correlation of the CFP-responses from figure 2.39 is shown in figure 2.40.

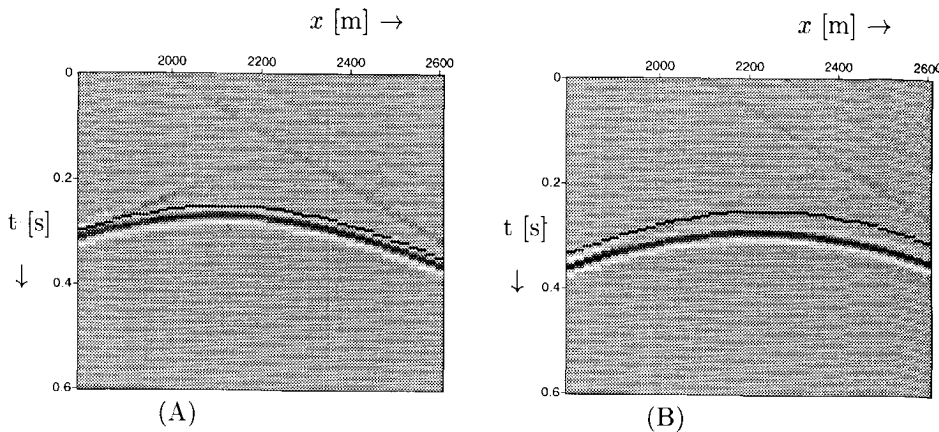


**Fig. 2.37** The CFP-responses for the focus points A and B with overlaying the two focusing operators.

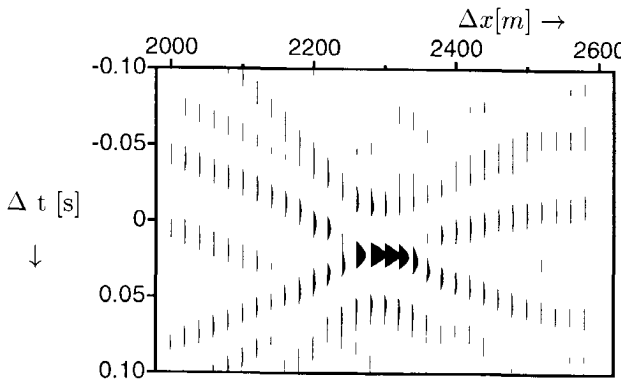


**Fig. 2.38** The cross correlation of the two CFP gathers showing a maximum shifted from  $\Delta t = 0$  due to the local dip.

The maximum value is found at  $\Delta t = 0$ . This means that there is no dip. This corresponds to the almost flat reflector in figure 2.2.

## 2.10 The reflection coefficient gather

### 2.10.1 Building the RC gather

In section 1.4 we discussed the imaging of one reflector, resulting in the reflectivity-gather. The amplitude cross section at  $\Delta\tau=0$  of the reflectivity-gather shows the reflection coefficients for plane waves of the imaged reflector. In the earth we have many reflectors, as shown in the example of figure 2.27 where we imaged one reflector

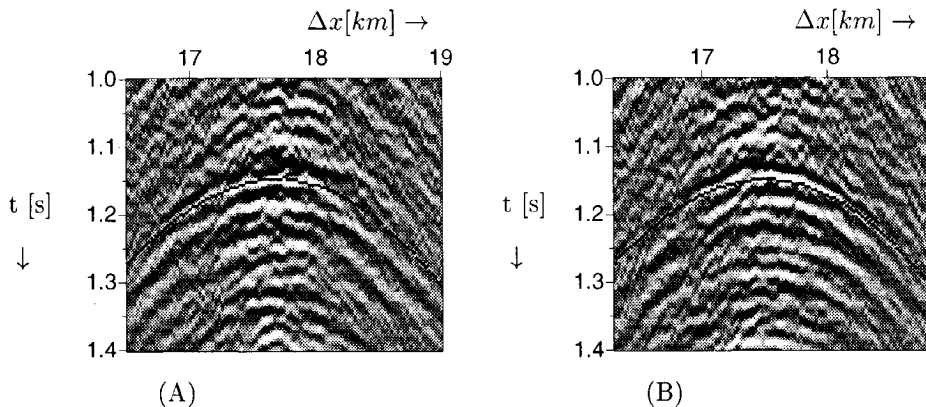


Fig. 2.39 The CFP-responses for the focus points at a lateral distance of 200m with overlaying the two focusing operators.

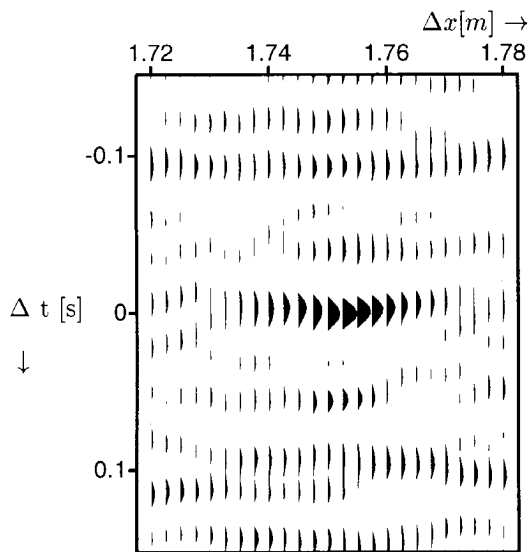
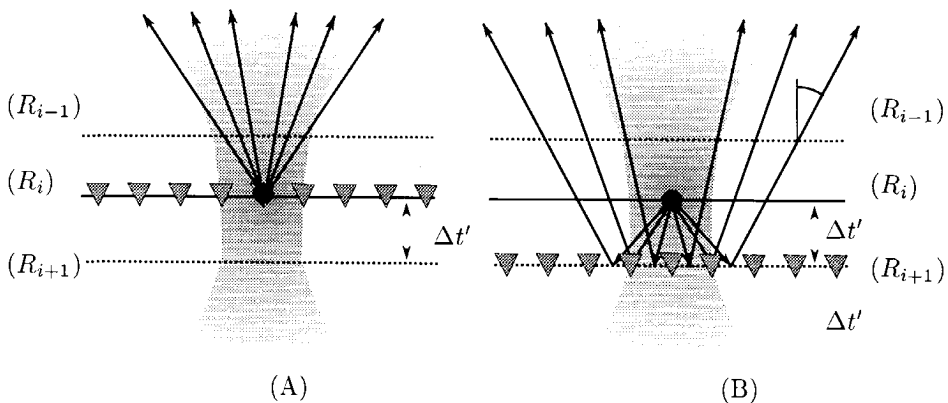


Fig. 2.40 The cross correlation of the two CFP gathers showing a maximum at  $\Delta t=0$ , indicating a zero dip.

at  $\Delta\tau=0$  correctly. The reflectors above and below are imaged, but they are not aligned along a straight line in  $p$ . They are present as curved events above and below  $\Delta\tau=0$ . Note that it is this curvature that is used in the CFP velocity estimation method (Thorbecke, 1997) (Kabir, 1997).

The RC gather, which gives the imaged RC functions at every time  $t'$ , can be built up by defining a focus point at every time sample and selecting  $\Delta\tau=0$  from



**Fig. 2.41** In (A) the first and second focus points are at the same boundary  $R_i$ . In (B) the second focus point is on boundary  $R_{i+1}$  at  $\Delta t$  below the first focus point. The arrows show the response in the CFP gather.

the corresponding gridpoint gathers in the radon domain. This procedure will give a correct RC gather, but it can be made more efficient. As already shown in Thorbecke (1996), the width of the focusing beam is approximately constant over a certain time range  $\Delta T$  around the focus point. This means that for the first focusing step we do not need to focus at every time sample, but we can use one first focusing step for a range of time samples. So if we want to image reflector  $R_{i+1}$  in figure 2.41, we can use the CFP gather corresponding to the focus point on reflector  $R_i$ , if reflector  $R_{i+1}$  is less than  $\Delta T$  away from reflector  $R_i$  in travel time.

Note that the difference in travel time between event  $R_i$  and  $R_{i+1}$  in the CFP gather is in *two-way* time, whereas the reflector  $R_i$  is located in the CFP in *one-way* time. This is shown in figure 2.41B, where reflector  $R_{i+1}$  is 'illuminated' by a focused source above the interface, instead of on the interface. So the event  $R_{i+1}$  is located in the CFP gather at the sum of the one-way travel time from  $R_{i+1}$  to the surface *plus* the travel time from reflector  $R_i$  to  $R_{i+1}$ , as indicated by the arrows in figure 2.41. We should account for this in the second focusing step.

This can be approximated by using a second focusing operator at time  $t'_i + 2\Delta t'$  for imaging the reflector at  $t'_i + \Delta t'$ , using the CFP gather for a focus point at  $t'_i$ . In this way we can build up the RC gather with less CFP gathers as shown in figure 2.42. The number of second focusing steps is the same as the number of time samples in the RC gather. Figure 2.43 shows the RC gather (only in focus at  $t'=1.9$ s) together with the RC gather for one lateral position of the marine dataset (at all times in focus).

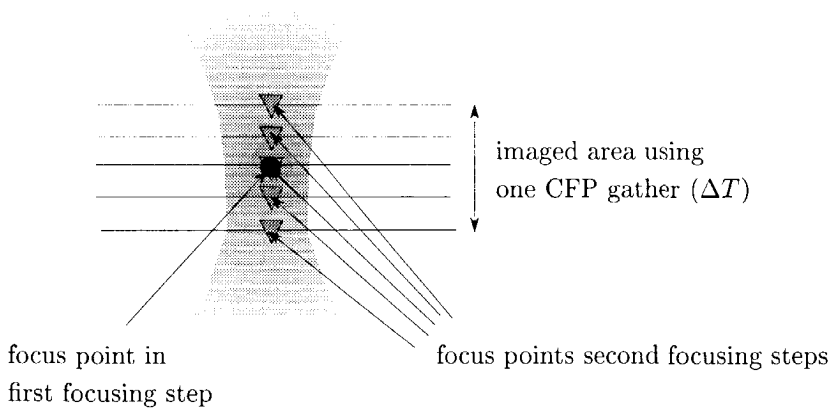


**Fig. 2.42** The use of one CFP gather for imaging the RC gather over a range of time samples  $\Delta T$ .

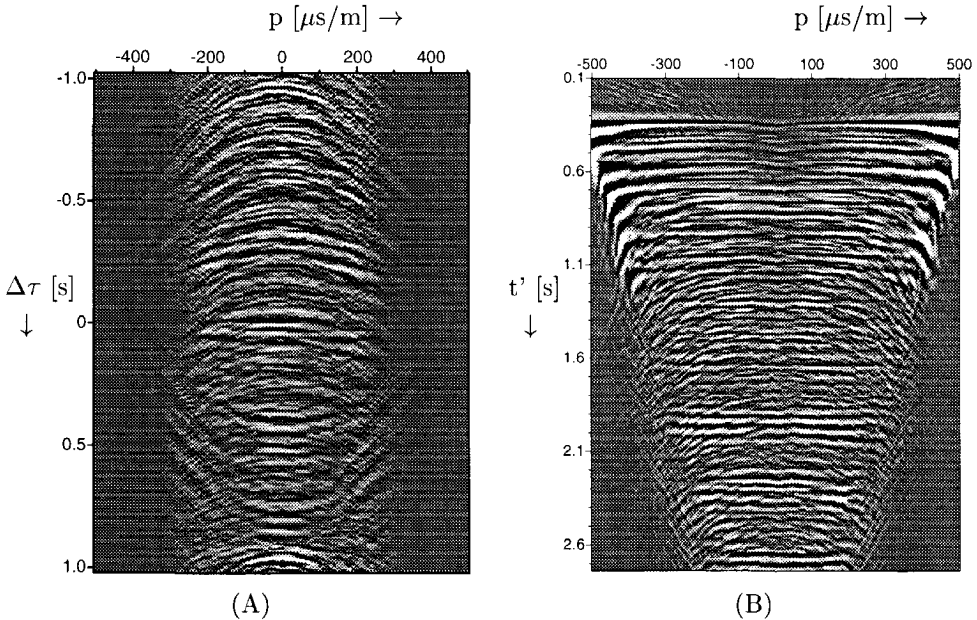


**Fig. 2.43** (A) The RC gather for a focus point at 2.2s and (B) the RC gather, showing the reflection coefficients for 0.1s to 2.7s.

### 2.10.2 Removing noise and aliasing in the gridpoint domain

We used a real density log from the North Sea area with a constant P-wave velocity of 2500 m/s to model a synthetic 1D shot record. This shot record, shown in Figure

2.44(A), has been migrated and the imaged RC gather is shown in figure 2.44(B). In

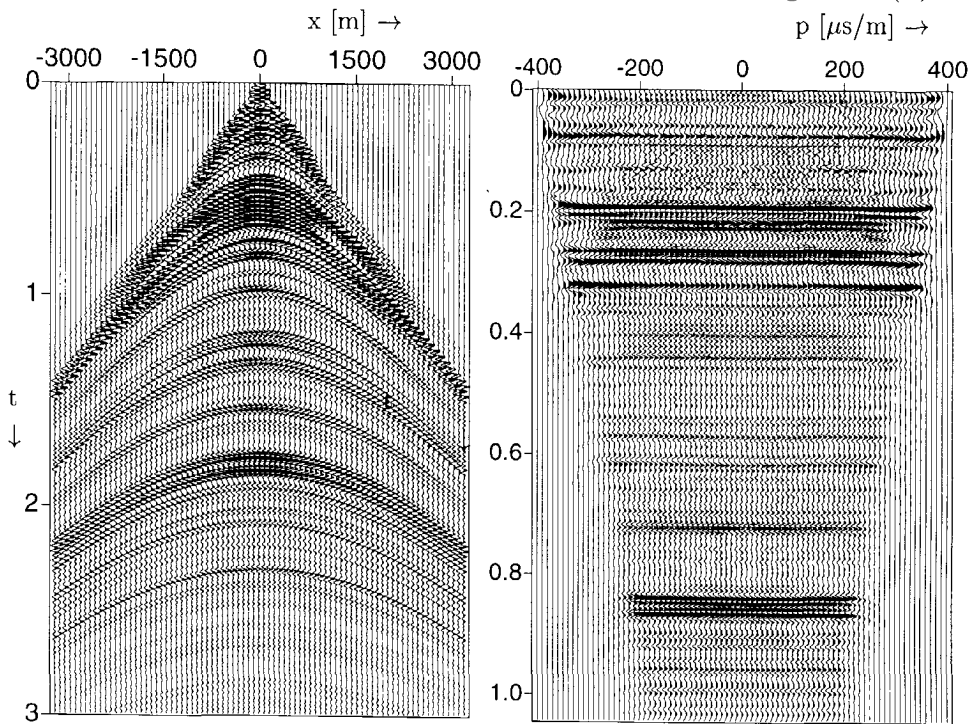


**Fig. 2.44** The shot record (left) and migrated RC gather (right) using only the density log and a constant  $c_p$  of 2500 m/s.

figure 2.45 the gridpoint gather and the corresponding gather in the Radon domain are shown for one focus point at 500m. Clearly the focused energy is in the centre of the gridpoint gather, and the aliased energy is scattered around. The aliased energy results in jittering noise in the gridpoint gather in figure 2.45.

By tapering around  $\delta\tau = 0, \delta x = 0$ , most of the aliased energy is removed, as can be seen in 2.46(A). The jittering in the gridpoint gather is also removed (see figure 2.46(C)) and we see a smooth amplitude cross section curve in figure 2.47(A). Note that in general by tapering the gridpoint gather the amplitudes near critical angles will be reduced strongly. But if we are only interested in small angles ( $< 40^\circ$ ), this is a powerful method to remove noise and aliased energy.

A less crude method is preferred, if we want to preserve the critical angle information. This can be done by a so-called focusing mute. The mute is defined by two crossing lines through the center of the gridpoint gather, which correspond to

$p$ -values of  $\pm p_{max}$ . The data in the left and right cone defined by these crossing lines is muted, with the exception of an area around the center.

An example of this 'focusing mute' is shown in figure 2.46(B). Clearly most aliased energy has been muted and the corresponding gather in the Radon domain in figure 2.45(D) looks much cleaner. The amplitude cross section curve in figure 2.47(B) is also much cleaner, but shows more detail than the curve in 2.47(A).

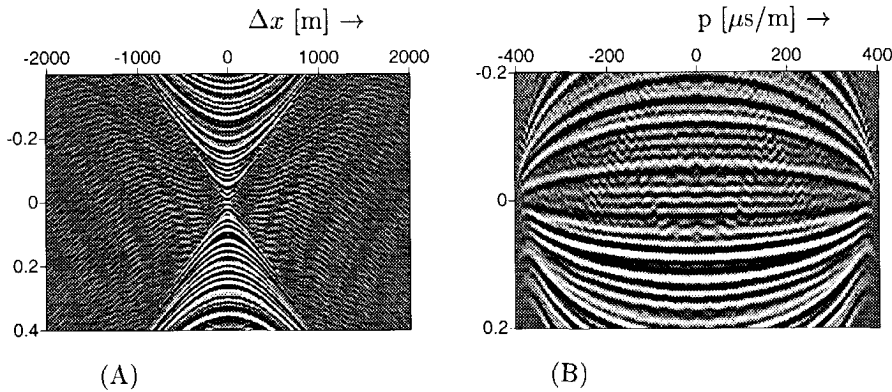


**Fig. 2.45** The gridpoint gather (A) and its Radon transform (B) for one focus point at 500m using the density contrast medium.

In this specific example of only density contrasts, there will be no critical angle (for incident angles  $< 90^\circ$ ). The averaged imaged reflectivity of the small layers with only density contrasts should be a fairly smooth function. In figure 2.47 the amplitude cross sections of the filtered and original gridpoint gathers are shown. The improvement is clearly visible.

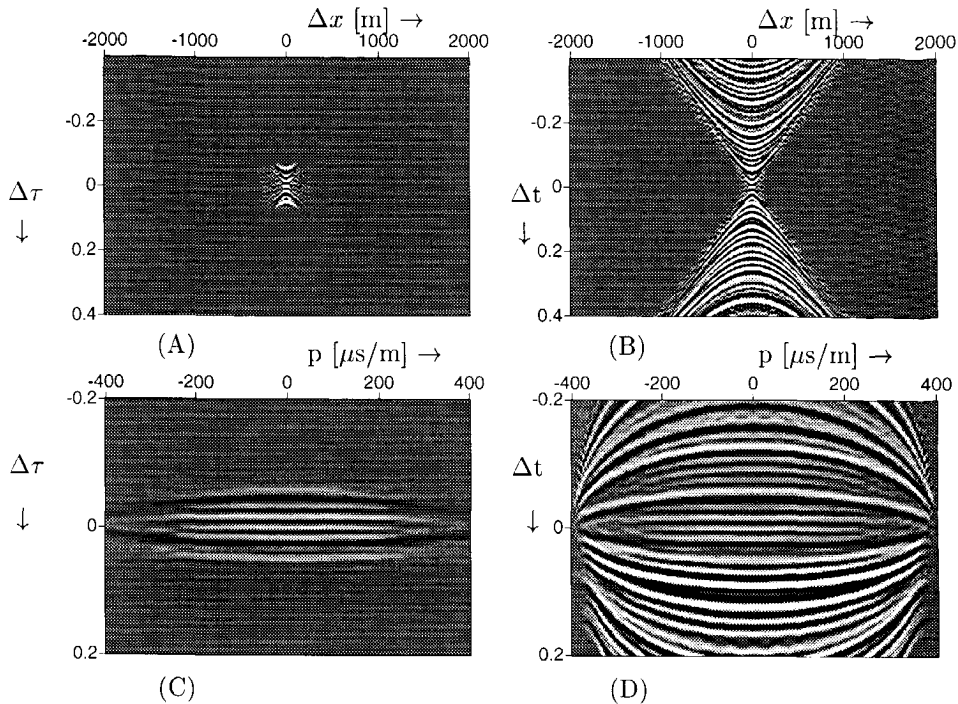


**Fig. 2.46** The gridpoint gathers (A,B) and their Radon transform (C,D) for one focus point at 500m using the density contrast medium and using a mute around the focus point respectively a focusing mute (mute boundary given by  $\pm 2600\text{m/s}$ ).

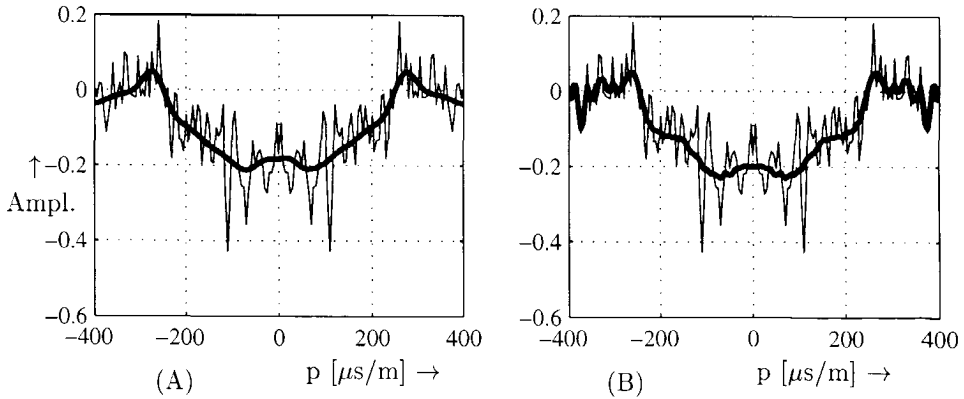


**Fig. 2.47** The smooth amplitude cross sections (thick line) at  $\Delta\tau=0$  of the gridpoint gathers with tapering (A) respectively muting (B) in the space-time domain (figure 2.46(C,D)) and the strongly fluctuating (thin line) amplitude cross section of the gridpoint gather without tapering in the space-time domain (figure 2.45(B)).



## Appendix II

# Multi component imaging of angle-dependent reflection information.

*This appendix describes the imaging of the angle-dependent reflectivity for multi component data. This appendix is an extension from the PP data in the previous chapter to PS<sup>1</sup>, SP and SS data.*

### II.1 Introduction

In chapter 2 the imaging of the reflection coefficients  $\tilde{R}_{PP}(p; z_m)$  for PP-data has been described. In a similar way the imaging of the reflection coefficients  $\tilde{R}_{PS}(p; z_m)$  for PS,  $\tilde{R}_{SP}(p; z_m)$  for SP and  $\tilde{R}_{SS}(p; z_m)$  for SS data can be done (Berkhout et al., 1997). The four components of the RC matrix are shown schematically in figure II.1.

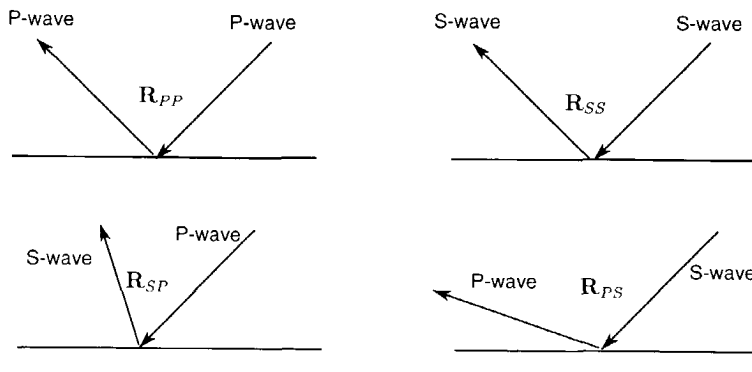


Fig. II.1 The four components of the RC matrix.

<sup>1</sup>PS means from S-wave to P-wave converted data.

## II.2 General elastic forward modeling using the 'WRW model'

The general description for elastic wave propagation of primary reflections is shown in equation II.1. In this equation also the conversions during the propagation from the surface to interface  $S_m$  and vice versa are incorporated. The data is assumed to be free of surface-related effects (which is the situation after decomposition and the removal of the direct wave and the surface-related multiples) and only the primary reflections are incorporated.

$$\begin{aligned} & \begin{pmatrix} \mathbf{P}_{PP}^-(S_0) & \mathbf{P}_{PS}^-(S_0) \\ \mathbf{P}_{SP}^-(S_0) & \mathbf{P}_{SS}^-(S_0) \end{pmatrix} = \\ & \begin{pmatrix} \mathbf{D}_P^-(S_0) & \mathbf{0} \\ \mathbf{0} & \mathbf{D}_S^-(S_0) \end{pmatrix} \sum_m \left[ \begin{pmatrix} \mathbf{W}_{PP}(S_0, S_m) & \mathbf{W}_{PS}(S_0, S_m) \\ \mathbf{W}_{SP}(S_0, S_m) & \mathbf{W}_{SS}(S_0, S_m) \end{pmatrix} \times \right. \\ & \left. \begin{pmatrix} \mathbf{R}_{PP}(S_m) & \mathbf{R}_{PS}(S_m) \\ \mathbf{R}_{SP}(S_m) & \mathbf{R}_{SS}(S_m) \end{pmatrix} \begin{pmatrix} \mathbf{W}_{PP}(S_m, S_0) & \mathbf{W}_{PS}(S_m, S_0) \\ \mathbf{W}_{SP}(S_m, S_0) & \mathbf{W}_{SS}(S_m, S_0) \end{pmatrix} \right] \begin{pmatrix} \mathbf{S}_P^+(S_0) & \mathbf{0} \\ \mathbf{0} & \mathbf{S}_S^+(S_0) \end{pmatrix} \end{aligned} \quad (\text{II.1})$$

The matrices  $\mathbf{S}_P^+(S_0)$  and  $\mathbf{S}_S^+(S_0)$  define the source (array) signature and its directivity characteristics for downgoing P and S-waves, the matrices  $\mathbf{D}_P^-(S_0)$  and  $\mathbf{D}_S^-(S_0)$  define the directivity characteristics of the receiver (array) for upgoing P and S-waves after decomposition.

A simplification of the forward model can be made by restricting the conversion of P-waves to S-waves and vice versa to take place only in the reflection at interface  $S_m$ . This simplified model for elastic wave propagation of primary reflections is described in equation II.2 and is shown in figure II.2.

$$\begin{aligned} & \begin{pmatrix} \mathbf{P}_{PP}^-(S_0) & \mathbf{P}_{PS}^-(S_0) \\ \mathbf{P}_{SP}^-(S_0) & \mathbf{P}_{SS}^-(S_0) \end{pmatrix} = \\ & \begin{pmatrix} \mathbf{D}_P^-(S_0) & \mathbf{0} \\ \mathbf{0} & \mathbf{D}_S^-(S_0) \end{pmatrix} \sum_m \left[ \begin{pmatrix} \mathbf{W}_P(S_0, S_m) & \mathbf{0} \\ \mathbf{0} & \mathbf{W}_S(S_0, S_m) \end{pmatrix} \times \right. \\ & \left. \begin{pmatrix} \mathbf{R}_{PP}(S_m) & \mathbf{R}_{PS}(S_m) \\ \mathbf{R}_{SP}(S_m) & \mathbf{R}_{SS}(S_m) \end{pmatrix} \begin{pmatrix} \mathbf{W}_P(S_m, S_0) & \mathbf{0} \\ \mathbf{0} & \mathbf{W}_S(S_m, S_0) \end{pmatrix} \right] \begin{pmatrix} \mathbf{S}_P^+(S_0) & \mathbf{0} \\ \mathbf{0} & \mathbf{S}_S^+(S_0) \end{pmatrix} \end{aligned} \quad (\text{II.2})$$

In the multi-component imaging process the focusing in detection can be split into two parts: the operator  $\vec{F}_{P,i}^\dagger(S_m, S_0)$  for focusing in detection for P-waves for a certain focus point  $x_i$  at depth  $S_m$ , defined by

$$\vec{F}_{P,i}^\dagger(S_m, S_0) \mathbf{D}_P^-(S_0) \mathbf{W}_P(S_0, S_m) = \vec{I}_i^\dagger(S_m) \quad (\text{II.3})$$

and the operator  $\vec{F}_{S,i}^\dagger(S_m, S_0)$  for focusing in detection for S-waves is defined for a

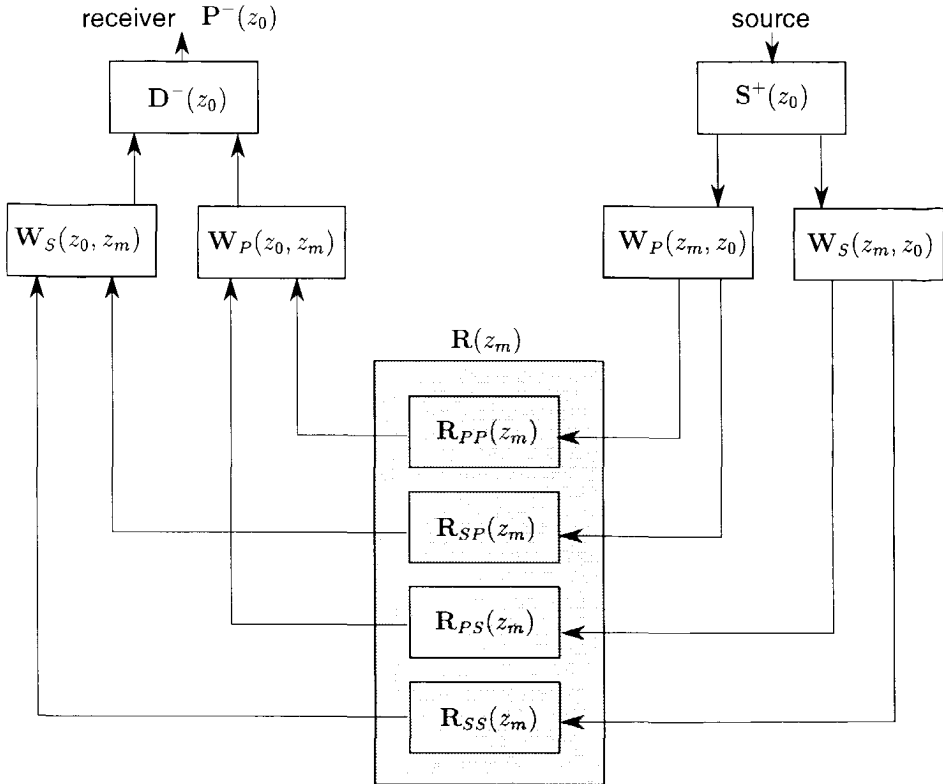


**Fig. II.2** The scheme for elastic forward modeling of primary reflections after surface-related preprocessing.

certain focus point  $x_i$  at depth  $S_m$  by

$$\vec{F}_{S,i}^\dagger(S_m, S_0) \mathbf{D}_S^-(S_0) \mathbf{W}_S(S_0, S_m) = \vec{I}_i^\dagger(S_m). \quad (\text{II.4})$$

The focusing in emission can also be split into two parts: the operator  $\vec{F}_{P,j}(S_0, S_m)$  for focusing in detection for P-waves, for a certain focus point  $x_j$  at depth  $S_m$ , defined by

$$\mathbf{W}_P(S_m, S_0) \mathbf{S}_P^+(S_0) \vec{F}_{P,j}(S_0, S_m) = \vec{I}_j(S_m) \quad (\text{II.5})$$

and the operator  $\vec{F}_{S,j}(S_0, S_m)$  for focusing in detection for S-waves is defined for a certain focus point  $x_j$ , at depth  $S_m$  by

$$\mathbf{W}_S(S_m, S_0) \mathbf{S}_S^+(S_0) \vec{F}_{S,j}(S_0, S_m) = \vec{I}_j(S_m). \quad (\text{II.6})$$

With the use of equation II.1 - II.6 we can define the following double focusing processes for a focus point at depth  $S_m$ :

$$\vec{F}_{P,i}^\dagger(S_m, S_0) \mathbf{P}_{PP}^-(S_0) \vec{F}_{P,j}(S_0, S_m) = R_{PP,ij}(S_m) + \dots \quad (\text{II.7})$$

$$\vec{F}_{S,i}^\dagger(S_m, S_0) \mathbf{P}_{SP}^-(S_0) \vec{F}_{P,j}(S_0, S_m) = R_{SP,ij}(S_m) + \dots \quad (\text{II.8})$$

$$\vec{F}_{P,i}^\dagger(S_m, S_0) \mathbf{P}_{PS}^-(S_0) \vec{F}_{S,j}(S_0, S_m) = R_{PS,ij}(S_m) + \dots \quad (\text{II.9})$$

$$\vec{F}_{S,i}^\dagger(S_m, S_0) \mathbf{P}_{SS}^-(S_0) \vec{F}_{S,j}(S_0, S_m) = R_{SS,ij}(S_m) + \dots \quad (\text{II.10})$$

where the dots denote the reflection data from above and below the focus point (see equation 2.15 and 2.18). Note that for  $i = j$  the reflectivity describes the angle-averaged *confocal* migration result and for  $i \neq j$  the reflectivity describes the angle-dependent *bifocal* migration result.

This section can be summarized by stating that by using focusing operators in detection and emission for both P and S-waves the complete multi-component reflection coefficients matrix at interface  $S_m$  given by

$$R_{i,j}(S_m) = \begin{pmatrix} R_{PP,i,j}(S_m) & R_{PS,i,j}(S_m) \\ R_{SP,i,j}(S_m) & R_{SS,i,j}(S_m) \end{pmatrix} \quad (\text{II.11})$$

can be imaged in the same way as described in chapter 2.

Of course the imaging is only possible if we can decompose the source and receiver data into the up respectively downgoing waves and in P and S-waves at both source and receiver side (Herrmann, 1992). The matrix  $\mathbf{R}$  can also only be imaged within the temporal band limitation of the source signal  $S_0$ , if we assume the medium and receivers to be loss free.

It may also not be possible to compensate completely for the acquisition ‘footprints’ at the source and receiver side (equation II.2-II.6), as also discussed in chapter 2. If we ignore the source and receiver directivity, we often use the modified matched inverse operators for stable inverse extrapolation. The focusing operators are then given by

$$\vec{F}_{P,j}(S_0, S_m) = [\mathbf{W}_P(S_0, S_m)]^* \vec{I}_j, \quad (\text{II.12})$$

$$\vec{F}_{S,j}(S_0, S_m) = [\mathbf{W}_S(S_0, S_m)]^* \vec{I}_j, \quad (\text{II.13})$$

$$\vec{F}_{P,i}^\dagger(S_m, S_0) = \vec{I}_i^\dagger [\mathbf{W}_P(S_m, S_0)]^*, \quad (\text{II.14})$$

and

$$\vec{F}_{S,i}^\dagger(S_m, S_0) = \vec{I}_i^\dagger [\mathbf{W}_S(S_m, S_0)]^*. \quad (\text{II.15})$$

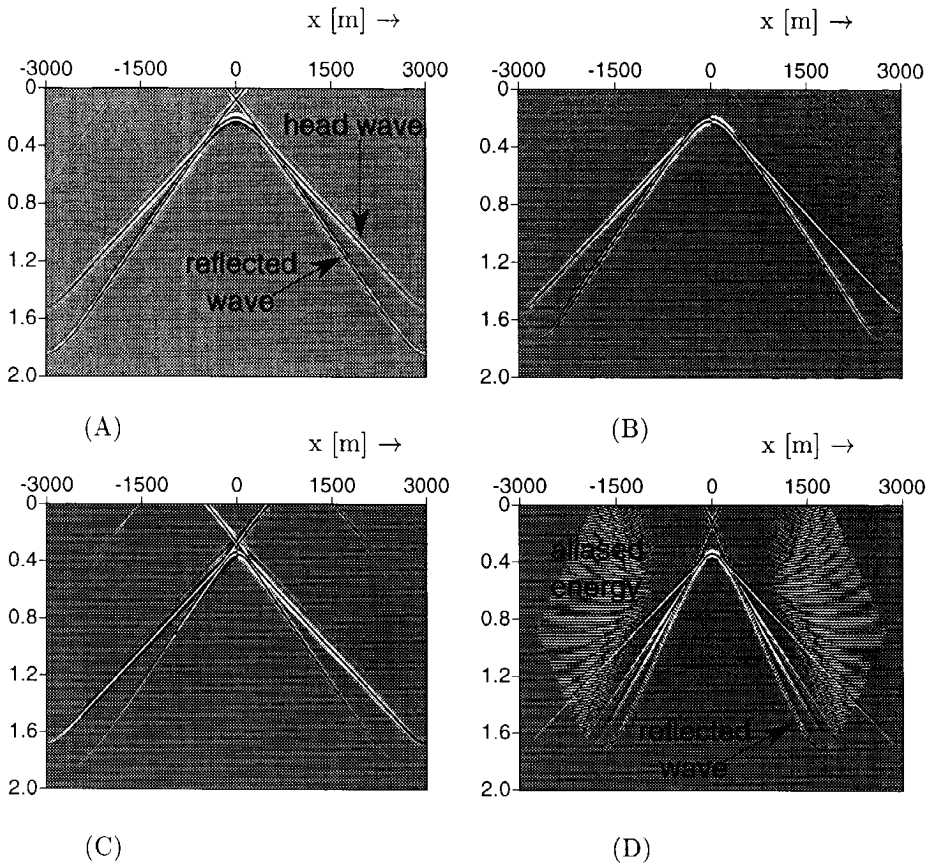


**Fig. II.3** The CFP gathers for PP-data (A), PS-data (B), SP-data (C) and SS-data (D).

### II.3 Numerical multi component example for one layer model

In this section we show a numerical example for the elastic response of one boundary (see figure II.4). The four CFP gathers for the P and S-waves are shown in figure II.3. The gridpoint gathers for all four components are shown in figure II.5. The corresponding reflectivity gathers are shown in figure II.6 and the amplitude cross sections at  $\Delta\tau=0$  of the reflectivity gathers are shown in figure II.7 together with the exact RC functions. Note that due to the low S-wave velocity there is some aliased energy in the CFP and gridpoint gather for SS data.

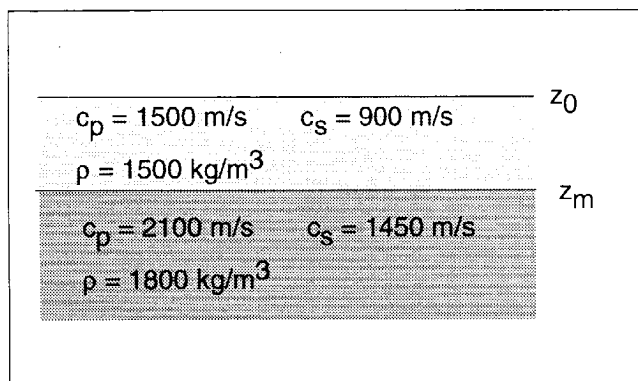


Fig. II.4 The model for the elastic numerical experiment with one boundary.

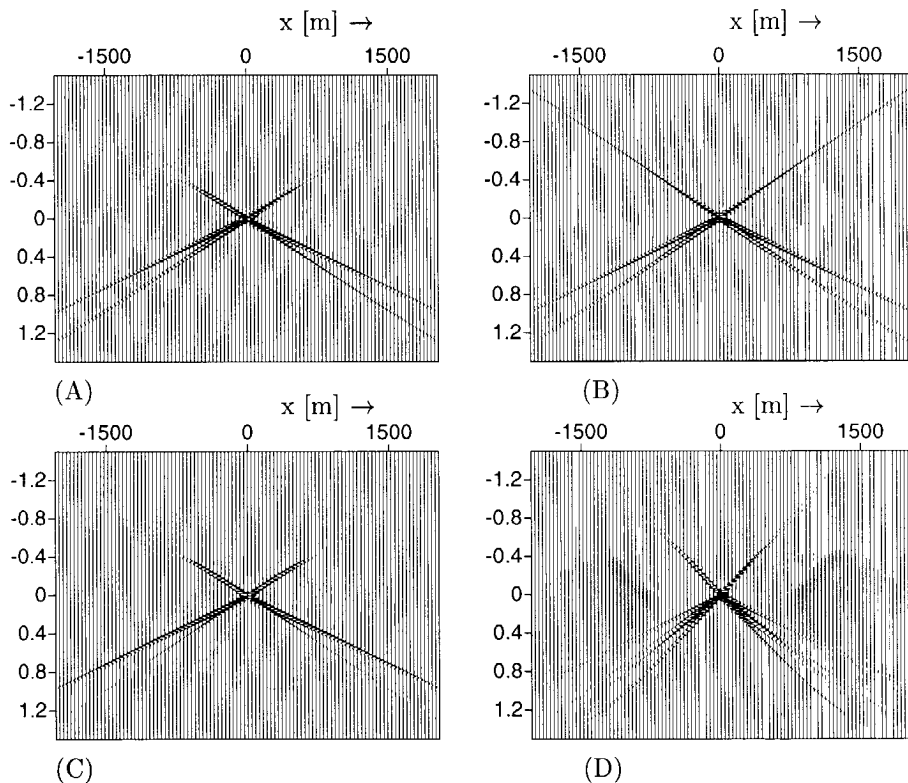
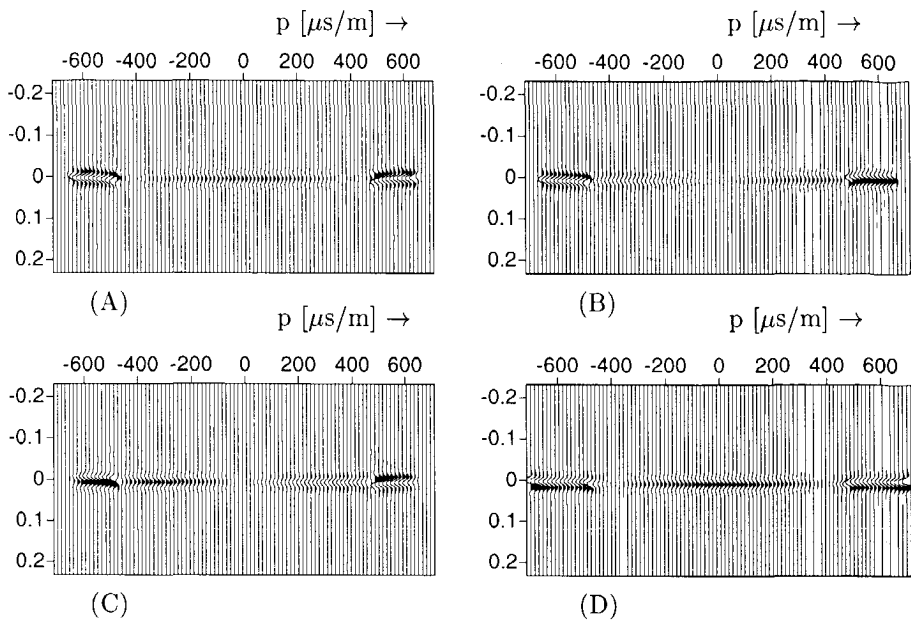
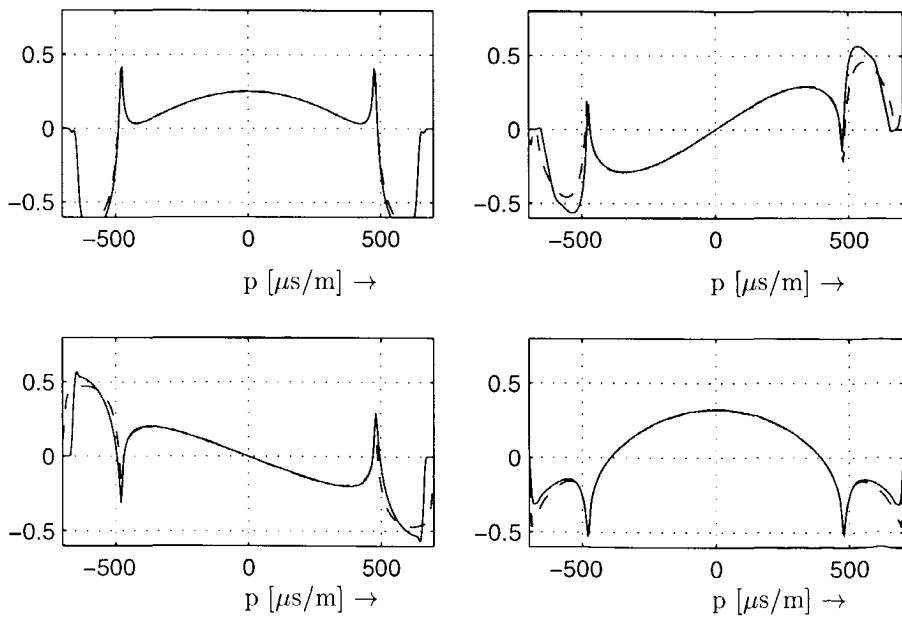


Fig. II.5 The gridpoint gathers for PP-reflection (A), PS-reflection (B), SP-reflection (C) and SS-reflection (D).



**Fig. II.6** The reflectivity gathers for PP-reflection (A), PS-reflection (B), SP-reflection (C) and SS-reflection (D).



**Fig. II.7** The amplitude cross sections for *PP*-reflection (*A*), *PS*-reflection (*B*), *SP*-reflection (*C*) and *SS*-reflection (*D*), with the exact theoretical reflection coefficient functions indicated by the dashed lines.

### II.3.1 Numerical multi component example for multi layer model

In the second example we used the data of well A from the Mobil AVO dataset (Verschuur et al., 1998) (van Wijngaarden et al., 1995). We used the blocked density, P and S-wave sonics. The logs are shown in figure II.8. The model consists of 70 layers. In order to make full use of the multi-component data, we simulated a sea bottom acquisition, with both P and S sources and receivers at the sea bottom, by removing the water layer from the logs.

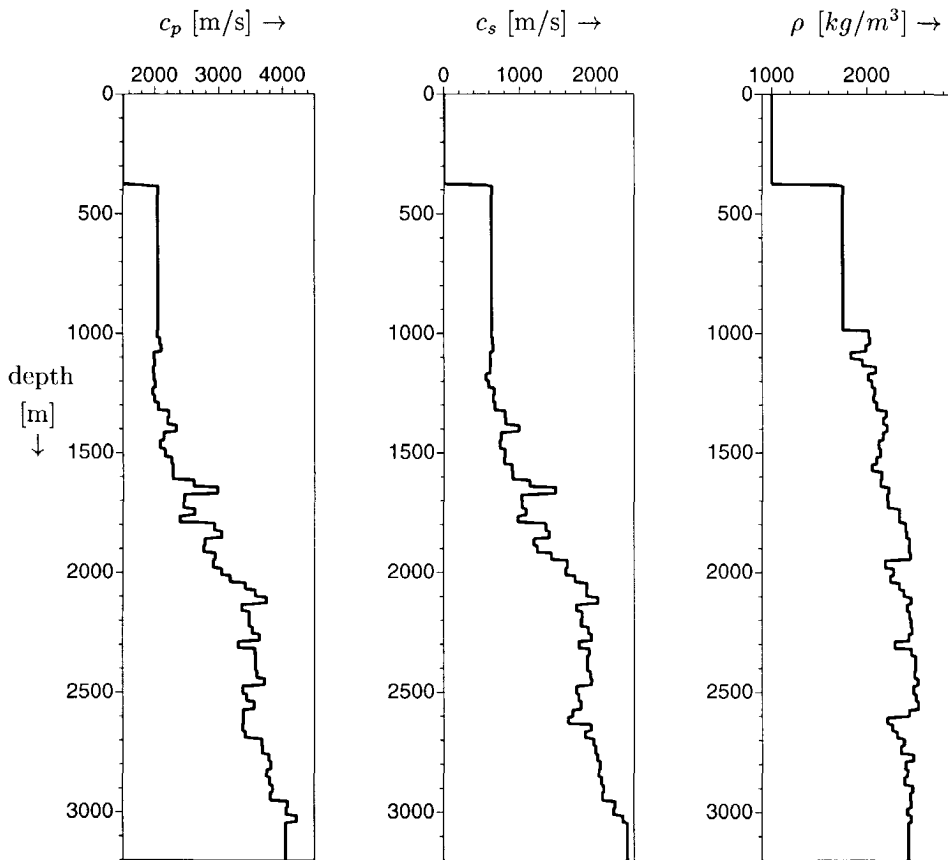


**Fig. II.8** The well log sonics and density.

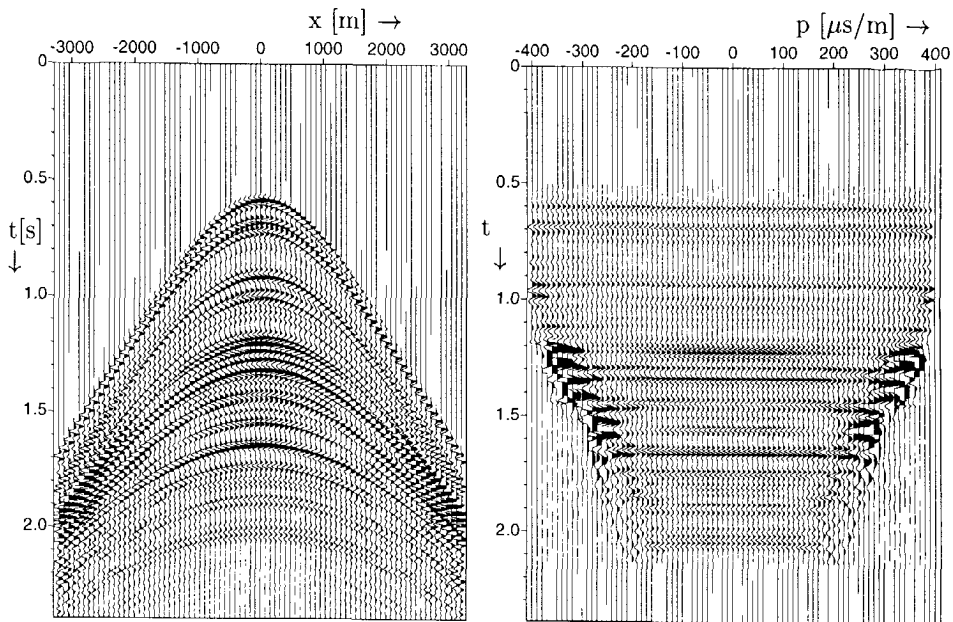


**Fig. II.9** The elastic  $R_{pp}$  shot record (left) and migrated RC (PP) gather (right) using the well logs.

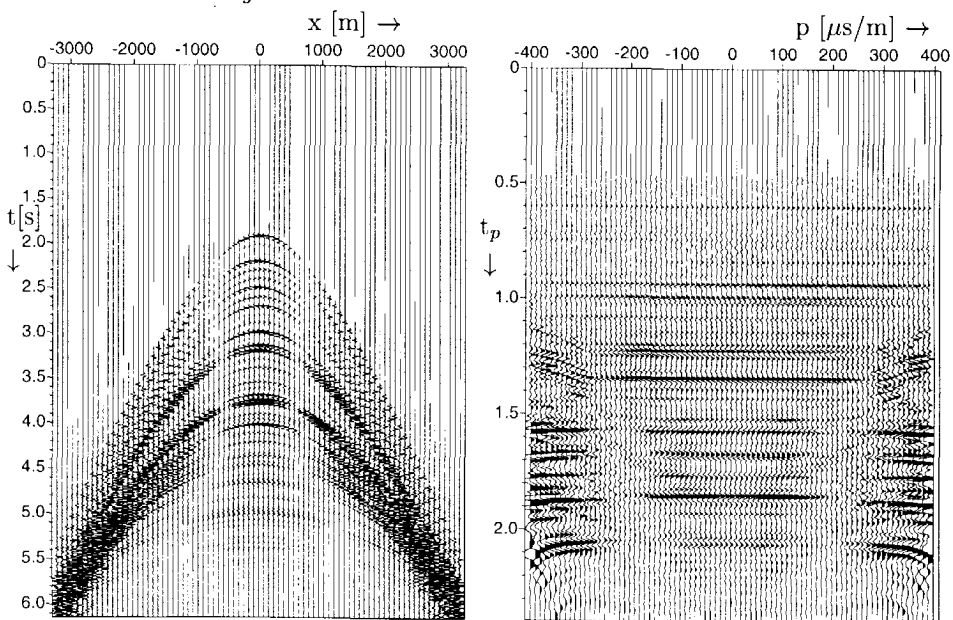


**Fig. II.10** The elastic  $R_{ss}$  shot record (left) and migrated RC (SS) gather (right) using the well logs.

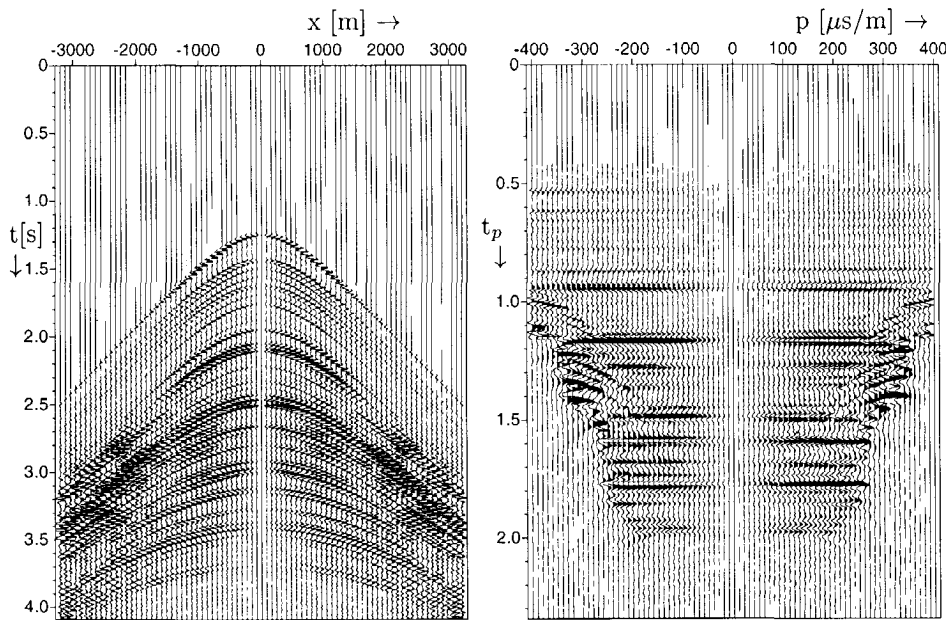


**Fig. II.11** The elastic  $R_{sp}$  shot record (left) and migrated RC (SP) gather (right) using the well logs.

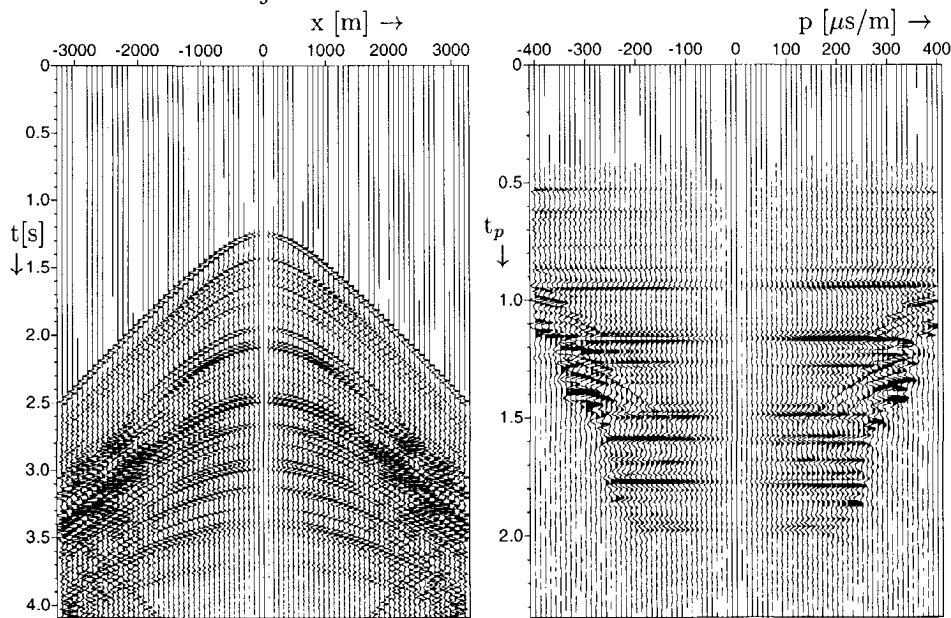


**Fig. II.12** The elastic  $R_{ps}$  shot record (left) and migrated RC (PS) gather (right) using the well logs.

### II.3.2 Forward modeling

We used these log data for elastic 1D forward modeling, without the 385m water layer. The reflectivity modeling was done in the  $k_x - \omega$  domain with a so-called 'reflectivity method' or 'layer-code'. The surface-related multiples are not included, but the conversions, internal multiples and transmission coefficients are included.

The shot records and the migrated RC gathers (in two-way image time for P-waves, indicated by  $t_p$ ) are shown in figure II.9 - II.12 for  $R_{pp}$ ,  $R_{ss}$ ,  $R_{ps}$  and  $R_{sp}$ . The two-way P-wave image time makes it possible to compare the RC gathers with each other (this will be used in chapter 5), but only for the PP data the travel times in the shot record can directly be compared with those in the RC gather.

The artifacts in the RC gathers for the converted data (PS and SP) at 1.0 and 1.5s are due to the cut off of high amplitudes in the shot records for high offsets. Tapering of the shot records will reduce this effect, but will also influence the imaged amplitudes in the RC gather.



---

# Chapter 3

## Zoeppritz equations and interference effects

*This chapter starts with the theoretical description of the reflectivity between two half spaces. First the nonlinear equations are discussed, followed by the linearized equations. Next the interference effects of layers which are in the order of or smaller than the seismic wavelength are numerically modeled and discussed. The models in this chapter consist of layers with Zoeppritz boundaries (step functions). The elastic parameters for the layers are computed using the Gassmann equation for two lithotypes: a sandstone and a shale.*

### 3.1 Introduction

The reflection coefficients function at a boundary between two half spaces is described by the full Knott-Zoeppritz matrix equation (Knott, 1899), (Aki and Richards, 1980, p. 149). The elastic parameters in this medium show as function of depth the behaviour of an isolated step function: constant medium parameters above and below the interface, and a jump at the interface, as shown in figure 3.1A. The reflection coefficients are computed by finding a solution for the boundary conditions between the two half spaces.

A profile of the elastic parameters in the earth as function of depth shows a much more complicated structure. There are almost an infinite number of ‘layers’. Inside these layers the parameters are not constant and the boundaries are not clear step functions, as shown in the well log measurements in figure 3.1B. Note that the earth may very well be much more complicated than the well log measurements show, as the well log tool averages the earth respond to the scale of measurement (in the order of decimeters).

The waves which are used in seismic exploration, have a much larger wavelength than these layer thicknesses. The imaged response of the seismic P and S-waves shows an averaged reflectivity of these layers on the seismic scale. In order to correlate the well log measurements (scale  $10^{-1}[\text{m}]$ ) with the seismic measurements (scale

$10^1 - 10^2$  [m]) and in order to be able to use the derived theoretical descriptions of the reflectivity for step functions, the well log measurements are often blocked into layers. The layer thickness used here is in the order of the seismic wavelength, as shown in figure 3.1C.

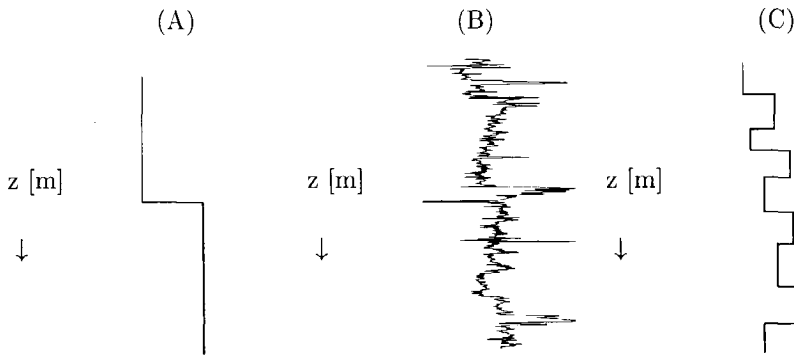


**Fig. 3.1** (A) a step function between two half spaces, (B) a typical well log measurement and (C) a blocked well log.

In AVO inversion the Zoeppritz equation is the basic expression for the computation of the RC (reflection coefficient) function. In practice only the linear part of the Zoeppritz equation is used, i.e. the pre-critical part (figure 3.2). This means that we linearize the expression for the RC function in relative contrasts of the elastic parameters.

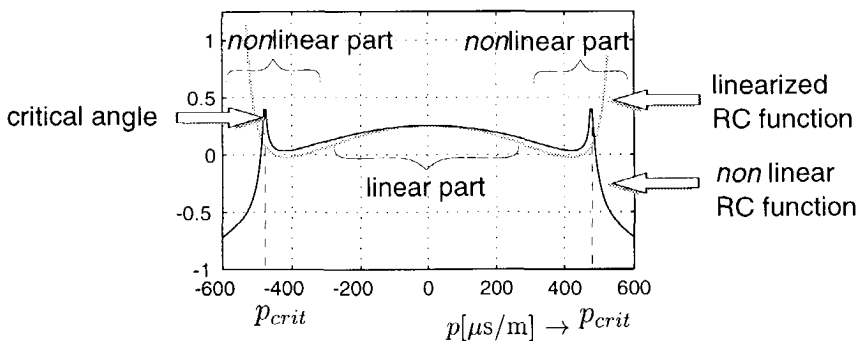


**Fig. 3.2** The elastic reflection coefficient function, showing the linear and nonlinear part. In gray also the linearized reflection coefficient function is shown.

Primarily the behaviour of the linearized RC function is examined in this chapter for single interfaces and interfering responses of layers on the seismic scale. The S-waves in this chapter are the SV-waves, and not the SH-waves.

### 3.2 The nonlinear reflection coefficient functions

The reflection coefficients for the reflection of downgoing incident waves, indicated with the superscript  $+$ , and for the reflection of upgoing incident waves, indicated with the superscript  $-$  and the transmission coefficients for up and downgoing waves, indicated with the capitals  $T^-$  and  $T^+$ , can be written elegantly in a complete scattering matrix, given by Aki and Richards (1980).

$$\begin{pmatrix} R_{PP}^+ & R_{PS}^+ & T_{pp}^- & T_{ps}^- \\ R_{SP}^+ & R_{SS}^+ & T_{sp}^- & T_{ss}^- \\ T_{pp}^+ & T_{ps}^+ & R_{PP}^- & R_{PS}^- \\ T_{sp}^+ & T_{ss}^+ & R_{SP}^- & R_{SS}^- \end{pmatrix} = \mathbf{M}^{-1} \mathbf{N}. \quad (3.1)$$

The matrix  $\mathbf{M}$  is given by  $\mathbf{M} =$

$$\begin{pmatrix} -c_{p,1}p & -\sqrt{1-c_{s,1}^2p^2} & c_{p,2} & \sqrt{1-c_{s,2}^2p^2} \\ \sqrt{1-c_{p,1}^2p^2} & -c_{s,1}p & \sqrt{1-c_{p,2}^2p^2} & -c_{s,2}p \\ 2\rho_1 c_{s,1}^2 p \sqrt{1-c_{p,1}^2 p^2} & 2\rho_1 c_{s,1} (1-2c_{s,1}^2 p^2) & 2\rho_2 c_{s,2}^2 p \sqrt{1-c_{p,2}^2 p^2} & 2\rho_2 c_{s,2} (1-2c_{s,2}^2 p^2) \\ -\rho_1 c_{p,1} (1-2c_{s,1}^2 p^2) & 2\rho_1 c_{s,1}^2 \sqrt{1-c_{s,1}^2 p^2} & \rho_2 c_{p,2} (1-2c_{s,2}^2 p^2) & -2\rho_2 c_{s,2}^2 p \sqrt{1-c_{s,2}^2 p^2} \end{pmatrix}$$

and the matrix  $\mathbf{N}$  is given by  $\mathbf{N} =$

$$\begin{pmatrix} c_{p,1}p & \sqrt{1-c_{s,1}^2p^2} & -c_{p,2} & -\sqrt{1-c_{s,2}^2p^2} \\ \sqrt{1-c_{p,1}^2p^2} & -c_{s,1}p & \sqrt{1-c_{p,2}^2p^2} & -c_{s,2}p \\ 2\rho_1 c_{s,1}^2 p \sqrt{1-c_{p,1}^2 p^2} & 2\rho_1 c_{s,1} (1-2c_{s,1}^2 p^2) & 2\rho_2 c_{s,2}^2 p \sqrt{1-c_{p,2}^2 p^2} & 2\rho_2 c_{s,2} (1-2c_{s,2}^2 p^2) \\ \rho_1 c_{p,1} (1-2c_{s,1}^2 p^2) & -2\rho_1 c_{s,1}^2 \sqrt{1-c_{s,1}^2 p^2} & -\rho_2 c_{p,2} (1-2c_{s,2}^2 p^2) & 2\rho_2 c_{s,2}^2 p \sqrt{1-c_{s,2}^2 p^2} \end{pmatrix}.$$

In this thesis only the reflection coefficients of downgoing incidence fields are discussed. Therefore the superscripts  $+$  are omitted for notational convenience in  $R_{PP}$ ,  $R_{PS}$ ,  $R_{SP}$  and  $R_{SS}$ . Explicit equations can be derived for the RC functions  $R_{PP}$ ,  $R_{PS}$ ,  $R_{SP}$  and  $R_{SS}$  from equation 3.1. These expressions are given in the appendix of this chapter.

### 3.3 The linearized reflection coefficient functions

#### 3.3.1 The PP reflection coefficients

Following Aki and Richards (1980), the linearized Zoeppritz equation for P→P reflection coefficients can be written for small angles and small contrasts as

$$R_{PP}(p) = \frac{1}{2}(1 - 4\bar{c}_S^2 p^2) \frac{\Delta\rho}{\bar{\rho}} + \frac{1}{2\cos^2\theta} \frac{\Delta c_P}{\bar{c}_P} - 4\bar{c}_S^2 p^2 \frac{\Delta c_S}{\bar{c}_S}, \quad (3.2)$$

with  $p \times \bar{c}_P = \sin\theta$ .

Using the following substitutions for the acoustic impedance  $Z$

$$\frac{\Delta Z}{Z} = \frac{\Delta c_P}{\bar{c}_P} + \frac{\Delta\rho}{\bar{\rho}} \quad (3.3)$$

and for the shear modulus  $\mu$

$$\frac{\Delta\mu}{\bar{\mu}} = \frac{\Delta\rho}{\bar{\rho}} + 2\frac{\Delta c_S}{\bar{c}_S}, \quad (3.4)$$

this can be rewritten as

$$R_{PP}(p) = \frac{1}{2} \frac{\Delta Z}{Z} + \frac{1}{2} \left( \frac{\bar{c}_P^2 p^2}{1 - \bar{c}_P^2 p^2} \right) \frac{\Delta c_P}{\bar{c}_P} - 2\bar{c}_S^2 p^2 \frac{\Delta\mu}{\bar{\mu}}. \quad (3.5)$$

Using series expansion, this can be written as

$$R_{PP}(p) \approx \frac{1}{2} \frac{\Delta Z}{Z} + \left[ \frac{1}{2} \frac{\Delta c_P}{\bar{c}_P} - 2\left(\frac{\bar{c}_S}{\bar{c}_P}\right)^2 \frac{\Delta\mu}{\bar{\mu}} \right] \bar{c}_P^2 p^2 + \left( \frac{1}{2} \frac{\Delta c_P}{\bar{c}_P} \right) \bar{c}_P^4 p^4. \quad (3.6)$$

This means that for small angles ( $\bar{c}_P^2 p^2 \ll 1$ ), the RC can be described by two parameters,

$$R_{PP}(p) \approx \frac{1}{2} \frac{\Delta Z}{Z} + \left[ \frac{1}{2} \frac{\Delta c_P}{\bar{c}_P} - 2\left(\frac{\bar{c}_S}{\bar{c}_P}\right)^2 \frac{\Delta\mu}{\bar{\mu}} \right] \bar{c}_P^2 p^2. \quad (3.7)$$

#### 3.3.2 The SS reflection coefficients

Following Aki and Richards (1980) the linearized Zoeppritz equation for S→S reflection coefficients can be written for small angles and small contrasts as

$$R_{SS}(p) = \frac{1}{2}(1 - 4\bar{c}_S^2 p^2) \frac{\Delta\rho}{\bar{\rho}} + \left( \frac{1}{2\cos^2\varphi} - 4\bar{c}_S^2 p^2 \right) \frac{\Delta c_S}{\bar{c}_S}, \quad (3.8)$$

with  $p \times \bar{c}_S = \sin\varphi$ .

This can be rewritten as

$$R_{SS}(p) = \frac{1}{2} \frac{\Delta\rho}{\bar{\rho}} + \frac{1}{2} \frac{1}{1 - \bar{c}_S^2 p^2} \frac{\Delta c_S}{\bar{c}_S} - \frac{1}{2} 4\bar{c}_S^2 p^2 \frac{\Delta\mu}{\bar{\mu}} \quad (3.9)$$

Using the series expansion this can be rewritten as

$$R_{SS}(p) \approx \left[ \frac{1}{2} \frac{\Delta \rho}{\bar{\rho}} + \frac{1}{2} \frac{\Delta c_S}{\bar{c}_S} \right] - 3 \frac{1}{2} \frac{\Delta c_S}{\bar{c}_S} \bar{c}_S^2 p^2 - 4 \frac{\Delta \rho}{\bar{\rho}} \bar{c}_S^2 p^2. \quad (3.10)$$

Using the following substitution for the shear impedance  $Z_S$

$$\frac{\Delta Z_S}{Z_S} = \frac{\Delta c_S}{\bar{c}_S} + \frac{\Delta \rho}{\bar{\rho}}, \quad (3.11)$$

this results again in a 2 term description of the RC for small angles ( $\bar{c}_S^2 p^2 \ll 1$ )

$$\begin{aligned} R_{SS}(p) &\approx \frac{1}{2} \frac{\Delta Z_S}{Z_S} + \left[ \frac{1}{2} \left( \frac{\bar{c}_S}{\bar{c}_P} \right)^2 \frac{\Delta c_S}{\bar{c}_S} - 4 \left( \frac{\bar{c}_S}{\bar{c}_P} \right)^2 \frac{\Delta Z_S}{Z_S} \right] \bar{c}_P^2 p^2 \\ &= \frac{1}{2} \frac{\Delta Z_S}{Z_S} + \left[ \frac{1}{2} \left( \frac{\bar{c}_S}{\bar{c}_P} \right)^2 \frac{\Delta \mu}{\bar{\mu}} - 4 \frac{1}{2} \left( \frac{\bar{c}_S}{\bar{c}_P} \right)^2 \frac{\Delta Z_S}{Z_S} \right] \bar{c}_P^2 p^2. \end{aligned} \quad (3.12)$$

### 3.3.3 The SP reflection coefficients

Following Aki and Richards (1980) the linearized Zoeppritz equation for P→S reflection coefficients can be written for small angles and small contrasts as

$$\begin{aligned} R_{SP}(p) &= -\frac{p \bar{c}_S}{2 \cos \varphi} \times \\ &\left\{ \left[ 1 - 2 \bar{c}_S^2 p^2 + 2 \bar{c}_S^2 \frac{\cos \theta}{\bar{c}_P} \frac{\cos \varphi}{\bar{c}_S} \right] \frac{\Delta \rho}{\bar{\rho}} - \left[ 4 \bar{c}_S^2 p^2 - 4 \bar{c}_S^2 \frac{\cos \theta}{\bar{c}_P} \frac{\cos \varphi}{\bar{c}_S} \right] \frac{\Delta c_S}{\bar{c}_S} \right\}. \end{aligned} \quad (3.13)$$

This can be rewritten in

$$R_{SP}(p) = -\frac{1}{2} \frac{\bar{c}_S p}{\sqrt{1 - \bar{c}_P^2 p^2}} \frac{\Delta \rho}{\bar{\rho}} + \frac{\bar{c}_S^3 p^3}{\sqrt{1 - \bar{c}_S^2 p^2}} \frac{\Delta \mu}{\bar{\mu}} - \bar{c}_S \bar{c}_P \frac{\bar{c}_S p}{\sqrt{1 - \bar{c}_P^2 p^2}} \frac{\Delta \mu}{\bar{\mu}}. \quad (3.14)$$

Using the series expansion this can be written as

$$R_{SP}(p) = -\frac{\bar{c}_S}{\bar{c}_P} \left[ \frac{1}{2} \frac{\Delta \rho}{\bar{\rho}} + \frac{\bar{c}_S}{\bar{c}_P} \frac{\Delta \mu}{\bar{\mu}} \right] \bar{c}_P p - \left[ \frac{1}{4} \frac{\bar{c}_S}{\bar{c}_P} \frac{\Delta \rho}{\bar{\rho}} - \left( 1 - \frac{1}{2} \frac{\bar{c}_S^2}{\bar{c}_P^2} \right) \frac{\Delta \mu}{\bar{\mu}} \right] \bar{c}_P^3 p^3, \quad (3.15)$$

or using an approximation for small angles ( $\bar{c}_P p \ll 1$ ) the RC can be described by one  $p$ -dependent term

$$R_{SP}(p) \approx -\frac{\bar{c}_S}{\bar{c}_P} \left[ \frac{1}{2} \frac{\Delta \rho}{\bar{\rho}} + \frac{\bar{c}_S}{\bar{c}_P} \frac{\Delta \mu}{\bar{\mu}} \right] \bar{c}_P p. \quad (3.16)$$

### 3.3.4 The PS reflection coefficients

Following Aki and Richards (1980) the linearized Zoeppritz equation for S→P reflection coefficients can be written for small angles and small contrasts as

$$R_{PS}(p) = -\frac{\cos\theta}{\bar{c}_S} \frac{\bar{c}_P}{\cos\varphi} R_{SP} \quad (3.17)$$

$$= -\sqrt{\frac{1 - \bar{c}_S^2 p^2}{1 - \bar{c}_P^2 p^2}} \times \frac{\bar{c}_P}{\bar{c}_S} \times R_{SP} \quad (3.18)$$

$$\approx -\frac{\bar{c}_P}{\bar{c}_S} \times R_{SP} \quad (3.19)$$

$$\approx \left[ \frac{1}{2} \frac{\Delta\rho}{\bar{\rho}} + \left( \frac{\bar{c}_S}{\bar{c}_P} \right) \frac{\Delta\mu}{\bar{\mu}} \right] \bar{c}_P p \quad (3.20)$$

### 3.3.5 Overview reflection coefficients p-dependency

In the previous sections we have derived the RC functions for PP and SS reflection in two terms, an angle dependent term and an angle independent term. For SP and PS only the angle dependent term is present. This is schematically shown in the table 3.1 on this page.

	angle indepent term	angle dependent term	angle dependence
$R_{PP}$	$\frac{1}{2} \frac{\Delta Z}{Z}$	$\frac{1}{2} \frac{\Delta c_P}{\bar{c}_P} - 2 \left( \frac{\bar{c}_S}{\bar{c}_P} \right)^2 \frac{\Delta\mu}{\bar{\mu}}$	$\bar{c}_P^2 p^2$
$R_{SS}$	$\frac{1}{2} \frac{\Delta Z_S}{Z_S}$	$\frac{1}{2} \left( \frac{\bar{c}_S}{\bar{c}_P} \right)^2 \frac{\Delta c_S}{\bar{c}_S} - 4 \left( \frac{\bar{c}_S}{\bar{c}_P} \right)^2 \frac{\Delta Z_S}{Z_S}$	$\bar{c}_P^2 p^2$
$R_{SP}$	—	$-\left[ \frac{1}{2} \frac{\bar{c}_S}{\bar{c}_P} \frac{\Delta\rho}{\bar{\rho}} + \left( \frac{\bar{c}_S}{\bar{c}_P} \right)^2 \frac{\Delta\mu}{\bar{\mu}} \right]$	$\bar{c}_P p$
$R_{PS}$	—	$\left[ \frac{1}{2} \frac{\Delta\rho}{\bar{\rho}} + \left( \frac{\bar{c}_S}{\bar{c}_P} \right) \frac{\Delta\mu}{\bar{\mu}} \right]$	$\bar{c}_P p$

Table 3.1 The first order angular dependence of the RC functions.

### 3.4 Numerical modeling of interfaces between two half spaces

In order to show the influence of converted and multiple reflections and to show the interference effects of layers with small thicknesses on the imaged AVP curves, several simple 1D subsurface models are numerically modeled in this section. The models are built up using two lithotypes. We used a sandstone with 10% porosity ( $\phi=10\%$ ) and the same sandstone with 20% porosity and a shale with 5% porosity. The P and S-wave velocities and the densities are computed using the Gassmann equation and are shown in table 3.2.

lithotype	porosity	$c_P[m/s]$	$c_S[m/s]$	$\rho[kg/m^3]$
sandstone	$\phi=10\%$	3156	1522	2494
sandstone	$\phi=20\%$	2510	1141	2338
shale	$\phi=5\%$	4427	2641	2620

**Table 3.2** The elastic parameters used in the synthetic models.

### 3.4.1 Modeling the response of an interface between two half spaces

The numerical examples in the previous chapter show the imaged and theoretical RC functions for one layer on top of a half space. Since we removed the surface-related effects, we can also interpret this as the result of two half spaces. Figure 2.24B shows the perfect match between the imaged and theoretical RC functions within the imaged  $p$ -bandwidth.

Since there is only one boundary, there is no interference with the imaged primary reflection data of converted, multiple or other primary reflections.

### 3.4.2 Modeling the response of two interfaces between two identical half spaces

In order to investigate the tuning effect or the interference of two nearby boundaries we use in this section a model consisting of one layer between two identical half spaces. The upper half space is approximated by a layer of 600m shale, without surface-related multiples. The layer thickness  $\Delta z$  of the sandstone layer is varied from 100m to 5m. This means that the layer thickness is varied from larger to smaller than the seismic wavelength.

A schematic view of the model is shown in figure 3.3 together with an impression of the RC functions. This display can be obtained by computing the real part of the RC functions, convolving this with a wavelet and putting this at certain distances in a gather. Note that this is not a correctly modeled RC gather, but just an indication of the (pre-critical) RC function we can expect.

A reflectivity modeling code in the wavenumber-frequency domain has been used to model the elastic PP response in the medium described above. All internal multiples and conversions are included, except the surface-related multiples. The shot records for layer thicknesses of 100m, 50m, 10m and 5m are shown in figure 3.4(A)-(D).

The corresponding gridpoint gathers (in the Radon domain) are shown in figure 3.5(A)-(H). The imaged amplitude cross sections of the gridpoint gathers are shown in figure 3.6(A)-(H), together with the analytical exact RC-functions for isolated boundaries.

From the gridpoint gathers (figure 3.5(A,B)) for the two boundaries with a layer

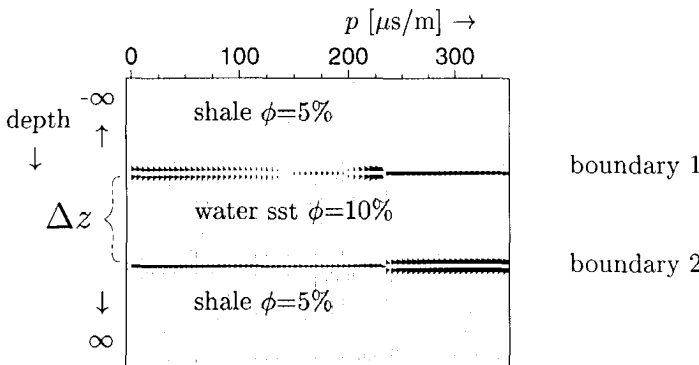


**Fig. 3.3** Schematic view of the model with the reflectivity for the two boundaries. Note that the real part of the RC function is used for indication of the RC function.

thickness of 100m, it is clear that the two responses are separated events. Accordingly the analytical RC-functions coincide perfectly with the amplitude cross sections of the gridpoint gathers in the Radon domain at  $\Delta\tau=0$  (within the  $p$ -bandwidth, given by the acquisition parameters). Due to the lower velocity of the sand layer, the RC-function of the second boundary is imaged over a smaller angle range.

Note the converted shear wave reflection ( $\text{P-} \rightarrow \text{SS-} \rightarrow \text{P}$ ) just below the second PP reflection in the shot record (figure 3.4A) and in the gridpoint gather in the Radon domain (figure 3.5B). This event can be recognized by the zero amplitude at  $p=0$ . It does not (yet) interfere with the PP-response.

In the gridpoint gathers in the Radon domain for the two boundaries with a layer thickness of 50m, the two responses are just next to each other. Since they are not yet interfering, the analytical RC-functions coincide perfectly with the amplitude cross sections of the gridpoint gathers at  $\Delta\tau=0$ .

Note that the converted shear wave starts to interfere with the second PP reflection in the gridpoint gather (figure 3.5D).

In the gridpoint gathers in the Radon domain for the two boundaries with a layer thickness of 10m the two responses are not separated anymore. The side lobes of the response of one boundary are interfering with the main lobe of the other boundary response. Since they are interfering, the analytical RC-functions do not coincide perfectly with the amplitude cross sections of the gridpoint gathers at  $\Delta\tau=0$ , as shown in figure 3.5(E) and (F). Since the analytical RC-functions are of opposite sign, the interfering responses may enhance each other, as shown by the large amplitudes in figure 3.5F.

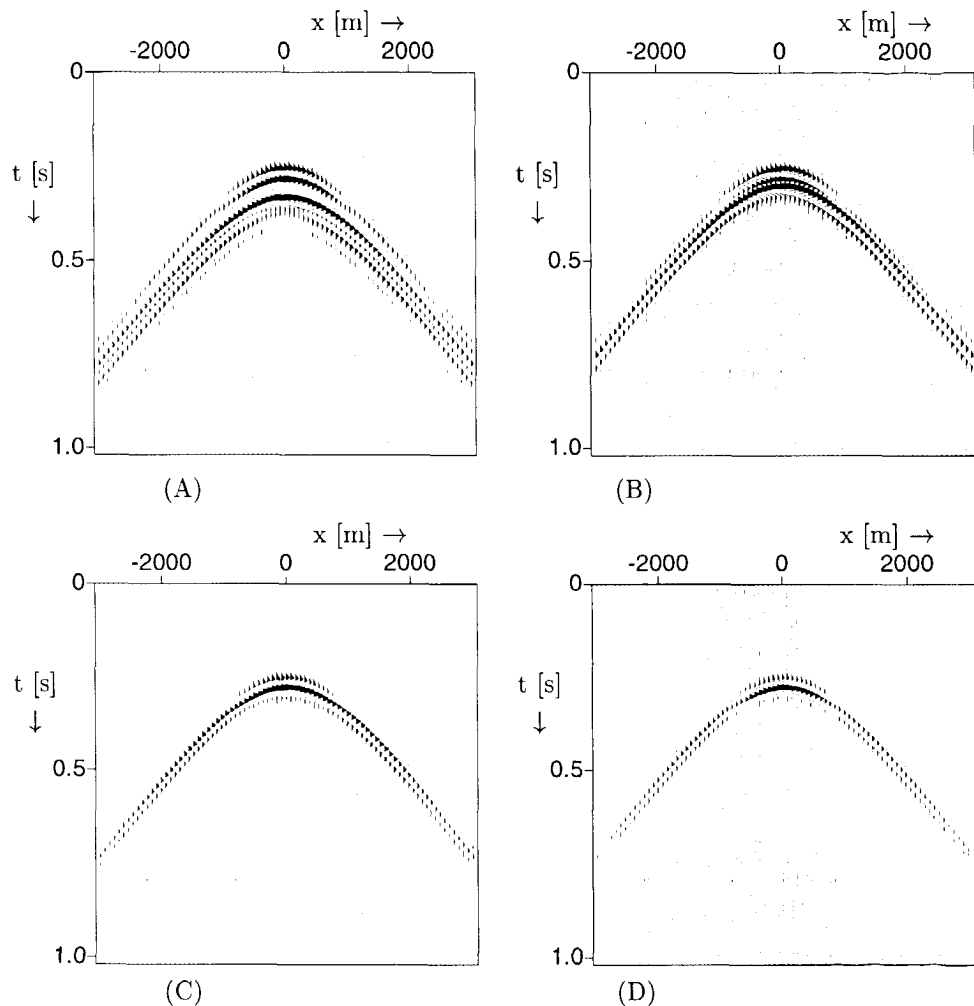
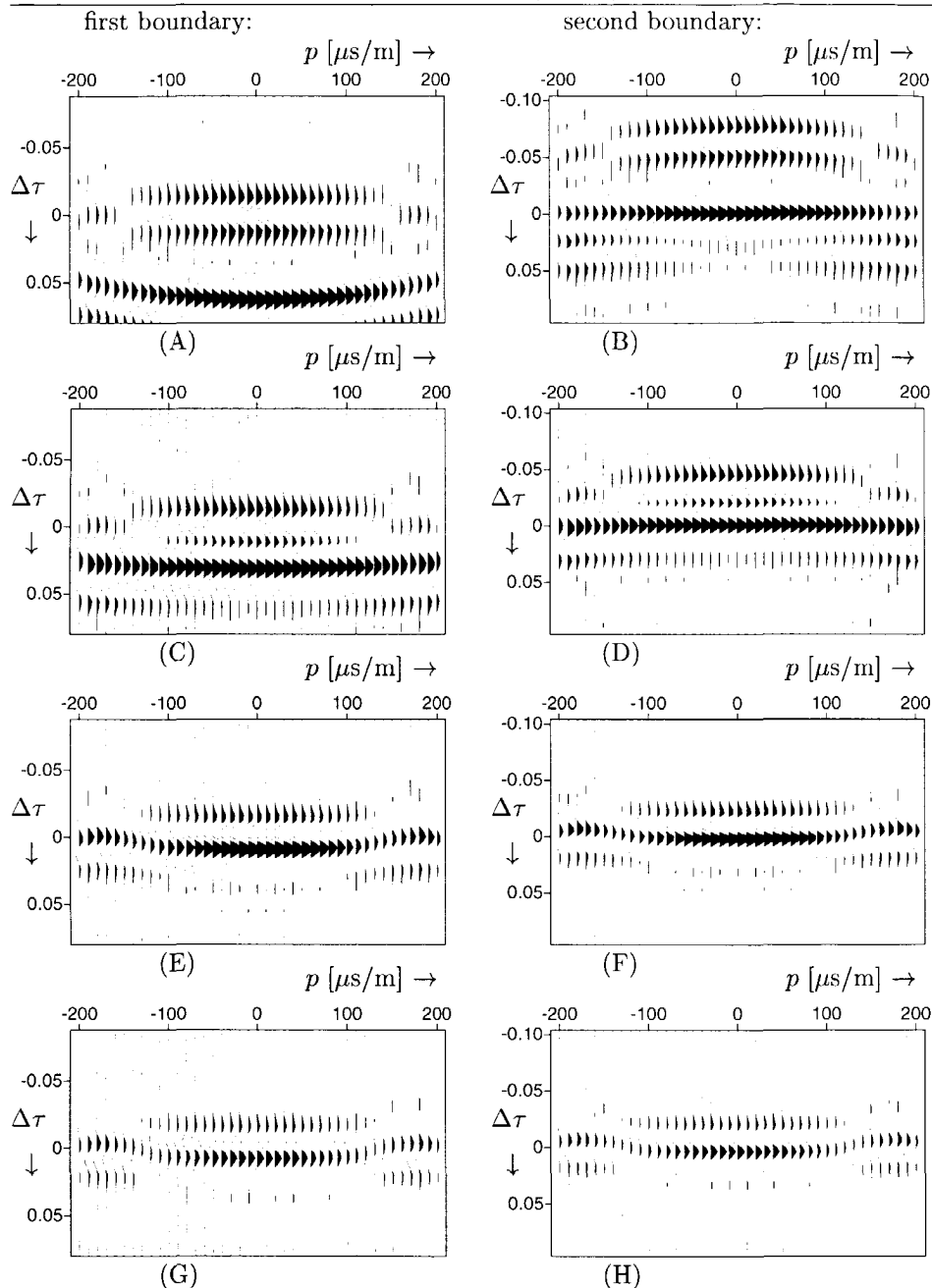
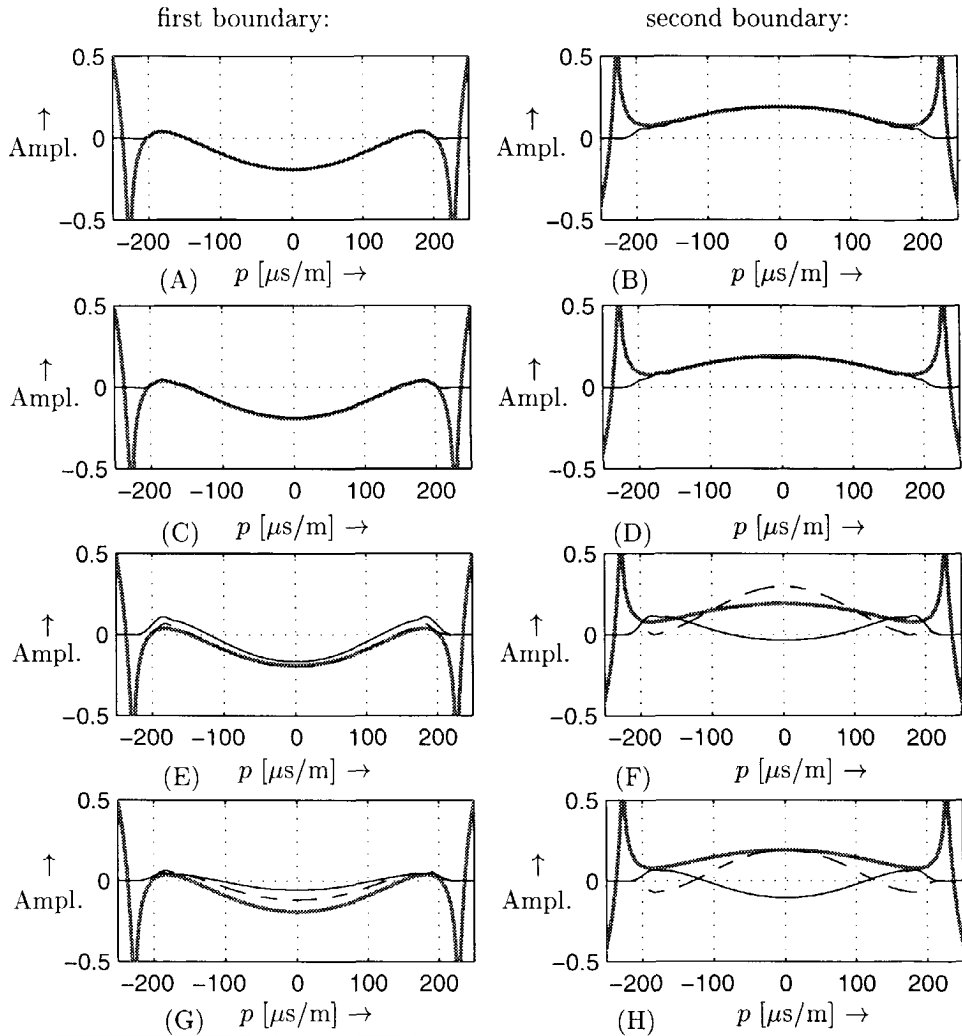


Fig. 3.4 shot records for layer thicknesses  $\Delta z$  of 100m (A), 50m (B), 10m (C) and 5m (D), using one sand layer between two shale half spaces.



**Fig. 3.5** The gridpoint gathers (in the Radon domain) for layer thicknesses  $\Delta z$  of 100m (A,B), 50m (C,D), 10m (E,F) and 5m (G,H), using one sand layer between two shale half spaces.



**Fig. 3.6** The amplitude cross sections of the gridpoint gathers in the Radon domain at  $\Delta\tau=0$  (figure 3.5) for layer thicknesses  $\Delta z$  of 100m (A,B), 50m (C,D), 10m (E,F) and 5m (G,H), using one sand layer between two shale half spaces. The analytical RC function is indicated by the thick gray line. In figure (E)-(H) the dashed amplitude cross sections are one or two samples shifted from  $\Delta\tau=0$ , in order to improve the match with the exact RC function.

In this numerical experiment we know exactly the position of the boundary in depth. If this would not be the case (like in field data), we would probably choose the amplitude cross section of the strongest event. In this example this would be the amplitude cross section at  $\Delta\tau = -0.004\text{ms}$  of the gridpoint gather in the Radon domain for the upper boundary. This imaged RC-function gives also the best match (accidentally almost perfect) with the analytical RC-function as shown by the dashed line in figure 3.5E.

For the lower boundary, the amplitude cross section at  $\Delta\tau = +0.004\text{ms}$  of the gridpoint gather in the Radon domain gives the best match with the analytical RC-function (the dashed line in figure 3.5F). The quite large mismatch is due to the converted shear wave which interferes with the second PP reflection.

In the gridpoint gathers in the Radon domain for the two boundaries with a layer thickness of 5m the two responses completely interfere. Since the interfering analytical RC-functions are of opposite sign, the amplitudes of the combined response are decreased. Even by taking the maximum amplitude cross sections at  $\Delta\tau = -0.004\text{ms}$  and  $\Delta\tau = +0.008\text{ms}$  for the upper and lower boundary (the dashed lines in figure 3.5G and H), the imaged RC-functions are smaller than the analytical functions. Again the larger mismatch of the lower boundary is due to the converted shear wave which interferes with the second PP reflection.

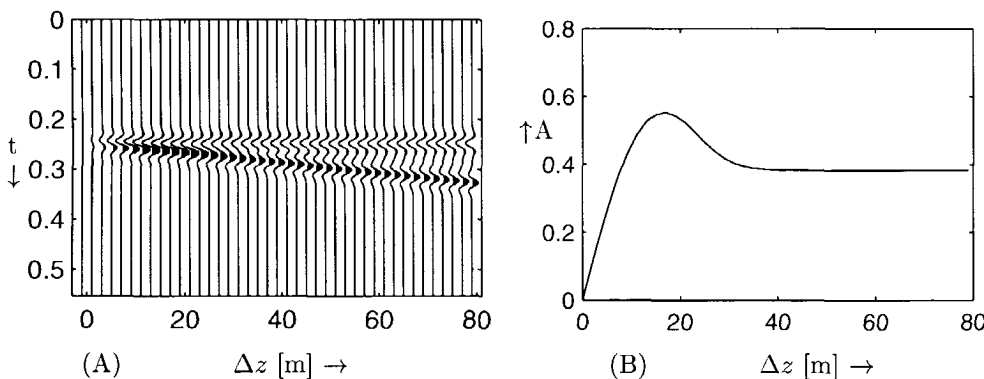


**Fig. 3.7** The tuning effect for normal incidence ( $p=0$ ) as function of layer thickness. (A) the imaged trace as function of  $\Delta z$  and (B) the amplitude of reflectivity of the upper boundary. The amplitudes of the reflectivity of the lower boundary is the same, but opposite of sign.

In conclusion one can say the following for a plane wave reflecting on a layer between two identical half spaces. For normal incidence ( $p=0$ ) the response as function of decreasing layer thickness  $\Delta z$  first increases due to interference and then decreases to zero in the limit of  $\Delta z \downarrow 0$ . This is the so-called tuning curve. For  $p=0$  the response can also be modeled by a convolution of the reflection coefficients  $R(p=0)$

of the two boundaries with a wavelet, as shown in figure 3.7.

The low amplitudes for small  $p$ -values are explained by the fact that the reflection response of a small layer between two identical half spaces can be seen as a 2-point differentiator  $t_n - t_{n-1}$  without a normalization term  $\Delta t$  working on the seismic wavelet, as shown schematically in figure 3.8.

$$RC(t, p = 0) \approx w(t + \Delta t) - w(t) \quad (3.21)$$

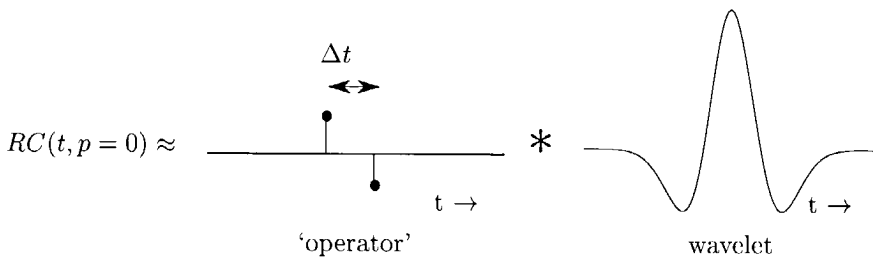


**Fig. 3.8** Schematic view of the reflection at a thin layer between two identical half spaces for  $p=0$ . The reflection can be interpreted as convolution of a two point differentiator with the wavelet.

In the limit  $\Delta t \downarrow 0$  the  $R(p = 0)$  will be zero.

For *nonperpendicular* incidence the situation is more complex. Because converted waves interfere with the PP response. This makes the tuning curve dependent on the ratio of P and S-wave velocities in the medium. Also the increasing vertical wavelength with increasing  $p$  (which will be discussed in more detail in the next chapter) will influence the interference (as a function of  $p$ ).

In a medium with high velocity layers and large incident angles the response becomes even more complicated, due to post critical reflection data, which is discussed in the next section.

### 3.4.3 Modeling the response of four interfaces between two identical half spaces

In order to investigate the effects of interference in a slightly more complex medium (with high velocity layers) a model consisting of three layers between two identical half spaces is used in this section. The layer thickness of the three layers is again varied in such a way, that it is larger, of comparable size and smaller than the seismic wavelength.

The model consists of an overburden of 600m water filled sandstone (porosity=10%) (which can be seen as a half space), a shale layer of thickness  $\Delta z$ , a water filled sandstone (porosity=20%) layer of thickness  $\Delta z$ , a shale layer of thickness  $\Delta z$  and below a water filled sandstone (porosity=10%). The layer thickness  $\Delta z$  is the same for the three layers and is varied between 100m and 5m.

The schematic view of the model with the RC functions is shown in figure 3.9. (Note that this is not a correctly modeled RC gather, but just an indication of the (real part of the) RC function we can expect).

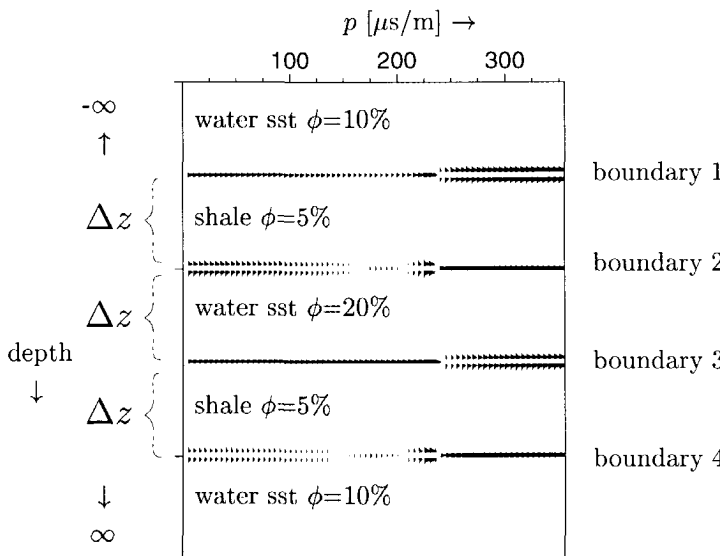


**Fig. 3.9** Schematic view of the model with the reflectivity for the four boundaries. Note that the real part of the RC function is used for post-critical  $p$ -values.

The (real part of the) analytical RC functions (PP-data) for the isolated boundaries as function of ray parameter  $p$  are shown in figure 3.10.

A reflectivity modeling code in the wavenumber-frequency domain has been used to model the elastic PP response in the medium described above. All conversions and internal multiples are included, except the surface-related multiples. The shot records for layer thicknesses of 100m, 50m, 10m and 5m are shown in figure 3.11(A)-

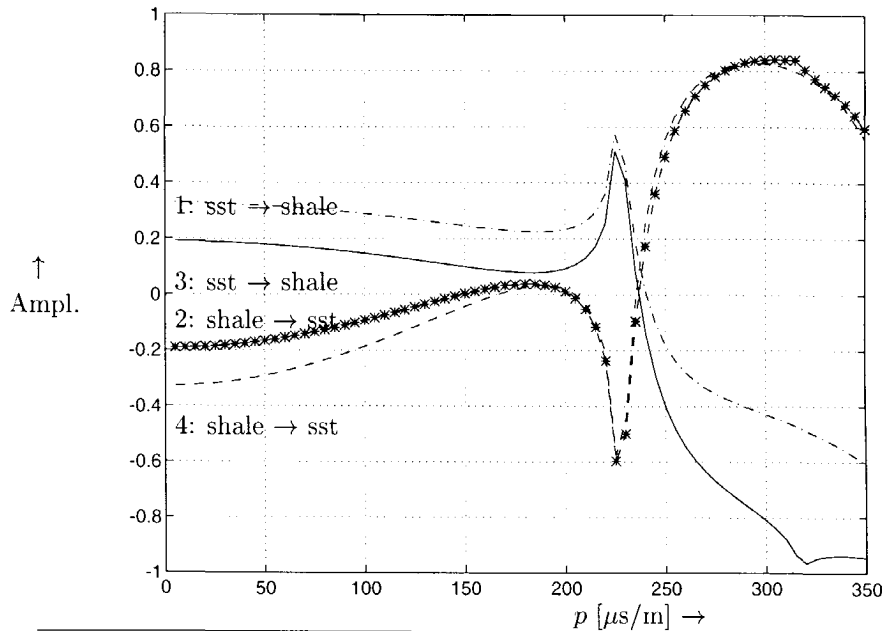


**Fig. 3.10** The real part of the analytical RC functions for the 4 boundaries as function of ray parameter  $p$ .

(D).

The gridpoint gathers in the Radon domain with focus points at the four boundaries for a layer thickness of 100m are shown in figure 3.12(A)-(D). The corresponding amplitude cross sections of these gridpoint gathers are shown in figure 3.12(E)-(H), together with the analytical exact RC-functions for isolated boundaries.

The PP reflections are not interfering with each other. But due to the conversions to shear waves, some converted waves interfere with the primary PP reflections. This can be seen in the migrated gathers as well as in the amplitude cross sections. The amplitude cross sections for the first two boundaries (figure 3.12(E) and (F)) do resemble the theoretical RC functions (shown in gray), which are the same as in figure 3.10. The imaged RC functions for third and fourth boundary are distorted for high  $p$ -values by interfering conversions (figure 3.12(G) and (H)). The imaged RC-functions can not be approximated by analytical RC-functions for single boundaries at higher  $p$ -values, due to the complexity of the model.

The gridpoint gathers in the Radon domain with focus points at the four boundaries for a layer thickness of 50m are shown in figure 3.13(A)-(D). The corresponding amplitude cross sections of these gridpoint gathers are shown in figure 3.13(E)-(H), together with the analytical exact RC-functions for isolated boundaries.

The first two and last two PP reflections are clearly interfering with each other. Also due to the conversions to S-waves, some converted waves interfere with the

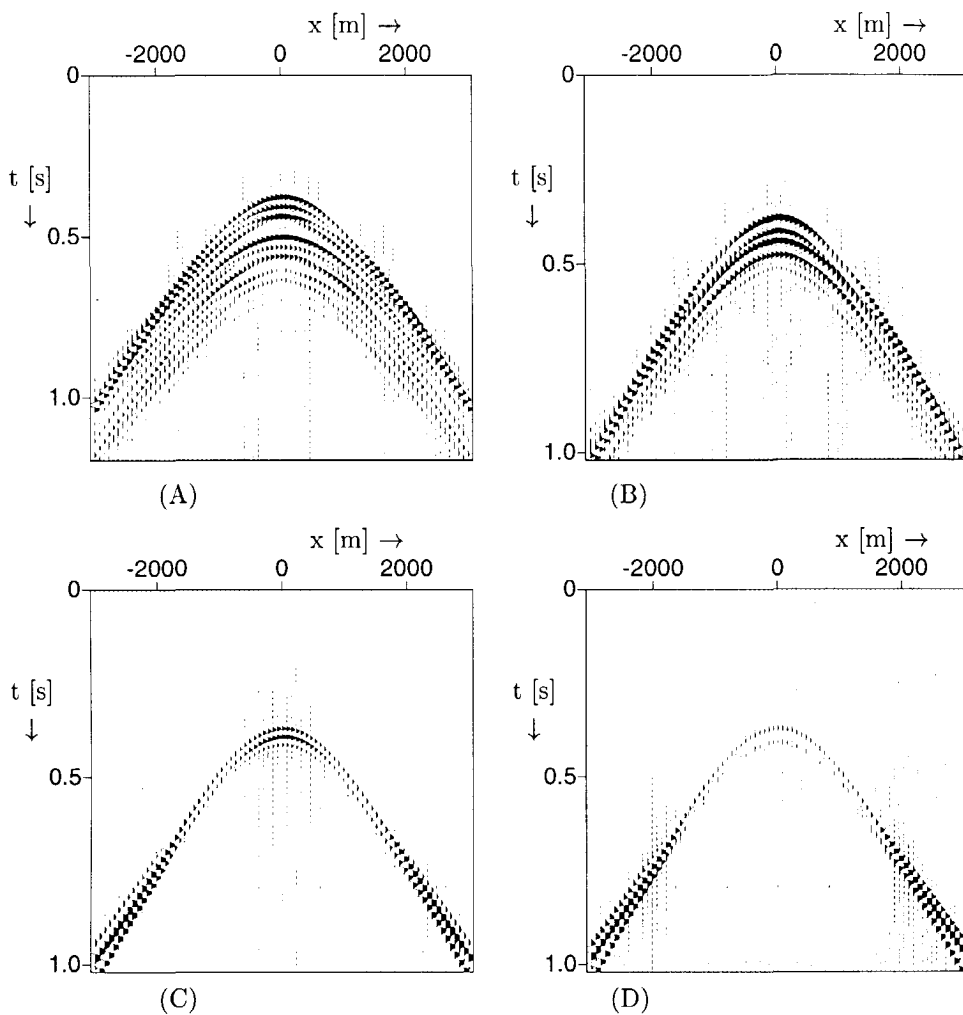


**Fig. 3.11** shot records for layer thicknesses  $\Delta z$  of 100m (A), 50m (B), 10m (C) and 5m (D), using two shale and one sand layer between two half spaces of sand.

primary PP reflections. This can be seen in the migrated gathers as well as in the amplitude cross sections. For the first and last boundary the maximum imaged reflection strength is not exactly at  $\Delta\tau=0$  in the gridpoint gather. In the cross sections in figure 3.13(E) and (H) the maximum amplitude cross sections are shown as dashed lines and the amplitude cross sections at  $\Delta\tau=0$  are shown as solid lines. Around  $p=0$  for all boundaries the amplitude cross sections match the analytical RC functions for single boundaries fairly well, but around the critical angles the behaviour is completely different.

The gridpoint gathers in the Radon domain with focus points at the four boundaries for a layer thickness of 10m are shown in figure 3.14(A)-(D). The corresponding amplitude cross sections of these gridpoint gathers are shown in figure 3.14(E)-(H), together with the analytical exact RC-functions for isolated boundaries.

All the PP reflections and the conversions to S-waves are clearly interfering with each other and the total response appears as two close reflections. The responses of the second and third boundary (the small sand layer) are canceling each other partly, which results in smaller amplitudes compared to the analytical single boundary RC functions in figure 3.14(F) and (G). The maximum amplitudes at the first and last boundary do not coincide with  $\Delta\tau=0$ . In figure 3.14(A) the maximum is shifted upwards with 4ms and in 3.14(D) the maximum negative amplitude is shifted downward with 8ms. The corresponding amplitude cross sections are shown as dashed lines in figure 3.14(E) and (H). Besides the shifted maxima and lower amplitudes, the shapes of the RC functions are also changed by the interference and are different from the analytical curves for single boundaries.

The gridpoint gathers in the Radon domain with focus points at the four boundaries for a layer thickness of 5m are shown in figure 3.15(A)-(D). The corresponding amplitude cross sections of these gridpoint gathers are shown in figure 3.15(E)-(H), together with the exact analytical RC-functions for isolated boundaries.

All the reflections are clearly interfering with each other and appear as one reflection in the shot record. In the gridpoint gathers and amplitude cross sections in figure 3.15 we see that the amplitudes of pre-critical reflection ( $p < p_{crit}$ ) are very small and only around the critical angles we find high amplitudes. The reflections almost cancel each other, as explained on page 83.

This is even more clear in figure 3.16 where the amplitude axis has been scaled to the small amplitudes and the amplitude cross sections with the highest amplitudes at  $p=0$  are shown. These amplitude cross sections show some amplitude variation, but the amplitudes are very low. Note that in real situations these amplitudes will probably be below noise level.

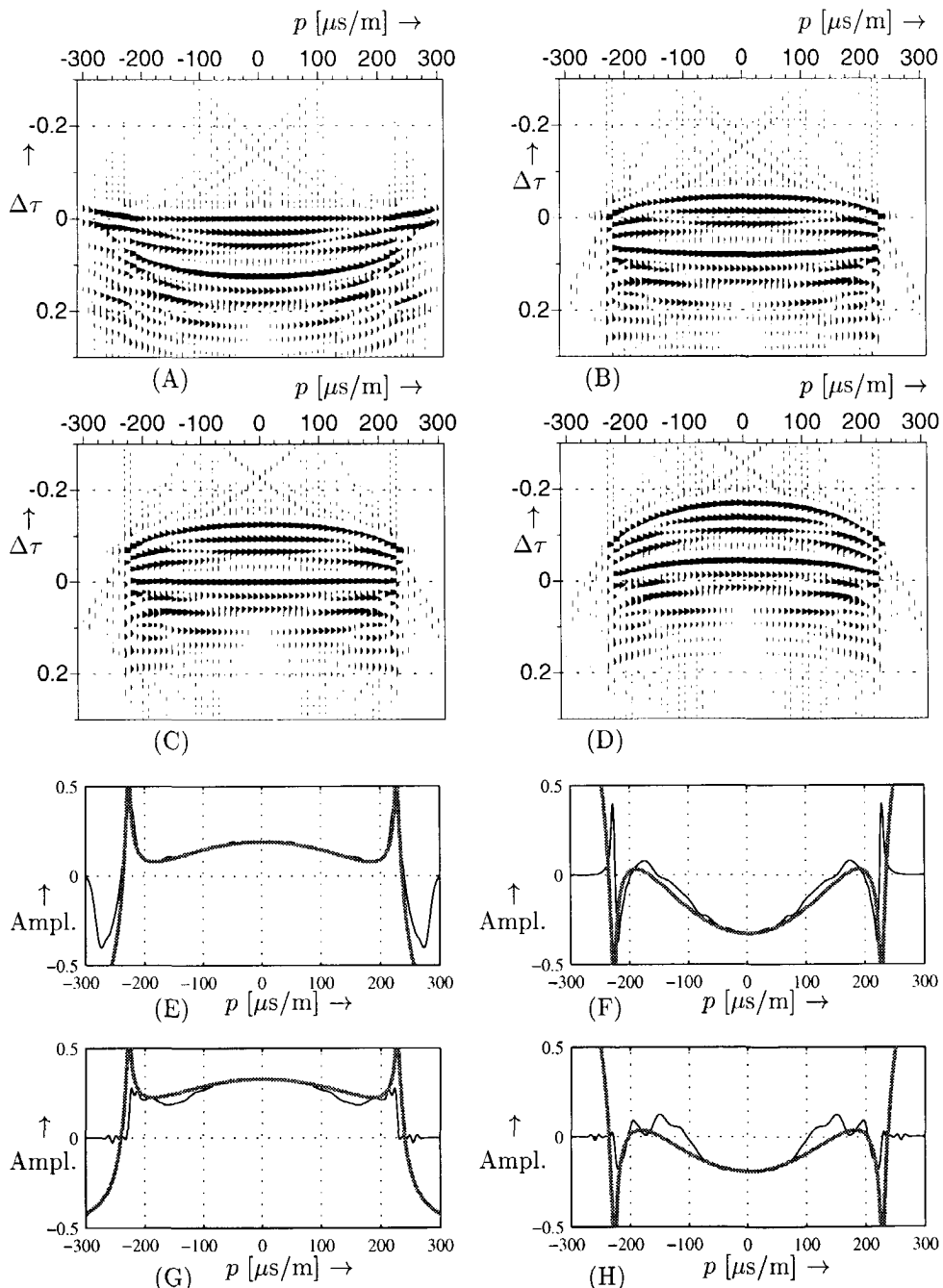


**Fig. 3.12** The gridpoint gathers in the Radon domain ( $\Delta z=100\text{m}$ ) and the imaged RC functions (amplitude cross sections at  $\Delta\tau=0$ ) displayed in black and the theoretical RC functions displayed in gray.

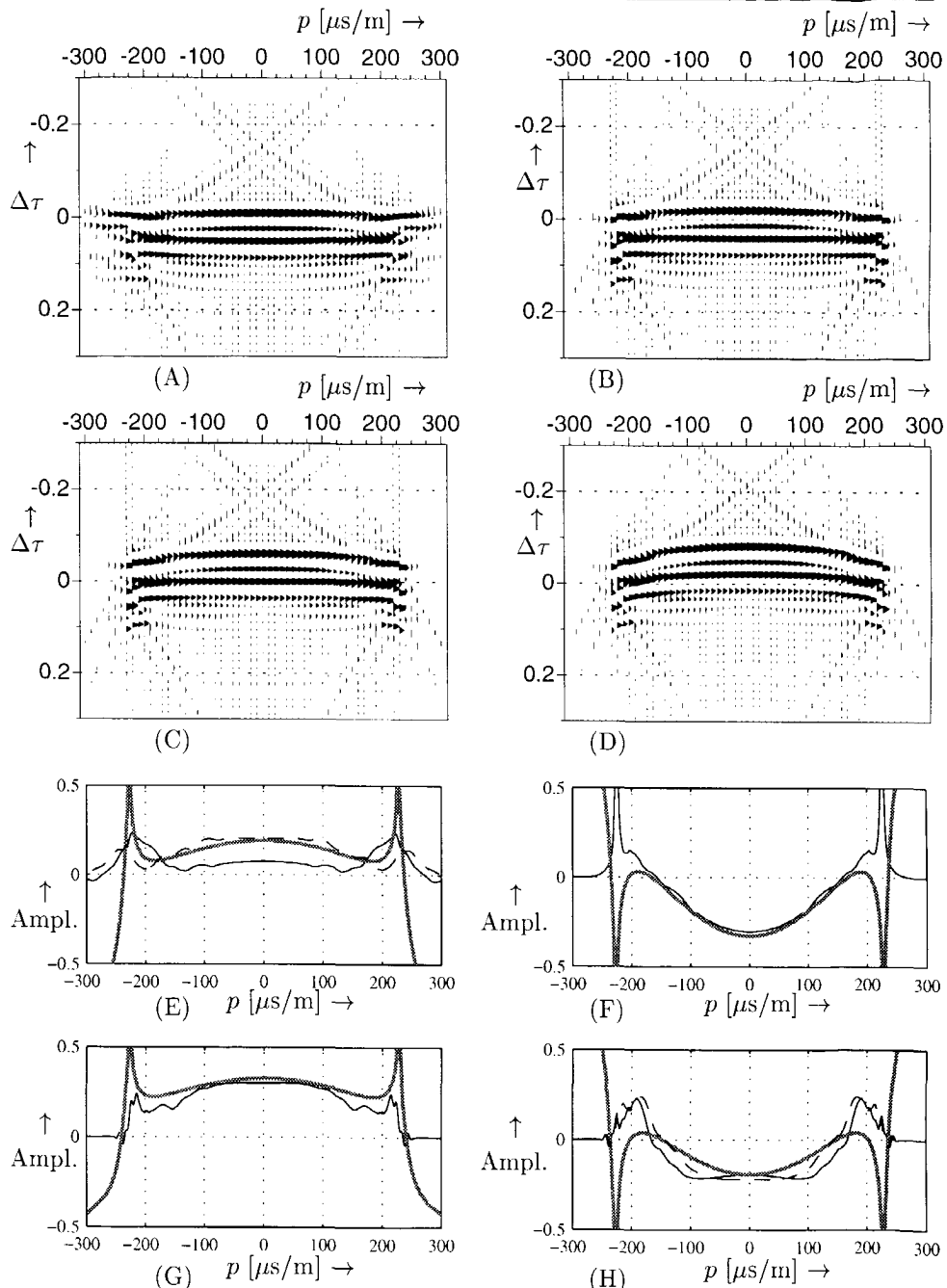


**Fig. 3.13** The gridpoint gathers in the Radon domain at the 4 boundaries ( $\Delta z=50\text{m}$ ) and the imaged RC functions (amplitude cross sections at  $\Delta\tau=0$ ) displayed in black and the theoretical RC functions displayed in gray. In (A) and (D) the nearest maximum RC-curve is shown in dashed line.

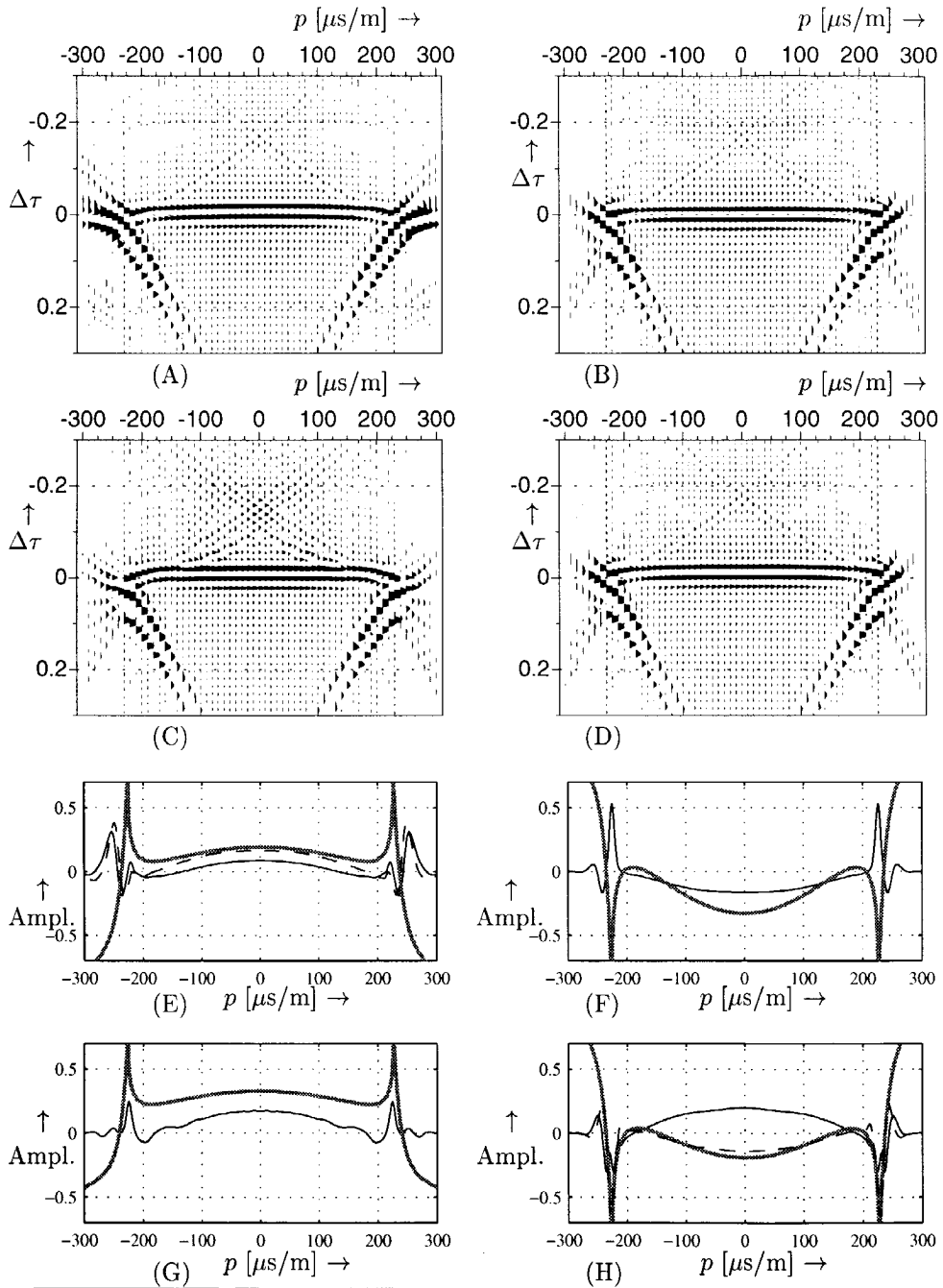


**Fig. 3.14** The gridpoint gathers in the Radon domain at the 4 boundaries ( $\Delta z=10m$ ) and the imaged RC functions (amplitude cross sections at  $\Delta\tau=0$ ) displayed in black and the theoretical RC functions displayed in gray. In (A) and (D) the nearest maximum RC-curve is shown in dashed line.

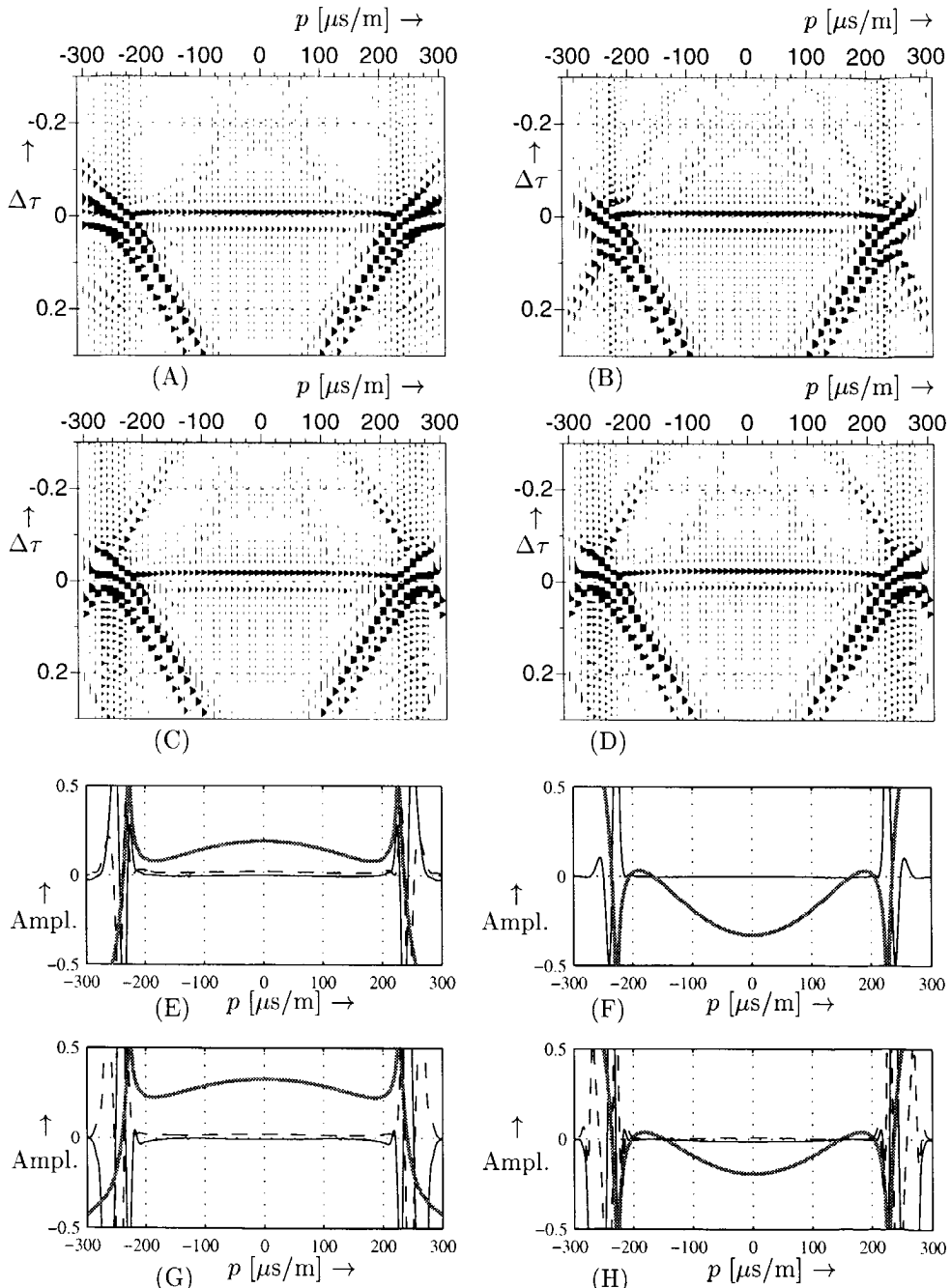


**Fig. 3.15** The gridpoint gathers in the Radon domain ( $\Delta z=5\text{m}$ ) and the imaged RC functions (amplitude cross sections at  $\Delta\tau=0$ ) displayed in black and the theoretical RC functions displayed in gray. In (A) and (D) the nearest maximum RC-curve is shown in dashed line.

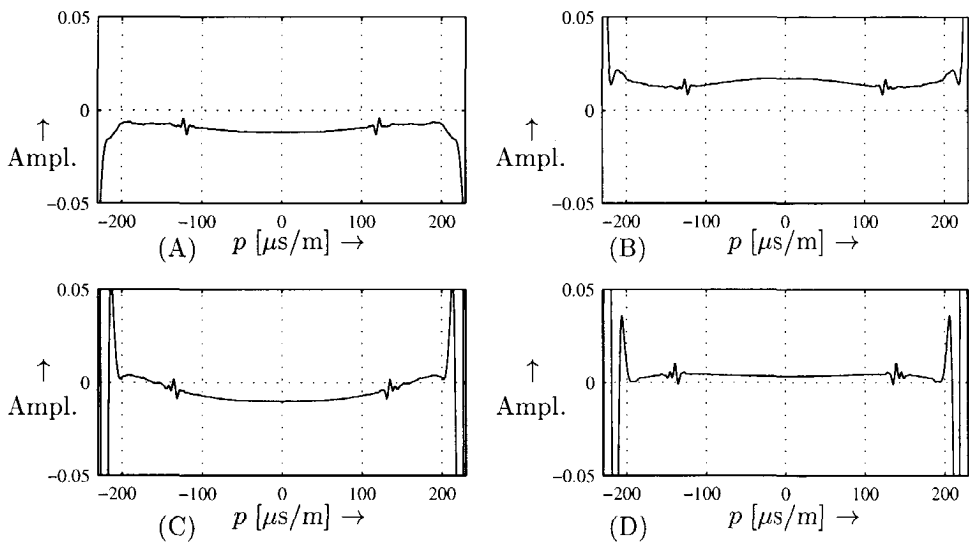


**Fig. 3.16** amplitude cross sections through the 4 maximum amplitude events in the imaged RC function for the 3rd boundary. Note the ten times smaller scale of the amplitudes compared to figure 3.15.

### 3.4.4 Modeling the response of one interface between two different half spaces

In order to investigate the tuning effect or the interference of a (high velocity) layer between two different half spaces we use in this section a model consisting of one layer between two different half spaces. The upper half space is approximated by an upper layer of 600m sandstone with 20% porosity, without surface-related multiples. The layer thickness of the shale layer is varied from 200m to 5m. This means that the layer thickness is varied from larger to smaller than the seismic wavelength. The lower half space is identical to the upper layer. The model is shown schematically in figure 3.17.

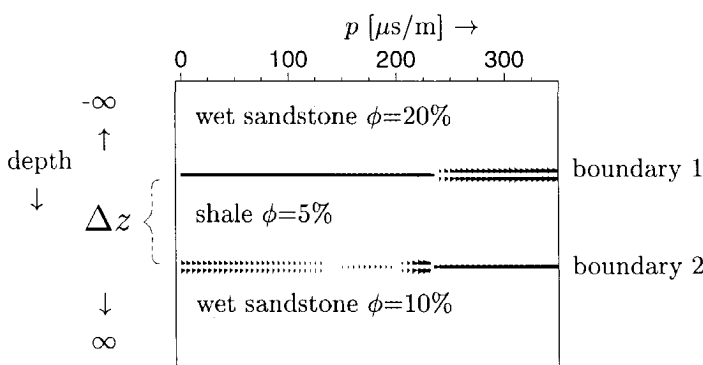


**Fig. 3.17** Schematic view of the model with the reflectivity for the two boundaries. Note that the real part of the RC function is used for post-critical  $p$ -values.

A reflectivity modeling code in the wavenumber-frequency domain has been used to model the elastic PP response in the medium described above. The shot records for layer thicknesses of 200m, 100m, 50m and 5m are shown in figure 3.18(A)-(D).

The corresponding gridpoint gathers in the Radon domain are shown in figure 3.19(A)-(H).

The amplitude cross sections of the gridpoint gathers are shown in figure 3.20(A)-(H), together with the analytical exact RC-functions for isolated boundaries.

In the gridpoint gathers in the Radon domain (3.19(A,B)) for the two boundaries with a layer thickness of 200m, the two PP responses are clearly separated. The analytical RC-functions for these two boundaries coincide perfectly with the amplitude cross sections of the gridpoint gathers at  $\Delta\tau=0$ . Note the converted wave just below the second PP reflection in the gridpoint gather (figure 3.19B). This event can be recognized by the zero amplitude at  $p=0$ . It almost interferes with the second PP-response.

In the gridpoint gathers in the Radon domain for the two boundaries with a layer

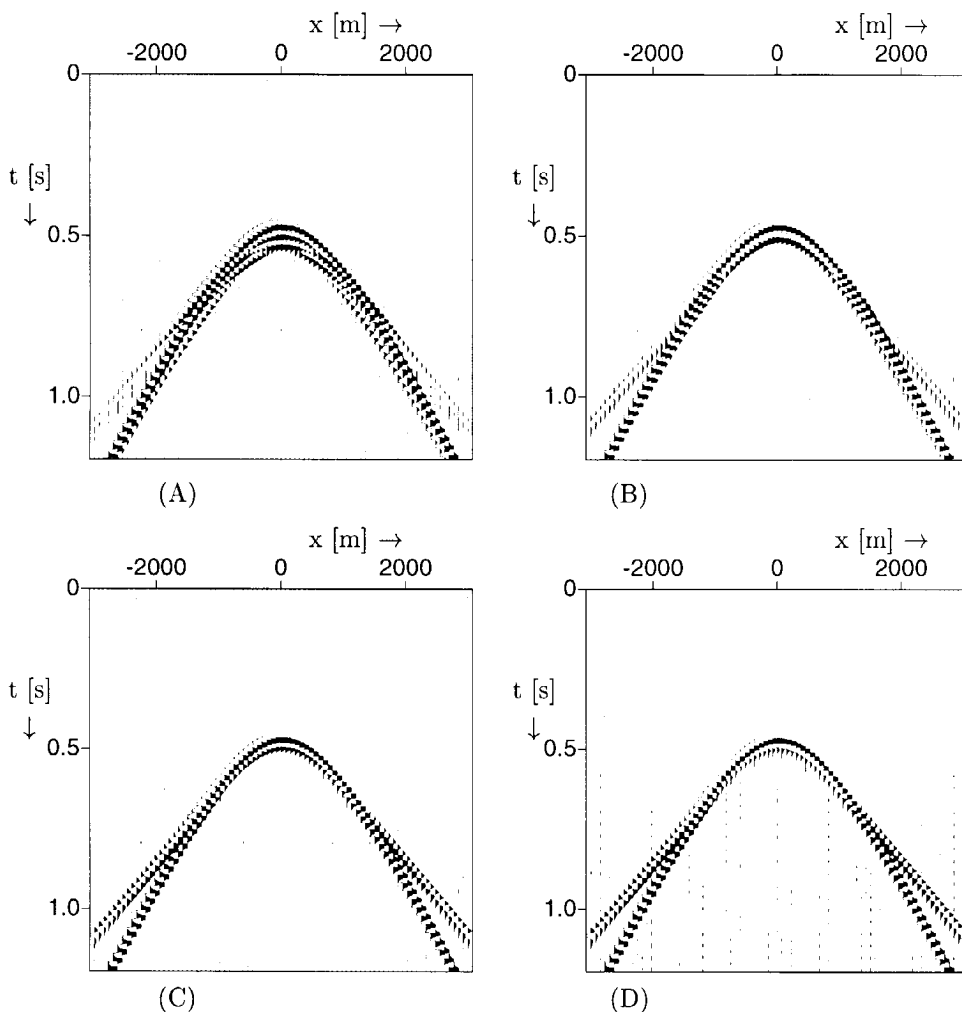


**Fig. 3.18** shot records for layer thicknesses  $\Delta z$  of 200m (A), 100m (B), 50m (C) and 5m (D), using one shale layer between two different half spaces of sandstone.

thickness of 100m, it is clear that the two responses just start to interfere. Due to the high velocity of the layer the thickness is smaller than the seismic wavelength, compared to the example in the previous sections. The analytical RC-function for the first boundary coincides perfectly with the amplitude cross sections of the gridpoint gather at  $\Delta\tau=0$ . Note the converted wave just below the second PP reflection in the gridpoint gather (figure 3.19B), which starts to interfere with the second PP-response at higher  $p$ -values.

In the gridpoint gathers in the Radon domain (3.19(E,F)) for the two boundaries

with a layer thickness of 50m the two responses clearly interfere. The side lobes of the response of one boundary are interfering with the main lobe of the other boundary response. The analytical RC-function for the first boundary still coincides perfectly with the amplitude cross sections of the reflectivity gathers at  $\Delta\tau=0$ , but the response of the second boundary has changed at higher  $p$ -values.

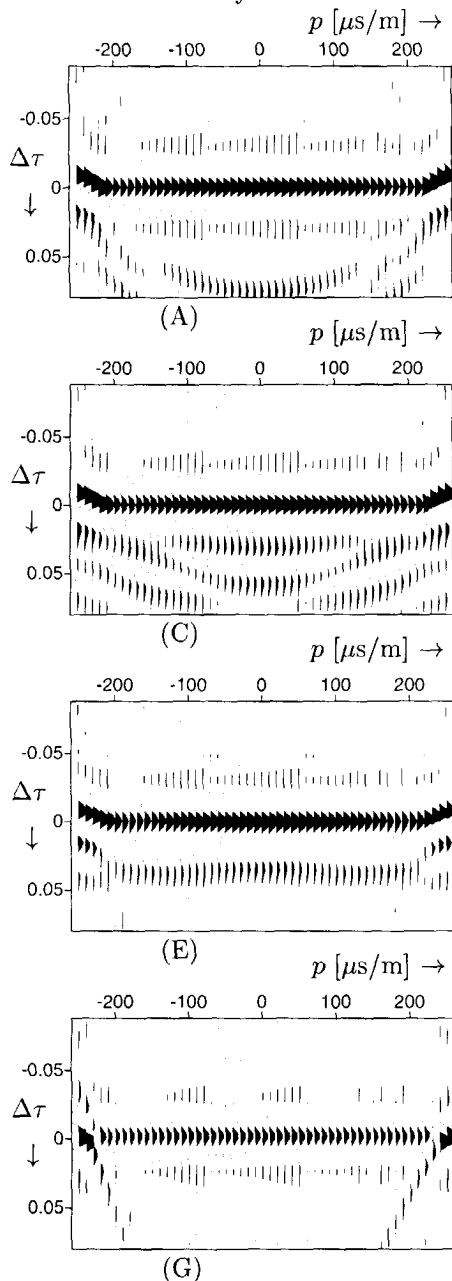
In the gridpoint gathers in the Radon domain for the two boundaries with a layer thickness of 5m the two responses completely interfere. Since the interfering analytical RC-functions are of opposite sign, the amplitudes of the combined response have decreased. The averaged response is almost the same as the response without the shale layer. In figure 3.20(G) the amplitude cross section of the gridpoint gather resemble the analytical RC function of the interface between the two different half spaces without the shale layer.

Even by taking amplitude cross sections at  $\Delta\tau=+0.008\text{ms}$  for the lower boundary (the dashed lines in figure 3.19(H)), the imaged RC-function does not resemble the analytical RC function of the second boundary, but resembles the analytical RC function of two half spaces with opposite sign.

So for a plane wave reflecting on a layer between two different half spaces we can conclude that for normal incidence ( $p=0$ ) the responses as function of decreasing layer thickness  $\Delta z$  first increases due to interference and then decreases to the response of a single boundary between the two half spaces in the limit of  $\Delta z \downarrow 0$ . The tuning curve for  $p=0$  (modeled by a convolution of the reflection coefficients  $R(p=0)$  of the two boundaries with a wavelet) is shown in figure 3.21.

The characteristics are the same as the tuning curve in figure 3.7. Only due to the two different half spaces, there are two different curves for the upper and lower boundary. Also the limit of  $\Delta z \downarrow 0$  has now the value of the RC function between the two half spaces.

first boundary:



second boundary:

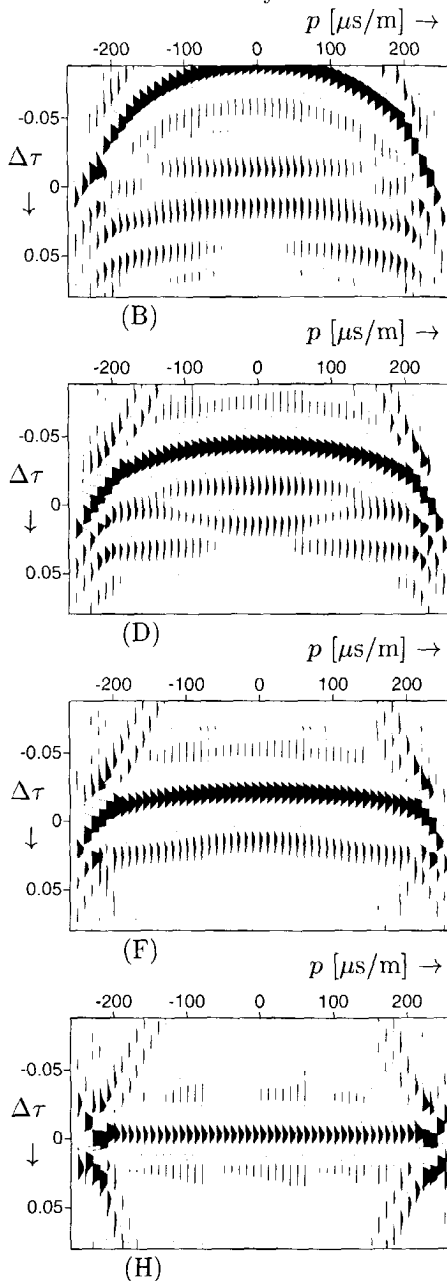


**Fig. 3.19** The gridpoint gathers in the Radon domain for layer thicknesses  $\Delta z$  of 200m (A,B), 100m (C,D), 50m (E,F) and 5m (G,H), using one shale layer between two different half spaces of sandstone.

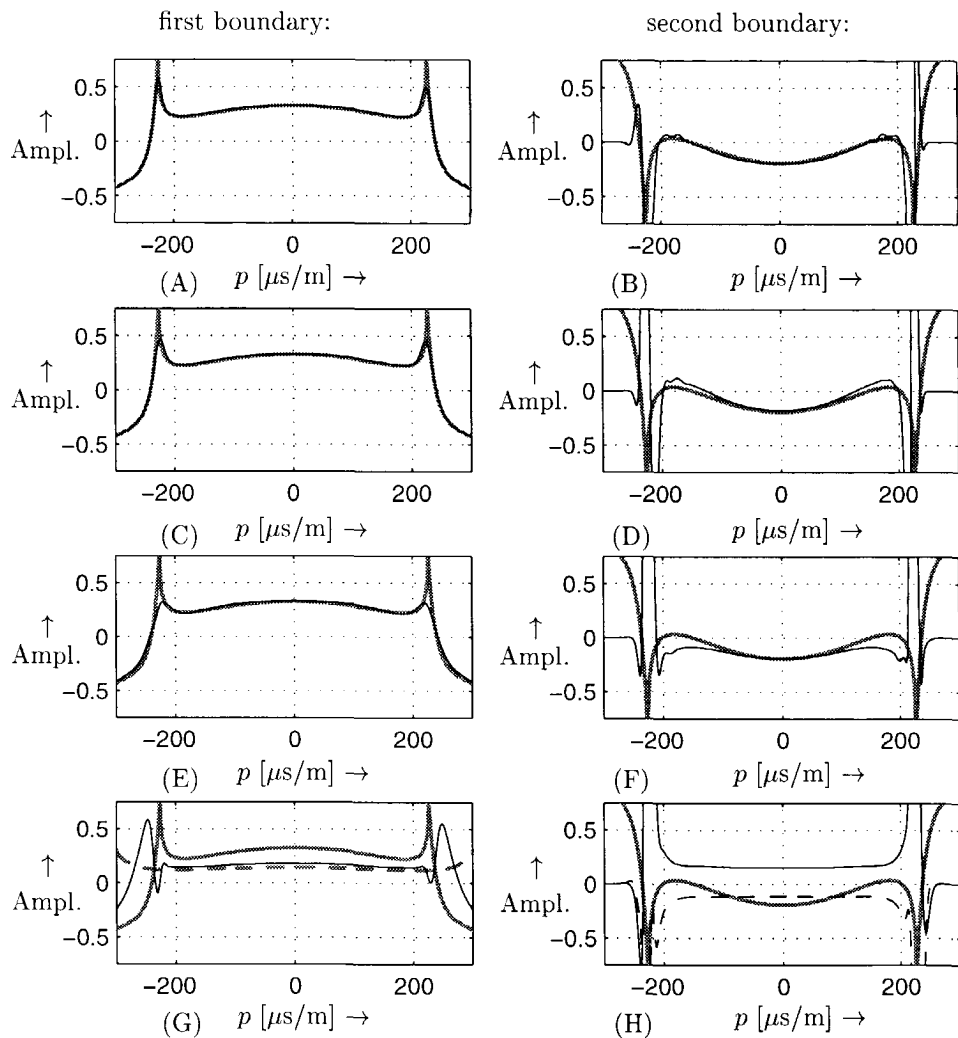


**Fig. 3.20** The amplitude cross sections of the gridpoint gathers at  $\Delta\tau=0$  (figure 3.5) for layer thicknesses  $\Delta z$  of 200m (A,B), 100m (C,D), 50m (E,F) and 5m (G,H), using one shale layer between two different half spaces of sandstone. The analytical RC function for the isolated boundaries is indicated in gray. In figure (G) the dashed gray line indicates the analytical RC function for the isolated boundary between the upper and lower half space without the shale layer. The dashed line in figure (H) shows the amplitude cross section at  $\Delta\tau=8\text{ms}$  in the gridpoint gather.

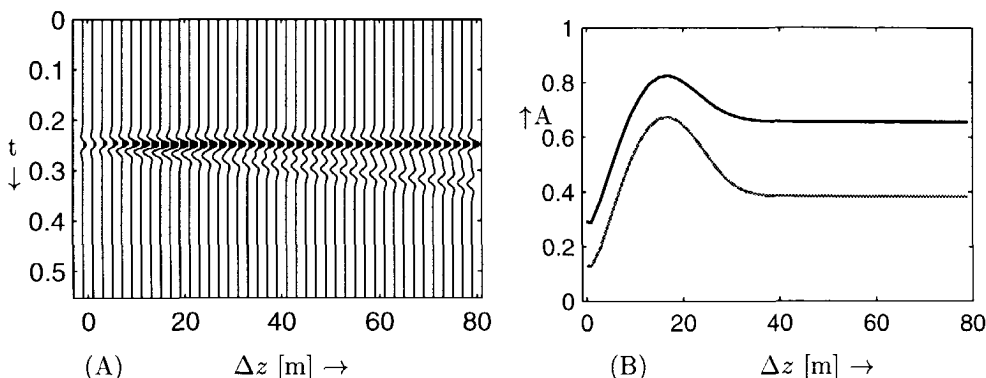


**Fig. 3.21** The tuning effect for perpendicular incidence ( $p=0$ ) as function of layer thickness for two different half spaces. (A) the imaged trace as function of  $\Delta z$  and (B) the amplitude of reflectivity of the upper boundary and of the lower boundary (absolute value) in gray.

### 3.5 Conclusions on numerical modeling of layers between half spaces

In case the distance between boundaries in a blocked 1D model is much larger than the seismic wavelength, the imaged RC function correlates accurately with the theoretical Zoeppritz functions for single boundaries. Only converted shear waves crossing the PP events distort the imaged RC curve. This was shown in the example with layer thicknesses of 200 and 100m.

When the distance between the boundaries of a blocked 1D model are in the range of the seismic wavelength, the imaged RC functions deviate from the analytical Zoeppritz functions for single boundaries. This effect starts for high  $p$ -values, due to the increasing converted energy and increasing vertical wavelength with increasing  $p$  (which will be discussed in more detail in the next chapter), as shown in the example with layer thicknesses of 50m.

If the distance between the boundaries of a blocked 1D model are smaller than the seismic wavelength, the imaged RC functions do not correlate with the analytical Zoeppritz functions for single boundaries. For a small layer between two identical half spaces the overall reflection strength is still significant for small  $p$ -values. This was shown for the layer thicknesses of 10m.

In case that the distance between boundaries in a blocked 1D model are much smaller than the seismic wavelength and the total thickness of the layers is smaller than the seismic wavelength, the total response of the layers becomes one event with the RC function of the single boundary between the half spaces for pre-critical angles. If the half spaces are the same, this means that the response vanishes. If the half spaces differ, the response resembles the response of the step function between the two half

spaces. This means that the background trend or low-frequencies in the velocity model are more important than the very high frequencies for the reflection at small  $p$ -values. The used model seems to smooth the velocity log to the scale of the used seismic wavelet. This was shown for the layer thicknesses of 5m.

This is in accordance with the empirical relation between the seismic amplitudes and the porosity  $\phi$  of a layer times the layer thickness  $\Delta z$ ,

$$Ampl. \sim \phi \times \Delta z. \quad (3.22)$$

For a layer in a background medium (between two identical half spaces) the normal incidence reflectivity  $R_{PP}(p = 0)$  is given by  $\pm \Delta Z / \bar{Z}$ . The tuning curve in section 3.4.2 shows then that the amplitudes are proportional to the impedance contrast times the layer thickness,

$$R \sim \Delta Z / \bar{Z} \times \Delta z, \quad (3.23)$$

for layers which are smaller than the seismic wavelength ( $\Delta z \ll \lambda$ ). Since the impedance  $Z$  is directly related to the porosity  $\phi$ , the relation between the reflection strength and the porosity times the layer thickness in equation 3.22 is understandable.

The relation between the analytical RC function and the imaged RC function is much more complex for  $p > 0$  than for normal incidence. The interference of converted waves ( $p$ -dependent) which the primary PP response makes the total response already in case of a few layers quite complex. This is also described for field data by Simmons and Backus (1994).



## Appendix III

### Explicit nonlinear Knott-Zoeppritz equations.

The content of this appendix shows the matrix notation for the complete scattering matrix and explicit expression for the RC functions for downgoing waves.

#### III.1 The non linear reflection coefficient functions

The reflection coefficients for the reflection of downgoing incident waves, indicated with the superscript  $+$ , and for the reflection of upgoing incident waves, indicated with the superscript  $-$  and the transmission coefficients for up and downgoing waves, indicated with the capitals  $T^-$  and  $T^+$ , can be written elegantly in a complete scattering matrix, given by Aki and Richards (1980).

$$\begin{pmatrix} R_{pp}^+ & R_{ps}^+ & T_{pp}^- & T_{ps}^- \\ R_{sp}^+ & R_{ss}^+ & T_{sp}^- & T_{ss}^- \\ T_{pp}^+ & T_{ps}^+ & R_{pp}^- & R_{ps}^- \\ T_{sp}^+ & T_{ss}^+ & R_{sp}^- & R_{ss}^- \end{pmatrix} = \mathbf{M}^{-1} \mathbf{N}. \quad (\text{III.1})$$

The matrix  $\mathbf{M}$  is given by  $\mathbf{M} =$

$$\begin{pmatrix} -c_{p,1}p & -\sqrt{1-c_{s,1}^2p^2} & c_{p,2} & \sqrt{1-c_{s,2}^2p^2} \\ \sqrt{1-c_{p,1}^2p^2} & -c_{s,1}p & \sqrt{1-c_{p,2}^2p^2} & -c_{s,2}p \\ 2\rho_1 c_{s,1}^2 p \sqrt{1-c_{p,1}^2 p^2} & 2\rho_1 c_{s,1} (1-2c_{s,1}^2 p^2) & 2\rho_2 c_{s,2}^2 p \sqrt{1-c_{p,2}^2 p^2} & 2\rho_2 c_{s,2} (1-2c_{s,2}^2 p^2) \\ -\rho_1 c_{p,1} (1-2c_{s,1}^2 p^2) & 2\rho_1 c_{s,1}^2 \sqrt{1-c_{s,1}^2 p^2} & \rho_2 c_{p,2} (1-2c_{s,2}^2 p^2) & -2\rho_2 c_{s,2}^2 p \sqrt{1-c_{s,2}^2 p^2} \end{pmatrix}$$

and the matrix  $\mathbf{N}$  is given by  $\mathbf{N} =$

$$\begin{pmatrix} c_{p,1}p & \sqrt{1-c_{s,1}^2p^2} & -c_{p,2} & -\sqrt{1-c_{s,2}^2p^2} \\ \sqrt{1-c_{p,1}^2p^2} & -c_{s,1}p & \sqrt{1-c_{p,2}^2p^2} & -c_{s,2}p \\ 2\rho_1 c_{s,1}^2 p \sqrt{1-c_{p,1}^2 p^2} & 2\rho_1 c_{s,1} (1-2c_{s,1}^2 p^2) & 2\rho_2 c_{s,2}^2 p \sqrt{1-c_{p,2}^2 p^2} & 2\rho_2 c_{s,2} (1-2c_{s,2}^2 p^2) \\ \rho_1 c_{p,1} (1-2c_{s,1}^2 p^2) & -2\rho_1 c_{s,1}^2 \sqrt{1-c_{s,1}^2 p^2} & -\rho_2 c_{p,2} (1-2c_{s,2}^2 p^2) & 2\rho_2 c_{s,2}^2 p \sqrt{1-c_{s,2}^2 p^2} \end{pmatrix}.$$

### III.1.1 Explicit RC functions

From equation III.1 explicit equations can be derived for the RC functions  $R_{pp}$ ,  $R_{ps}$ ,  $R_{sp}$  and  $R_{ss}$  (for downgoing incident wave fields). These expressions are given below as function of ray parameter  $p$  (Aki and Richards, 1980).

$$R_{pp}(p) = [(b \frac{\sqrt{1 - c_{p,1}^2 p^2}}{c_{p,1}} - c \frac{\sqrt{1 - c_{p,2}^2 p^2}}{c_{p,2}})F - (a + d \frac{\sqrt{1 - c_{p,2}^2 p^2}}{c_{p,2}} \frac{\sqrt{1 - c_{s,2}^2 p^2}}{c_{s,2}})Hp^2]/D, \quad (\text{III.2})$$

$$R_{ps}(p) = 2 \frac{\sqrt{1 - c_{s,1}^2 p^2}}{c_{s,1}} (ab + cd \frac{\sqrt{1 - c_{p,2}^2 p^2}}{c_{p,2}} \frac{\sqrt{1 - c_{s,2}^2 p^2}}{c_{s,2}})pD, \quad (\text{III.3})$$

$$R_{sp}(p) = -2 \frac{\sqrt{1 - c_{p,1}^2 p^2}}{c_{p,1}} (ab + cd \frac{\sqrt{1 - c_{p,2}^2 p^2}}{c_{p,2}} \frac{\sqrt{1 - c_{s,2}^2 p^2}}{c_{s,2}})pD \quad (\text{III.4})$$

and

$$R_{ss}(p) = [(b \frac{\sqrt{1 - c_{s,1}^2 p^2}}{c_{s,1}} - c \frac{\sqrt{1 - c_{s,2}^2 p^2}}{c_{s,2}})E - (a + d \frac{\sqrt{1 - c_{p,2}^2 p^2}}{c_{p,2}} \frac{\sqrt{1 - c_{s,1}^2 p^2}}{c_{s,1}})Gp^2]/D. \quad (\text{III.5})$$

Using the variables

$$\begin{aligned} a &= \rho_2(1 - 2c_{s,2}^2 p^2) - \rho_1(1 - 2c_{s,1}^2 p^2) \\ b &= \rho_2(1 - 2c_{s,2}^2 p^2) + \rho_1 c_{s,1}^2 p^2 \\ c &= \rho_1(1 - 2c_{s,1}^2 p^2) + \rho_2 c_{s,2}^2 p^2 \\ d &= 2(\rho_2 c_{s,2}^2 - \rho_1 c_{s,1}^2) \end{aligned} \quad (\text{III.6})$$

and the angle-dependent variables

$$\begin{aligned}
 E &= b \times \frac{\sqrt{1 - c_{p,1}^2 p^2}}{c_{p,1}} + c \times \frac{\sqrt{1 - c_{p,2}^2 p^2}}{c_{p,2}} \\
 F &= b \times \frac{\sqrt{1 - c_{s,1}^2 p^2}}{c_{s,1}} + c \times \frac{\sqrt{1 - c_{s,2}^2 p^2}}{c_{s,2}} \\
 G &= a - d \times \frac{\sqrt{1 - c_{p,1}^2 p^2}}{c_{p,1}} \times \frac{\sqrt{1 - c_{s,2}^2 p^2}}{c_{s,2}} \\
 H &= a - d \times \frac{\sqrt{1 - c_{p,2}^2 p^2}}{c_{p,2}} \times \frac{\sqrt{1 - c_{s,1}^2 p^2}}{c_{s,1}} \\
 D &= E \times F + G \times H \times p^2.
 \end{aligned} \tag{III.7}$$

Note that these coefficients are based on the reflection of potentials as used in this thesis rather than for particle displacement as defined in Aki and Richards (1980).



# Chapter 4

## Compensation for $p$ -dependent resolution

*This chapter describes the dependency of the vertical resolution as function of ray parameter and its impact on the imaged RC-gather. Two methodologies are presented to compensate for this effect: deconvolution and bandpass filtering. This will result in an optimal input gather for the linearized AVP inversion.*

### 4.1 Introduction

The imaged reflectivity  $R(p, t_z)$  from seismic data is always a scaled version of the real reflectivity of the earth  $R_{\text{earth}}(p, t_z)$ <sup>1</sup>. It is well known that the relation between  $R_{\text{earth}}(p, t_z)$  and the imaged reflectivity is complicated by many factors (Ostrander, 1984). Some of these factors are ‘reflection related’ (such as thin bed tuning, reflector curvature), others ‘propagation related’ (such as geometrical spreading, transmission and/or an-elastic losses) or ‘acquisition related’ (such as source/receiver directivity, geophone coupling).

The acquisition related ‘footprints’ were discussed in Chapter 2 and the thin bed tuning in Chapter 3. In this chapter the reflection related effects of interference and scaling in (finely) layered media are discussed.

### 4.2 $P$ -dependent resolution

The scale or vertical resolution of the reflectivity is a function of velocity and angle (Wapenaar et al., 1996; van Wijngaarden and Wapenaar, 1995). This phenomenon is illustrated in figure 4.1. In this figure a well-log measurement is shown twice, representing an 1D model.

In the upper left-hand (A) and upper right-hand part (B) of figure 4.1 the model is illuminated by plane waves with the same wavelength  $\lambda$  but with different ray parameters  $p$ . As a result the vertical wavelength  $\lambda_z$  is different in the case on the right-hand side (A) from the one of the left-hand side (B). In other words, illuminating the medium with the same plane wave under different angles changes

---

<sup>1</sup>the time  $t_z$  indicates the depth in two-way travel time

the scale or resolution in depth at which the medium is observed.

In the lower left-hand (C) and lower right-hand part (D) of figure 4.1 the models are illuminated by plane waves with different wavelengths  $\lambda$  and  $\lambda'$  for different ray parameters  $p$ , but both with the same vertical wavelength  $\lambda_z$ . If each frequency component is treated separately, the wavelength per frequency  $\omega$  in the  $z$ -direction as function of angle  $\phi$  or ray parameter  $p$  is given by

$$\lambda_z = \frac{2\pi c}{\omega \cos \phi}, \quad \cos \phi = \sqrt{1 - c^2 p^2}. \quad (4.1)$$

This means that for an increasing angle  $\phi$  the resolution in depth  $\lambda_z^{-1}$  decreases.

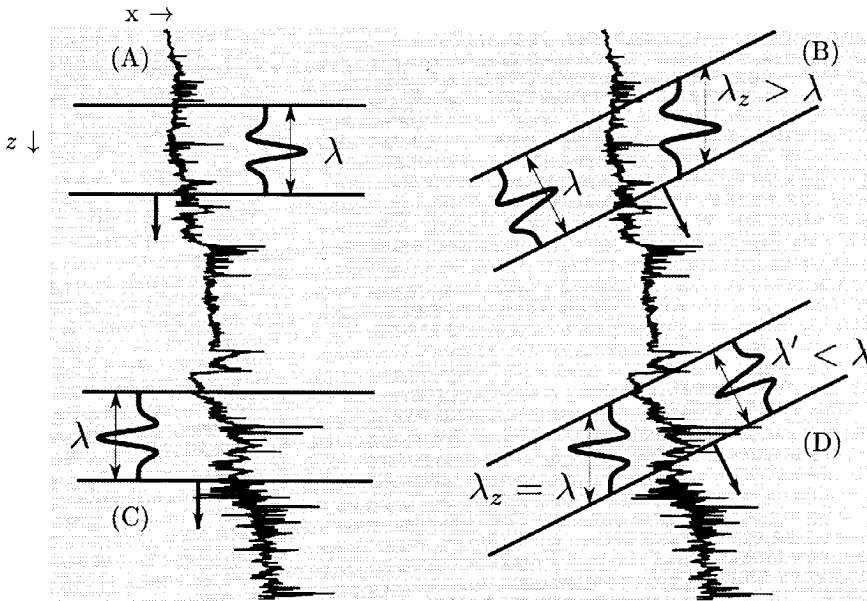


**Fig. 4.1** The relation between the resolution in depth  $\lambda_z^{-1}$  and the angle of the illuminating plane wave. Note that in (A) and (B) the resolution in depth is not equal, whereas in (C) and (D) the resolution in depth is the same.

This phenomenon of  $p$ -dependent resolution in depth is well-known as stretching with offset in NMO correction of CMP gathers, in prestack migration of shot records or in RC gathers. In the following sections several compensation methods will be discussed. The goal is to have one scale for all  $p$ -values.

### 4.3 Transformation of the RC-gather to one scale

#### 4.3.1 Constant velocity medium

For a constant velocity medium, the resolution in depth  $\lambda_z^{-1}$  or scale  $\sigma$  for a given seismic wavelength  $\lambda$  is only dependent on  $p$ . Equation 4.1 shows that the resolution

decreases with increasing  $p$ . This means that if a medium is illuminated with a certain wavelet for a range of  $p$ -values (i.e. a constant temporal bandwidth in  $p - \omega$ , see figure 4.2), the imaged reflectivity  $R(p; z_m)$  at a certain depth  $z_m$  is also a function of scale  $\sigma$ :  $R(p, \sigma(p); z_m)$ .

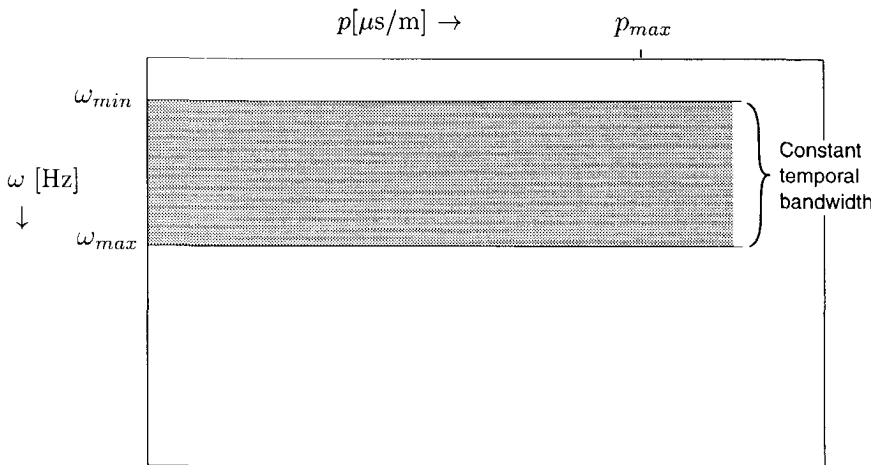


**Fig. 4.2** The frequency spectrum of the illuminating field as function of  $p$  for a constant temporal bandwidth.

The influence of these two parameters ( $\sigma, p$ ) can easily be separated in an acoustic layered model with only density variations. In this case the separate boundaries do not have a varying reflectivity as function of  $p$ , i.e.  $R(p; z_m) = \text{constant}$ . If these layers are thinner than the scale of the seismic resolution and a constant temporal bandwidth is used, then the imaged amplitude cross section of the reflectivity gather or *AVP* (*Amplitude-Versus-P*) curve will show amplitude variations as function of  $p$ . This apparent AVP behaviour does not show the  $p$ -dependent reflectivity, but the  $\sigma$ -dependent reflectivity, as shown in the example in figure 4.3. Due to the (small) change in scale (often called 'stretching') the imaged reflectivity is the averaged reflectivity over an increasing depth range with increasing  $p$ -values. Therefore does the amplitude change as function of  $p$ .

This can be compensated for by applying a  $p$ -dependent frequency filter to the data in such a way, that the scale  $\sigma$  is constant in  $p$ . The reflectivity will now be at the same scale for all depths and for all  $p$ -values.

This compensation filter can be applied before imaging, on the illuminating and detecting field, or after imaging, on the RC gather.

First the application before imaging will be discussed. This means the illuminat-

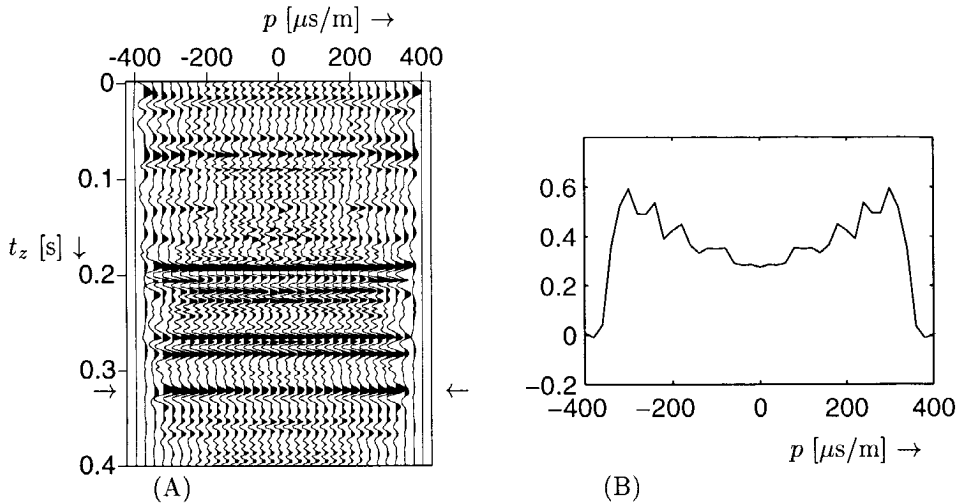


**Fig. 4.3** (A) The imaged reflectivity gather belonging to a layered acoustic model with only density contrasts and (B) the AVP-curve at  $t=0.32s$ .

ing and detecting field must be constructed in such a way that the resolution in depth of the illuminating field is constant as a function of  $p$ . In the ray parameter-frequency domain this means that the frequency content of the gridpoint gather must be between curves of constant resolution  $\lambda_z$ . Normally the gridpoint has a constant temporal bandwidth (after removing the 'acquisition footprints'). This means that a filter must be applied, which limits the frequency content of the illuminating field between the curves of constant  $\lambda_z$ , given by  $2\pi c/\omega_{min} \cos\phi$  and  $2\pi c/\omega_{max} \cos\phi$ . This is shown in figure 4.4.

A compensation filter can also be applied to the data after imaging, i.e. on the RC gather. In the ray parameter-frequency<sup>2</sup> domain the filter between the curves of constant  $\lambda_z$  becomes a bandpass filter, as shown in figure 4.5, which can be applied on the RC-gather.

#### 4.3.2 Varying velocity medium

For a varying velocity medium, the resolution in depth ( $\lambda_z$ ) is not only depending on  $p$ , but also on depth (see equation 4.1). The velocity in the term  $2\pi c(z)/\omega$  will give a change in scale as function of depth for one  $p$ -value. The depth dependent velocity in the term  $\cos\phi = \sqrt{1 - c(z)^2 p^2}$  results in the fact that the change in scale with  $p$  becomes depth dependent; for larger velocities the change in scale with  $p$  becomes also larger. This means that if the RC gather would be displayed in depth, for each depth the filter must be adapted in order to get the maximum resolution.

<sup>2</sup>note that here the frequency denotes the Fourier transform  $\omega_z$  of the time  $t_z$

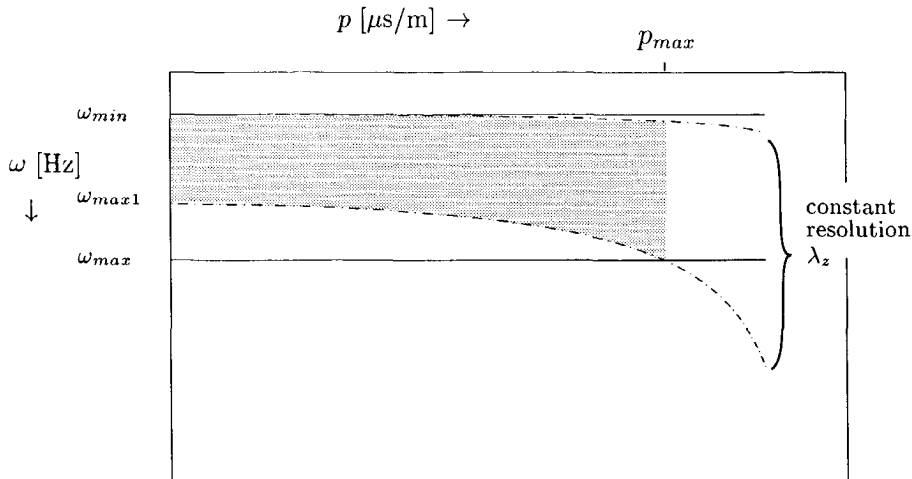


**Fig. 4.4** The frequency spectrum of a typical gridpoint gather (indicated by  $\omega_{\min}$  and  $\omega_{\max}$ ) and the constant spatial bandwidth filter (gray area). Note that the resolution after imaging is constant for all  $p$ -values and equal to the resolution of the filtered gridpoint gather at  $p = 0$ .

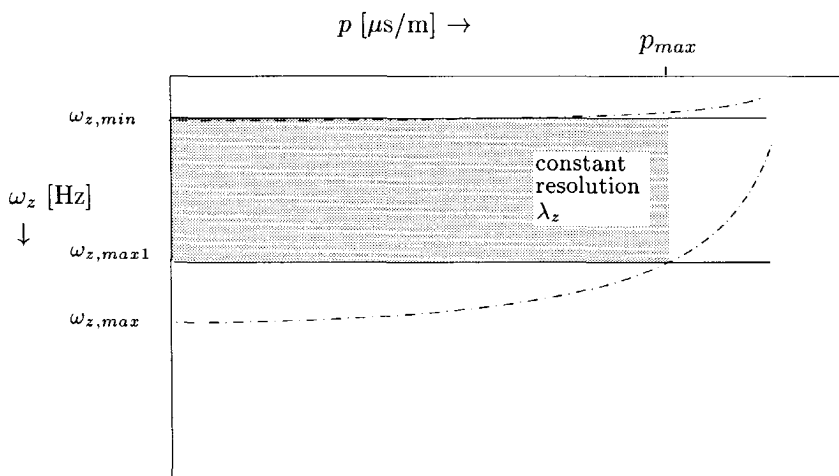


**Fig. 4.5** The frequency spectrum of the data after imaging (RC-gather, indicated by  $\omega_{z,\min}$  and  $\omega_{z,\max}$ ) and the constant spatial bandwidth filter (gray area). Note that the resolution after imaging is constant for all  $p$ -values.

Or if one filter is used, then the highest velocity/lowest resolution determines the overall resolution. Since the RC-gather is normally used as a function of time, the scale as function of time is constant for  $p = 0$  (if absorption/dispersion is ignored).

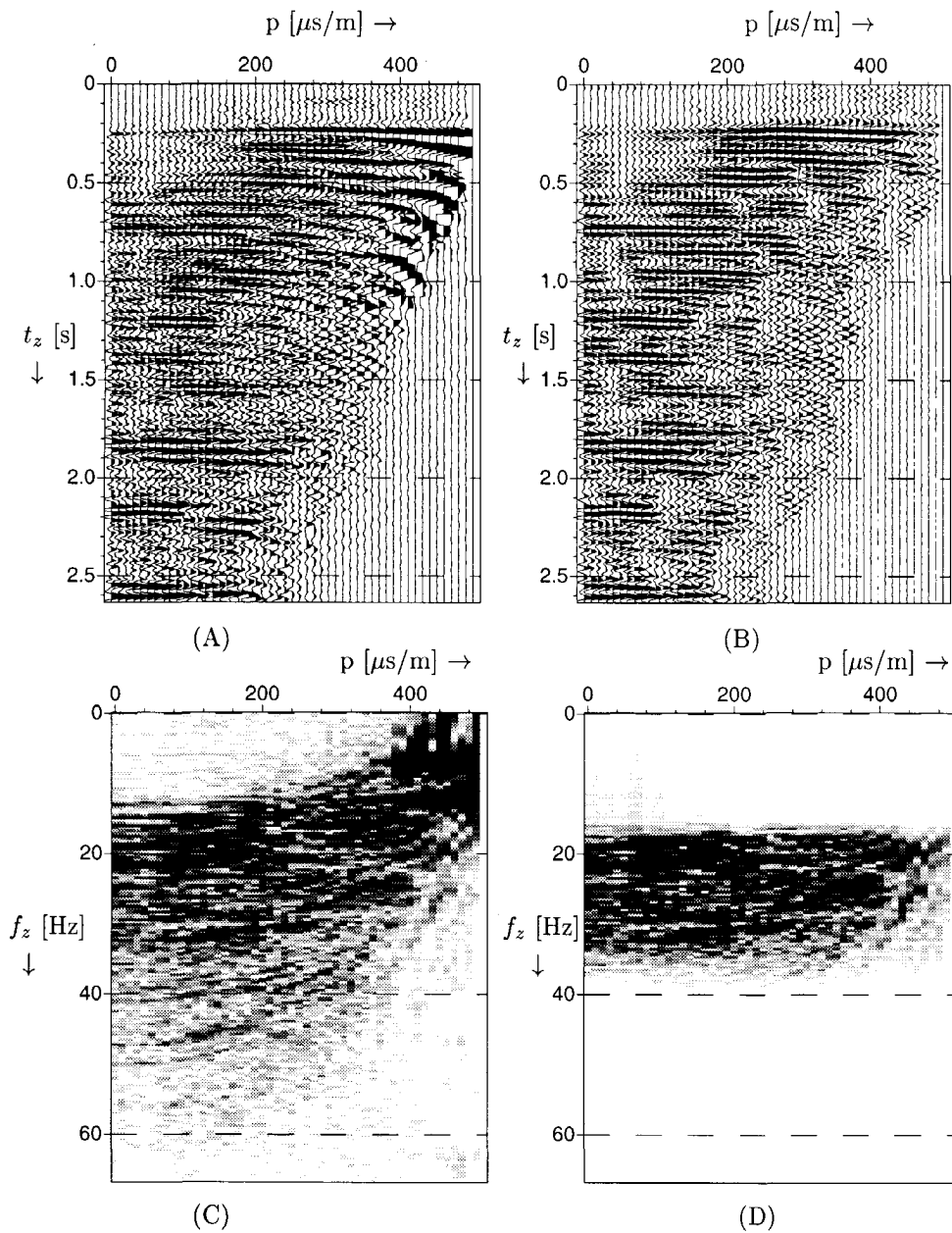


**Fig. 4.6** (A) The RC-gather and (B) the RC-gather after filtering in the  $p, \omega$ -domain. (C) The frequency spectrum of the unfiltered RC-gather and (D) the frequency spectrum of the filtered RC-gather.

The resolution in time becomes with ' $\lambda_{z_t}$ ' ( $= T = \lambda_z / c(z)$ ),

$$\lambda_{z_t} = \frac{2\pi}{\omega \cos\phi}, \quad \cos\phi = \sqrt{1 - c(z)^2 p^2}. \quad (4.2)$$

If the change in scale due to the velocity in the  $\cos\phi$  term is ignored, then one filter can be applied to the whole RC gather. An example on field data is given in figure 4.6. In the ideal case we would like not to filter out information or loose resolution. This will be discussed in section 4.4.

In figure 4.6A an imaged RC gather from a 2D offshore dataset is shown. Clearly the decrease of resolution for  $p$ -values above  $400\mu\text{s}/\text{m}$  in the upper part can be recognized. This can also be seen in the frequency spectrum in figure 4.6C. The frequency content shifts to lower values for increasing  $p$ -values. In the deeper part of the data (below 1.5s) this phenomenon is not so clear in the RC gather. This is expected since imaged angle range is smaller for the deeper data.

A bandpass filter has been applied to the RC gather to reduce the data below 20Hz and above 40 Hz in order to compensate for the  $p$ -dependent resolution. The filtered gather is shown in figure 4.6B together with the frequency spectrum in 4.6D. Clearly the low-frequent (post-critical) part has been removed in 4.6B and the filtered gather shows an overall constant scale. The improvement in figure 4.6B is more prominent in the top part than in the lower part. Overall the events in the RC gather are more continuous as function of  $p$ , because the imaged reflectivity is averaged over the same  $\lambda_z$  for all  $p$ -values. This will be important in the local inversion of AVP data in Chapter 5 and 6.

#### 4.3.3 Transformation of angle gathers

If we look at equation 4.2, we see that the resolution is dependent on the local angle,  $\cos\phi = \sqrt{1 - c(z)^2 p^2}$ . This means that due to a changing  $c(z)$ , the local angle  $\phi$  in a trace belonging to one  $p$ -value is not constant. Due to the change in  $\cos\phi$  within the trace, also the scale  $\sigma$  will change within the trace as function of depth. If the RC gather is correctly transformed from the time-ray parameter domain to the time-angle domain, the scale  $\sigma$  will be constant within each trace (under the assumption of an absorption/dispersion free domain). In this domain one filter can be correctly applied to the RC gather without loosing additional resolution due to varying velocities. Figure 4.7 shows an example for the RC gather from figure 4.6. The scale or resolution of the velocity model, which is used to transform the RC gather to the angle domain, is of the same scale as the seismic data. Although there is no prove given here, it is plausible that the scale of a well log measurement is to fine and that the scale of a macro model (used in the imaging) is too coarse. This subject is discussed in more detail in the next chapter.

It seems to be a disadvantage of the angle gathers that an accurate velocity model is needed for the conversion of local ray parameter to local angle. But this velocity model is also needed for optimum filtering in the  $\omega - p$  domain and it is needed in the AVA inversion of the RC-gathers (discussed in the next chapter). This means that the conversion to the angle domain is an advantage, because in the first place it shows the influence of the velocity model and secondly the angle gathers are easier to interpret than the  $p$ -gathers. Another advantage will be shown in the next section.

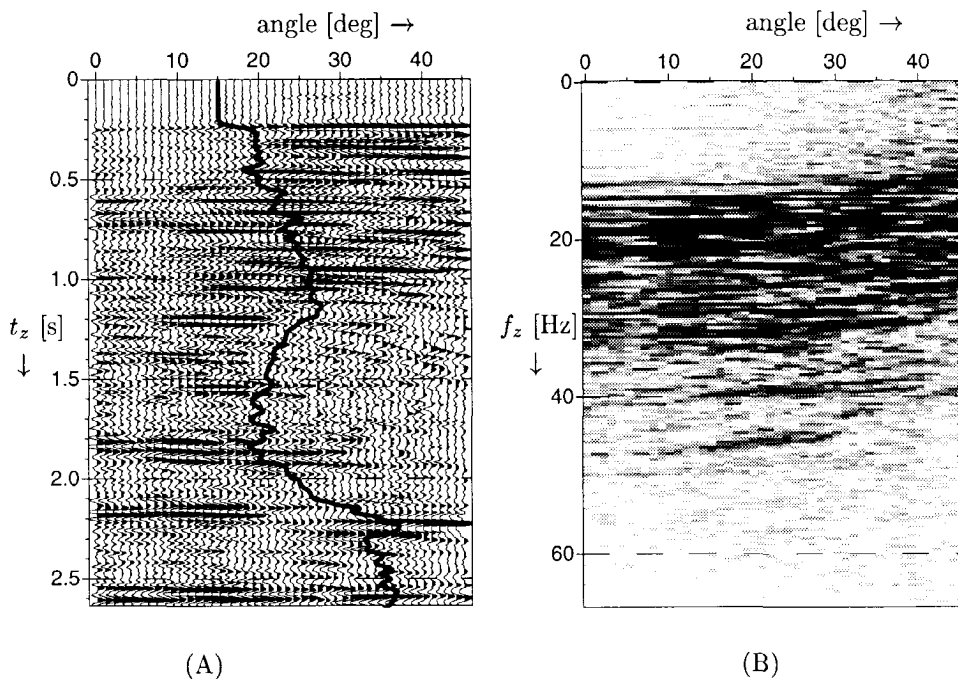


**Fig. 4.7** (A) The RC-gather from figure 4.6 after transformation to the angle domain and (B) the frequency spectrum of the RC-gather as function of angle. The velocity used in the conversion from ray parameter to angle is overlaying the RC gather.

#### 4.4 Improving the resolution by deconvolution

In the previous sections the RC-gathers were transformed to one scale by filtering the finer scales to the coarsest scale. This means that for small  $p$ -values or angles we loose resolution. Of course it would be more attractive to 'add' frequencies which are missing than to remove data.

Instead of adding data we try to flatten the spectrum of the data by (predictive) deconvolution. This process is often used in seismic processing (before and after stack), to derive a sharp minimum phase wavelet. The assumption of a white spec-

trum for the reflectivity is used in a statistical way to increase the high frequencies in order to narrow the length of the seismic wavelet or, in other words, to increase the resolution. Note that if the prediction lag is chosen to be 1 sample, this process is called 'spiking deconvolution'. A detailed discussion of the predictive deconvolution is beyond the scope of this thesis. For further information on this subject the reader is referred to o.a. Yilmaz (1985).

#### 4.4.1 Improving the resolution by deconvolution in the $p$ -domain

In this section the application of the combination of predictive deconvolution and spatial bandpass filtering on a RC gather is shown. In the example a predictive deconvolution with a gap of 12ms and an operator length of 80ms has been used. The operator design is averaged over 61  $p$  traces, in order get a smooth  $p$  consistent operator.

The primary goal is not to improve the resolution for small  $p$ -values, but only to change the frequency spectrum for the larger  $p$ -values. For this reason we used a gap of 12ms and applied a band filter (10-20-45-55 Hz) to remove the noise at high and low frequencies. This means that after the deconvolution we have approximately the same frequency content for normal incidence, and a flat spectrum as function of  $p$ . Figures 4.8(A) and (E) show the RC gather before and after deconvolution and figure 4.9(A) shows the RC gather after predictive deconvolution and bandpass filtering. The data before deconvolution (figure 4.8(A)) shows a decreasing frequency content with  $p$ . The averaged spectrum shows a central frequency around 20 Hz. Analysis of the autocorrelation of the data (not shown here) gives a wavelet length in the order of 75ms.

The data after deconvolution (figure 4.8(E)) has an approximate flat spectrum up to 45Hz. The boosted high frequency makes the data looks noisy.

After bandpass filtering, the RC gather looks much cleaner again (figure 4.9(A)). The overall spectrum (figure 4.9(B)) is fairly flat between 15 and 45 Hz and the spectrum as function of  $p$  looks quite flat (figure 4.9(C)), which is the main goal in applying the deconvolution.

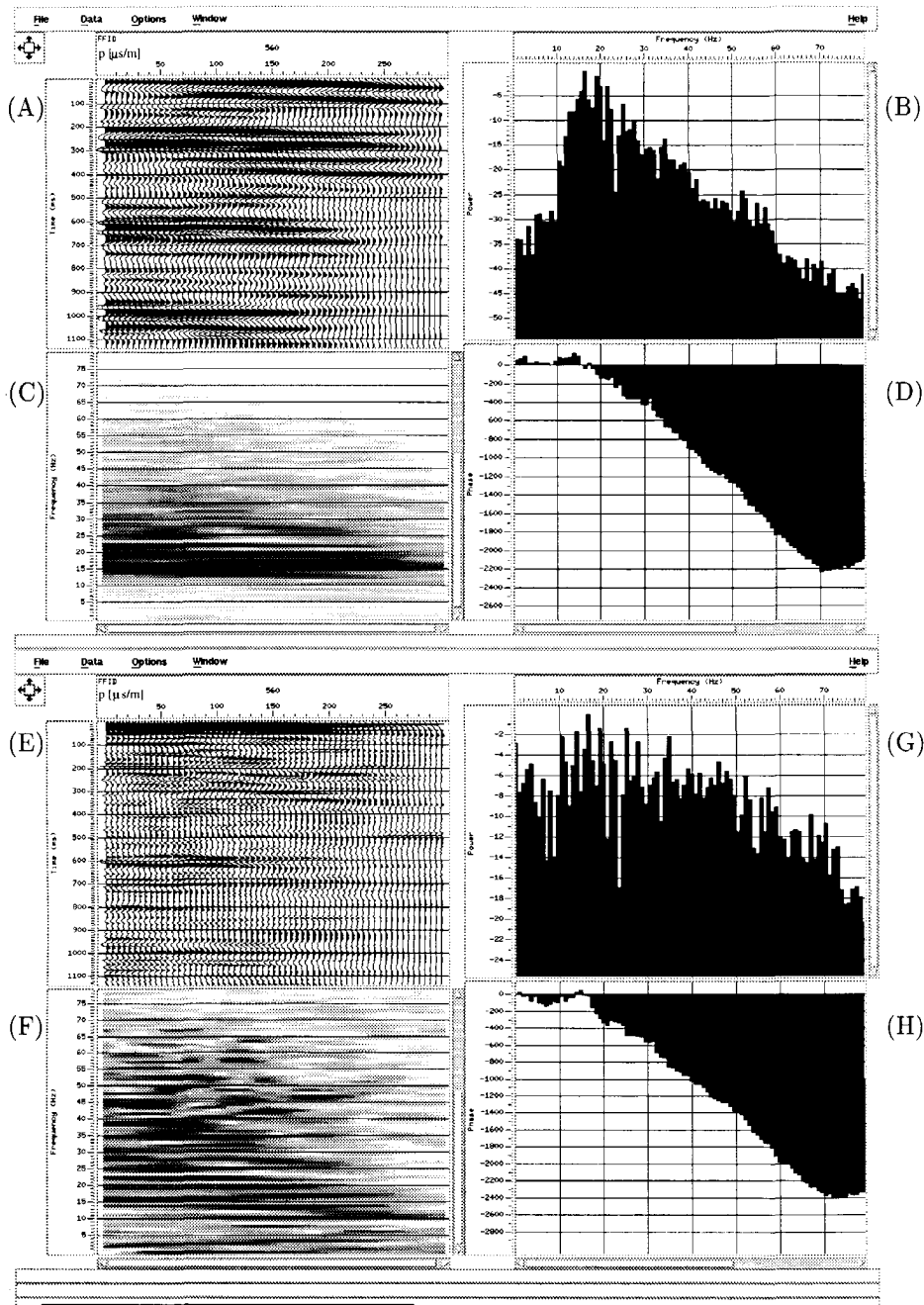
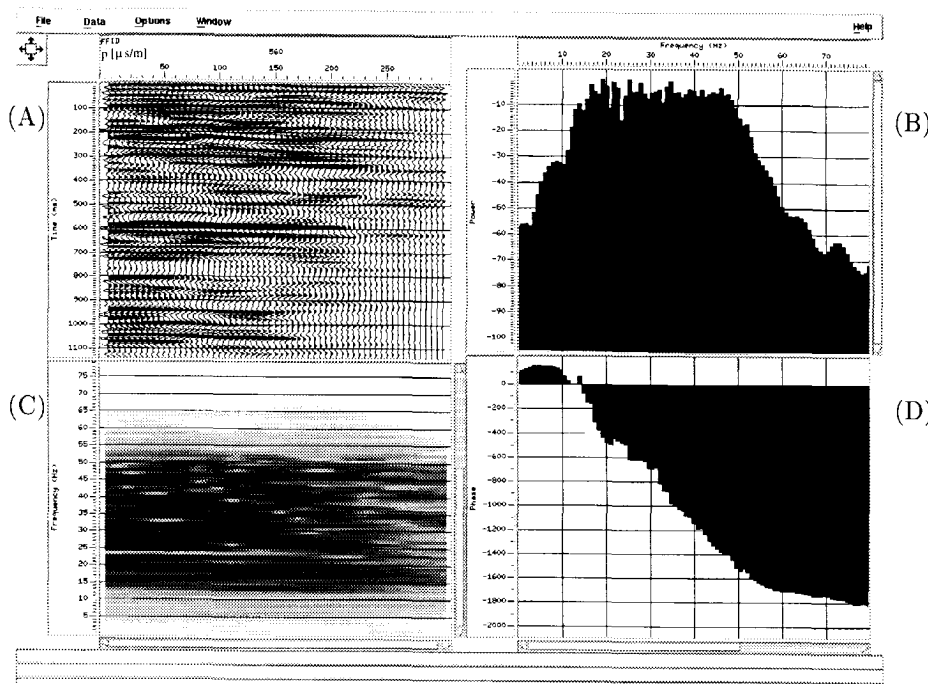


Fig. 4.8 The RC-gather (A), its frequency spectrum as function of ray parameter (C), averaged over all  $p$ -values (B) and the phase spectrum (D). (E)-(H) The RC-gather in the ray parameter domain after predictive deconvolution.



**Fig. 4.9** The  $RC(t_z, p)$ -gather after predictive deconvolution and bandpass filtering (A), frequency spectrum as function of ray parameter (C) and averaged over all  $p$ -values (B) and the phase spectrum (D).

#### 4.4.2 Improving the resolution by deconvolution in the angle-domain

One of the assumptions in the predictive deconvolution process is that the source waveform does not change as it travels in the subsurface; i.e., it is stationary. This assumption is violated in case of absorption/dispersion, which can be compensated by inverse Q-filtering or by using several time windows. In each time window the source waveform is expected to be stationary.

Without absorption/dispersion the assumption is still violated by the fact that in each trace of the  $RC(t_z, p)$ -gather the scale is changing due to the varying velocity. But if we translate the  $RC(t_z, p)$ -gather to the angle domain  $RC(t_z, \alpha)$ , the scale is constant within each trace. This makes the angle gather more suitable as input in the predictive deconvolution than the ray parameter gather.

Figures 4.10 and 4.11 illustrates this on the field data. Figure 4.12 compares the results between deconvolution of bandpass filtering in the  $p$ -domain and in the angle domain.

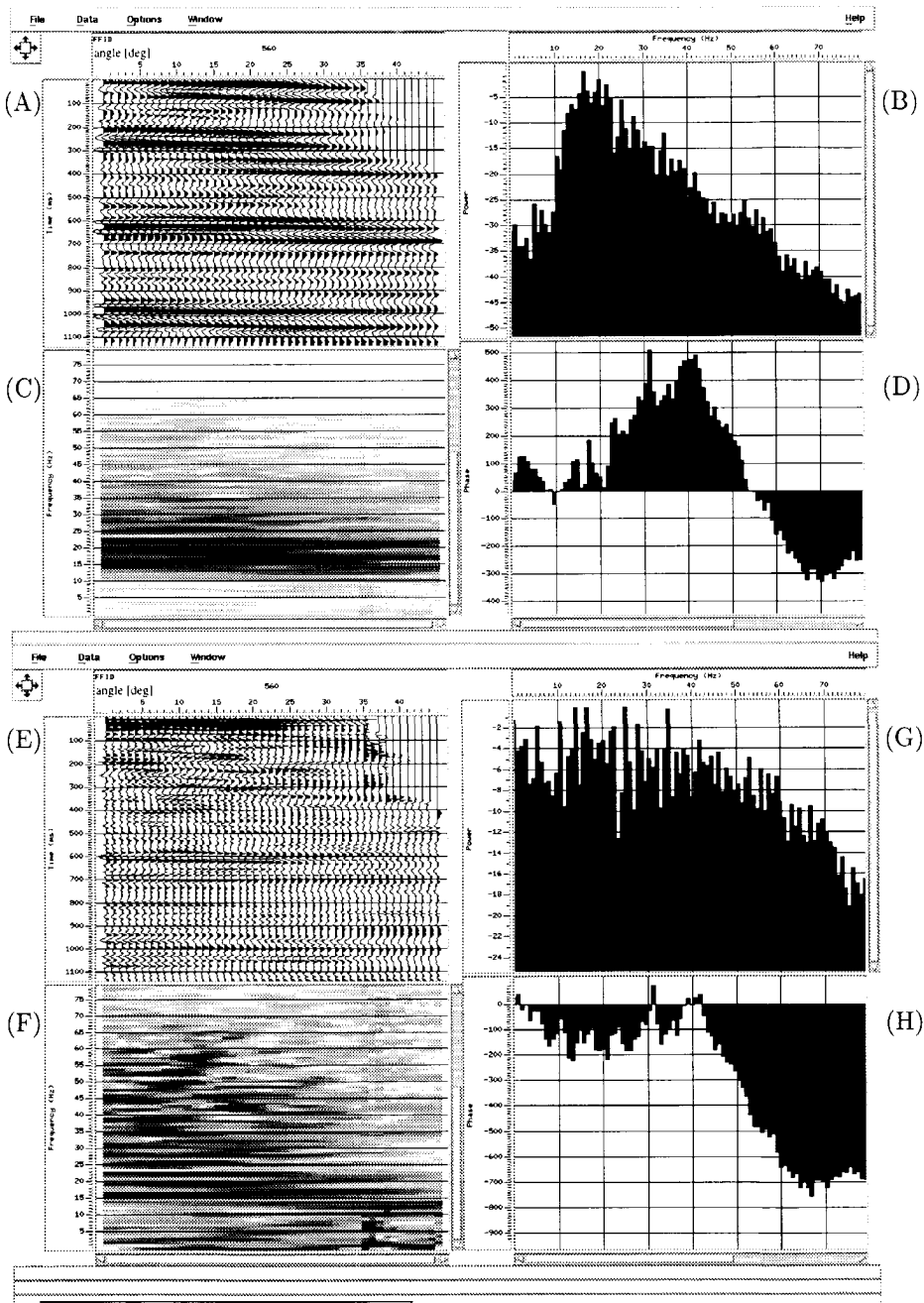


**Fig. 4.10** The RC-gather (A), frequency spectrum of the RC-gather as function of angle (C), averaged over all angles (B) and the phase spectrum (D). (E)-(H) The RC-gather in the angle domain after predictive deconvolution.

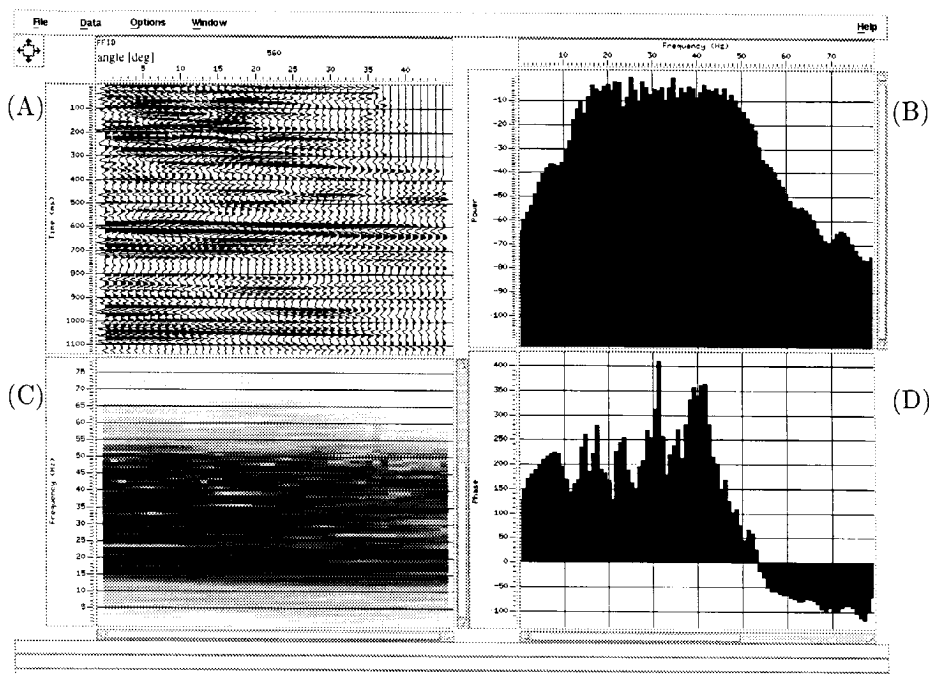


**Fig. 4.11** The RC-gather after predictive deconvolution and bandpass filtering (A), frequency spectrum as function of angle (C) and averaged over all angles (B) and the phase spectrum (D).

Figure 4.14 shows the estimated acoustic impedance (see Chapter 5) using the RC-gathers after deconvolution/filtering with the well synthetic pasted in the middle. The well synthetic for a constant scale in depth  $\sigma_z$  was made by convolving the product of the sonic and density log with the first derivative of a Gaussian divided by the convolution of the product of the sonic and density log with the Gaussian itself. This procedure was repeated for a range of scales  $\sigma_z$ . By choosing a varying scale in depth (as shown in figure 4.13(B)), a constant scale in time  $\sigma_t$  has been selected (shown in figure 4.13(C)). For a more extensive discussion on this subject the reader is referred to Verhelst and van Wijngaarden (1997b). Finally on the trace (with the constant scale in time) the same bandpass filter has been applied as applied to the data. After 4 minor adjustments in the depth-to-time conversion, we have an almost perfect match with the seismic data, *without* any wavelet matching.

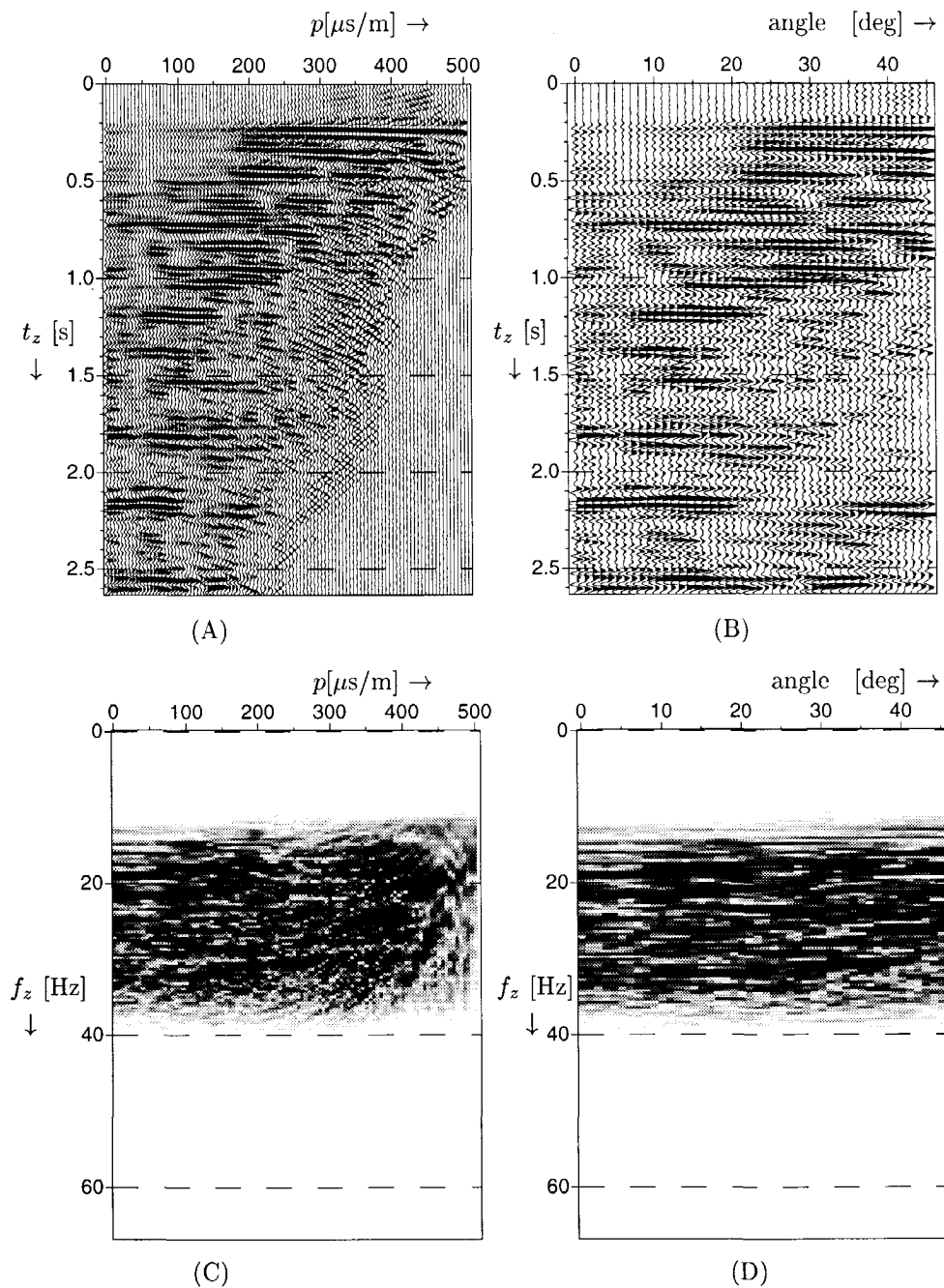


**Fig. 4.12** (A) The RC-gather after predictive deconvolution filtering in the  $p, \omega_z$ -domain and (B) after predictive deconvolution and filtering in the  $\alpha, \omega_z$ -domain. The frequency spectra of the gathers are shown in (C) and (D).

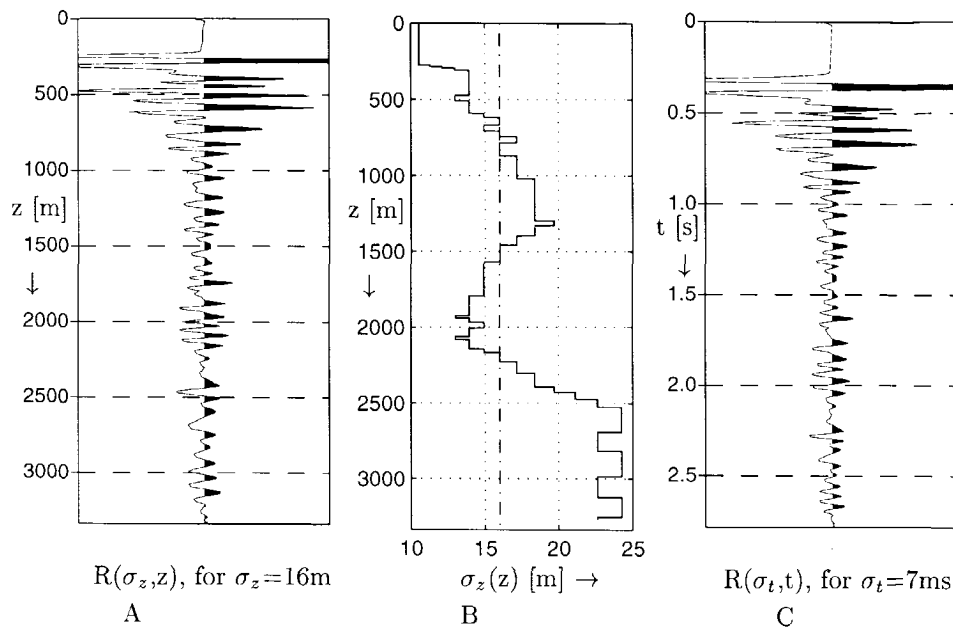


**Fig. 4.13** Results for the selection of a depth dependent scale, in order to obtain a constant scale in time. (A) is the result from the selection procedure, using the  $\sigma_z$  description from the iterative scheme drawn in (B). This procedure results in a constant scale in time  $\sigma_t = 7\text{ ms}$ , as can be seen after depth to time conversion (C). This result can be compared with figure 4.14. Note that the amount of detail (scale  $\sigma_t$ ) remains constant in time (C), but that the scale in depth  $\sigma_z$  is varying (B).

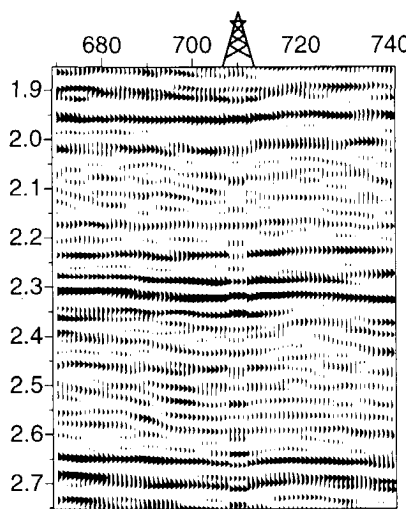


**Fig. 4.14** The estimated acoustic impedance in the target area from the marine dataset using the RC-gathers after deconvolution and spatial bandpass filtering in the angle domain with the well synthetic pasted in the middle.

#### 4.5 Transformation of the RC-gather to ray parameter-scale cube

In the previous section we forced the RC-gather into one scale. By repeating this process for a number of scales, we can build up a RC-cube, as function of time  $t$ , ray parameter  $p$  and scale  $\sigma$  as shown in figure 4.15A. Normally only the plane with the

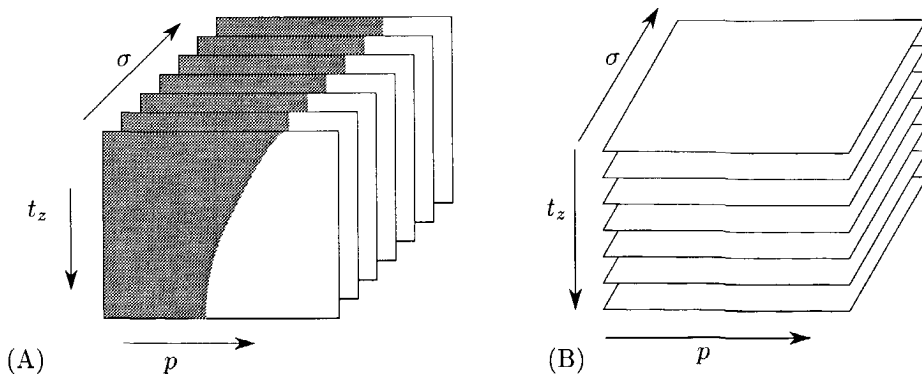


**Fig. 4.15** (A) The RC-gather for a range of scales, showing the reflectivity as function of  $p$  and time. (B) The cross sections for a constant time of the cube in (A), showing the reflectivity as function of  $p$  and  $\sigma$ .

highest resolution in figure 4.15A is used for structural imaging or inversion. The data in this cube can also be ordered in another way. By looking at cross planes through this cube, the reflectivity at a certain time/event, is imaged as function of scale and ray parameter. Figure 4.16 shows a part of the RC-cube for the marine dataset in the target area. Figure 4.17 shows a cube together with the structural image of the target area from the marine dataset.

The scale analysis of the RC gather gives a new domain for characterization of the subsurface. Elaboration on this topic is beyond the scope of this thesis and the reader is referred to Wapenaar et al. (1997) and Verhelst and van Wijngaarden (1997a) for further discussions.

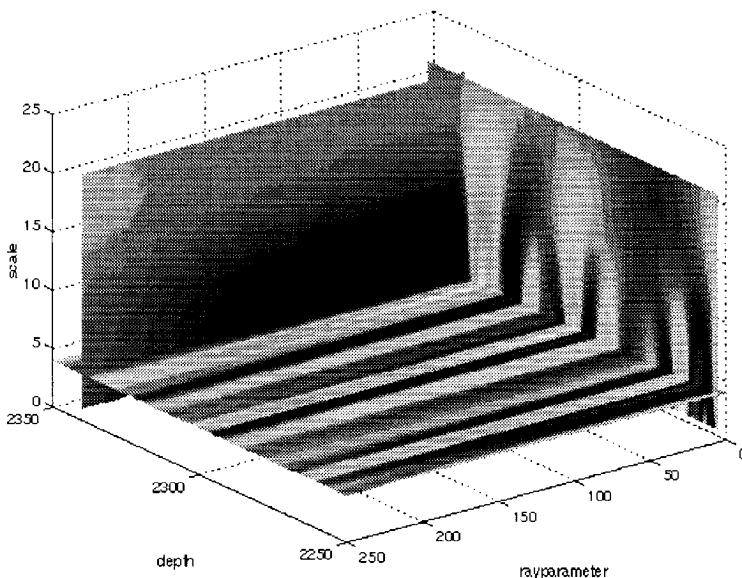


**Fig. 4.16** Three slides through a RC-cube in the target area from the marine dataset.

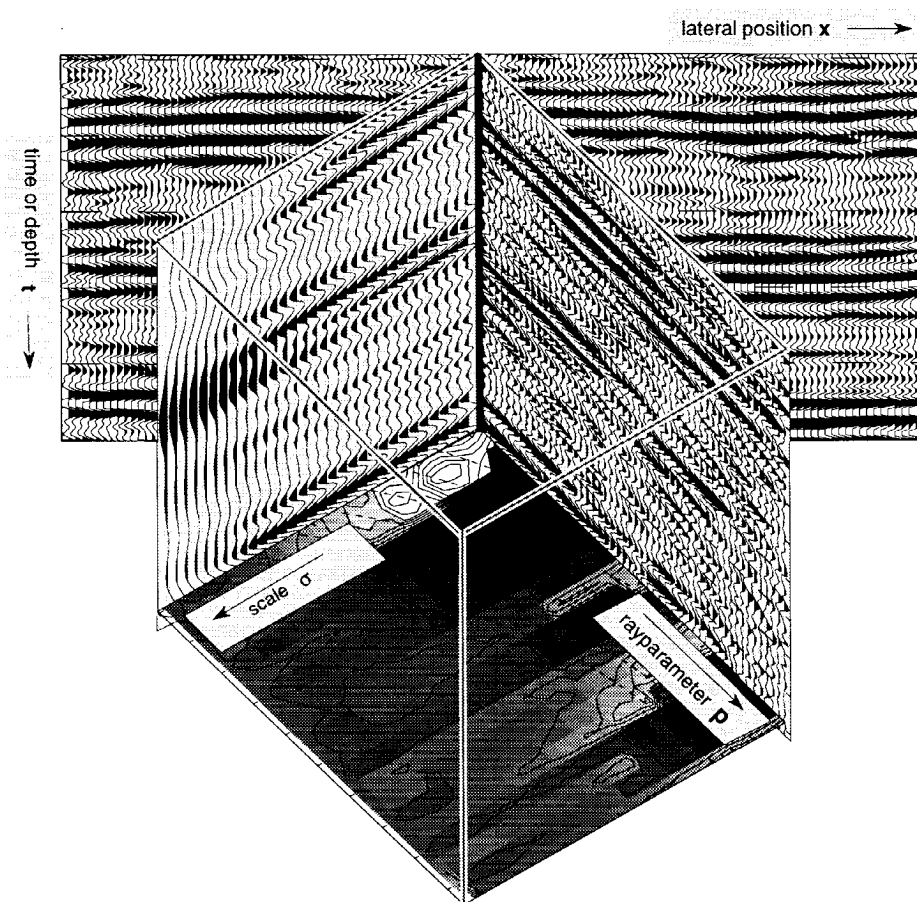


**Fig. 4.17** The RC-cube at one lateral position, together with the structural image (averaged angle-dependent reflectivity) in the background.

---

# Chapter 5

## Linear constrained elastic inversion

In this chapter the estimation of contrasts in elastic parameters from RC-functions is described. First the least squares inversion of imaged RC gathers of PP data is treated. Next the influence of a priori information is discussed and the influence of a velocity model. Finally the inversion of P-to-S reflection data and S-to-S reflection data will be discussed.

### 5.1 Introduction

In chapter 2 the imaging of the reflectivity has been discussed. The imaged reflectivity is given by the RC gather. An amplitude cross section of a RC gather belonging to a lateral position  $x_i$  at a certain time  $t_z$ , gives the *local* RC-function at  $(x_i, t_z)$  in the subsurface (here the depth is given through the time  $t_z$ ). This AVP (Amplitude-Versus- $p$ ) data is used in the inversion process as the input data vector  $\tilde{\vec{d}}$

$$\tilde{\vec{d}}(p_1, \dots, p_n) = \tilde{\vec{r}}(p_1, \dots, p_n; t_z). \quad (5.1)$$

Note that the data vector  $\tilde{\vec{d}}$  can represent P-P, S-P, P-S or S-S reflection data. In the inversion process a linearized model, indicated by the matrix  $\tilde{\mathbf{A}}$ , is used to describe the relationship between the local reflectivity data  $\tilde{\vec{d}}$  and the local elastic contrast parameters. These elastic contrast parameters are indicated by the vector  $\tilde{\vec{\lambda}}$ . A general local forward model is given by

$$\tilde{\vec{d}} = \tilde{\mathbf{A}} \tilde{\vec{\lambda}} + \tilde{\vec{n}}. \quad (5.2)$$

The vector  $\tilde{\vec{n}}$  describes (for a range of  $p$ -values) the noise and all other nonlinear events in the data which are not incorporated in the forward model  $\tilde{\mathbf{A}}$ .

The inversion process is summarized in figure 5.1. The input data is given by the RC gathers. Each RC gather (one lateral position) is treated separately. Within a RC gather the local inversion is carried out for all times, by selecting the corresponding

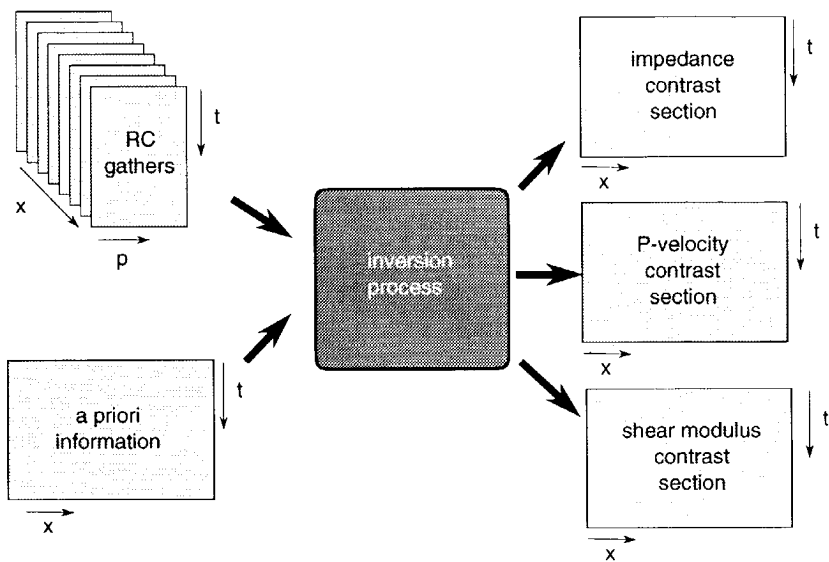


Fig. 5.1 Overview of the inversion process (for PP reflection data).

AVP curve  $\tilde{d}$  for each time and inverting the AVP curve for the elastic contrast parameters (as shown in figure 5.1 for the PP data). By repeating the inversion process for all AVP curves corresponding to one RC gather, for each contrast parameter a time trace is built. By repeating the process for all RC gathers (all lateral positions), the contrast traces build up contrast sections for each contrast parameter.

## 5.2 Weighted least-squares inversion

### 5.2.1 Seismic data

The relation between the measured AVP data and the estimated contrast parameter vector  $\tilde{\lambda}$  is given again in the following matrix notation

$$\tilde{d} = \tilde{\mathbf{A}} \tilde{\lambda} + \tilde{n}. \quad (5.3)$$

For PP reflection the data vector<sup>1</sup> is given by

$$\tilde{d} = (\tilde{r}_{PP}(p_1), \dots, \tilde{r}_{PP}(p_n))^t. \quad (5.4)$$

<sup>1</sup>the transposed of a vector or matrix is denoted by  $t$

Using the linearized model (equation 3.5)

$$\tilde{r}_{PP}(p) = \frac{1}{2} \frac{\Delta Z}{\bar{Z}} + \frac{1}{2} \left( \frac{\bar{c}_P^2 p^2}{1 - \bar{c}_P^2 p^2} \right) \frac{\Delta c_P}{\bar{c}_P} - 2 \left( \frac{\bar{c}_S}{\bar{c}_P} \right)^2 \bar{c}_P^2 p^2 \frac{\Delta \mu}{\bar{\mu}} \quad (5.5)$$

the contrast parameter vector is given by

$$\tilde{\lambda} = \left( \frac{\Delta Z}{\bar{Z}}, \frac{\Delta c_P}{\bar{c}_P}, \frac{\Delta \mu}{\bar{\mu}} \right)^t. \quad (5.6)$$

The general forward model for the seismic data becomes

$$\tilde{d} = \begin{pmatrix} 1/2 & \frac{1}{2} \left( \frac{\bar{c}_P^2 p_1^2}{1 - \bar{c}_P^2 p_1^2} \right) & -2 \frac{\bar{c}_S^2}{\bar{c}_P^2} \bar{c}_P^2 p_1^2 \\ \vdots & \vdots & \vdots \\ 1/2 & \frac{1}{2} \left( \frac{\bar{c}_P^2 p_n^2}{1 - \bar{c}_P^2 p_n^2} \right) & -2 \frac{\bar{c}_S^2}{\bar{c}_P^2} \bar{c}_P^2 p_n^2 \end{pmatrix} \begin{pmatrix} \Delta Z / \bar{Z} \\ \Delta c_P / \bar{c}_P \\ \Delta \mu / \bar{\mu} \end{pmatrix} + \tilde{n} \quad (5.7)$$

with the nonlinear events in the data given by

$$\tilde{n} = (n(p_1), \dots, n(p_n))^t. \quad (5.8)$$

The least-squares inversion process estimates those elastic contrasts  $\tilde{\lambda}$ , which minimize the squared difference between the measured data  $\tilde{d}$  and the forward modeled data  $\tilde{\mathbf{A}}\tilde{\lambda}$ . In other words, the expression  $\|\tilde{d} - \tilde{\mathbf{A}}\tilde{\lambda}\|^2$  as function of  $\tilde{\lambda}$  is minimized.

### 5.2.2 A priori data

Often not only seismic data is available, but also other types of information. This information will be called a priori information and can also be used in the estimation of the elastic contrasts. In this chapter two types of information are used:

1. linear relations between the contrast parameters
2. absolute values of the contrast parameters themselves.

The a priori data can be written in the same formulation as the seismic data (equation 5.3). Linear relations between the contrast parameters of the form

$$\lambda_j + \gamma_i \lambda_i = 0, \quad (i, j \in \{1, 2, 3\}, i \neq j) \quad (5.9)$$

or a priori values for the contrast parameters

$$\lambda_i = c_i, \quad (i \in \{1, 2, 3\}) \quad (5.10)$$

can be written in one and the same matrix equation

$$\tilde{d}_{ap} = \tilde{\mathbf{A}}_{ap} \tilde{\lambda} + \tilde{n}_{ap}, \quad (5.11)$$

with

$$\tilde{\mathbf{A}}_{ap} = \begin{pmatrix} 1 & \gamma_2 & 0 \\ 0 & 1 & \gamma_3 \\ \gamma_1 & 0 & 1 \end{pmatrix} \quad (5.12)$$

and

$$\tilde{\vec{d}}_{ap} = \begin{pmatrix} c_1 \\ c_2 \\ c_3 \end{pmatrix}. \quad (5.13)$$

For linear relations between the contrast parameters (equation 5.9) the constants  $c_1, c_2$  and  $c_3$  in  $\tilde{\vec{d}}_{ap}$  are taken zero. In case absolute values of the contrast parameters are known (equation 5.10), these are given by the values  $c_1, c_2$  and  $c_3$  in  $\tilde{\vec{d}}_{ap}$  and the parameters  $\gamma_i$  are zero. The deviation from the a priori data is given by

$$\tilde{\vec{n}}_{ap} = (n_{ap,1}, n_{ap,2}, n_{ap,3})^t. \quad (5.14)$$

In the inversion process the a priori data is treated in the same way as the seismic data, i.e. by minimization of  $\|\tilde{\vec{d}}_{ap} - \tilde{\mathbf{A}}_{ap}\tilde{\vec{\lambda}}\|^2$  as function of  $\tilde{\vec{\lambda}}$ . Of course the a priori information will always be used together with the seismic data, as described in the next section.

### 5.2.3 Combination of seismic and a priori data

The combined inversion result  $\hat{\vec{\lambda}}$  of seismic and a priori data is given by the minimization of weighted least squares

$$\left[ \left[ \tilde{\vec{d}} - \tilde{\mathbf{A}}\tilde{\vec{\lambda}} \right]^t \tilde{\mathbf{C}}^{-1} \left[ \tilde{\vec{d}} - \tilde{\mathbf{A}}\tilde{\vec{\lambda}} \right] + \left[ \tilde{\vec{d}}_{ap} - \tilde{\mathbf{A}}_{ap}\tilde{\vec{\lambda}} \right]^t \tilde{\mathbf{C}}_{ap}^{-1} \left[ \tilde{\vec{d}}_{ap} - \tilde{\mathbf{A}}_{ap}\tilde{\vec{\lambda}} \right] \right]. \quad (5.15)$$

Both seismic and a priori data are used simultaneously and the (diagonal) matrices  $\tilde{\mathbf{C}}$  and  $\tilde{\mathbf{C}}_{ap}$  give weighting terms to the mismatch of the estimated data with the seismic data and the mismatch with the a priori data. In most cases the diagonal of the matrix  $\tilde{\mathbf{C}}$  is chosen constant. The diagonal elements of the matrix  $\tilde{\mathbf{C}}_{ap}$  give the weight to the a priori relations. The ratio of the determinants  $\|\tilde{\mathbf{C}}\| / \|\tilde{\mathbf{C}}_{ap}\|$  shows the relative influence of the seismic data on the inversion compared to the a priori information. In the next chapter the influence will be discussed in more detail. Normally most emphasis is put on the seismic data and the a priori information is only used to stabilize the inversion process. In this case the determinant of the matrix  $\tilde{\mathbf{C}}$  must be much larger than the determinant of the matrix  $\tilde{\mathbf{C}}_{ap}$ .

### 5.2.4 Maximum likelihood estimation

The weighted least squares estimation of the seismic contrast parameters is given by equation 5.15. If the weighting matrices  $\tilde{\mathbf{C}}$  and  $\tilde{\mathbf{C}}_{ap}$  correspond to the covariance matrices of the seismic data and a priori data, the weighted least-squares solution equals the *maximum likelihood* estimate. For the discussed linear forward model the solution can also be written as a generalized inverse

$$\hat{\lambda} = \left[ \tilde{\mathbf{A}}^t \tilde{\mathbf{C}}^{-1} \tilde{\mathbf{A}} + \tilde{\mathbf{A}}_{ap}^t \tilde{\mathbf{C}}_{ap}^{-1} \tilde{\mathbf{A}}_{ap} \right]^{-1} \left[ \tilde{\mathbf{A}}^t \tilde{\mathbf{C}}^{-1} \tilde{d} + \tilde{\mathbf{A}}_{ap}^t \tilde{\mathbf{C}}_{ap}^{-1} \tilde{d}_{ap} \right]. \quad (5.16)$$

The seismic and a priori model and data can also be combined in one model matrix  $\tilde{\mathbf{A}}_{tot}$  and one data vector  $\tilde{d}_{tot}$ , with one covariance matrix  $\tilde{\mathbf{C}}_{tot}$ , using

$$\begin{aligned} \hat{\lambda} &= \left[ \left( \tilde{\mathbf{A}}^t \tilde{\mathbf{A}}_{ap}^t \right) \begin{pmatrix} \tilde{\mathbf{C}}^{-1} & 0 \\ 0 & \tilde{\mathbf{C}}_{ap}^{-1} \end{pmatrix} \begin{pmatrix} \tilde{\mathbf{A}} \\ \tilde{\mathbf{A}}_{ap}^t \end{pmatrix} \right]^{-1} \left[ \left( \tilde{\mathbf{A}}^t \tilde{\mathbf{A}}_{ap}^t \right) \begin{pmatrix} \tilde{\mathbf{C}}^{-1} & 0 \\ 0 & \tilde{\mathbf{C}}_{ap}^{-1} \end{pmatrix} \begin{pmatrix} \tilde{d} \\ \tilde{d}_{ap} \end{pmatrix} \right] \\ &= \left[ \tilde{\mathbf{A}}_{tot}^t \tilde{\mathbf{C}}_{tot}^{-1} \tilde{\mathbf{A}}_{tot} \right]^{-1} \left[ \tilde{\mathbf{A}}_{tot}^t \tilde{\mathbf{C}}_{tot}^{-1} \tilde{d}_{tot} \right]. \end{aligned} \quad (5.17)$$

If the covariance matrices of the seismic and a priori data are diagonal matrices with the squared standard deviations on the diagonal, then equation 5.17 can easily be rewritten as

$$\hat{\lambda} = \left[ \tilde{\mathbf{A}}_w^t \tilde{\mathbf{A}}_w \right]^{-1} \left[ \tilde{\mathbf{A}}_w^t \tilde{d}_w \right], \quad (5.18)$$

with  $\tilde{\mathbf{A}}_w$  denoting the total forward model matrix  $\tilde{\mathbf{A}}_{tot}$  divided by the standard deviations and with  $\tilde{d}_w$  denoting the total data vector  $\tilde{d}_{tot}$ , also divided by the standard deviations.

### 5.2.5 Singular value decomposition

The minimization of equation 5.15 can be done by a generalized inversion using the singular value decomposition (SVD) (Menke, 1984). The  $n \times m$  matrix  $\tilde{\mathbf{A}}_w$  ( $m=3$  using equation 5.5) is decomposed in a  $n \times n$  matrix  $\tilde{\mathbf{U}}$  of vectors that span the data space and a  $m \times m$  matrix of vectors  $\tilde{\mathbf{V}}$  that span the model parameters space and a  $n \times m$  diagonal singular value matrix  $\tilde{\mathbf{S}}$  whose diagonal elements are nonnegative and are called singular values. The vectors in  $\tilde{\mathbf{U}}$  are orthogonal to one another and can be chosen to be of unit length, so that  $\tilde{\mathbf{U}}^t \tilde{\mathbf{U}}$  equals the identity matrix  $\mathbf{I}$  ( $n \times n$ ). Also the vectors in the matrix  $\tilde{\mathbf{V}}$  are orthonormal, such that  $\tilde{\mathbf{V}}^t \tilde{\mathbf{V}}$  equals the identity matrix  $\mathbf{I}$  ( $m \times m$ ). This yields that the forward model (equation 5.2) can be written as

$$\tilde{\mathbf{A}}_w = \tilde{\mathbf{U}} \tilde{\mathbf{S}} \tilde{\mathbf{V}}^t. \quad (5.19)$$

The generalized inversion is now given by

$$\hat{\lambda} = (\tilde{\mathbf{V}} \tilde{\mathbf{S}}^t \tilde{\mathbf{S}} \tilde{\mathbf{V}}^t)^{-1} (\tilde{\mathbf{V}} \tilde{\mathbf{S}}^t \tilde{\mathbf{U}}^t) \tilde{d} = \tilde{\mathbf{V}} [\tilde{\mathbf{S}}^t \tilde{\mathbf{S}}]^{-1} \tilde{\mathbf{S}}^t \tilde{\mathbf{U}}^t \tilde{d}_w. \quad (5.20)$$

The matrix product  $[\tilde{\mathbf{S}}^t \tilde{\mathbf{S}}]^{-1} \tilde{\mathbf{S}}^t$  is easily computed as the inverse matrix of the upper  $m \times m$  part of the matrix  $\tilde{\mathbf{S}}$  (and padded with zeros to a  $n \times m$  matrix), because  $\tilde{\mathbf{S}}$  is a diagonal matrix. Only if the diagonal elements (singular values) of this matrix are too small, the inversion becomes instable. This can be prevented by using a priori information, as described in section 5.2.2.

### 5.3 Numerical and field data example

For a numerical example a single interface between two thick layers is considered. The model parameters and the imaged RC gather for the PP reflection are shown in figure 5.2.

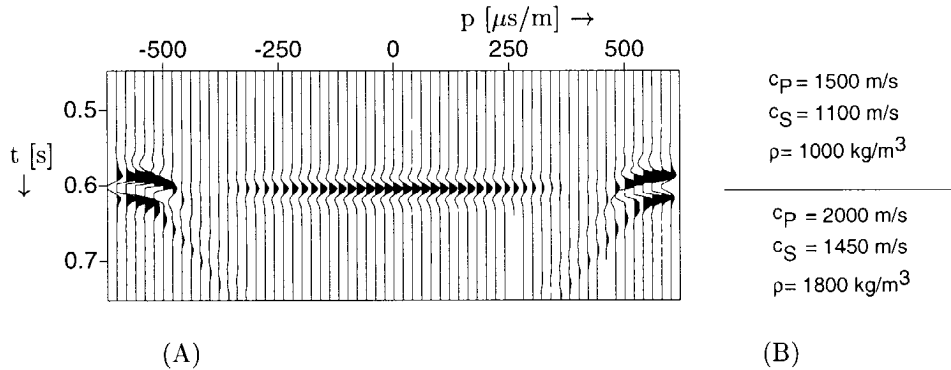


**Fig. 5.2** (A) The imaged RC gather for PP reflection and (B) the model parameters.

For the local inversion of the RC gather an amplitude cross section of the RC gather at  $t=0.60\text{s}$  is used. This AVP curve is shown in figure 5.3 in light gray, together with the estimated RC-function ( $\tilde{\mathbf{A}}\tilde{\lambda}$ ). The imaged AVP curve is almost equal to the theoretical AVP curve. The difference between these two AVP curves is less than 0.005 for angles smaller than the critical angle. This corresponds with the accuracy of the input data in the inversion, which is given by a standard deviation of 0.005. The linearized RC-functions are derived for small contrasts and small angles. For this reason, only the data for angles smaller than 40 degrees are used (i.e.  $|p| < 400\mu\text{s/m}$ ), as shown in figure 5.3.

The estimated contrasts are given in table 5.1 together with the theoretical exact values. In this example no a priori information was used. For the background velocity a constant velocity model with the velocity of the upper layer was used.

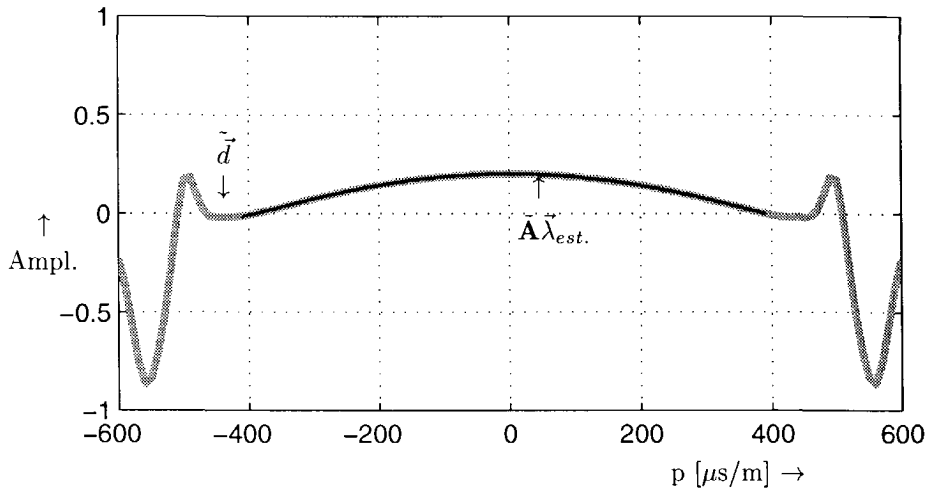


**Fig. 5.3** The estimated AVP curve in the inversion process ( $\tilde{\mathbf{A}}\lambda_{est.}$ ) in black and the imaged AVP curve in light gray.

The estimated contrasts are in perfect agreement with the exact values within the accuracy given by the estimated standard deviation for the contrast parameters.

	estimated	sd	exact
$\Delta c_P / \bar{c}_P$	0.402	0.002	0.400
$\Delta c_S / \bar{c}_S$	0.196	0.039	0.222
$\Delta \rho / \bar{\rho}$	0.714	0.033	0.704

**Table 5.1** Estimated and exact elastic contrast parameters in the synthetic example together with the estimated standard deviation. The accuracy of the input data is given by its standard deviation  $sd_{data}=0.005$ .

For the field data example the marine dataset from chapter 2 is used. Figure 5.4 shows an RC gather with the three estimated contrast traces (for display purpose these traces are repeated five times). An exponential gain function ( $e^t$ ) has been applied to the data in the RC gather for display. The acoustic impedance matches clearly the RC gather for small  $p$ -values. The high amplitudes in the shallow part of the estimated shear modulus contrast may be due to the rather small  $p$ -range which was used and multiple energy at 0.7s.

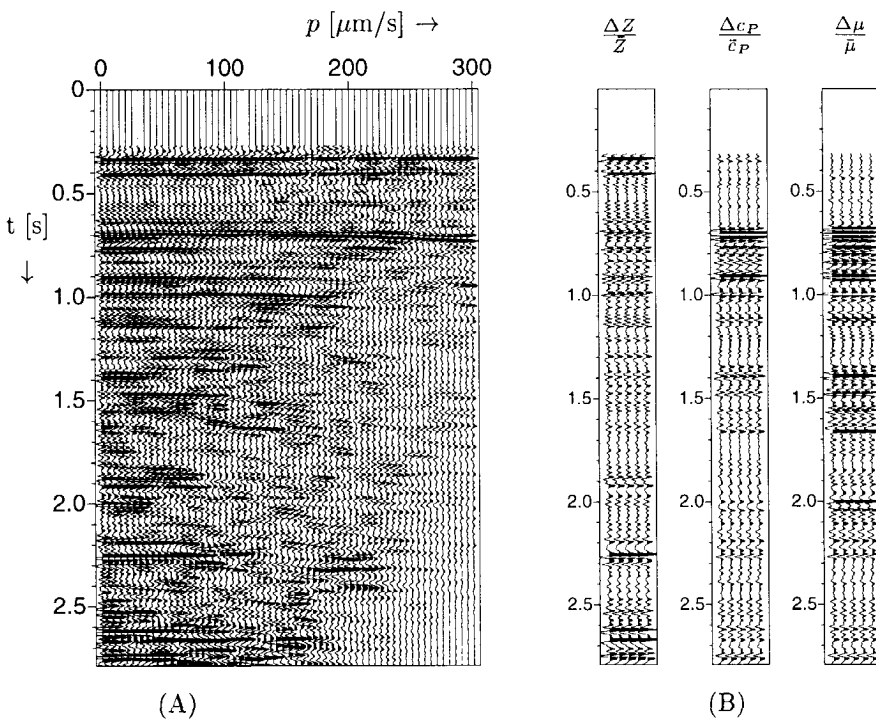


**Fig. 5.4** (A) The imaged RC gather and (B) the estimated contrasts traces. The data in the RC gather up to a maximum angle of 30 degrees has been used.

#### 5.4 Influence of background velocity

In the inversion the linearized Zoeppritz equation is used to relate the imaged AVP curve with the estimated contrasts. The RC-function in equation 5.5 is a function of ray parameter  $p$ . The background velocity  $\bar{c}_P$  is assumed to be known. In the equation  $p$  is always present as a product of  $p \times \bar{c}_P$ . This means that the RC-function is in fact a function of angle ( $\sin \bar{\alpha} = p \times \bar{c}_P$ ) in stead of  $p$ . This corresponds to a depth model, where the dip is given in angle, opposite to the model in time, where the dip is given in  $p$ . So the background velocity  $\bar{c}_P$  is used to transform a  $p$ -axis to an angle axis and the values of the angles are directly depending on the values of the velocity (just like the offset to angle conversion by ray tracing is directly depending on the velocity model).

The velocity used should be an averaged velocity over the interface, as shown in Aki and Richards (1980). This means that the angle  $\bar{\alpha} = \arcsin(\bar{c}_P \times p)$  is the averaged angle of a ray through an interface. Note that the difference between incident and transmitted angle can only be made for clearly separate interfaces. In a medium in which layer thicknesses are much smaller than the seismic wavelength, the individual

incident/transmitted angles at the interfaces can not be used, only the averaged angle over a certain depth range (in the order of the seismic wavelength) is meaning full.

	upper layer	lower half space
$c_P$ [m/s]	1750	1850 or 1650
$c_S$ [m/s]	1200	1300 or 1100
$\rho$ [kg/m <sup>3</sup> ]	1500	1600 or 1400

**Table 5.2** The elastic parameters corresponding to 8 different subsurface models for the examples in figure 5.5 - 5.12. The parameters in the upper layer are constant in all models. The parameters in the lower half space either increase or decrease with respect to those in the upper half space.

#### 5.4.1 Numerical examples

The influence of the background velocity will be discussed using eight different single interface models. The elastic parameters in the upper layer are the same in all models, but the elastic parameters in the lower half space vary. The elastic parameters are given in table 5.2 and all possible combinations of the lower half space parameters result in eight different models. In the following eight examples (figures 5.5 to 5.12) the used elastic parameters are shown in the top left figure. The contrast parameters are estimated using the background velocities  $\bar{c}_P$  between 1400 m/s and 2500 m/s. The estimated contrasts are shown as function of  $\bar{c}_P$  in figure 5.5 - 5.12. The ratio  $\bar{c}_P/\bar{c}_S$  is computed using the over the interface averaged velocities and is not altered. The analytical values for the contrasts are indicated by a dashed gray line. The asterix denotes the averaged background velocity.

The estimated impedance contrast does not depend in the inversion process on the background velocity  $\bar{c}_P$ . This is expected, since the impedance contrast is not depending on  $\bar{c}_P$  (angle-independent term). The estimated impedance contrasts matches in all examples the analytical impedance contrast perfectly.

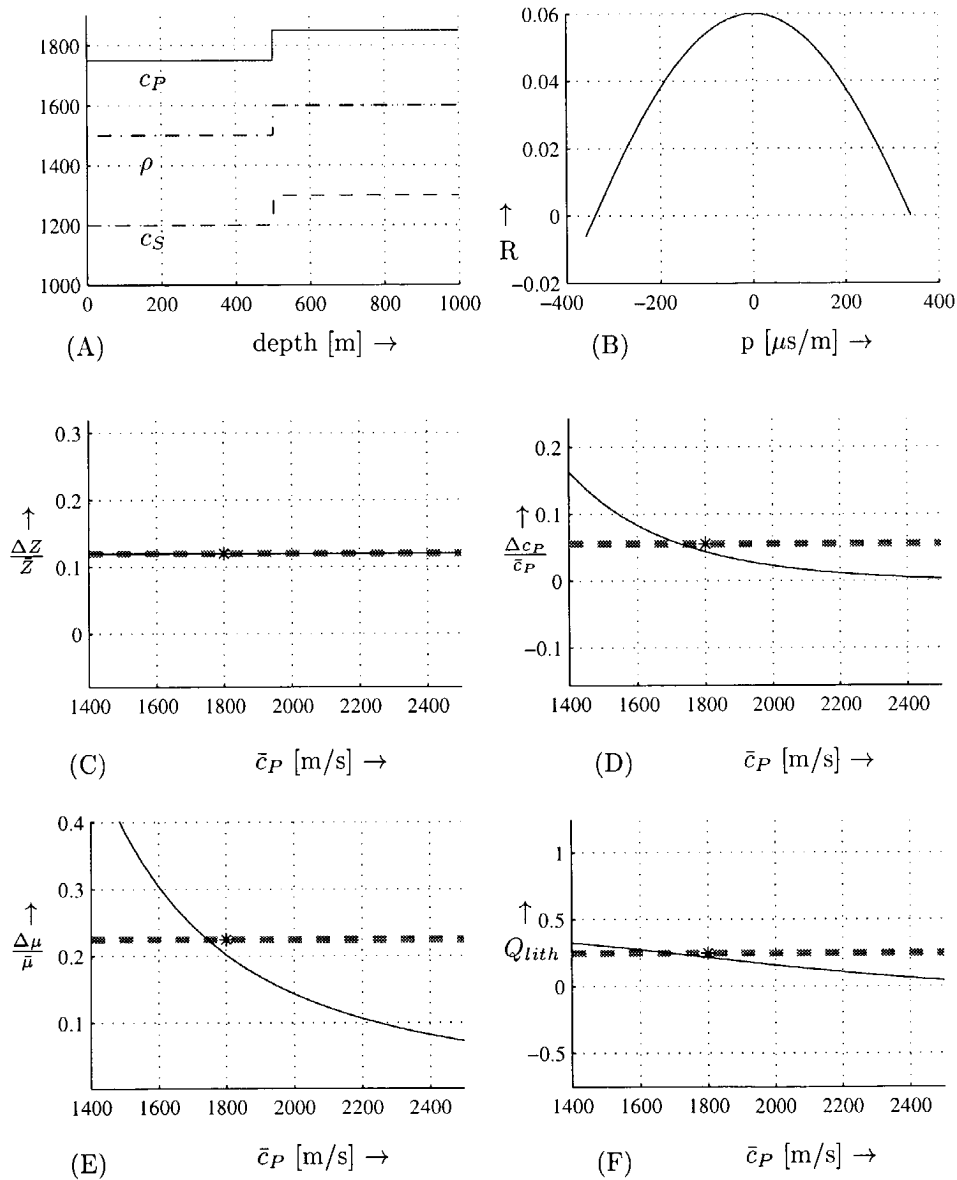


**Fig. 5.5** (A) The elastic model parameters. (B) The AVP curve obtained from the RC gather. (C)-(E) The estimated contrasts as function of background velocity  $\bar{c}_P$ . The dashed gray line indicates the analytical value of the contrasts and the asterisk denotes the averaged  $P$ -velocity over the interface. (F) The ratio  $Q_{\text{lith}} = \frac{\Delta c_P}{\bar{c}_P} / \frac{\Delta \mu}{\bar{\mu}}$  as function of background velocity  $\bar{c}_P$ .

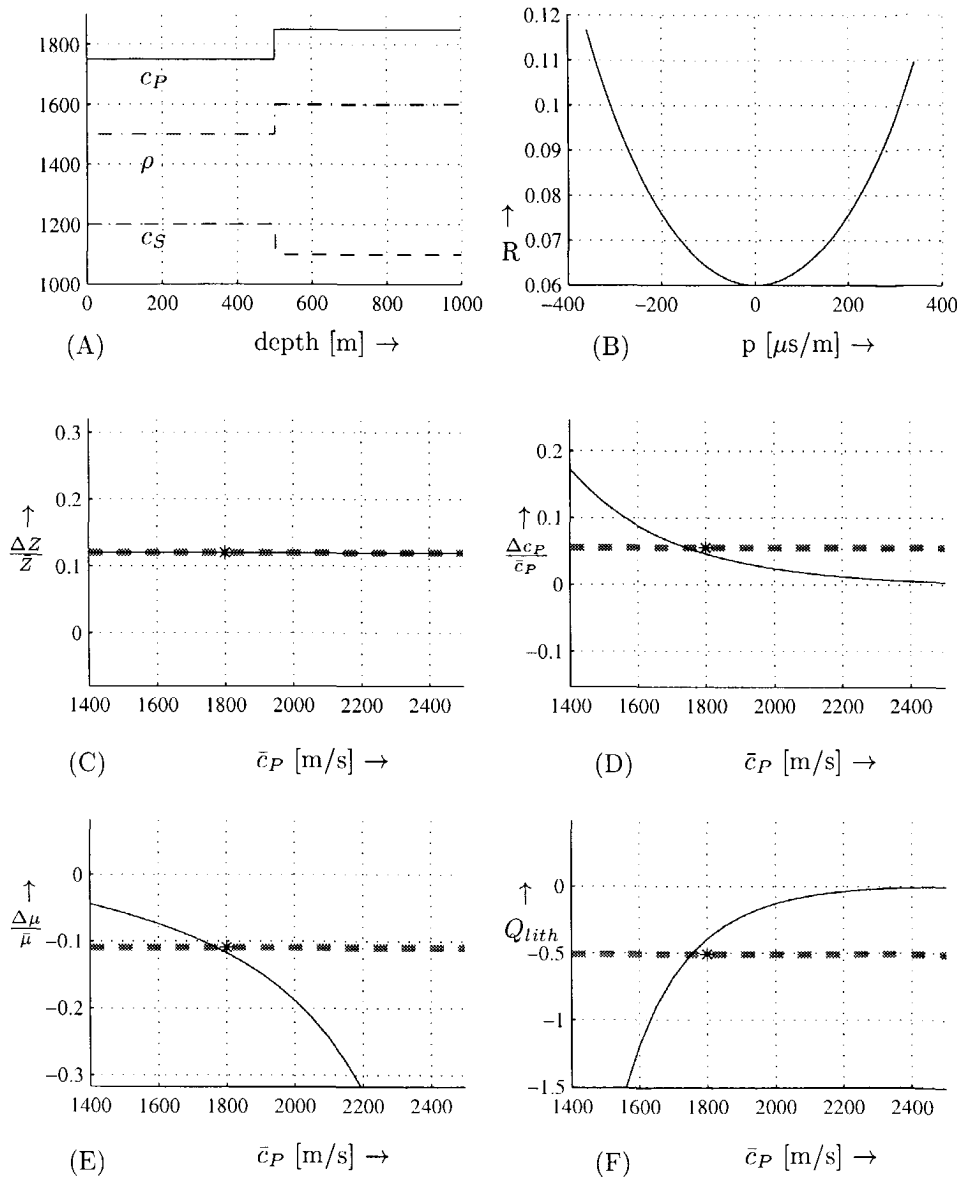
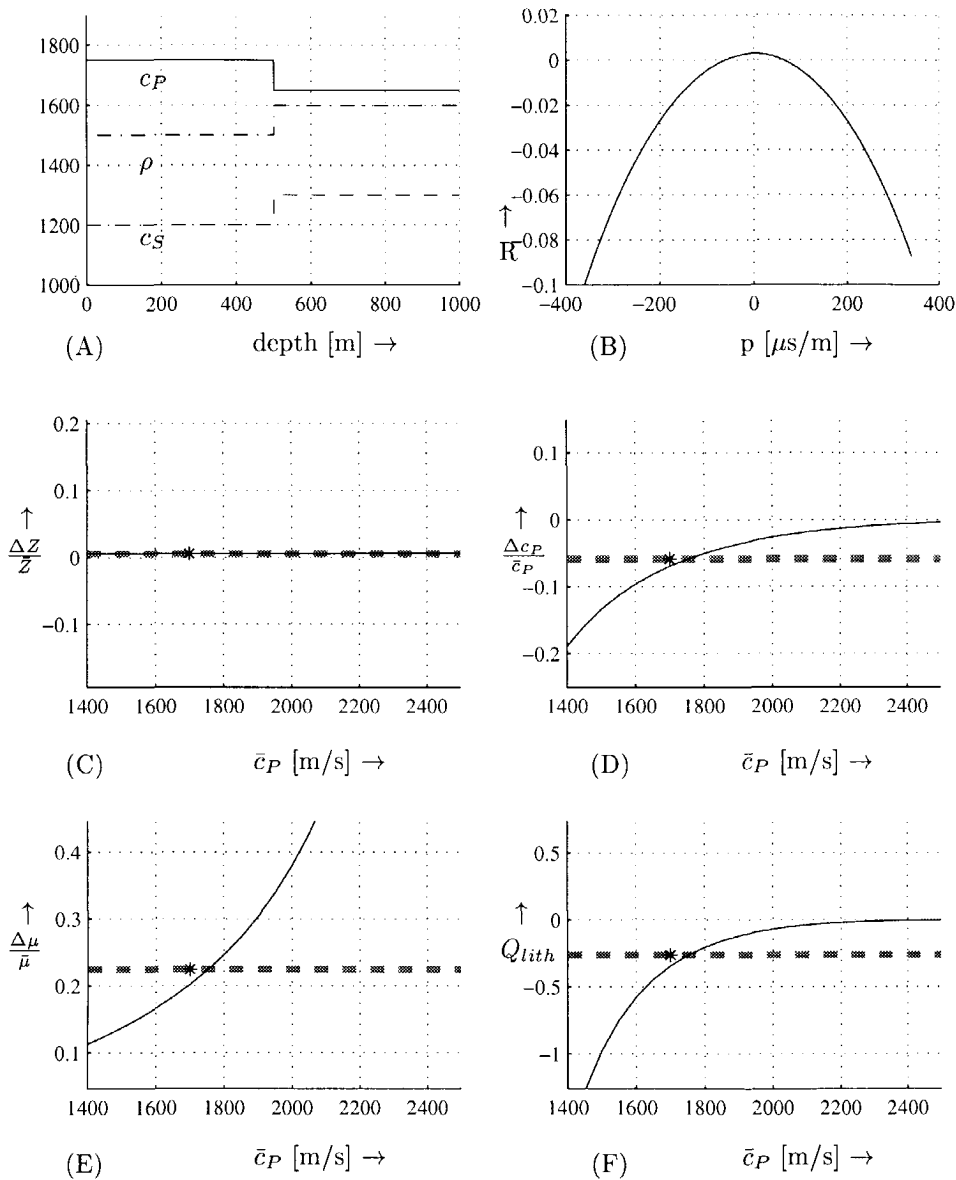
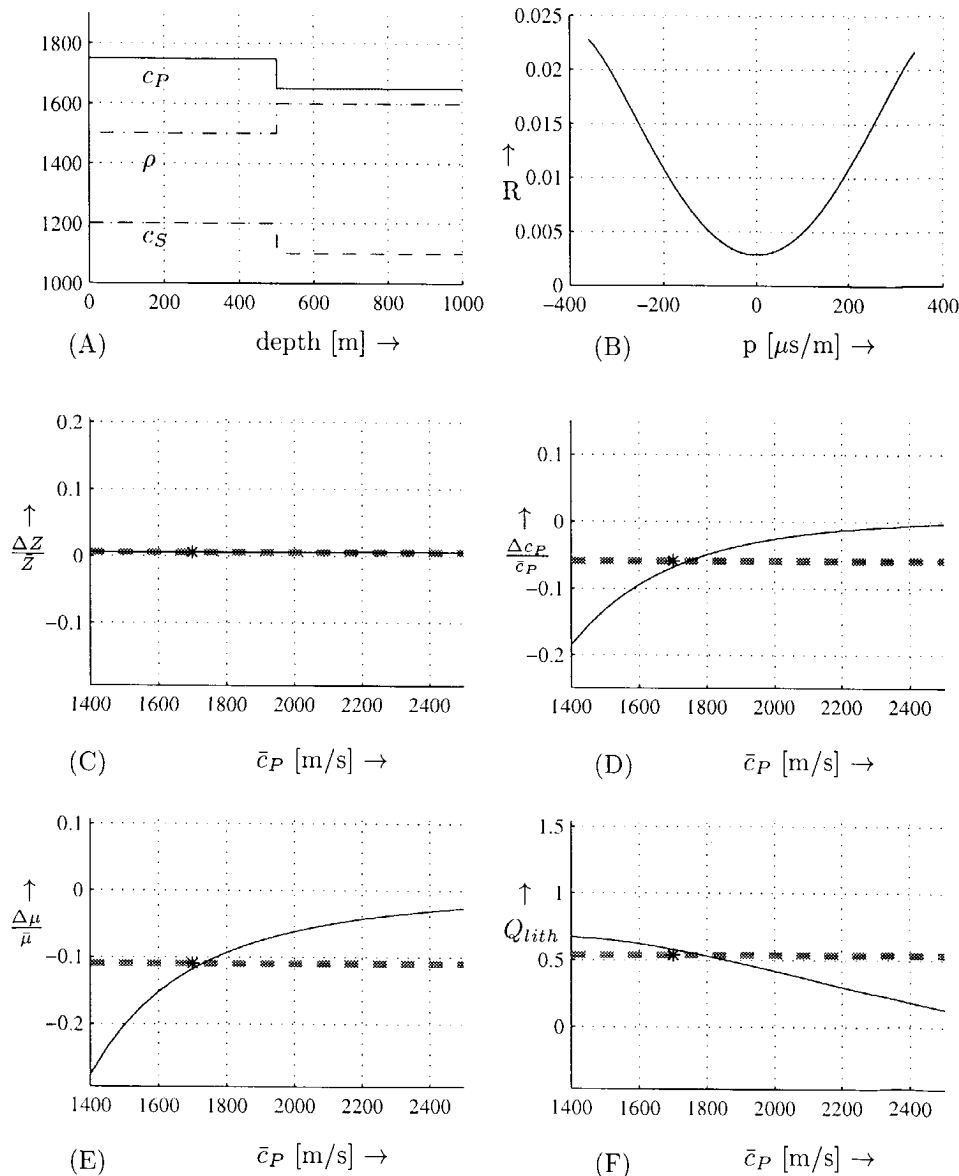


Fig. 5.6 (A) The elastic model parameters. (B) The AVP curve obtained from the RC gather. (C)-(E) The estimated contrasts as function of background velocity  $\bar{c}_P$ . The dashed gray line indicates the analytical value of the contrasts and the asterisk denotes the averaged  $P$ -velocity over the interface. (F) The ratio  $Q_{lith} = \frac{\Delta c_P}{\bar{c}_P} / \frac{\Delta \mu}{\mu}$  as function of background velocity  $\bar{c}_P$ .



**Fig. 5.7** (A) The elastic model parameters. (B) The AVP curve obtained from the RC gather. (C)-(E) The estimated contrasts as function of background velocity  $\bar{c}_P$ . The dashed gray line indicates the analytical value of the contrasts and the asterisk denotes the averaged P-velocity over the interface. (F) The ratio  $Q_{\text{lith}} = \frac{\Delta c_P}{\bar{c}_P} / \frac{\Delta \mu}{\bar{\mu}}$  as function of background velocity  $\bar{c}_P$ .



**Fig. 5.8** (A) The elastic model parameters. (B) The AVP curve obtained from the RC gather. (C)-(E) The estimated contrasts as function of background velocity  $\bar{c}_P$ . The dashed gray line indicates the analytical value of the contrasts and the asterisk denotes the averaged  $P$ -velocity over the interface. (F) The ratio  $Q_{lith} = \frac{\Delta c_P}{\bar{c}_P} / \frac{\Delta \mu}{\mu}$  as function of background velocity  $\bar{c}_P$ .

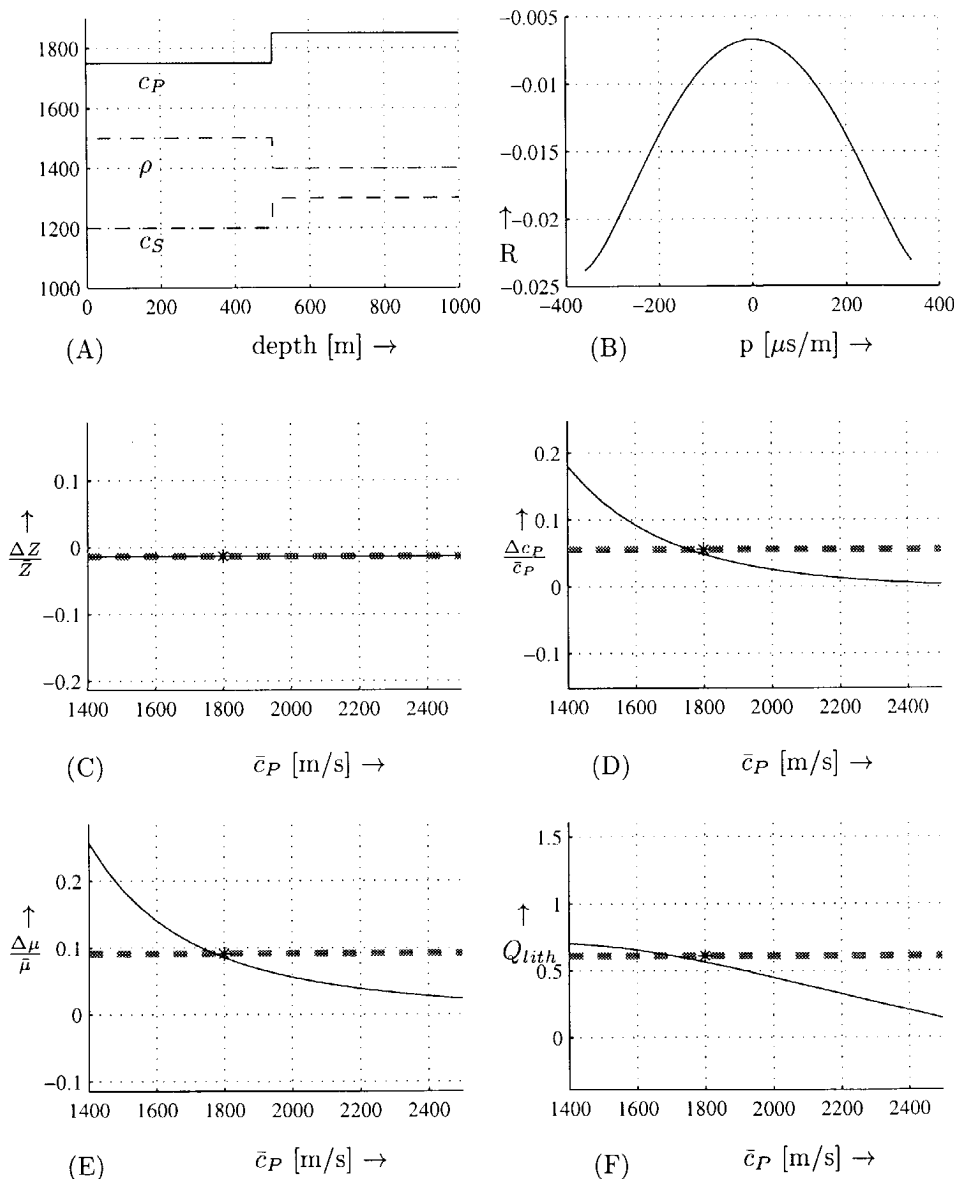


**Fig. 5.9** (A) The elastic model parameters. (B) The AVP curve obtained from the RC gather. (C)-(E) The estimated contrasts as function of background velocity  $\bar{c}_P$ . The dashed gray line indicates the analytical value of the contrasts and the asterisk denotes the averaged  $P$ -velocity over the interface. (F) The ratio  $Q_{lith} = \frac{\Delta c_P}{\bar{c}_P} / \frac{\Delta \mu}{\bar{\mu}}$  as function of background velocity  $\bar{c}_P$ .

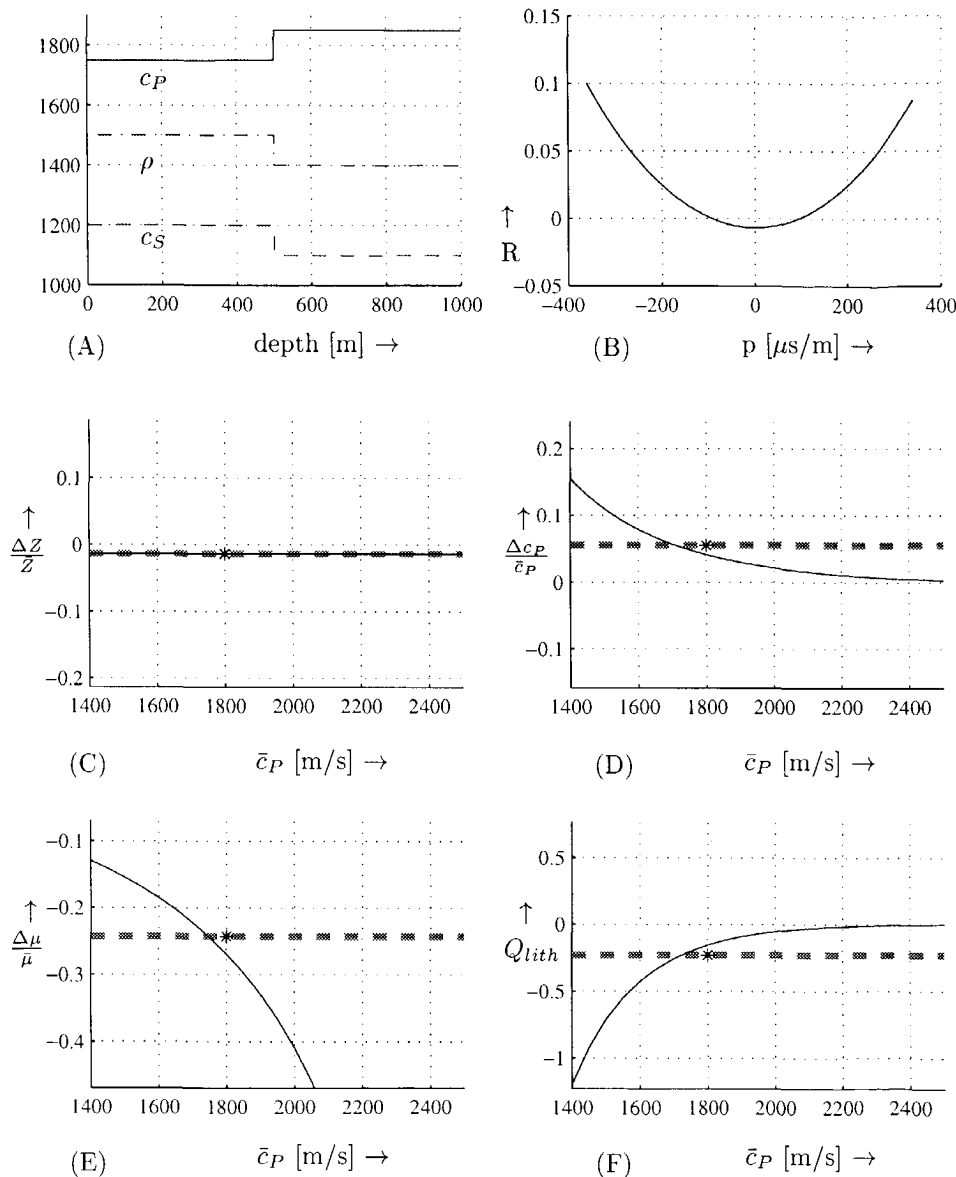


**Fig. 5.10** (A) The elastic model parameters. (B) The AVP curve obtained from the RC gather. (C)-(E) The estimated contrasts as function of background velocity  $\bar{c}_P$ . The dashed gray line indicates the analytical value of the contrasts and the asterisk denotes the averaged P-velocity over the interface. (F) The ratio  $Q_{\text{lith}} = \frac{\Delta c_P}{\bar{c}_P} / \frac{\Delta \mu}{\bar{\mu}}$  as function of background velocity  $\bar{c}_P$ .

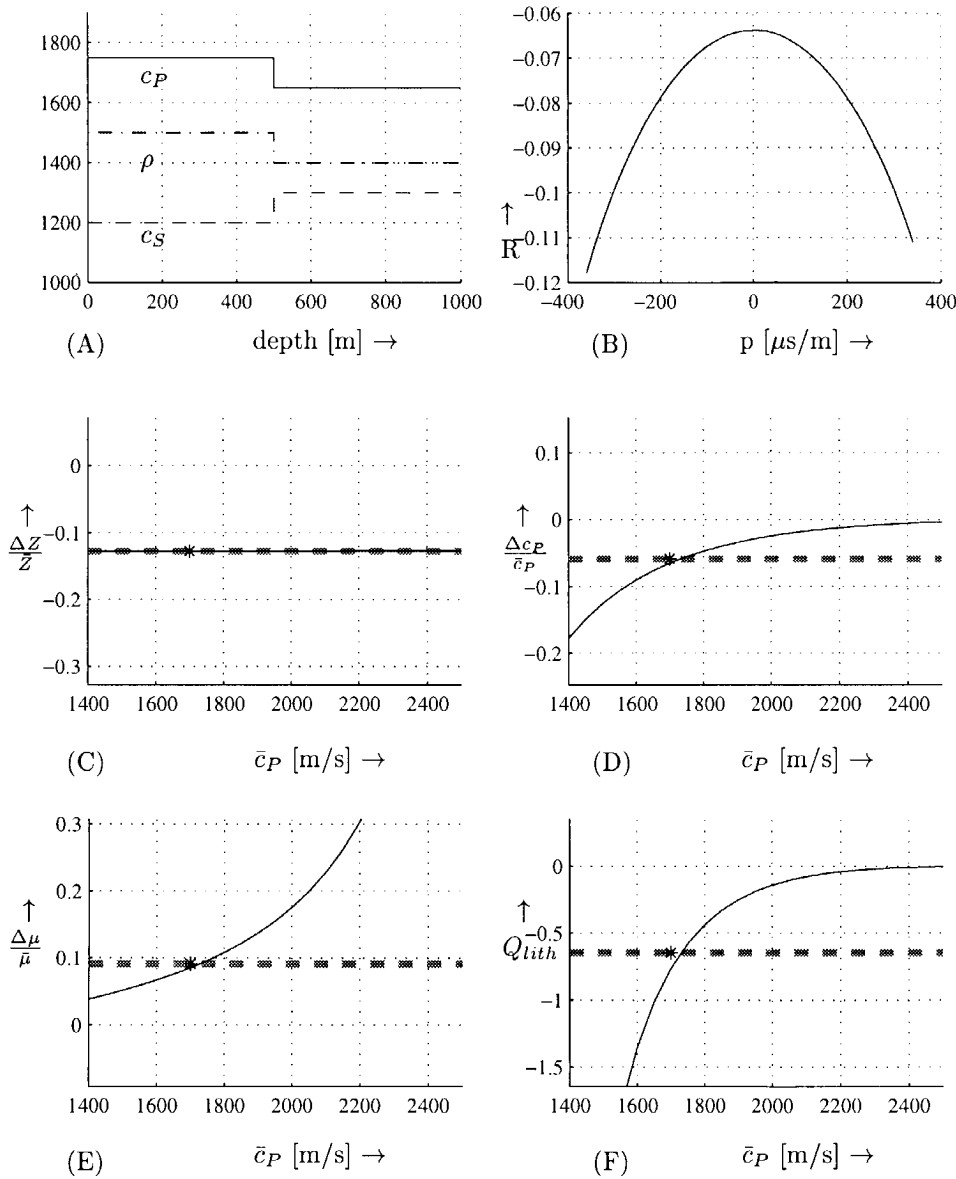


**Fig. 5.11** (A) The elastic model parameters. (B) The AVP curve obtained from the RC gather. (C)-(E) The estimated contrasts as function of background velocity  $\bar{c}_P$ . The dashed gray line indicates the analytical value of the contrasts and the asterisk denotes the averaged  $P$ -velocity over the interface. (F) The ratio  $Q_{lith} = \frac{\Delta c_P}{\bar{c}_P} / \frac{\Delta \mu}{\bar{\mu}}$  as function of background velocity  $\bar{c}_P$ .

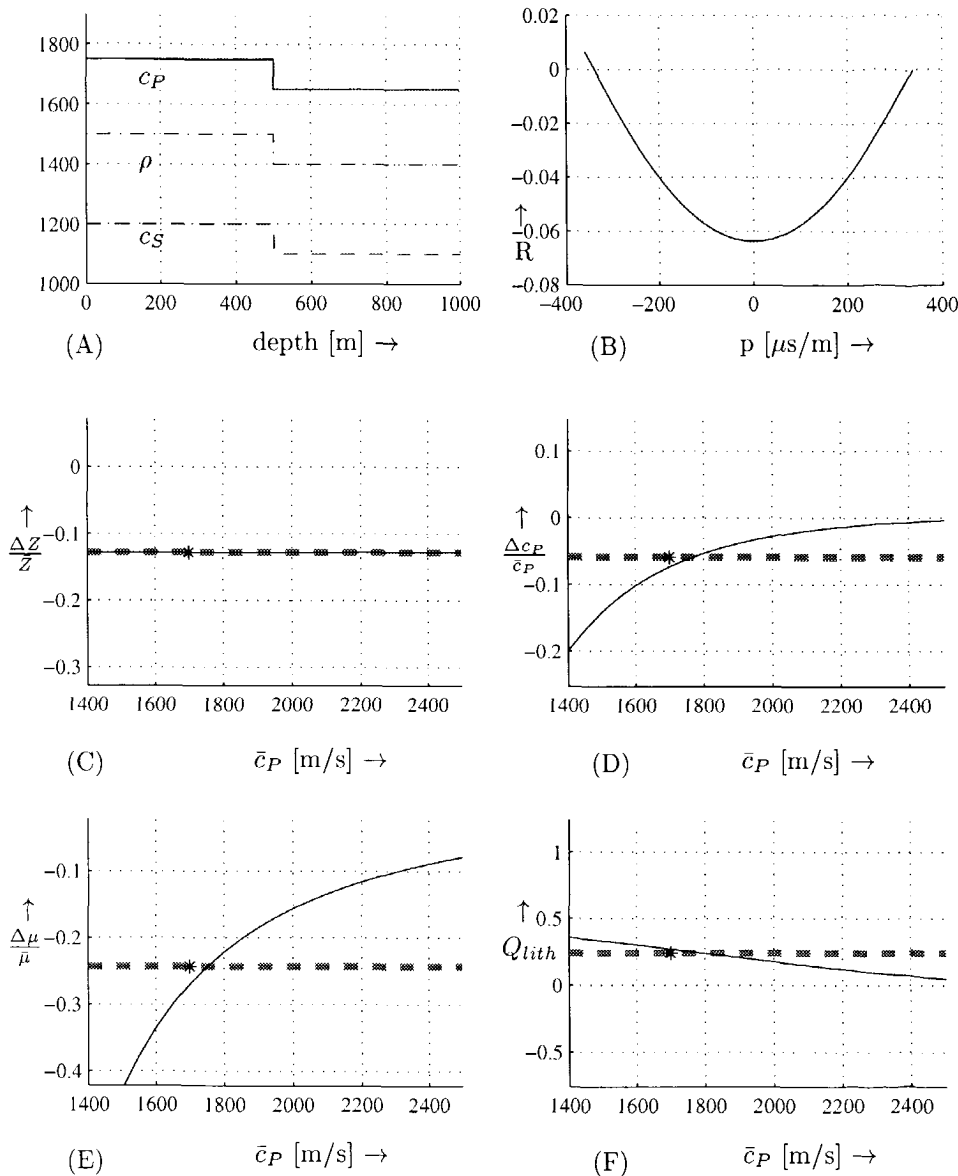


**Fig. 5.12** (A) The elastic model parameters. (B) The AVP curve obtained from the RC gather. (C)-(E) The estimated contrasts as function of background velocity  $\bar{c}_P$ . The dashed gray line indicates the analytical value of the contrasts and the asterisk denotes the averaged  $P$ -velocity over the interface. (F) The ratio  $Q_{lith} = \frac{\Delta c_P}{\bar{c}_P} / \frac{\Delta \mu}{\bar{\mu}}$  as function of background velocity  $\bar{c}_P$ .

The P-velocity and shear modulus contrasts are clearly depending on  $\bar{c}_P$ . This means that different background velocity models will give different angle-dependent contrasts. Note that in these numerical examples in all cases a background velocity which equals the P-velocity of the upper layer gives more accurate estimates of the contrasts than using the averaged P-velocity over the interface (indicated by the asterisk). This was not expected since in the derivation of the linearized Zoeppritz equation (Aki and Richards, 1980) the average velocity over the interface is used. Furthermore it is interesting to note that in all examples for high background velocities the estimated contrasts in P-velocity decrease asymptotically to zero and that *underestimating* the background velocity results in most cases in *overestimating* the p-dependent contrasts.

The influence of the background velocity is especially important for direct-hydrocarbon-indicators (DHI), which depend on the ratio of the angle-dependent contrasts (van Wijngaarden, 1995). This ratio often shows a regional trend for silici-clastic rocks, which is discussed in more detail in chapter 7. Deviations from this trend are associated with changes in lithology or fluid fill (e.g. water versus gas). For example the fluid factor (Smith and Gidlow, 1987) is related to the difference between the two angle-dependent contrast factors. Figures 5.5 - 5.12 show that an error in background velocity introduces an error in the estimated contrast parameters, which may give a deviation from a regional trend (or deviations may be masked by erroneous velocities).

For this reason the ratio of the angle-dependent contrasts

$$Q_{lith} = \frac{\Delta c_P / \bar{c}_P}{\Delta \mu / \bar{\mu}} \quad (5.21)$$

is shown as function of the background velocity. Again the analytical value is indicated by the dashed gray line. It is clear that the background velocity  $\bar{c}_P$  has a direct influence on the ratio  $Q_{lith}$ .

From these examples the dependence can be divided in two classes. The first class is characterized by a slow decrease in  $Q_{lith}$  as function of  $\bar{c}_P$ . All the examples in which both  $c_P$  and  $c_S$  either increase or decrease show this behaviour. The second class is characterized by a logarithmic-like increase in  $Q_{lith}$  as function of  $\bar{c}_P$ . The examples in which  $c_P$  increases and  $c_S$  decreases or vice versa belong to the second class. This means that the behaviour of  $Q_{lith}$  versus  $\bar{c}_P$  can be used for characterization<sup>2</sup> of the boundary.

On the other hand if the ratio  $Q_{lith}$  is known as function of depth, this ratio can be used to improve the background velocity  $\bar{c}_P$ . In this case the velocity model will have the same vertical resolution as the seismic data. This is much more detail than the macro velocity model, which consists typically of five to ten layers.

<sup>2</sup>note that this is only true if the S-wave velocity contrast is of the same order as the density contrast. Otherwise the ratio of P-wave velocity and shear modulus should be used.

## 5.5 Type of norm and two versus three parameter inversion

In most cases a Gaussian distribution is assumed for the noise in equation 5.2. For that situation the least squares or L2 norm inversion gives the maximum likelihood result. On the other hand if there are outliers present in the data, a L1 norm is more robust (Menke, 1984). This means that the choice for a L1 or L2 norm depends on the noise present in the imaged AVP curves. The amount of noise also determines together with the amount of data the limitations of the inversion process.

In case of PP data and angle ranges over 40 degrees, three contrast parameters can be estimated (see equation 3.5). But we should be careful that the assumptions made in the derivation of the linearized RC functions are not violated.

If the imaged AVP curves are limited to angles smaller than 25 degrees and the contrasts are rather small, then an approximation for the linearized RC functions in two contrast terms should be used (see equation 3.7). Due to a limited angle range in the imaged AVP curve and a small accuracy in the amplitudes only two contrast parameters can be estimated from an AVP curve: the intercept and the gradient. The intercept is defined as the reflection coefficient for normal incidence and the gradient is defined as the linear slope of the  $R_{PP}$  as function of  $\bar{c}_P^2 p^2$ . These terms can be estimated fairly accurate, since only two terms are estimated.

The parameterization for two parameters is given in table 5.3 for all modes of reflection. Note that in the case that we only have PP reflection data, we can only estimate  $\frac{\Delta Z}{Z}$  and  $\frac{1}{2} \frac{\Delta c_P}{\bar{c}_P} - 2(\frac{\bar{c}_S}{\bar{c}_P})^2 \frac{\Delta \mu}{\bar{\mu}}$ . From these two terms we can not deduce the contrasts in the P and S-wave and density quantitatively. Use of shear waves (SP and SS data) gives additional information which can be used to overcome this problem.

	angle independent term or intercept	angle dependent term or gradient	angle dependence
$R_{PP}$	$\frac{1}{2} \frac{\Delta Z}{Z}$	$\frac{1}{2} \frac{\Delta c_P}{\bar{c}_P} - 2(\frac{\bar{c}_S}{\bar{c}_P})^2 \frac{\Delta \mu}{\bar{\mu}}$	$\bar{c}_P^2 p^2$
$R_{SS}$	$\frac{1}{2} \frac{\Delta Z_S}{Z_S}$	$\frac{1}{2} (\frac{c_S}{c_P})^2 \frac{\Delta c_S}{\bar{c}_S} - 4(\frac{c_S}{c_P})^2 \frac{\Delta Z_S}{Z_S}$	$\bar{c}_P^2 p^2$
$R_{SP}$	0	$-[\frac{1}{2} \frac{\bar{c}_S}{\bar{c}_P} \frac{\Delta \rho}{\bar{\rho}} + (\frac{\bar{c}_S}{\bar{c}_P})^2 \frac{\Delta \mu}{\bar{\mu}}]$	$\bar{c}_P p$
$R_{PS}$	0	$[\frac{1}{2} \frac{\Delta \rho}{\bar{\rho}} + \frac{\bar{c}_S}{\bar{c}_P} \frac{\Delta \mu}{\bar{\mu}}]$	$\bar{c}_P p$

Table 5.3 The first order angular dependence of the RC functions, as derived in chapter 3 table 3.1.

## 5.6 Use of multi mode PS, SP and SS data

In the case that we have PP reflection data and SP reflection data, we can estimate at least 3 terms:  $\frac{\Delta Z}{Z}$ ,  $\frac{1}{2} \frac{\Delta c_P}{\bar{c}_P} - 2(\frac{\bar{c}_S}{\bar{c}_P})^2 \frac{\Delta \mu}{\bar{\mu}}$  and  $\frac{\bar{c}_S}{\bar{c}_P} [\frac{1}{2} \frac{\Delta \rho}{\bar{\rho}} + \frac{\bar{c}_S}{\bar{c}_P} \frac{\Delta \mu}{\bar{\mu}}]$  (see table 5.3). Together with the relation  $\frac{\Delta \mu}{\bar{\mu}} = \frac{\Delta \rho}{\bar{\rho}} + 2 \frac{\Delta c_S}{\bar{c}_S}$  we can now deduce the contrasts in the P, S-wave or density quantitatively. Note that any inaccuracy in the estimated terms or the ratio between P and S-wave velocity directly deteriorates the deduced results and that the ratio  $\bar{c}_S/\bar{c}_P$  is assumed to be known.

In case we have both PP and SS reflection data, we can estimate at least 4 terms:  $\frac{\Delta Z}{Z}$ ,  $\frac{\Delta Z_s}{Z_s}$ ,  $\frac{1}{2} \frac{\Delta c_P}{\bar{c}_P} - 2(\frac{\bar{c}_S}{\bar{c}_P})^2 \frac{\Delta \mu}{\bar{\mu}}$  and  $\frac{1}{2} (\frac{c_S}{c_P})^2 \frac{\Delta c_S}{\bar{c}_S} + 2(\frac{c_S}{c_P})^2 \frac{\Delta \mu}{\bar{\mu}}$ . Together with the relation  $\frac{\Delta \mu}{\bar{\mu}} = \frac{\Delta \rho}{\bar{\rho}} + 2 \frac{\Delta c_S}{\bar{c}_S}$  we can again deduce the contrasts in the P, S-wave or density quantitatively. Since we have more relations than parameters we compute, we can use the redundancy to get more robust contrasts or to check the ratio  $\bar{c}_S/\bar{c}_P$ . This will of course be improved if also the converted reflections (PS and SP) are used. This was also shown for nonlinear inversion by de Haas and Berkhouw (1988).

### 5.6.1 Use of $R_{PP}$ and $R_{SP}$

For example in case of OBS<sup>3</sup> data, we can expect to have at least  $R_{PP}$  and  $R_{SP}$  data. This means that from the inversion, using the parameterization given in table 5.3, we have estimates for

$$A = \frac{1}{2} \frac{\Delta Z}{Z}, \quad (5.22)$$

$$B = \frac{1}{2} \frac{\Delta c_P}{\bar{c}_P} - 2(\frac{\bar{c}_S}{\bar{c}_P})^2 \frac{\Delta \mu}{\bar{\mu}}, \quad (5.23)$$

$$C = -\frac{\bar{c}_S}{\bar{c}_P} [\frac{1}{2} \frac{\Delta \rho}{\bar{\rho}} + \frac{\bar{c}_S}{\bar{c}_P} \frac{\Delta \mu}{\bar{\mu}}]. \quad (5.24)$$

Note that the  $R_{SP}$  data gives only one estimated parameter. Using these relations we can derive the following equations for the elastic contrast parameters:

$$\frac{\Delta c_P}{\bar{c}_P} = \frac{B - 2\gamma A - 2C}{0.5 - \gamma} \quad \text{with } \gamma = \frac{\bar{c}_S}{\bar{c}_P}, \quad (5.25)$$

$$\frac{\Delta c_S}{\bar{c}_S} = \frac{-1}{2\gamma^2} \times [C + \gamma(0.5 + \gamma) \times \frac{A - B + 2C}{0.5 - \gamma}], \quad (5.26)$$

<sup>3</sup>Ocean Bottom Stations, measuring 3-component velocity data and the pressure data at the ocean floor

$$\frac{\Delta\rho}{\bar{\rho}} = \frac{A - B + 2C}{0.5 - \gamma}. \quad (5.27)$$

From these relations it becomes immediately clear that for values of  $\gamma$  around 0.5 the derivation of P and S-wave contrasts becomes instable. Unfortunately the value of  $\gamma$  varies often around 0.5. In the well log measurements used for the numerical example in the next section,  $\gamma$  ranges from 0.4 at shallow levels up to 0.7 in the deeper part. For stability it is necessary that  $|A - B + 2C| \ll 1$ , which could be used as a QC-tool or as a priori information in the inversion.

In case we use 3-parameter inversion for the  $R_{PP}$  data (see equation 5.5), we have 4 estimated parameters,

$$A = \frac{\Delta Z}{\bar{Z}}, \quad (5.28)$$

$$B = \frac{\Delta c_P}{\bar{c}_P}, \quad (5.29)$$

$$C = \frac{\Delta\mu}{\bar{\mu}}, \quad (5.30)$$

$$D = -\frac{\bar{c}_S}{\bar{c}_P} \left[ \frac{1}{2} \frac{\Delta\rho}{\bar{\rho}} + \frac{\bar{c}_S}{\bar{c}_P} \frac{\Delta\mu}{\bar{\mu}} \right]. \quad (5.31)$$

These four parameters can be used to estimate the elastic contrasts in P and S-wave velocities and in density in a least-squares way. The fact that each of the three parameters in equations 5.28 - 5.30 may be less accurate than the two parameters in equations 5.22 and 5.23, is compensated by the redundancy in the over-determined set of equations in the least-squares inversion.

### 5.6.2 Use of $R_{PP}$ and $R_{SS}$

In case we have both  $R_{PP}$  and  $R_{SS}$  data and we use for both modes a 2 parameter inversion, we have 4 estimated parameters:

$$A = \frac{1}{2} \frac{\Delta Z}{\bar{Z}}, \quad (5.32)$$

$$B = \frac{1}{2} \frac{\Delta c_P}{\bar{c}_P} - 2 \left( \frac{\bar{c}_S}{\bar{c}_P} \right)^2 \frac{\Delta\mu}{\bar{\mu}}, \quad (5.33)$$

$$C = \frac{1}{2} \frac{\Delta Z_s}{\bar{Z}_s}, \quad (5.34)$$

$$D = \frac{1}{2} \left( \frac{c_S}{c_P} \right)^2 \frac{\Delta c_S}{\bar{c}_S} - 4 \left( \frac{c_S}{c_P} \right)^2 \frac{\Delta Z_S}{\bar{Z}_S}. \quad (5.35)$$

Using these relations we can derive the following explicit equations for the elastic contrast parameters (using  $\gamma = \bar{c}_S/\bar{c}_P$ ):

$$\frac{\Delta c_P}{\bar{c}_P} = \frac{(4\gamma^2 + 1)A - B - 8\gamma^2C}{2\gamma^2}, \quad (5.36)$$

$$\frac{\Delta c_S}{\bar{c}_S} = \frac{A - B - 4\gamma^2C}{2\gamma^2}, \quad (5.37)$$

$$\frac{\Delta \rho}{\bar{\rho}} = \frac{A - B - 8\gamma^2C}{-2\gamma^2} \quad (5.38)$$

Note that these derivations are stable for all ratios  $\gamma \neq 0$ . As a final check on the ratio  $\gamma$  the following relation can be used:

$$D = \frac{1}{4}A - \frac{1}{4}B - 9\gamma^2C. \quad (5.39)$$

The four equations 5.32 - 5.35 give an over determined system to derive the three elastic contrasts. The most stable way to use all the information is to estimate the three contrasts from the estimated parameters A-D by a least squares inversion.

### 5.6.3 Numerical example multi mode inversion

In appendix II a numerical multi-mode migration example has been shown for a multi-layer model. The blocked well logs which are used to define the model, are from well A of the Mobil AVO data set (see chapter 8). A full elastic reflectivity modeling scheme has been used to model the multi-mode shot record. All internal multiples were included in the modeling, only the surface related multiples have not been modeled. The CFP based migration result for the PP data is shown in figure 5.13 together with the estimated four contrast traces. The first three contrast parameters have been estimated using a parameterization in three terms (see equation 5.5). The gradient has been estimated using a parameterization in two terms, as indicated in table 5.3.

The estimated contrasts and gradient are also compared with direct computed contrast traces in figure 5.14. The estimated impedance contrast matches the direct computed impedance contrast very well. The match between the estimated gradient and the direct computed gradient is reasonably good. The estimated shear modulus contrast overestimates the contrasts at a number of depths. At these depths also the P-velocity contrasts have been overestimated and the gradient has been underestimated. The accuracy of the P-velocity contrast is the lowest of the four estimates.

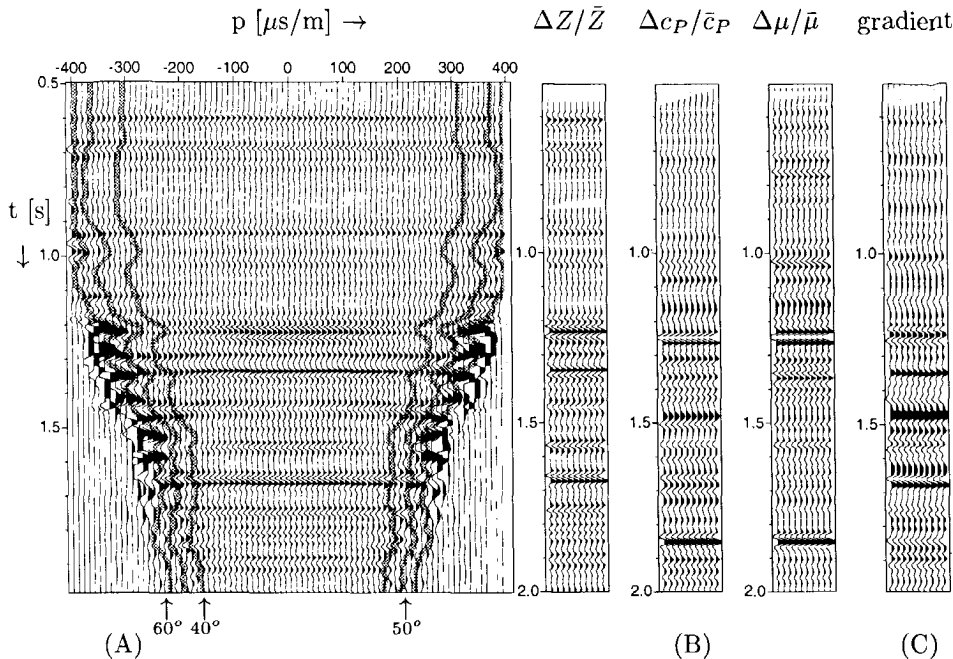


**Fig. 5.13** (A) The imaged RC gather for PP data, (B) the three estimated contrast parameters and (C) the gradient, using the 2 parameter inversion. The gray lines indicate the angles of 40, 50 and 60 degrees. Data up to 45 degrees has been used in the inversion.

The CFP based migration result for the SP data is shown in figure 5.15(A), together with the estimated gradient in (C). In the two parameter inversion also the intercept or  $\tilde{r}_{SP}(p = 0)$  has been estimated. The intercept was almost equal to zero, as it should according to the expression for  $\tilde{r}_{SP}$ .

The migrated RC gather has not only been band filtered in order to have a flat spectrum as function of  $p$  (see chapter 4), but also to have the same frequency content as the PP data. This is needed if both PP and SP data are used for characterization. The CFP based migration result for the SS data is shown in figure 5.15(C), together with the estimated shear impedance and gradient. The lines of constant incidence angle in figure 5.15(C) show clearly the much smaller incidence angles for the same  $p$ -range, compared to the PP data. Also the polarity change around 20 degrees is clearly visible.

The migrated RC gather has been band filtered in order to match the frequency content of the PP data and to ensure a flat spectrum as function of  $p$ .

An example of combining (in a least squares inversion) the results from the PP and SP (equation 5.28 - 5.31) in order to estimate the contrasts in P-velocity, S-velocity

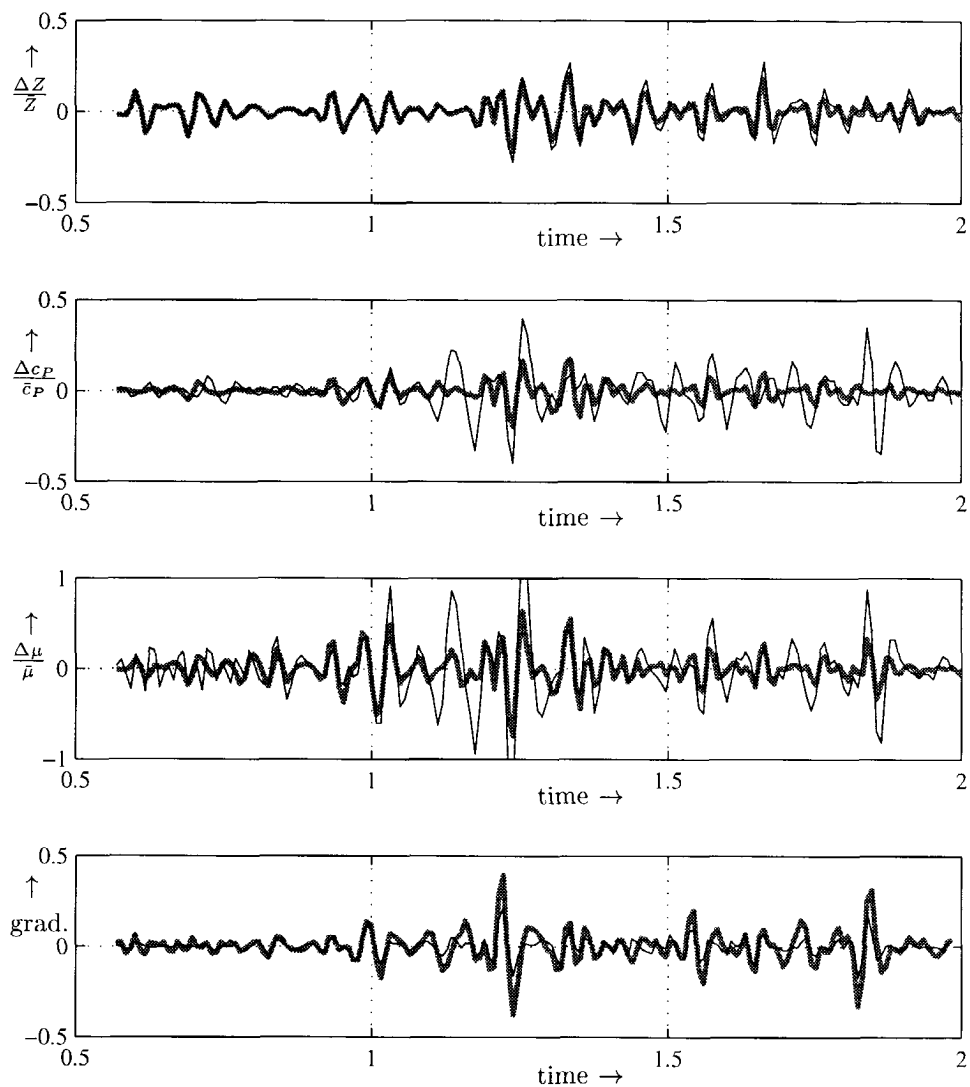


**Fig. 5.14 (A)** The estimated elastic contrasts using PP data and the direct computed contrasts indicated with the thick gray line.

and density is shown in figure 5.16. The estimated P-velocity contrast and S-velocity contrast show a reasonable match with the reference traces.

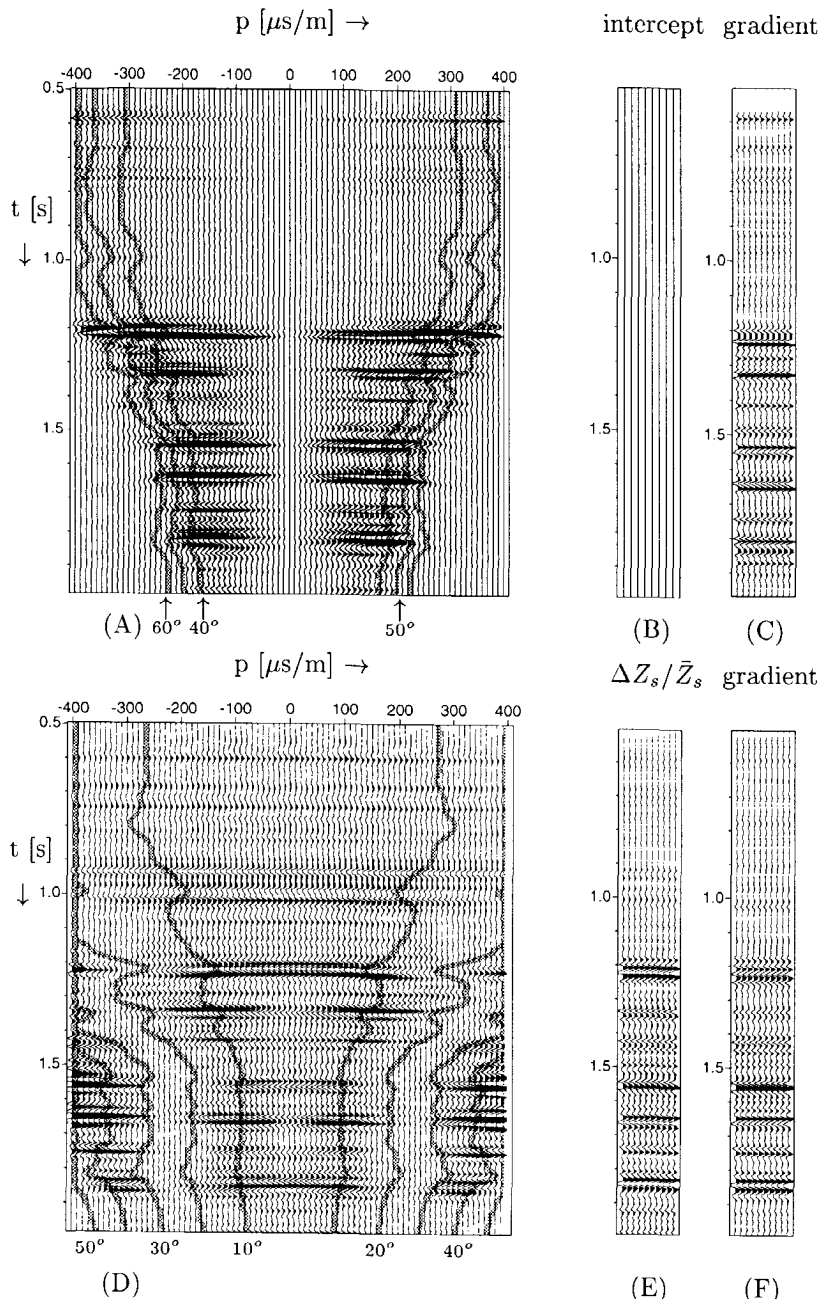


**Fig. 5.15** (A) The imaged RC gather for SP (A) and SS data (C) and the estimated intercepts (B,E) and gradients (C,F), using the 2 parameter inversion. The dark gray lines indicate the incident angles.

The density contrast is clearly less accurate, and only up to one second there is a reasonable match with the reference trace. An example of combining (in a least squares inversion) the results from the PP and SS (equation 5.32 - 5.35) in order to estimate the contrasts in P-velocity, S-velocity and density is shown in figure 5.17. The estimated P-velocity contrast and S-velocity contrast show a good match with the reference traces. The density contrast is clearly again less accurate, especially in the area around 1.2s.

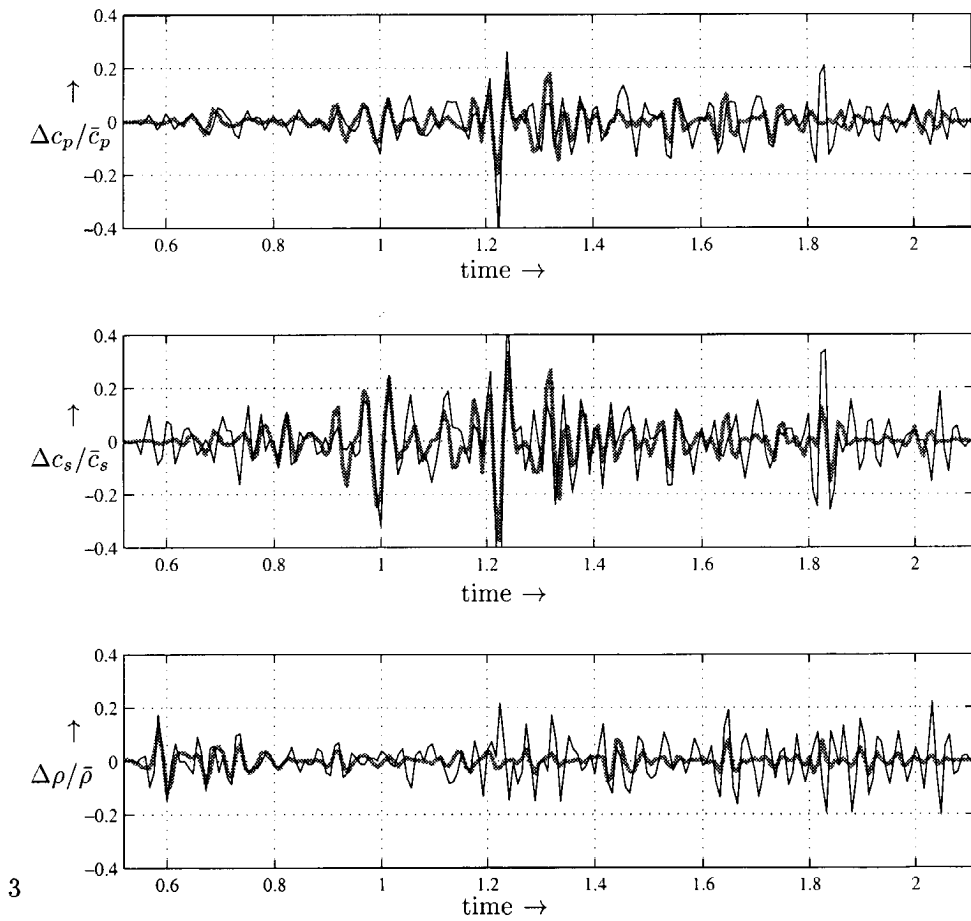


**Fig. 5.16** The computed elastic contrasts, using the three parameters from the inversion of the PP data and the estimated gradient from the SP data, in black and the reference contrasts in light gray.

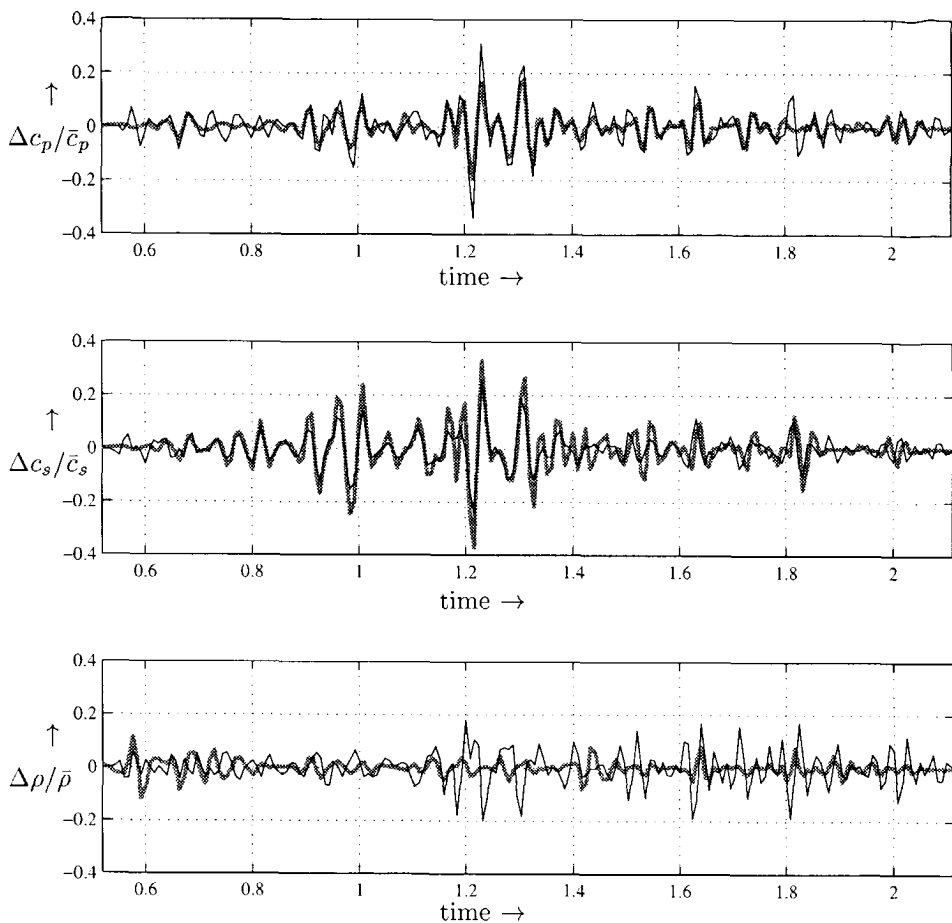


**Fig. 5.17** The computed elastic contrasts using the inversion results (intercepts and gradients) from PP and SS data in black and the reference contrasts in light gray.

#### 5.6.4 Use of AVO terms for lithology indication

The AVO terms which are estimated in the inversion of the (multi mode) RC gathers are not only used to derive the contrast in elastic parameters, but they are also directly used to differentiate lithologies (Swan, 1993). From well data cross plots can be made between the different terms in order to find the optimum combination for differentiating the lithologies. In chapter 7 this will be discussed in more detail.



# Chapter 6

## Resolution and residue analysis

In the previous chapter the inversion of RC gathers into contrast traces has been discussed. In this chapter the accuracy or resolution of the estimated contrast parameters will be discussed. Also the relation between the linearized forward model and the input data will be investigated. By means of a residue analysis the nonlinear events and noise in the input data will be examined. Furthermore the relative influence of the a priori information compared to the seismic data will be quantified. Finally the multi gather inversion and residual move-out will be discussed.

### 6.1 The ZLF and residue analysis

In the previous chapter the local inversion of RC gathers has been discussed. The general local forward model to describe an AVP curve (amplitude cross section of a RC gather at a certain time) was given by

$$\tilde{d} = \tilde{\mathbf{A}}\tilde{\lambda} + \tilde{n}. \quad (6.1)$$

The input data vector  $\tilde{d}$  denotes the imaged AVP curve, the matrix  $\tilde{\mathbf{A}}$  describes the forward model and the vector  $\tilde{n}$  contains all the nonlinear events and noise. The inversion process minimizes the vector  $\tilde{n}$  or *residue* in a least squares way.

The data vector  $\tilde{d}$  and the residue vector  $\tilde{n}$  are related to the local inversion of the data in a RC gather at a certain time. In the previous chapter the inversion process has been described to estimate the contrast vector  $\tilde{\lambda}$ . But not only the vector  $\tilde{\lambda}$  contains useful information. Also the linear forward modeled data  $\tilde{\mathbf{A}}\tilde{\lambda}$  and the residue  $\tilde{n}$  can be used for interpretation (van Wijngaarden and Berkhouwt, 1995).

#### 6.1.1 Local ZLF and residue analysis

In order to make the interpretation possible, the forward modeled data  $\tilde{\mathbf{A}}\tilde{\lambda}$  and the residue  $\tilde{n}$  will be used for all times (i.e. a gather). The data  $\tilde{\mathbf{A}}\tilde{\lambda}(t)$  is called the *ZLF* (Zoeppritz-driven Linear Filtered) gather and the data  $\tilde{n}(t)$ , the difference between

the RC gather and the ZLF gather, is called the *residue* gather. The ZLF gather contains the linear part of the RC gather and the residue gather contains all the noise and the nonlinear events. This concept is illustrated in figure 6.1. Note that there is no data reduction due to stacking. The ZLF and residue gathers are still prestack data. The signal-to-noise improvement in the ZLF gather is due to the enforced Zoeppritz model.

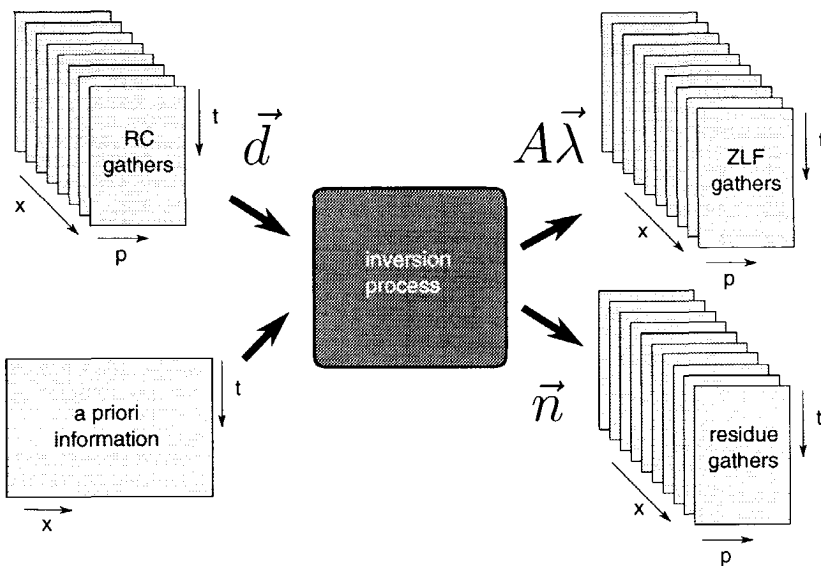
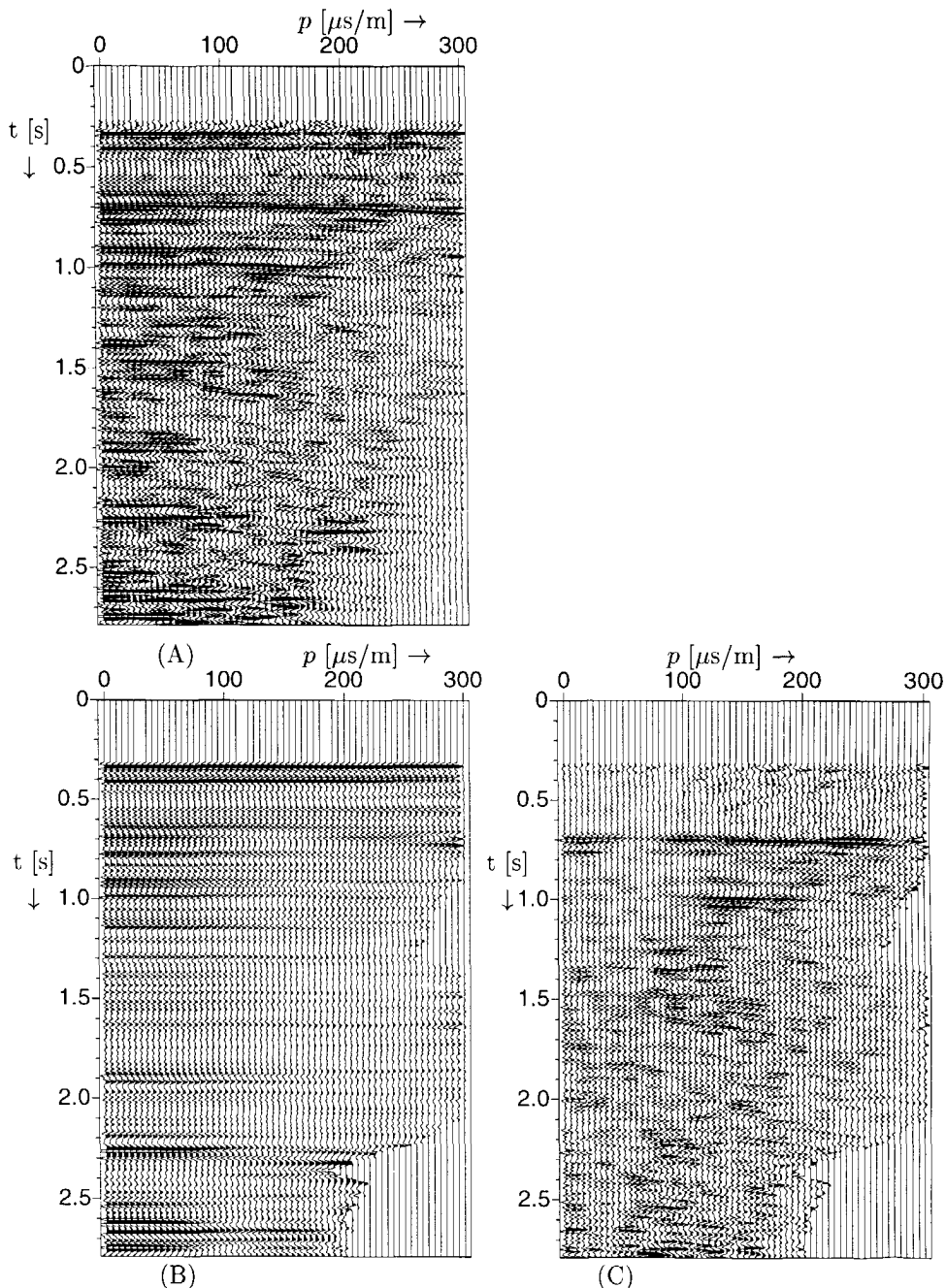


Fig. 6.1 Overview of the ZLF process for local analysis.

An example on field data is given in figure 6.2. The top left figure shows the RC gather at shot point location 707. The ZLF gather (bottom left) shows the best match of the Zoeppritz model with the RC gather; it shows the *linear* part of the data. In the residue gather (bottom right) all the nonlinear events and noise are present. Clearly a multiple is present at twice the two-way travel time (approx. 0.7s). This event caused the high amplitudes in the estimated shear modulus contrast in the previous chapter. Without this residue analysis the inverted contrasts around 0.7s might be interpreted in the wrong way. Clearly residual move-out can be recognized in the residue gather. Note that up to the first water bottom multiple there are no coherent events in the residue gather.

The ZLF gather can be used for interpretation of the events which may be hidden in the noise of the RC gather. Note that the ZLF gather shows the AVP curves focused at one lateral position. This means it is a *local* analysis tool.



**Fig. 6.2** (A) The RC gather, (B) the ZLF gather  $\tilde{\mathbf{A}}\tilde{\lambda}(t)$  and (C) the residue gather  $\tilde{\mathbf{n}}(t)$  from the 2D marine data set. Data up to  $45^\circ$  has been used. Note that above 0.7s there is no coherent energy in the residue gather.

In figure 6.3 the ZLF gather is compared with a synthetic impedance trace and the sonic well log at a well position. The filtered ZLF gathers makes it easy to relate the sonic and synthetic impedance contrast with the seismic data. Overall there is a very good match. Only the event just above 2.2s in the seismic data does not correspond to an event in the well log data. Residue analysis and global analysis (next section) show that this is probably multiple energy which is left in the seismic data after multiple elimination.

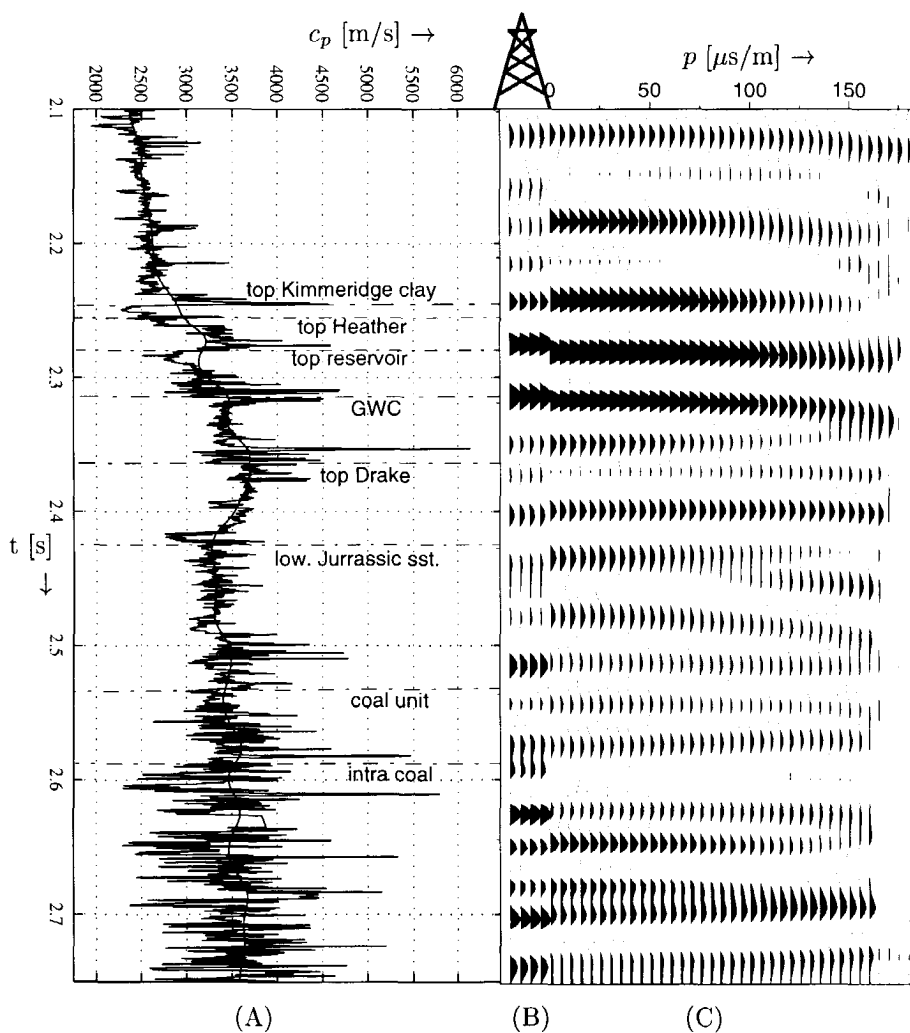


**Fig. 6.3** (A) The sonic well log, (B) the synthetic impedance contrast and (C) the ZLF gather  $\tilde{\lambda}(t)$  from the 2D marine data set with interpretation.

### 6.1.2 Global ZLF and residue analysis

In the previous section the *local* analysis was discussed using a single ZLF and residue gather at a certain lateral position. The ZLF gather can also be used to select at each lateral position the reflectivity for a certain  $p$ -value or angle as function of time. By repeating this process for all ZLF gathers (all lateral positions), a reflectivity section can be made for a certain  $p$ -value or angle. The section for  $p=0$  equals of course the estimated impedance contrast section. Note the difference between this method and a section, which is made by stacking over a small number of offsets or  $p$ -values. In the last case not all data is used, and often the signal-to-noise ratio is much lower than the full offset or  $p$  stack. By using the ZLF gathers, all data *and* the Zoeppritz model is used for a constant  $p$  or constant angle section. The signal-to-noise ratio is (almost) equal to the full stack over the prestack data (RC gather).

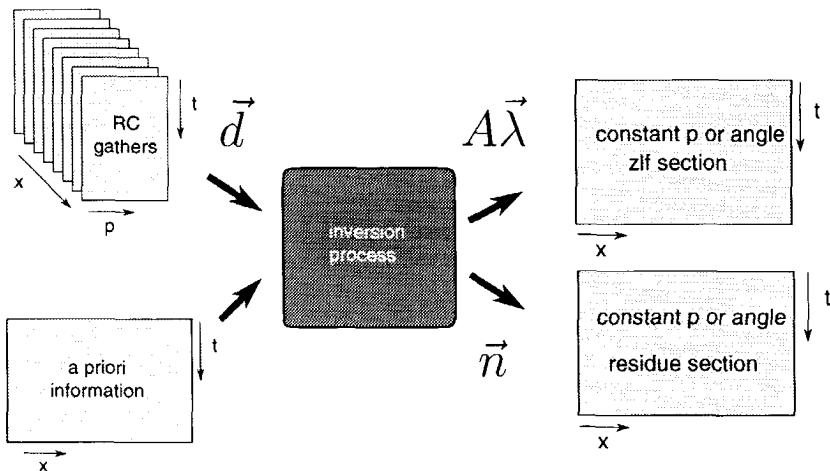
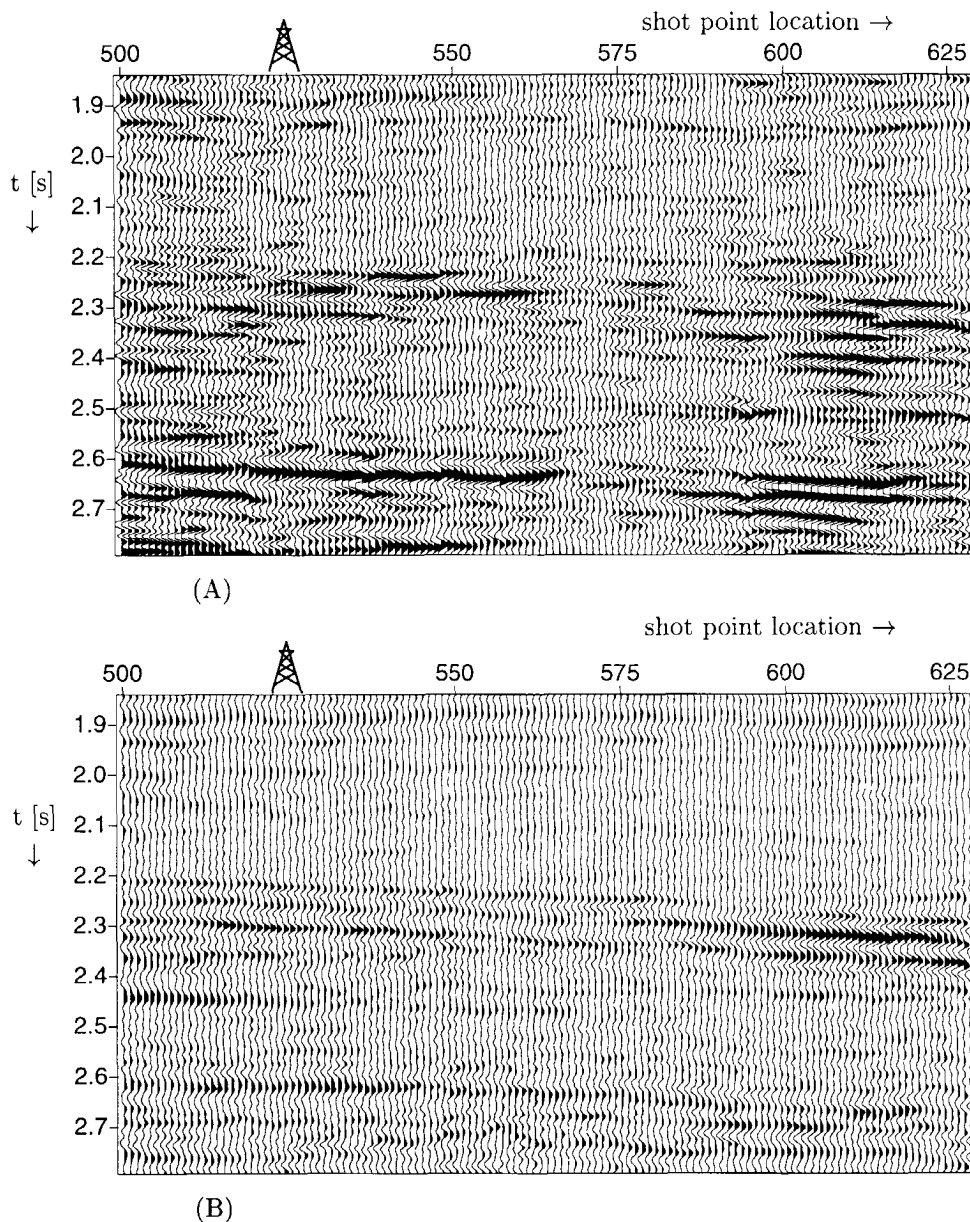


Fig. 6.4 Overview of the ZLF process for global analysis.

The same procedure can be used to make residue sections for a specific  $p$ -value or angle. Nonlinear events like multiples, residual move-out or critical angles can be recognized in a section, which is much faster than looking at all residue gathers alone.

In figure 6.5 two examples of ZLF sections for the 2D marine data set are shown. In figure 6.5A the ZLF section for  $p=0$  is shown. This section is of course the same as the impedance contrast section. Figure 6.5B shows the ZLF section for  $p=150\mu\text{s}/\text{m}$ , which corresponds approximately to an average angle of 30 degrees. The dipping top of the reservoir is clearly present. The last section shows a much more smooth and continuous behaviour than the impedance section.



**Fig. 6.5** Example of ZLF sections for global analysis, using the target area of the 2D marine data set. Top figure shows the ZLF section for  $p=0 \mu\text{s}/\text{m}$  (impedance contrast). Bottom figure shows the ZLF section for  $p=150 \mu\text{s}/\text{m}$ .

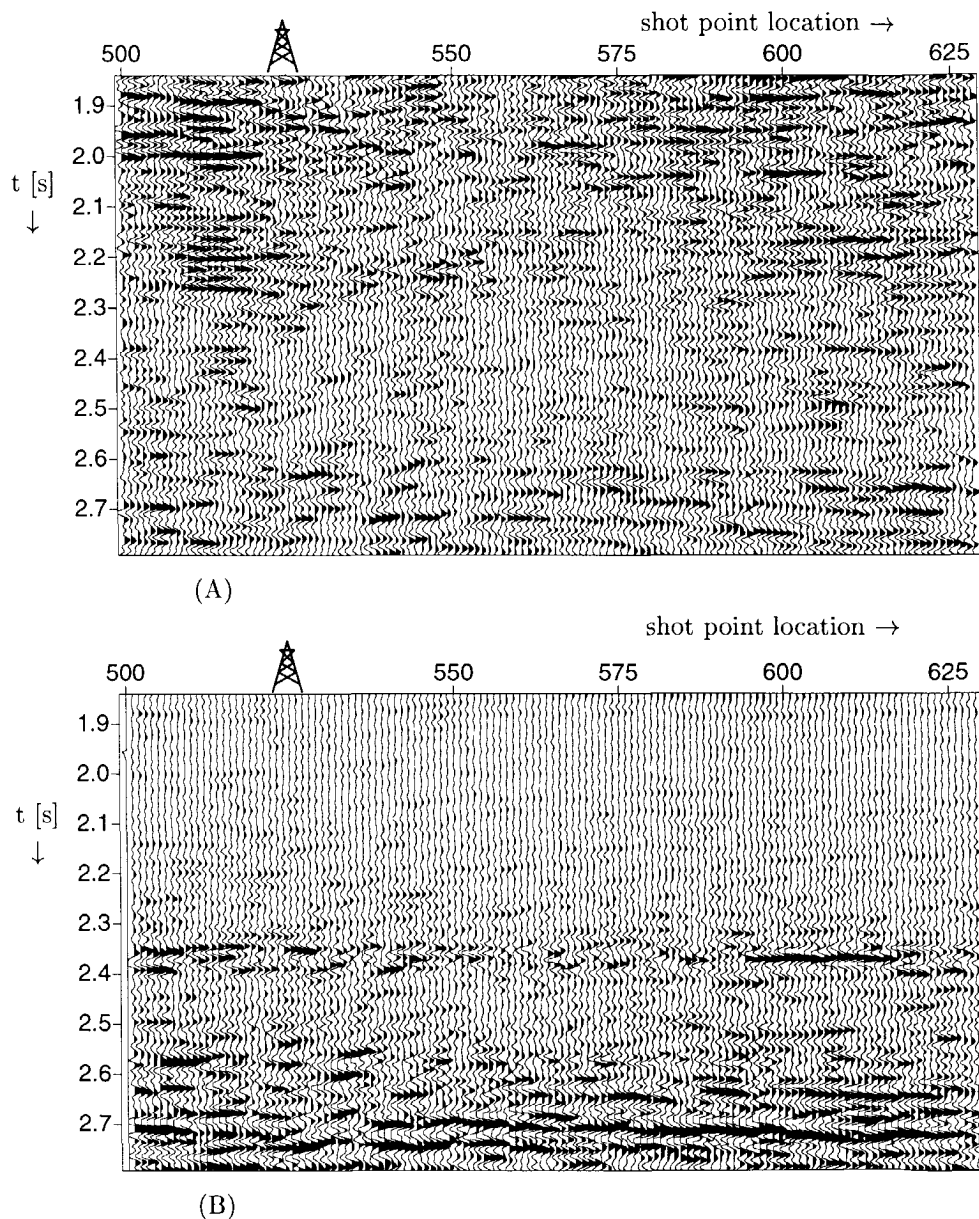


**Fig. 6.6** Example of residue sections for global analysis, using the target area of the 2D marine data set. Top figure shows the residue section for a stack over  $0 < |p| < 50 \mu\text{s}/\text{m}$ . Bottom figure shows the residue section for  $150 < |p| < 300 \mu\text{s}/\text{m}$ .

In figure 6.6 two residue sections are shown. In order to reduce the amount of noise and to emphasize the coherent events in the residue, a stack over a small  $p$ -range is shown. In 6.6A a stack over the residue for small angles ( $|p| < 50 \mu\text{s}/\text{m}$ , approximately  $0\text{--}10^\circ$ ) is shown, whereas in figure 6.6B a stack over residue of the larger angles ( $150 < |p| < 300 \mu\text{s}/\text{m}$ , approximately  $30\text{--}45^\circ$ ) is shown. Most residual energy for small angles ( $0\text{--}10^\circ$ ) is present between 1.8s and 2.2s, whereas for larger angles ( $30\text{--}45^\circ$ ) most residual energy is present in a strong event just above 2.4s and below 2.6s. The residual energy around shot point location 510 in figure 6.6A is related to unremoved (3D) multiple energy. Note that the residual event in 6.6B at 2.4s is almost flat and does not follow the dipping events in figure 6.5B. Therefore the residue could be related to a (internal) multiple of the upper flat reflectors or it could be related to a gas/fluid contact, since it is close to the gas/oil contact. This is discussed in more detail in chapter 8.

## 6.2 Estimation of covariance and standard deviations of estimated parameters

### 6.2.1 Weighted least-squares inversion

The least squares estimation was described in the previous chapter (equation 5.17) by

$$\hat{\lambda} = \left[ \tilde{\mathbf{A}}_{\text{tot}}^t \tilde{\mathbf{C}}_{\text{tot}}^{-1} \tilde{\mathbf{A}}_{\text{tot}} \right]^{-1} \left[ \tilde{\mathbf{A}}_{\text{tot}}^t \tilde{\mathbf{C}}_{\text{tot}}^{-1} \tilde{d}_{\text{tot}} \right] \quad (6.2)$$

and gives the *maximum likelihood* estimate. By weighting the forward matrix  $\mathbf{A}_{\text{tot}}$  and the data vector  $\vec{d}_{\text{tot}}$  with the inverse of the standard deviations of the seismic and a priori data (i.e.  $\mathbf{C}_{\text{tot}}^{-1/2}$ ), this could also be written as (equation 5.18)

$$\hat{\lambda} = \left[ \tilde{\mathbf{A}}_w^t \tilde{\mathbf{A}}_w \right]^{-1} \left[ \tilde{\mathbf{A}}_w^t \tilde{d}_w \right]. \quad (6.3)$$

### 6.2.2 Result analysis using the SVD

The Singular Value Decomposition (SVD) technique is a numerical operation for the decomposition of a matrix  $\tilde{\mathbf{A}}_w$  into three characteristic matrices

$$\tilde{\mathbf{A}}_w = \tilde{\mathbf{U}} \tilde{\mathbf{S}} \tilde{\mathbf{V}}^t. \quad (6.4)$$

As shown in the previous chapter, the forward model matrix  $\tilde{\mathbf{A}}$  ( $n \times m$ ) is decomposed in a matrix  $\tilde{\mathbf{U}}$ , which is a  $n \times n$  a matrix, a matrix  $\tilde{\mathbf{S}}$ , which is the  $n \times m$  diagonal singular value matrix and a  $m \times m$  matrix  $\tilde{\mathbf{V}}$ . The columns of  $\tilde{\mathbf{U}}$  and  $\tilde{\mathbf{V}}$  are an orthonormal set of vectors, called eigenvectors. Using equation 6.4, the noise free forward model can be written as

$$\tilde{d}_w = \tilde{\mathbf{A}}_w \tilde{\lambda} = \tilde{\mathbf{U}} \tilde{\mathbf{S}} \tilde{\mathbf{V}}^t \tilde{\lambda}. \quad (6.5)$$

Now using the least squares solution of the linear problem, equation 6.3, with the SVD of the matrix  $\tilde{\mathbf{A}}$ , the following relation can be derived

$$\tilde{\lambda} = (\tilde{\mathbf{V}}\tilde{\mathbf{S}}^t\tilde{\mathbf{S}}\tilde{\mathbf{V}}^t)^{-1}(\tilde{\mathbf{V}}\tilde{\mathbf{S}}^t\tilde{\mathbf{U}}^t)\tilde{d} = \tilde{\mathbf{V}}\left[\tilde{\mathbf{S}}^t\tilde{\mathbf{S}}\right]^{-1}\tilde{\mathbf{S}}^t\tilde{\mathbf{U}}^t\tilde{d}_w, \quad (6.6)$$

where  $\tilde{d}_w$  is the weighted data vector. The SVD allows an efficient calculation of the posteriori covariance matrix for low residuals and/or forward models with sufficient linearity according to

$$\tilde{\mathbf{C}}_p = (\tilde{\mathbf{V}}\tilde{\mathbf{S}}^t\tilde{\mathbf{S}}\tilde{\mathbf{V}}^t)^{-1} = \tilde{\mathbf{V}}\left[\tilde{\mathbf{S}}^t\tilde{\mathbf{S}}\right]^{-1}\tilde{\mathbf{V}}^t \quad (6.7)$$

From the posteriori covariance matrix the standard deviations for the estimated parameters can be computed; the diagonal of the covariance matrix contains the squared standard deviations of the estimated parameters.

An example is given in figure 6.7 for the inversion of the RC gather shown in figure 6.2. The estimated covariance of the data and the estimated contrast parameters are shown together with the estimated contrast traces and one trace from the RC gather ( $p=0$ ). The accuracy of the input data is given by the constant standard deviation of  $sd_{data}=0.005$  in figure 6.7A. Clearly the accuracy for the estimated impedance contrast (6.7B) is higher than for the other two contrasts and almost constant for all times. The standard deviation of the  $p$ -dependent contrasts depends ( $\Delta c_P/\bar{c}_P$  and  $\Delta\mu/\bar{\mu}$ ) on the amount of data used in the inversion, which is given by the mute line in figure 6.2B.

In order to investigate the influence of the width in  $p$ -values of the input data on the accuracy of the estimated contrast parameters, the following experiment is done. A simple one reflector model is used, with a RC gather for PP data of 60 traces, equidistant sampled in  $p$ . The amount of traces is kept constant. The width of the  $p$ -range is varied from  $[0; p_{max1}]$  to  $[0; p_{max2}]$ . The estimated standard deviations for the three contrast parameters are plotted in figure 6.8 as function of the maximum  $p$ -value used.

The standard deviation of the input data was chosen as  $sd_{data}=0.005$  (constant for all data points) and for the a priori information (two relative relations  $\Delta Z/\bar{Z} = \gamma_1 \times \Delta c_P/\bar{c}_P$  and between  $\Delta c_P/\bar{c}_P = \gamma_2 \times \Delta\mu/\bar{\mu}$ ) a standard deviation of  $sd_{\gamma} \approx 1.0$  was used. Clearly the accuracy of the estimated impedance contrast is the highest and almost independent of the maximum  $p$ -value used. This is expected for this  $p$ -independent contrast.

The accuracy of the P-velocity and shear modulus contrasts clearly increase with increasing maximum  $p$ -values. If no a priori information is used, in the limit  $p \downarrow 0$  the standard deviations for these estimated parameters become infinitely high, because for  $p_{max}=0$  these parameters are completely undetermined. Due to the (soft) a

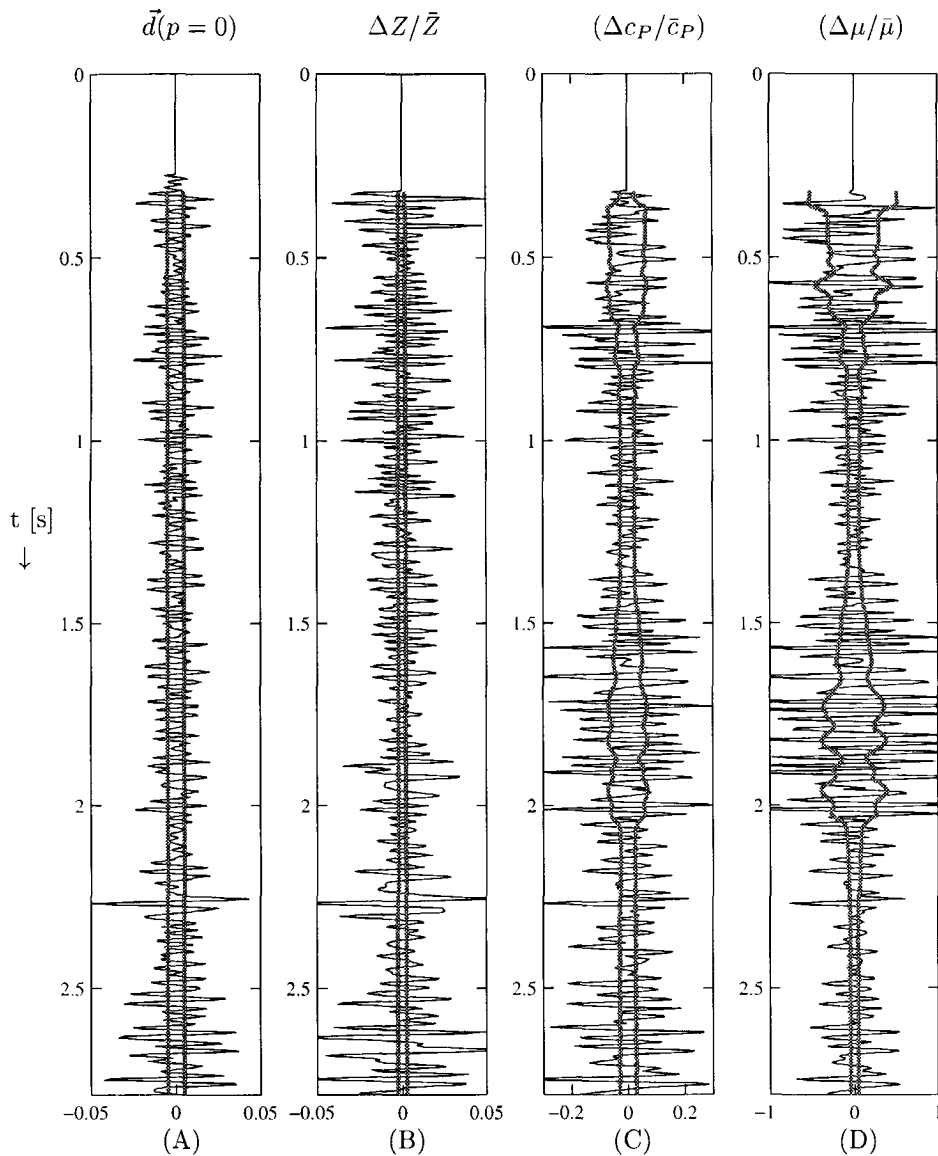


**Fig. 6.7** The standard deviations for the input data and the estimated contrast parameters for a field data example (plotted in gray) together with the input data (A) and estimated contrasts themselves (B-D).

priori information, the standard deviations of the estimated contrasts in P-velocity and shear modulus are finite. The influence of the a priori information will be quantified in the next section.

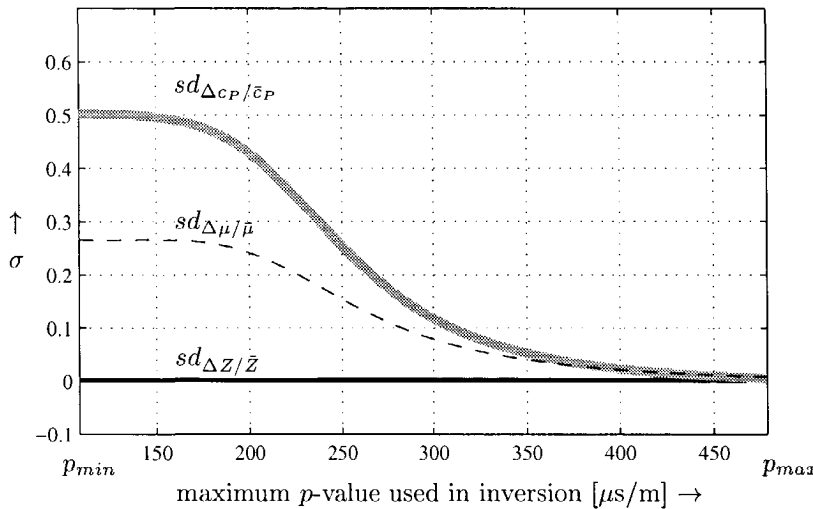


**Fig. 6.8** The estimated standard deviations as function of the p-values used in the inversion. The range of p-values varies from 0 up to  $p_{max1} - p_{max2}$ . The velocity in the upper layer is 1600m/s. This means that  $p_{max1}$  corresponds to an incidence angle of 10 degree and  $p_{max2}$  corresponds to an incidence angle of 50 degrees.

For moderately high p-values (corresponding to angles of 20-40 degrees), the accuracy of the P-velocity contrast is less than the accuracy of the shear modulus contrast. In other words, the shear modulus is better determined than the P-velocity contrast. Of course the impedance contrast is the best determined parameter.

### 6.2.3 Influence of a priori information on inversion result

For an objective measure of the resolution, a condition<sup>1</sup> number  $K$  can be introduced. The condition number  $K_i$  is defined as the ratio of the standard deviation  $\sigma_i^+$  of the estimated  $i^{th}$  parameter with empirical information and the standard deviation  $\sigma_i^-$  of the estimated  $i^{th}$  parameter without empirical information,

$$K_i = \frac{\sigma_i^+}{\sigma_i^-}. \quad (6.8)$$

This means that the condition number will have a value between 0 and 1. In case the additional a priori information does not influence the inversion, the estimated standard deviation will be the same with and without the a priori information, i.e. the condition number will be 1. In case the a priori information has a large influence

<sup>1</sup>Note that the condition number here does not indicate the ratio of smallest and largest eigenvalue of a matrix.

on the inversion, the estimated standard deviation  $\sigma^+$  with a priori information will be much smaller than the estimated standard deviation  $\sigma^-$  without a priori information, i.e. the condition number will be close to 0. As a rule of thumb one can say that for a condition number larger than one half, the seismic data has mainly determined the solution of the inversion and for a condition number smaller than one half the a priori data has determined the solution.

For the linear model of equation 6.1 the condition number for the  $i^{th}$  parameter can be written as

$$K_i = \frac{\sqrt{(\mathbf{A}_{seis,w}^t \mathbf{A}_{seis,w} + \mathbf{A}_{ap,w}^t \mathbf{A}_{ap,w})_{ii}^{-1}}}{\sqrt{(\mathbf{A}_{seis,w}^t \mathbf{A}_{seis,w})_{ii}^{-1}}}, \quad (6.9)$$

with  $\mathbf{A}_{seis,w}$  denoting the seismic forward model matrix  $\mathbf{A}$  weighted with the inverse standard deviations of the data and  $\mathbf{A}_{ap,w}$  denoting the a priori relations  $\mathbf{A}_{ap}$  weighted with the inverse standard deviations of the a priori relations.

In order to investigate the influence of the width in  $p$ -values of the input data on the condition number of the estimated contrast parameters, the same experiment as in the previous section has been repeated.

The same one reflector model is used, with a RC gather (containing PP data) of 60 traces, equidistant sampled in  $p$ . The amount of traces is kept constant again. The range the  $p$ -values is varied from  $[0; p_{max1}]$  to  $[0; p_{max2}]$ . The condition numbers for the contrast parameters are plotted in figure 6.9 as function of the maximum  $p$ -value used.

All the condition numbers increase with the maximum  $p$ -value used. This is expected, since a broader  $p$ -range gives a better determination of the contrast parameters. The estimated impedance contrast is largely determined by the seismic data for all maximum  $p$ -values, although the influence of the a priori data can be seen for maximum  $p$ -values below  $250\mu\text{s}/\text{m}$ . The two  $p$ -dependent contrasts are much more influenced by the a priori information. For maximum  $p$ -values below  $200\mu\text{s}/\text{m}$  the estimated contrasts are mainly determined by the a priori information. This is the reason why the estimated standard deviations in figure 6.8 are finite and the curves for the standard deviations flattens between  $100$  and  $200\mu\text{s}/\text{m}$ .

### 6.3 Improving the inversion result

Generally in AVP inversion the results are used to find deviations from a regional trend in the relations between the contrast parameters. Therefore these regional relations should not be used as strong a priori information, but the inversion should be determined by the seismic data. Using the condition numbers, it can be decided how large the standard deviations on the a priori data should be, in order to let the seismic data determine the inversion.

On the other hand, the accuracy of the estimated contrasts should be high enough

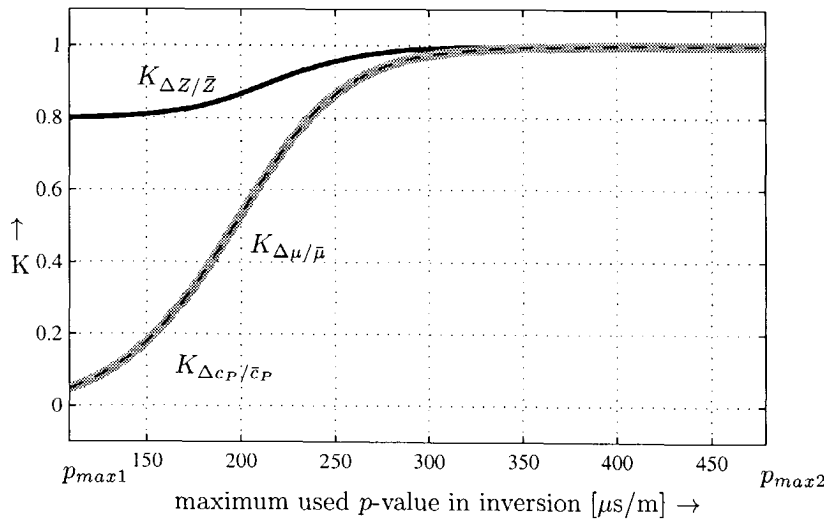


**Fig. 6.9** The estimated condition numbers  $K$  as function of the used  $p$ -values in the inversion. The range of  $p$ -values varies from 0 up to  $p_{max1} - p_{max2}$ . The velocity in the upper layer is 1600 m/s. This means that  $p_{max1}$  corresponds to an incidence angle of 10 degree and  $p_{max2}$  corresponds to an incidence angle of 50 degrees. The condition number  $K_{\Delta\mu/\bar{\mu}}$  for the shear modulus contrast (dashed line) is almost the same as the condition number  $K_{\Delta c_P/\bar{c}_P}$  for the  $p$ -velocity contrast (gray line).

to be useful. Since the accuracy of the estimated contrasts is positively influenced by the amount of a priori data, there is a conflict between accuracy and condition number.

The only way to improve both the accuracy of the estimated contrasts and to increase the condition number, is to use a larger amount of seismic data and more accurate seismic data in the local inversion process. This will be discussed in the next two sections.

### 6.3.1 Multi gather inversion

The amount of seismic data can be improved by a multi gather inversion process. This means that at one lateral position, the reflectivity data of neighboring lateral positions must be used to improve the inversion result. Of course there is a loss of lateral resolution in the inversion result, but the improvement in accuracy and condition number is more important than lateral resolution. A solution with a high lateral resolution, but low accuracy in contrasts and mostly determined by regional a priori information is meaningless.

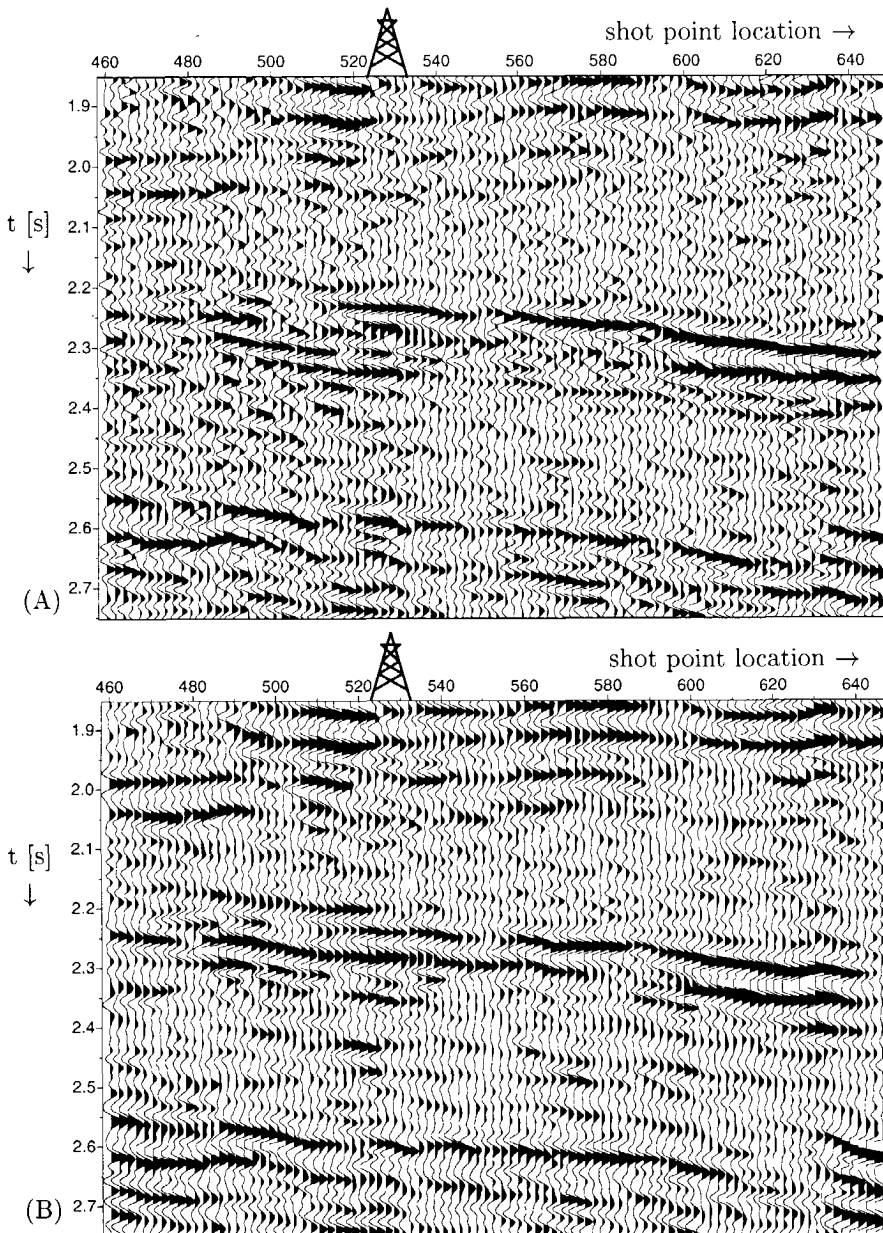


**Fig. 6.10** Field data example of a single gather versus a multi gather inversion. Figure (A) shows the shear modulus contrast section using only one RC gather at each lateral position. In figure (B) at each lateral position 3 RC gathers are averaged in the inversion process.

In figure 6.10 the multi gather inversion result for the estimated shear modulus contrast is compared with the single gather inversion for a 2D marine data set. Although only three RC gathers are averaged in the inversion process, a clear improvement in noise reduction can be seen. The multiple energy around shot point location 500 has been reduced at the top of the reservoir (around 2.25s) and also the estimated standard deviation and condition number have been improved (although not shown here).

Another way to improve the inversion result is averaging several neighboring RC gather into one super-gather. By doing so the signal-to-noise ratio of the RC gather is improved. This gives an improved inversion result, but again also a lower lateral resolution.

### 6.3.2 Residual move-out correction

Analysis of the imaged RC gathers shows that amplitude cross-sections for specified times do not give the expected smooth RC-functions. Due to small errors in the migration (velocity) the aligned events are not perfectly straight (even after removing the  $p$ -dependent scaling as described in chapter 4). The use of straight cross-sections of RC gathers gives then errors in the AVP inversion. In figure 6.12 a RC gather and some amplitude cross-sections are shown. Clearly the cross-sections show a more noisy behaviour than the RC gather.

The data quality of the RC gather can also be improved by a residual move-out correction. The advantage over the multi gather inversion is the fact that there is no lateral averaging. The idea to improve the RC-functions was inspired by work of Herrmann (1997) on modulus maxima lines and on scaling media. This is combined with the idea to use a correlation between a reference trace and the data to get a better alignment as commonly used in statics estimation. This has also been proposed for AVO by a.o. Ursin and Ekren (1995).

Note that the concept is based on the idea that by using a perfect velocity model, all imaged events should be completely horizontally aligned in the RC gather. This is only true for precritical reflection data (after removing the  $p$ -dependent scaling described in chapter 4). Post-critical reflection data will not be horizontally aligned, even if the correct velocity model has been used. For this reason may a thin high velocity layer in a stack of layers distort the alignment of the overall response of the stack of layers, even if the correct averaged velocity  $\bar{c}_P$  was used in the migration. Although the averaged angle of the ray through the stack of layers was smaller than the critical angle ( $\bar{c}_P \times p < 1$ ), within the high velocity layer there might have been a critical reflection due to a very high local velocity  $c_{P,local}$  ( $c_{P,local} \times p \geq 1$ ). Also converted reflections, (internal) multiples and noise may result in a distortion of the horizontal alignment of the primary reflection.

This means that although the correct velocity is used for the migration of the primary reflection, the events in the RC gather do not have to be perfectly horizontally

aligned. Therefore one must be careful not to reinforce the nonlinear events and noise in the data by residual move-out correction.

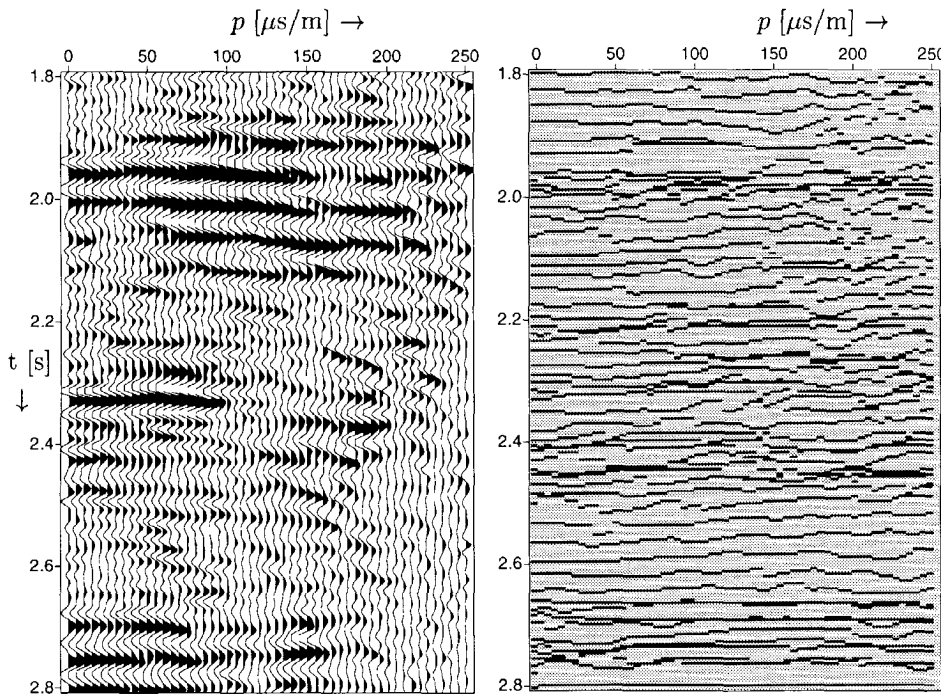


**Fig. 6.11** The RC gather and the corresponding maxima-minima lines.

As already shown by others, the AVP inversion can be made more robust for residual move-out errors, by using a correlation between a reference trace and the data (in a windowed selection around the area of interest) for estimation of a kind of static correction in order to improve the alignment. Instead of shifting the windowed part of the trace with some kind of 'static'-correction, also the straight amplitude cross-section can be replaced by a curved amplitude cross-section following the static shifts. This idea is closely related to following the modulus maxima lines (Herrmann, 1997). The difference is that the modulus maxima lines follow an absolute maximum, while the 'statics' approach follows maxima-minima lines; using a reference trace one tries to follow the same type of trace signature in the data as found in the reference trace. Note that the RC-functions can have zero crossings, which are incorporated in the maxima-minima lines, whereas the modulus maxima lines will not have zero crossings.

First we will concentrate on the position of the maxima-minima lines as function of  $p$  and the amplitudes along these maxima-minima lines. The data in between

these lines will be discussed later. The reference trace will determine the start of the maxima-minima line and the number of maxima-minima lines per gather. A small stack of 3-5 traces around  $p=0$  or the estimated impedance-contrast can be used as reference trace. The minima and maxima are found by examining the first derivatives.

Once the minima and maxima are found on the reference trace, the corresponding minima or maxima on the adjacent traces must be found, in order to construct the maxima-minima line. The time range in which the maxima-minima line lies, is constrained by half the distance to the neighboring extrema on the reference trace. This procedure is repeated for the remaining traces in the RC gather up to the last trace. This gives us the maxima-minima line for one minimum or maximum on the reference trace. By repeating this for all the minima and maxima on the reference trace, a maxima-minima line-gather is built up.

In Figure 6.11 a RC gather is shown and the corresponding gather with the positions of the maxima-minima lines.

In order to display the maxima-minima line-gathers in a seismic way, the (irregular sampled) maxima-minima line are interpolated in time with splines into a regular sampled gather and filtered in the frequency domain in order to get the same frequency content as the original RC gather. This interpolated gather is shown in Figure 6.12(B) together with the same amplitude cross-sections as shown in Figure 6.12(A). Clearly we see the improvement on the estimated RC-functions.

These sections are useful for display and comparison, but amplitude cross-sections in between the original maxima-minima lines should not be used as data for AVP inversion. The AVP inversion should be carried out only on the amplitudes along the maxima-minima lines. After the inversion the estimated contrasts can again be interpolated by splines for display. In the same way the ZLF-process can be redefined. Along the maxima-minima lines the ZLF filter can be applied ( $\mathbf{A}\vec{\lambda} = \vec{d} - \vec{n}$ ). After the ZLF process the filtered data can be interpolated for display use. Note that the amount of data in the inversion process is reduced. Additional computational costs are spent on displays (interpolation).

Figure 6.13 shows the ZLF and residue gathers corresponding to the original RC gather as shown in figure 6.12(A) and the ZLF and residue gathers corresponding to the RC gather after residual move-out correction as shown in figure 6.12(B). Clearly the residue gather after residual move-out correction has less energy, which indicates a better data quality for the inversion process. But one should be careful not to align residual multiple or converted energy, which is clearly present in figure 6.13(B). The difference in the ZLF gathers is less than the residue gathers, but note that the AVP behaviour at 2.0s is different in both ZLF gathers.

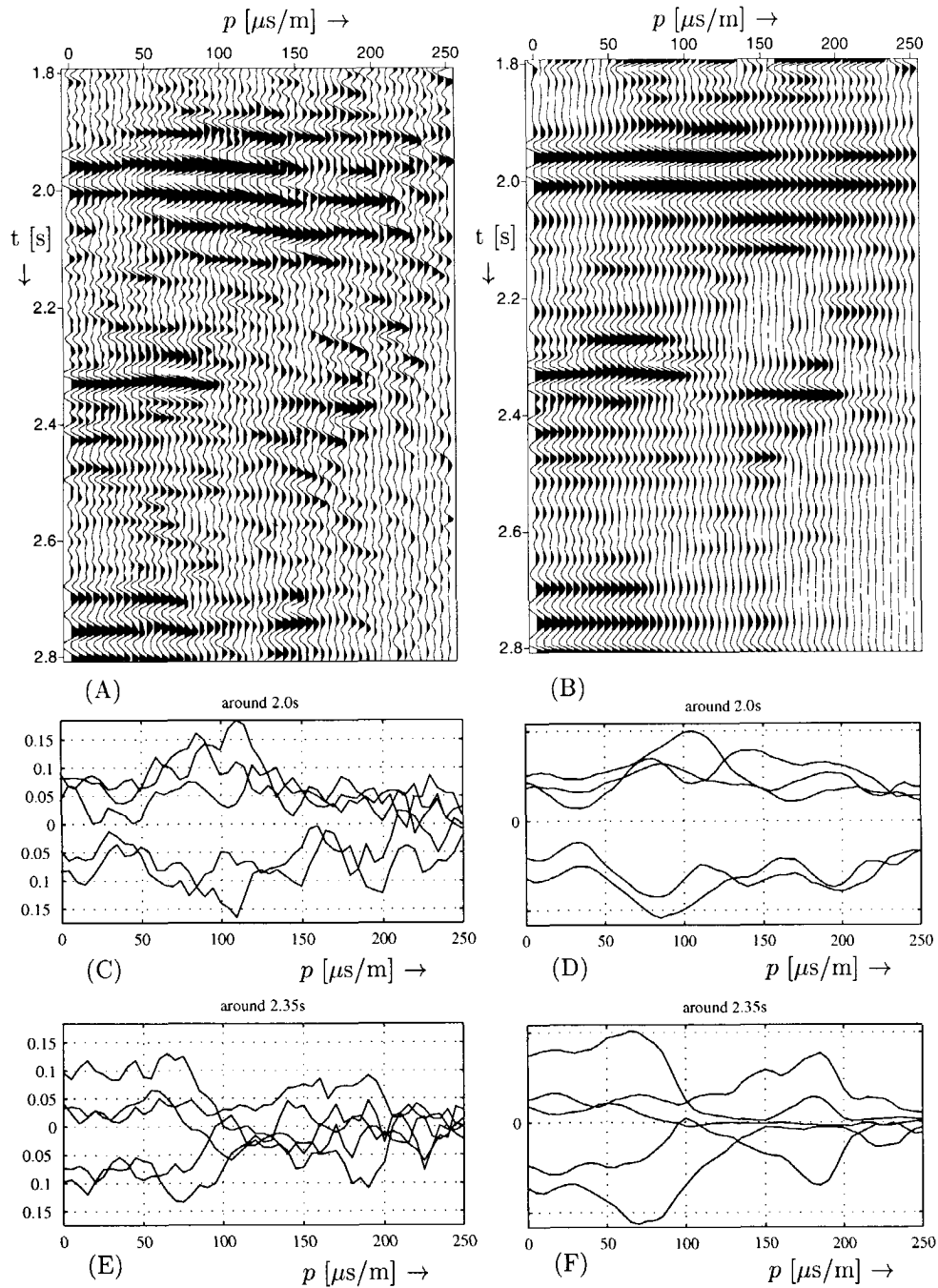


**Fig. 6.12** The  $RC$  gather and some amplitude cross-sections around  $2.0\text{s}$  and around  $2.35\text{s}$ . On the left the original data and on the right the data after residual move-out correction.

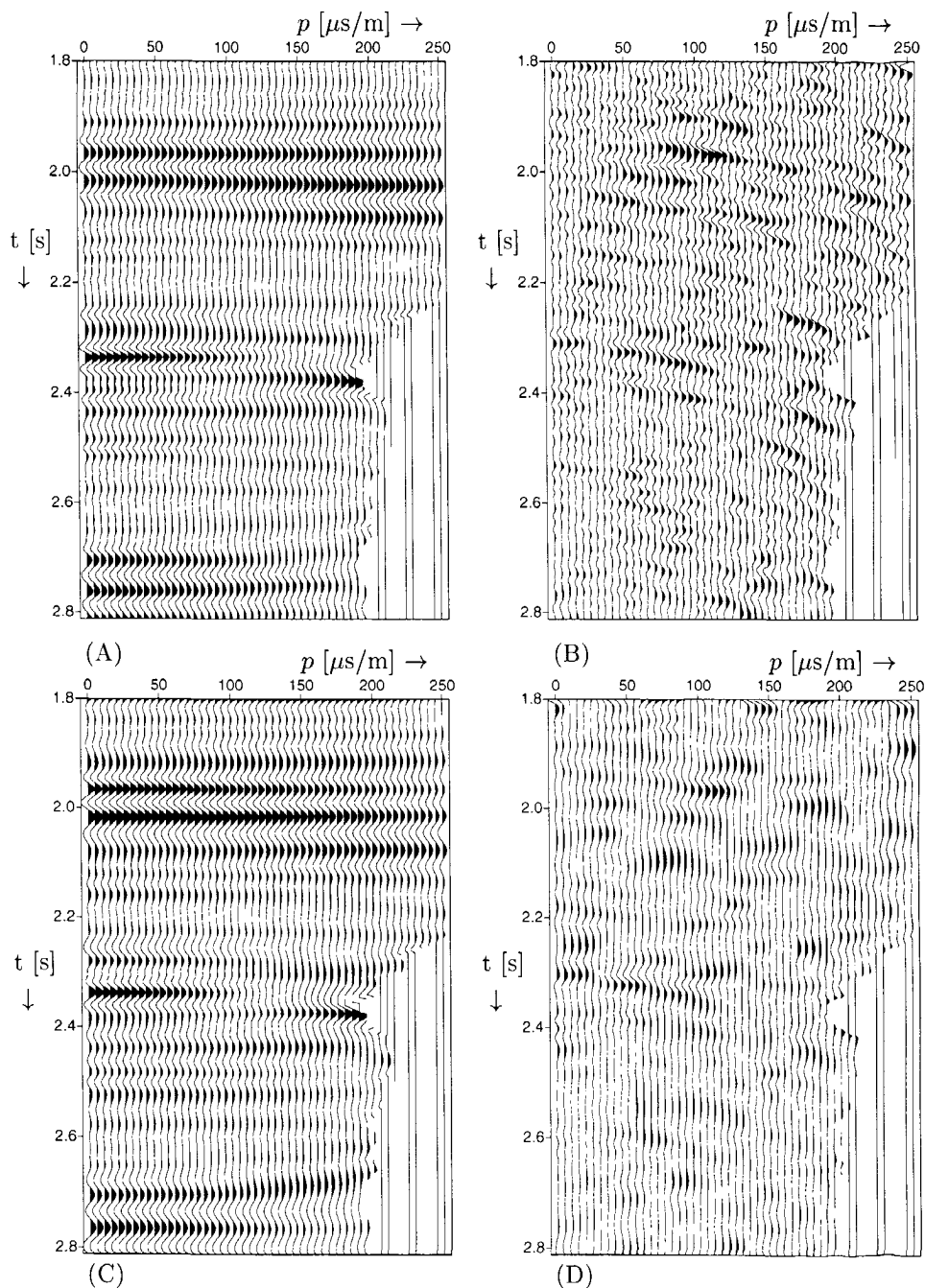


Fig. 6.13 The ZLF (A,C) and residue (B,D) gathers for the original data (A,B) and for the data after residual move-out correction (C,D).



# Chapter 7

## Lithology indicators

*In this chapter the use of AVP for lithology prediction is discussed. First some general relationships between lithotypes and elastic parameters are given. Next background trends between contrast parameters and amplitude cross plots are discussed. Finally indicators are described which distinguish different lithologies on their angle dependent reflectivity.*

### 7.1 Introduction

Normal prestack migration of seismic data results in a structural image of the subsurface, given by an angle-averaged reflectivity section. Using AVP inversion of prestack data, the subsurface can be characterized by contrasts in e.g. acoustic impedance, P-wave velocity and shear modulus. For oil and gas exploration these elastic parameters are used to estimate intrinsic rock and pore parameters like lithotype, porosity and pore fluid content. Generally direct translation of estimated elastic contrasts into rock and pore parameters is not possible, but the elastic contrasts can be used to discriminate between several lithoclasses (e.g. de Bruin, 1992).

The results of the AVP inversion are especially sensitive to the relative change in Poisson's ratio within the subsurface. Koefoed (1955) first pointed out the practical possibilities of using AVO analysis as an indicator of  $c_P/c_S$  variations. Ostrander (1984) showed that gas sand with an abnormally low Poisson's ratio embedded in sediments with a normal Poisson's ratio should result in an increase in reflected P-wave energy with angle of incidence. These 'bright spots' have been observed on conventional seismic data recorded over gas sands. This anomalous amplitude behaviour has been used as a direct hydrocarbon indicator (DHI) in many areas.

### 7.2 Rock properties

The variation of seismic reflection amplitude with offset is dependent on intrinsic rock parameters such as P-wave velocity, S-wave velocity, density, anisotropy and attenuation. An understanding of the interrelationships among these parameters

and rock properties such as lithology, porosity and pore fluid content is needed for the quantitative extraction of rock properties information by AVP analysis. Therefore some elementary rock physics concepts and empirical trend curves for common sedimentary lithologies between of  $c_P$  versus  $c_S$  and  $c_P$  versus  $\rho$  will be shown. Influence of temperature, pressure and diagenesis is beyond the scope of this thesis. For further information on these subjects the reader is referred to Castagna et al. (1993).

### 7.2.1 Velocity and elastic moduli

P- and S-wave velocities for an isotropic, homogeneous elastic material are given by

$$c_P = \sqrt{\frac{k + \frac{4}{3}\mu}{\rho}} \quad (7.1)$$

and

$$c_S = \sqrt{\frac{\mu}{\rho}}. \quad (7.2)$$

where

$$k = \text{rock bulk modulus} = \text{rock incompressibility} \quad (7.3)$$

$$\mu = \text{rock shear modulus} = \text{rock rigidity}. \quad (7.4)$$

The shear modulus is the ratio of shear stress to shear strain and similarly, the bulk modulus is the ratio of volumetric stress to volumetric strain. Equations 7.1 and 7.2 provide the fundamental link between seismic velocities and rock properties. For example, it has been demonstrated many times that the bulk modulus may be strongly dependent on the pore fluid bulk modulus while the rock shear modulus may be unaffected by the fluids (Domenico, 1976). Hence, when a compressible free gas replaces liquids in the pore space, the rock P-wave velocity will decrease significantly, whereas the rock S-wave velocity will be slightly increased due to the decreasing bulk rock density. Consequently, the ratio of P-to-S-wave velocity  $c_P/c_S$  is expected to be an excellent indicator of free gas in the pore space. This is the basis for direct hydrocarbon detection using AVP.

### 7.2.2 $c_P - c_S$ relationships for single lithologies

Because rocks are aggregates of mineral grains, we expect the velocity of a highly lithified, low porosity rock to be strongly dependent on the velocities of the grains. However, we expect the velocity of an unconsolidated rock to be only weakly dependent on the velocities of the grains due to the large pore volume and the influence of pore shape. The mineral velocity is generally referred to as the 'matrix' velocity

in log analysis and the 'grain' or 'solid' velocity in the rock physics literature. Because most sedimentary rock-forming minerals (such as quartz, calcite and clays) are not isotropic, mineral velocity is taken to be that of a zero-porosity polycrystalline aggregate of randomly oriented mineral grains.

When  $c_P$  and  $c_S$  are cross plotted, the common sedimentary rocks show an approximate linear relation for different lithologies. One end of the line is constituted by the mineral velocity for relatively pure (mono-mineralic) water-saturated rocks. The distribution of points represents varying porosities and effective pressures.

Using data reported in the compilations in Castagna et al. (1985) and Thomsen (1986), the  $c_P$ - $c_S$  relationships (in km/s) are for sandstone

$$c_S = 0.8042 c_P - 0.8559 \quad (7.5)$$

and for shale

$$c_S = 0.7700 c_P - 0.8674. \quad (7.6)$$

For a more exhaustive discussion and references on this subject the reader is referred to Castagna et al. (1993).

In this chapter another empirical relationship is proposed, between the square root of the shear modulus and the P-wave velocity

$$c_P = a\sqrt{\mu} + b. \quad (7.7)$$

In order to relate this relationship with the previous empirical relations, equations 7.2 and 7.5 and the well known Gardner relation (Gardner et al., 1974) between the P-wave velocity and the density

$$\rho = 1.741 c_P^{0.25}, \quad (7.8)$$

are combined into the relation

$$\sqrt{\mu} = a' c_P^{1.125} + b' c_P^{0.125}. \quad (7.9)$$

This relationship is very close to the empirical relation given in equation 7.7.

### 7.2.3 $c_P$ - $c_S$ relationships for mixed lithologies

In the majority of situations in hydrocarbon exploration, the lithologies are mixed. Hence, a method is required for the averaging of the properties or relationships developed for pure rock types. Examples of averaging schemes include e.g. Voigt-Reuss and Hashin-Shtrikman bounds (Watt et al., 1976).

A time-averaging approach is commonly taken in well log analysis by modifying the Wyllie equation (Wyllie et al., 1956) to include the effects of composition. The equation can be written as

$$1/c_P = X_{clay}/c_{P,clay} + X_{sand}/c_{P,sand} + \phi/c_{P,fluid}, \quad (7.10)$$

where  $X_{clay}$  equals the volume fraction of clay and  $X_{sand}$  equals the volume fraction of sand.

An alternative approach is composite media modeling. A variety of theoretical models have been developed to predict the velocities of porous media. In broad terms, the models developed for isotropic rocks fall into two categories:

1. pore geometry specific
2. global.

Well known examples of geometry specific models include Kuster and Töksöz (1974) and Xu and White (1995). Unfortunately, existing models require accurate and detailed information about the rock fabric before any calculations can be made. These models require the assumption of dilute distributions of idealized pores and have not been shown to be generally applicable to sedimentary rocks. Mavko and Nur (1977) demonstrated that the results can be strongly dependent on the assumed pore shape. Application of these models using the observed pore characteristics has proved difficult at best. Consequently, in many cases it is necessary to resort to empirical equations.

More applicable results have been obtained using the global or bulk properties of the rocks and fluids without referring to any specific pore geometry. Gassmann (1951) and Biot (1956) produced fundamental and yet relatively simple relationships where the most significant unknown parameters are the bulk and shear moduli of the rock framework (skeleton). Gassmann's equations are valid only at low (seismic) frequencies. The model is given by

$$k_w = k_d + \frac{(1-b)^2}{[(1-\phi-b)/k_{ma} + \phi/k_f]} \quad (7.11)$$

and

$$\mu_w = \mu_d, \quad (7.12)$$

where

$k_w$  = bulk modulus of the fluid filled rock,

$k_d$  = bulk modulus of frame or dry rock skeleton,

$k_{ma}$  = bulk modulus of matrix (individual grains),

$k_f$  = bulk modulus of pore fluid,

$b = k_d/k_{ma}$ ,

$\mu_w$  = shear modulus of the fluid filled rock, and

$\mu_d$  = shear modulus of rock skeleton

$\phi$  = porosity.

Using the Poisson's ratio of the bulk

$$\sigma_d = \frac{3k_d - 2\mu_d}{2(3k_d + \mu_d)}, \quad (7.13)$$

the seismic P-wave and S-wave velocity are then given by

$$c_P = \sqrt{\frac{k_{ma}}{\rho} \left[ 3b \left( \frac{1 - \sigma_d}{1 + \sigma_d} \right) + \frac{(1 - b)^2}{1 - b + \phi(k_{ma}/k_f - 1)} \right]} \quad (7.14)$$

and

$$c_S = \sqrt{\frac{k_{ma}}{\rho} \frac{3}{2} b \left( \frac{1 - 2\sigma_d}{1 + \sigma_d} \right)}. \quad (7.15)$$

Following Crans and Berkhou (1980) the Poisson's ratio  $\sigma_d$  can be approximated by a linear relation with depth

$$\sigma_d = \sigma_0 - \sigma_{grad} \times (z - z_0) \quad (7.16)$$

with  $\sigma_0$  and  $\sigma_{grad}$  being the intercept value at reference depth  $z_0$  and the gradient respectively. For a more exhaustive review on these models the reader is referred to Bakker et al. (1995).

The Gassmann equation is extensively used for fluid substitution in AVP modeling. The bulk parameters can be kept constant for a specific lithotype, whereas the fluid fill and porosity are changed. For examples the reader is referred to de Bruin (1992, chap. 5).

### 7.3 Indicators

In the previous section empirical linear relations between  $c_P$  and  $c_S$  and between  $c_P$  and  $\sqrt{\mu}$  were shown for certain lithotypes. These relations are used in most lithology indicators. For anomaly indicators the general regional trend is used to compute the deviations from these relations.

#### 7.3.1 Contrast deviation factor

The well known fluid factor of Smith and Gidlow (1987) is based on the linear empirical relation between P-wave and S-wave velocities

$$c_P = a c_S + \text{constant} \quad (7.17)$$

( $a$  is a constant, see equation 7.5 and 7.6).

Differentiating this relation to the depth coordinate  $z$  gives

$$\frac{\partial c_P}{\partial z} = a \frac{\partial c_S}{\partial z}. \quad (7.18)$$

Rewriting this relation to obtain a relation in relative contrasts gives

$$\frac{\Delta c_P}{\bar{c}_P} = a \frac{\bar{c}_S}{\bar{c}_P} \frac{\Delta c_S}{\bar{c}_S}. \quad (7.19)$$

Deviations from the linear relation in equation 7.17 are given by the fluid factor

$$\Delta F = \frac{\Delta c_P}{\bar{c}_P} - a \frac{\bar{c}_S}{\bar{c}_P} \frac{\Delta c_S}{\bar{c}_S}. \quad (7.20)$$

In case the contrasts in P- and S-wave velocity and the averaged ratio of the S- and P-wave velocities are known, the fluid factor can be computed. This factor will show the contrasts between lithologies, which deviate from the empirical relation given in equation 7.17.

In this thesis a different indicator is proposed, related to contrasts which are estimated in the inversion of PP reflection data (see chapter 5). The empirical relation given in equation 7.7 between the square root of the shear modulus and the P-wave velocity is used instead of a relation between the P- and S-wave velocity. Similar to equation 7.19 this relation becomes in relative contrasts

$$\frac{\Delta c_P}{\bar{c}_P} = \frac{a\sqrt{\bar{\mu}}}{2} \frac{\bar{c}_S}{\bar{c}_P} \frac{\Delta \mu}{\bar{\mu}}. \quad (7.21)$$

Now the new contrast deviation factor  $\Delta D$  is defined by

$$\Delta D = \frac{\Delta c_P}{\bar{c}_P} - \frac{a\sqrt{\bar{\mu}}}{2} \frac{\bar{c}_S}{\bar{c}_P} \frac{\Delta \mu}{\bar{\mu}}. \quad (7.22)$$

$\Delta D$  shows differences from the empirical linear relation between P-wave velocity and shear modulus given in equation 7.21. Note that interfaces satisfying equation (7.7) will show a contrast deviation factor  $\Delta D$  equal to zero.

An example is given in figure 7.1, where a cross plot of  $c_P$  versus  $\sqrt{\mu}$  (see eq. 7.7) using the well log data of well B of the Mobil AVO data set (van Wijngaarden et al., 1995) is shown. From this cross plot we can derive a linear relation between  $c_P$  and  $\sqrt{\mu}$

$$c_P = a\sqrt{\mu} + b \quad (7.23)$$

where  $a$  [ $\text{kg}^{-0.5}$ ] and  $b$  [m/s] are constants.

Figure (7.2) shows a cross plot of  $c_P$  versus  $\sqrt{\mu}$  of well log data for well A of the Mobil AVO data set. Using the well interpretation, we were able to differentiate the hydrocarbon bearing sandstones from their surrounding shales and sands. In the cross plot the surrounding shales and wet sandstones and most sandstones containing oil are scattered fairly close to the dashed line and can hardly be separated. The

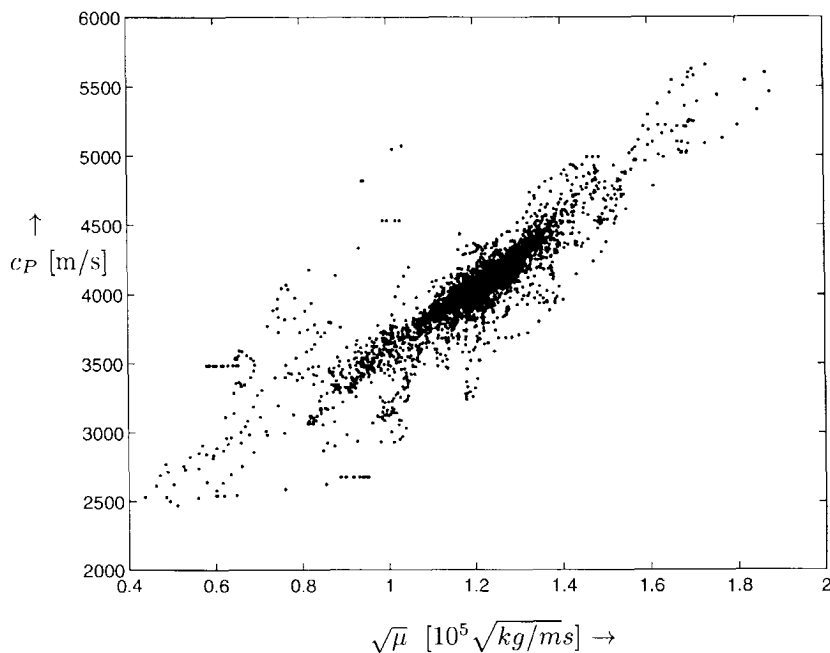
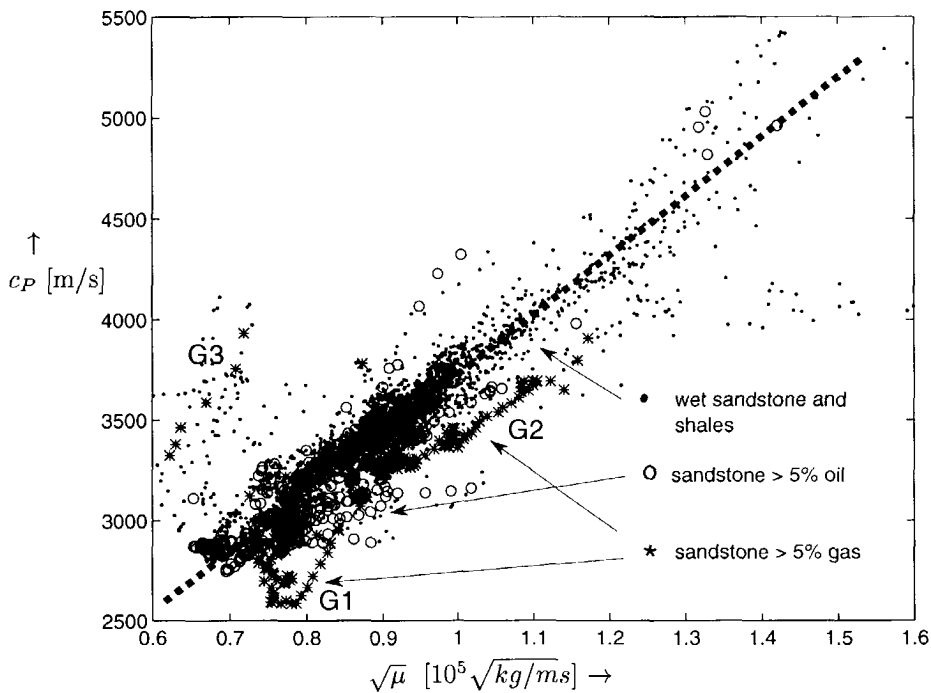


Fig. 7.1 Cross plot of  $c_P$  and  $\sqrt{\mu}$  at well B of the Mobil AVO data set.

gas sands near G1, G2 and G3 show a larger deviation from the background trend indicated by the dashed line. Using this line as an empirical relation as in equation (7.23), the gas layers at G1, G2 and G3 should be resolved by the contrast deviation factor from equation (7.22).

Figure (7.3) shows the contrast deviation factor  $\Delta D$  for well A using the well log densities and velocities. Also the amount of gas and oil, given by the well log, as function of depth are indicated with 'o' and '+' respectively. The gas sands around 2000 m correspond with the gas sands at 'G1' in Figure (7.2) and the gas sands around 2650 m correspond to the gas sands at 'G2'. Although the shallower gas sands at G1 are as well separated from the dashed line in Figure (7.2) as the deeper gas sands at G2, the gas sands at G2 are clearly indicated by the contrast deviation factor, and the gas sands at G1 less. This is explained by the fact that we use down scaled relative contrasts instead of absolute values of  $c_P$  and  $\mu$  in the contrast deviation factor. The influence of single deviating data points in the well log measurement is reduced by down scaling, i.e. averaging over a certain depth range.



**Fig. 7.2** Cross plot of  $c_P$  versus  $\sqrt{\mu}$  at well A of the Mobil AVO data set between 1800 - 3200 m, showing different lithologies.

### 7.3.2 Anomaly indicator

In equation (7.22) we need to know the factor  $a\sqrt{\rho}(\bar{c}_S/\bar{c}_P)$  at every point in the subsurface in order to compute deviations from equation (7.23). At or near a well we can use the well log data to compute/estimate this factor. Further away from a well, or if there is no well log data available, we have to estimate this factor. This problem can be overcome by the following procedure.

In order to find anomalies in relation 7.22 between the P-wave velocity and shear modulus contrast, the two output sections  $\Delta c_P/\bar{c}_P$  and  $\Delta \mu/\bar{\mu}$  of the linear inversion process are used. A ratio-section  $\Gamma(x, t)$  between them is estimated by least squares inversion and averaging over a small time range

$$\frac{\Delta c_P}{\bar{c}_P}(x, t) = \Gamma(x, t) \frac{\Delta \mu}{\bar{\mu}}(x, t). \quad (7.24)$$

Next the ratio is averaged in the lateral direction in order to get the general trend  $\bar{\Gamma}(x, t)$ . Now this averaged ratio is used to compute deviations from the trend between the relative P-wave velocity and  $\mu$  contrast.

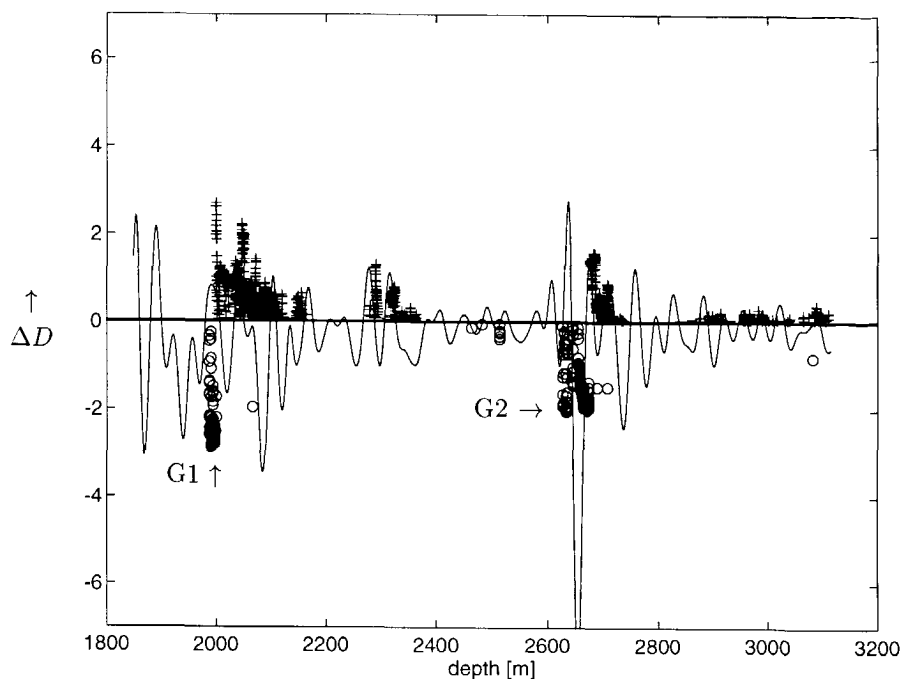


**Fig. 7.3** Contrast deviation factor  $\Delta D$  at well A between 1800-3200 m, and an indication for oil '+' and gas '0'

The anomaly indicator (section) is defined by

$$\bar{D}(x, t) = \frac{\Delta c_P}{\bar{c}_P}(x, t) - \bar{\Gamma}(x, t) \frac{\Delta \mu}{\bar{\mu}}(x, t) \quad (7.25)$$

In chapter 8 this indicator will be further discussed and examples of are shown for a field data set.



## Chapter 8

# Case study using a 2D marine data set from offshore Norway

*In this chapter the results of AVP imaging and inversion are demonstrated on a field data set. First a geological description of the area of the 2D marine data set is given. Next the results of the AVP inversion are given in the form of contrast sections. Furthermore a residue analysis is given and the influence of background velocity is examined. Finally the synthetic modeled seismic traces are compared with the field data.*

### **8.1 The SAGA 2D marine data set**

In this case study a 2D seismic data set from offshore Norway (Haltenbanken terrace, courtesy SAGA) is used. The line crosses 2 wells. For these wells P-velocity and density logs are available. A part of the migration is shown in figure 8.1. The wells are located at shot point location 525 (well A) and at shot point location 707 (well B). The main target is the Middle Jurassic sandstone between 2.2 and 2.4s two-way time. In the previous chapters especially the area around sp 707 (well B) has been studied.

#### **8.1.1 Geological description of the reservoir**

The field must be classified as a structural trap. It is formed by a tilted horst which is cut by cross-faults. These faults are responsible for the delineation of three compartments. The development of the horst was initiated by the Middle-Late Jurassic tectonic events. The structure was further developed during Cretaceous times through rapid differential subsidence. A Cretaceous argillaceous sequence also forms the cap-rock for the field. In well A a gas-oil contact was found at 2488m followed by a 11.5m oil zone, resulting in an oil-water contact at 2499.5m below sea level. In well B only a gas-down-to level (GDT) was identified.

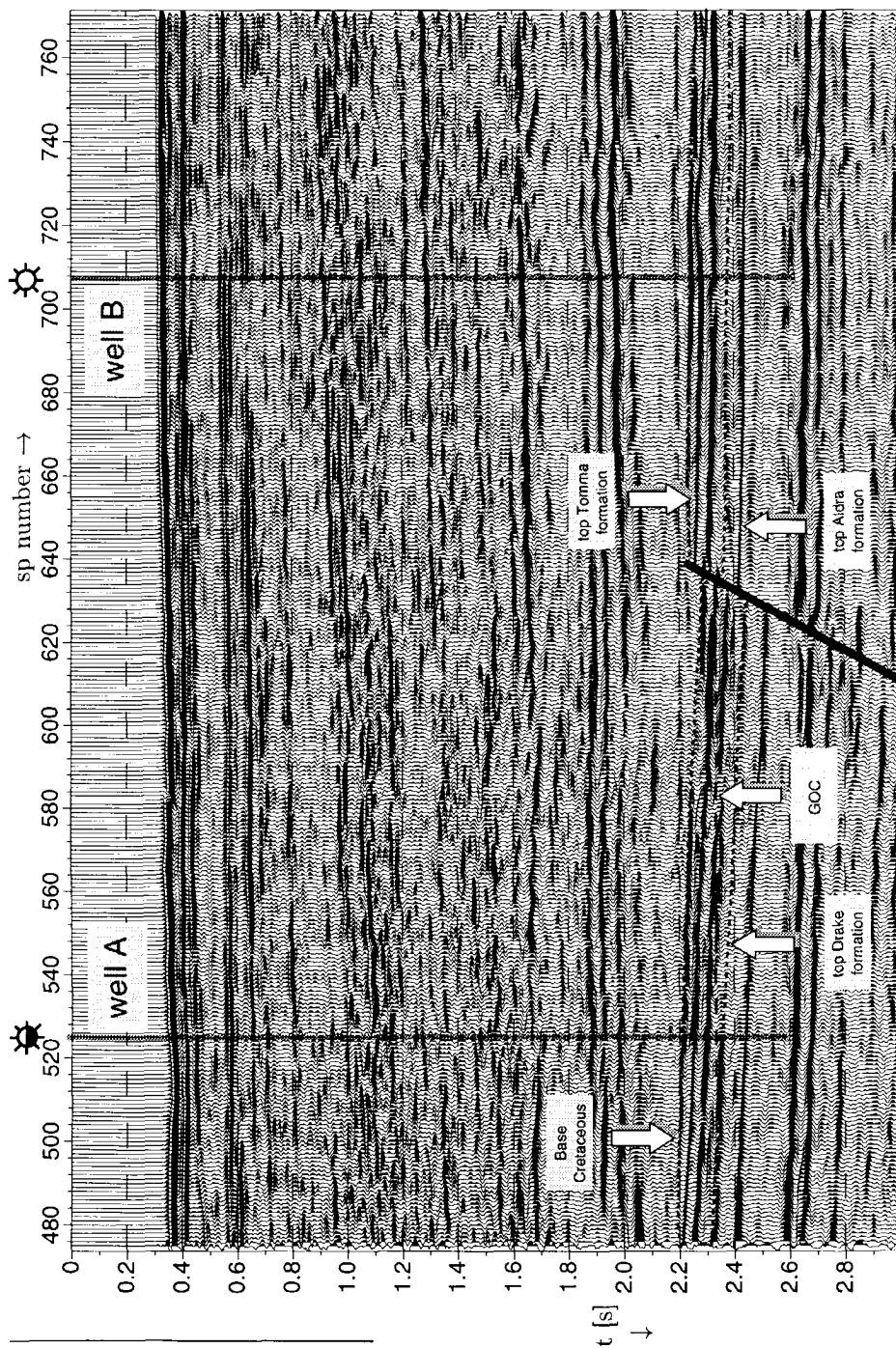
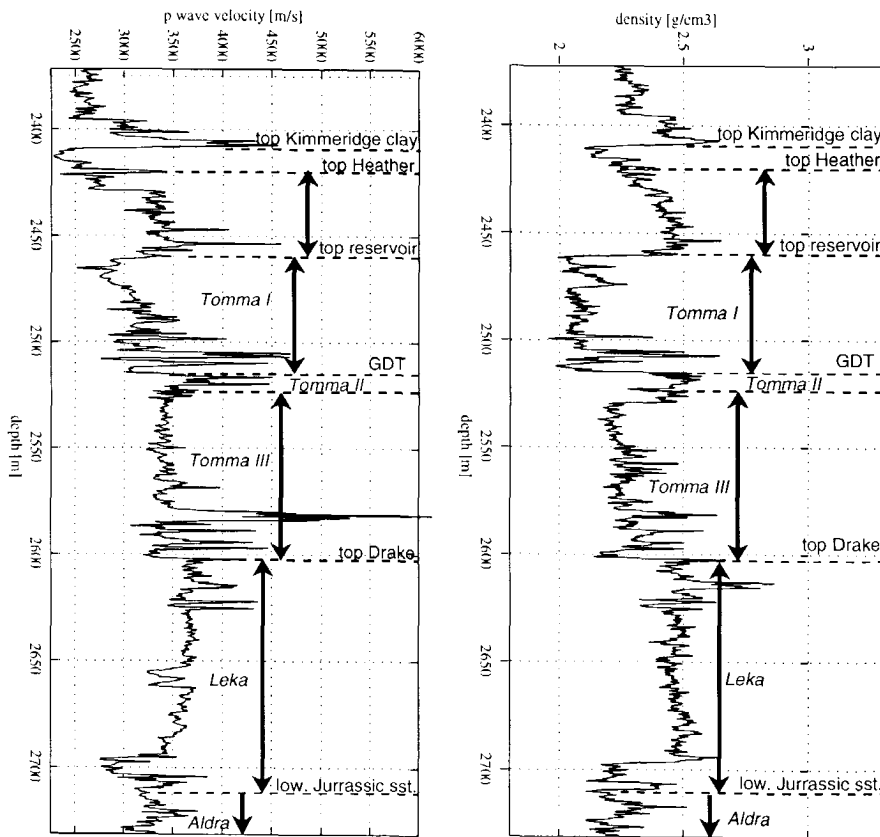


Fig. 8.1 The prestack migration of the 2D dataset, with interpretation and well locations.

The reservoir in the field is represented by sandstone sequences of early and middle Jurassic age. The distribution of hydrocarbons in these two units is a function of the structural development and subsequent erosion of the Upper Jurassic strata. The Lower Jurassic sequence, the Aldra formation, contains the main hydrocarbon reserves in the northern segment (which is not included in this chapter) while the Middle Jurassic Tomma formation constitutes the reservoir in the rest of the field. The Jurassic units show only small thickness variations along the strike of the field. The Aldra formation has been found to be 191m and 183m in the wells A and B in figure 8.1. The Tomma formation has thicknesses of 124m and 142m in the wells A and B.



**Fig. 8.2** The measured sonic log and density log as function of depth around the reservoir (well B) and the indication of the main formations.

Both reservoir formations are products of transgressive and regressive cycles. The Lower Jurassic transgression introduced marginal to shallow marine conditions. The Aldra formation is thus represented by coastal lagoonal deposits in the lower part,

changing into bar-type deposits upwards in the sequence. During the Late Toarcian times a regressive phase developed, changing the environment into a tidally influenced coast-line. This system is represented by the lower part of the Tomma formation. During deposition of the upper part of the Tomma formation, the marine influence increased, producing upper-lower shore face deposits. These fluctuations during Middle Jurassic times allow a subdivision of the Tomma formation into three units. These units can be identified over large parts of the Haltenbank area. The reservoir units have very good reservoir properties. Porosity values for the Tomma formation are in the range 26-29%. Permeabilities range up to several darcies. The properties for the Aldra formation are slightly poorer, with porosities ranging from 22 to 25% and permeabilities in the range 10-1500mD.

The sonic and density logs in depth around the reservoir are shown in Figure 8.2, with the most important geological units indicated. Note that the Middle Jurassic Leka formation is also known as the Drake formation. For further geological information and interpretation see Ekern (1987).

### 8.1.2 General processing sequence

The raw shot records of the data set have been preprocessed by the following processing sequence

- mute for direct wave
- high cut filter
- insert missing near offsets
- $t^{0.5}$  gain (3D to 2D correction)
- deconvolution for wavelet tail of common offsets
- surface-related multiple elimination (SRME), combined with Radon based multiple elimination
- deconvolution with wavelet estimated in SRME
- exponential gain function in the time direction  $e^t$  for transmission correction.

The preprocessing is followed by the imaging processing sequence

- bifocal imaging RC gathers for PP reflection data
- predictive deconvolution of RC gathers (operator length 80ms, prediction lag 20ms)
- bandpass filtering in  $p - \omega$  domain for constant spatial bandwidth (4-8-55-70Hz).

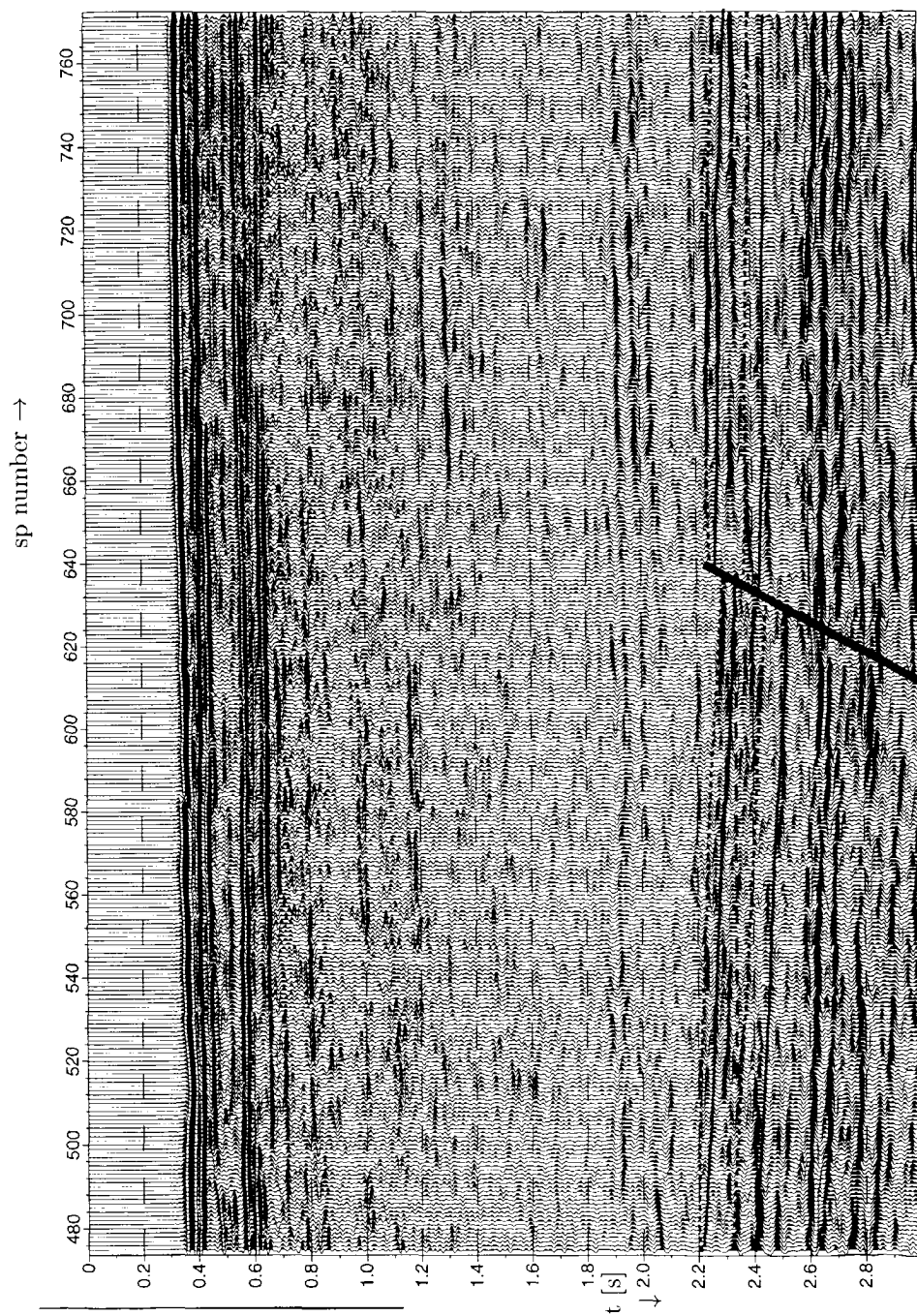
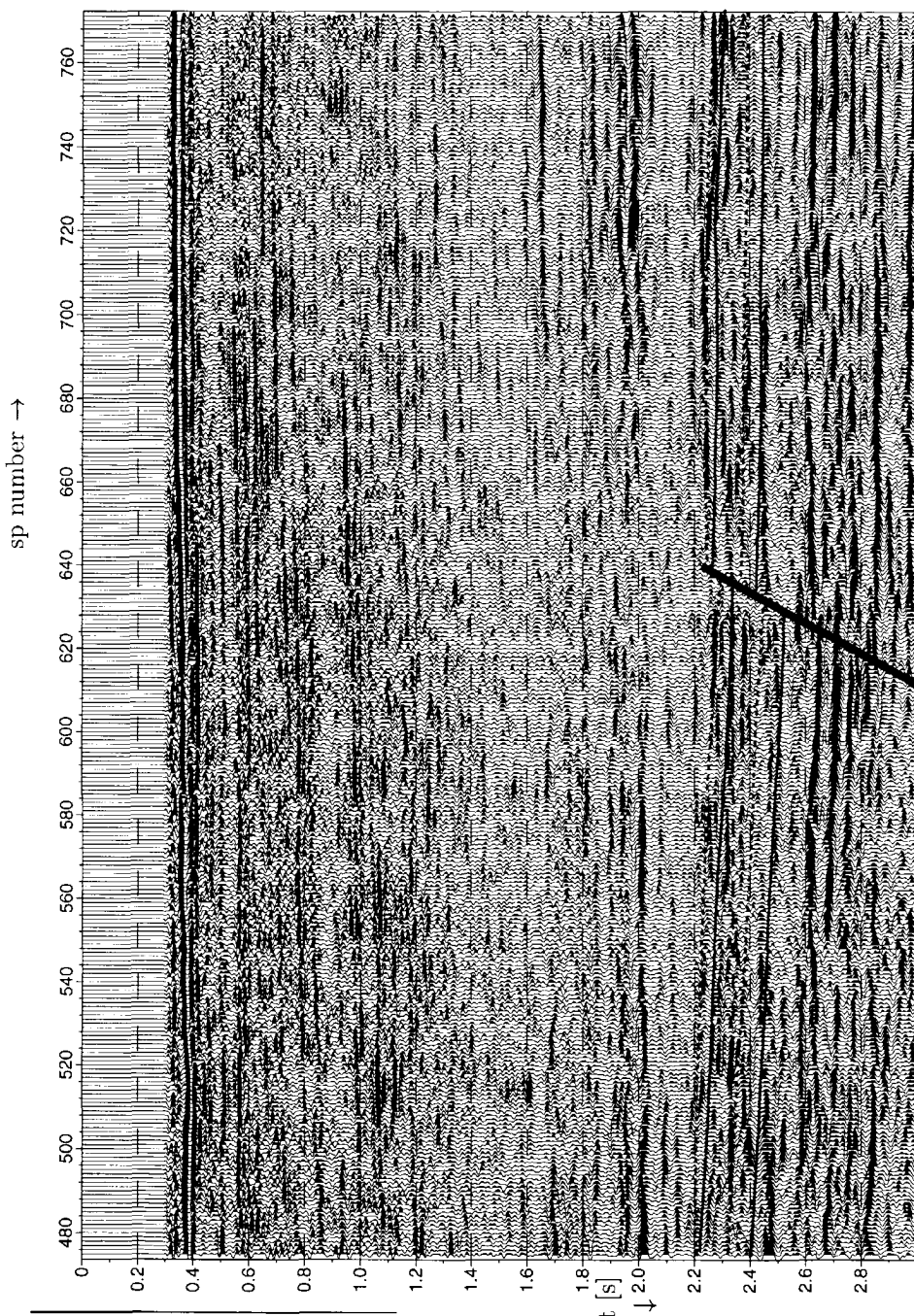


Fig. 8.3 The estimated acoustic impedance contrast section  $\Delta Z/\bar{Z}$  for the 2D marine data set.



**Fig. 8.4** The estimated P-wave velocity contrast section  $\Delta c_P / \bar{c}_P$  for the 2D marine data set.

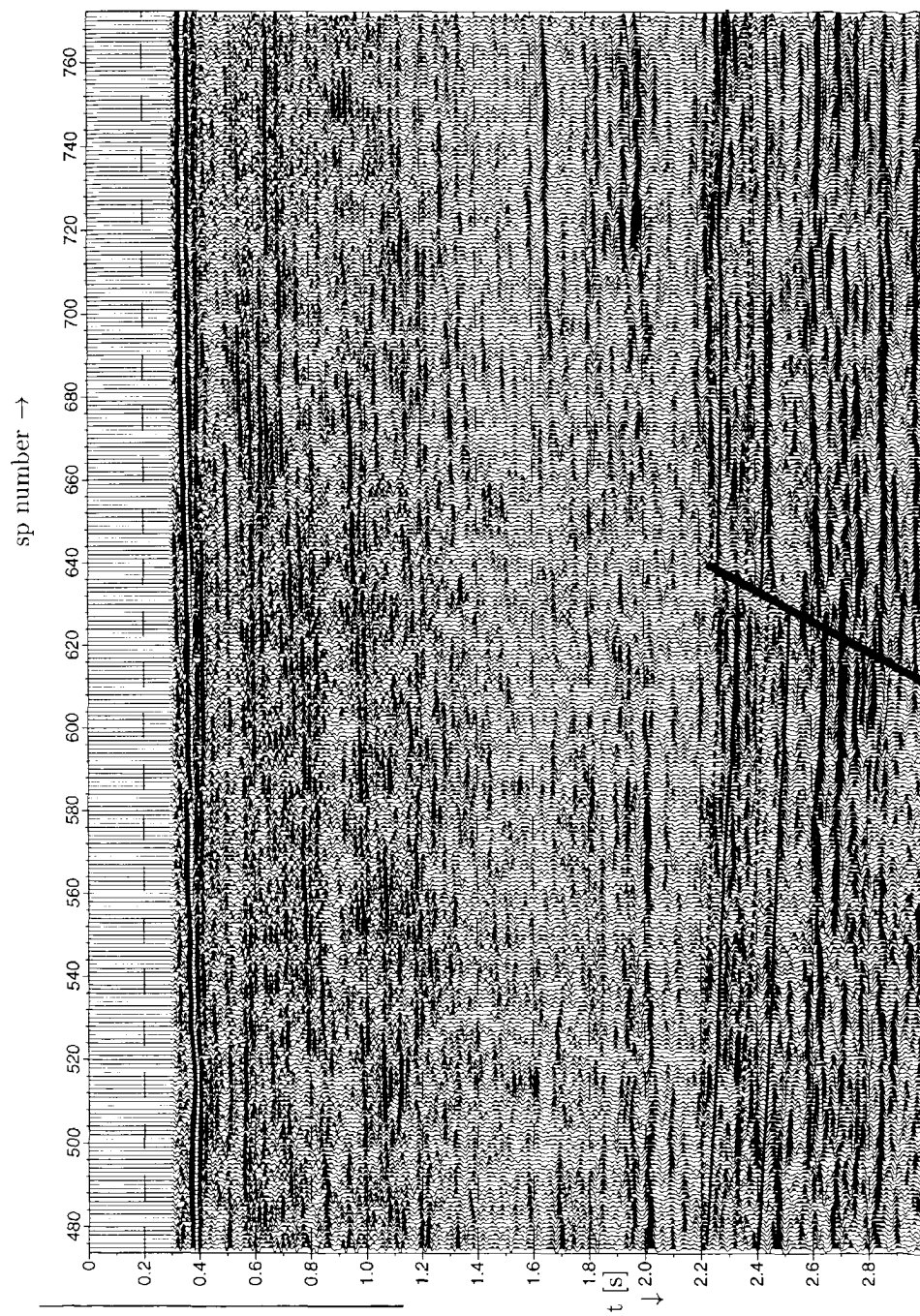


Fig. 8.5 The estimated shear modulus contrast section  $\Delta\mu/\bar{\mu}$  for the 2D marine data set.

### 8.1.3 Estimated contrast sections

The CFP bifocal migration (see chapter 2) has been used to image the PP reflectivity in the RC gathers. The three parameter linear inversion (see section 5.2 equation 5.5) of the PP reflection data resulted in three contrast sections. A maximum  $p$ -value of  $300\mu\text{s}/\text{m}$  has been used together with a mute at 35 degrees.

The contrast section for the estimated acoustic impedance is shown in figure 8.3. The contrast section for the estimated P-wave velocity contrast is shown in figure 8.4 and the contrast section for the estimated shear modulus is shown in figure 8.5. The results are displayed together with the interpretation used in figure 8.1. The contrast sections show a larger lateral variation in amplitudes compared to the migration in figure 8.1. The sections also look a little bit noisy, which will be improved in the next section.

### 8.1.4 Multi-gather inversion

In order to improve the accuracy of the inversion (see section 6.3.1), a multi-gather inversion has been applied to the RC gathers. In the inversion three RC gathers are inverted simultaneously. Again three parameters were used in the parameterization of the PP reflection function and a maximum  $p$ -value of  $300\mu\text{s}/\text{m}$  was used together with a mute at 35 degrees.

The contrast section for the estimated acoustic impedance is shown in figure 8.6. The contrast section for the estimated P-wave velocity is shown in figure 8.7 and the contrast section for the estimated shear modulus is shown in figure 8.8. The resulting contrasts sections are clearly less noisy than the sections shown in figures 8.3 - 8.5. Although the lateral resolution decreased compared to the single-gather inversion, there is still less continuity in the events if the results are compared with the full migration (stacked RC gathers). This will be discussed in the next section.

### 8.1.5 Residue analysis

The ZLF filter process (see chapter 6) has been applied to the RC gathers. The results for the *global* analysis are shown in this section. Figure 8.9 shows the ZLF filtered section for a constant angle ( $\text{asin}(p \times \bar{c}_P)$ ) of  $30^\circ$ . The ZLF filtered section for normal incidence is of course the acoustic impedance section shown in figure 8.3. Note that if the large angle section is more continuous than the normal incidence section. This means that the continuity in the (normal) prestack migration (approximately equal to the stacked RC gathers) is mainly determined by the large angles or far offsets. Therefore the events in the  $30^\circ$  angle section match the overlaying interpretation in figure 8.9 perfectly. Especially the Gas-Oil-Contact is clearly visible.

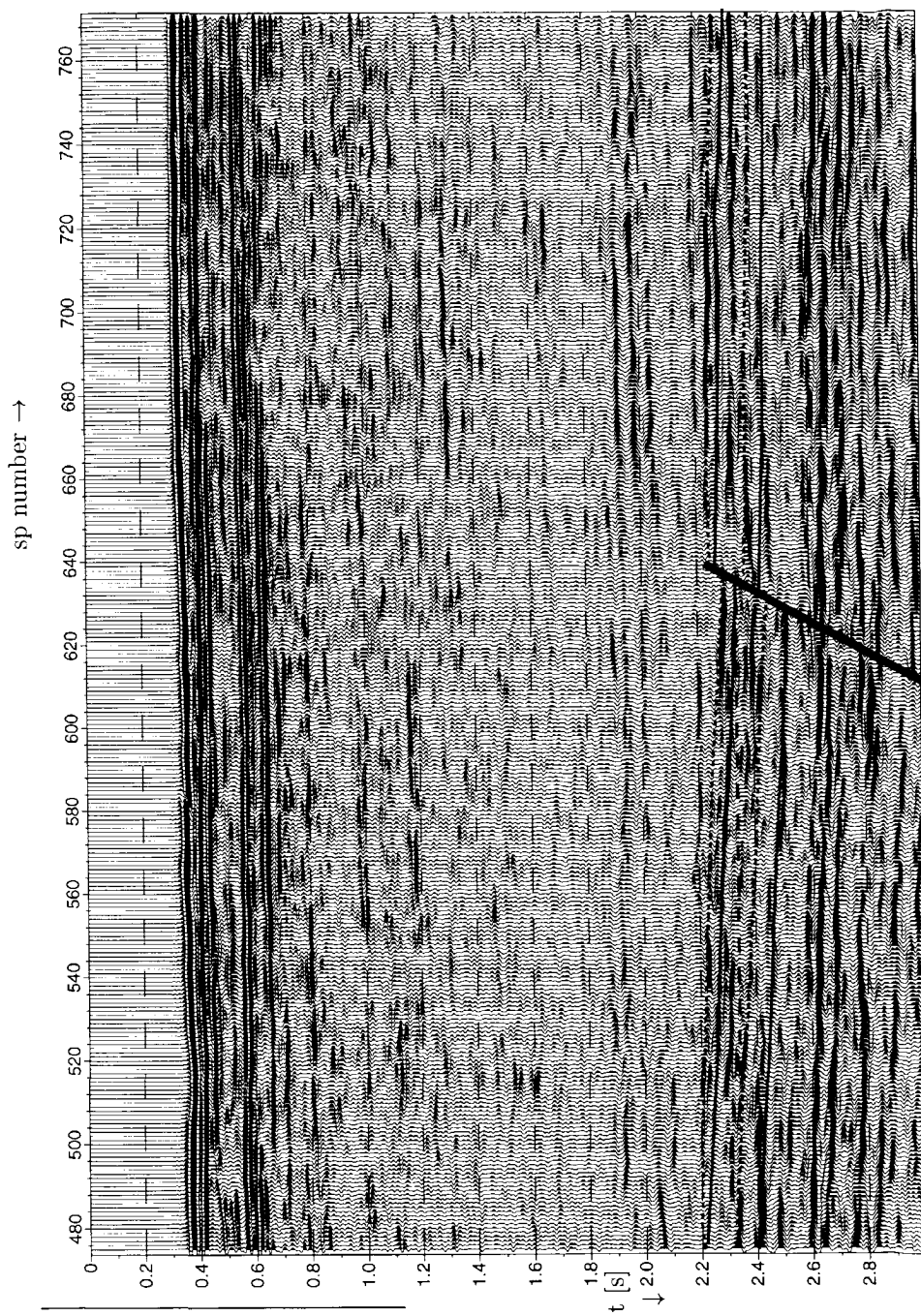
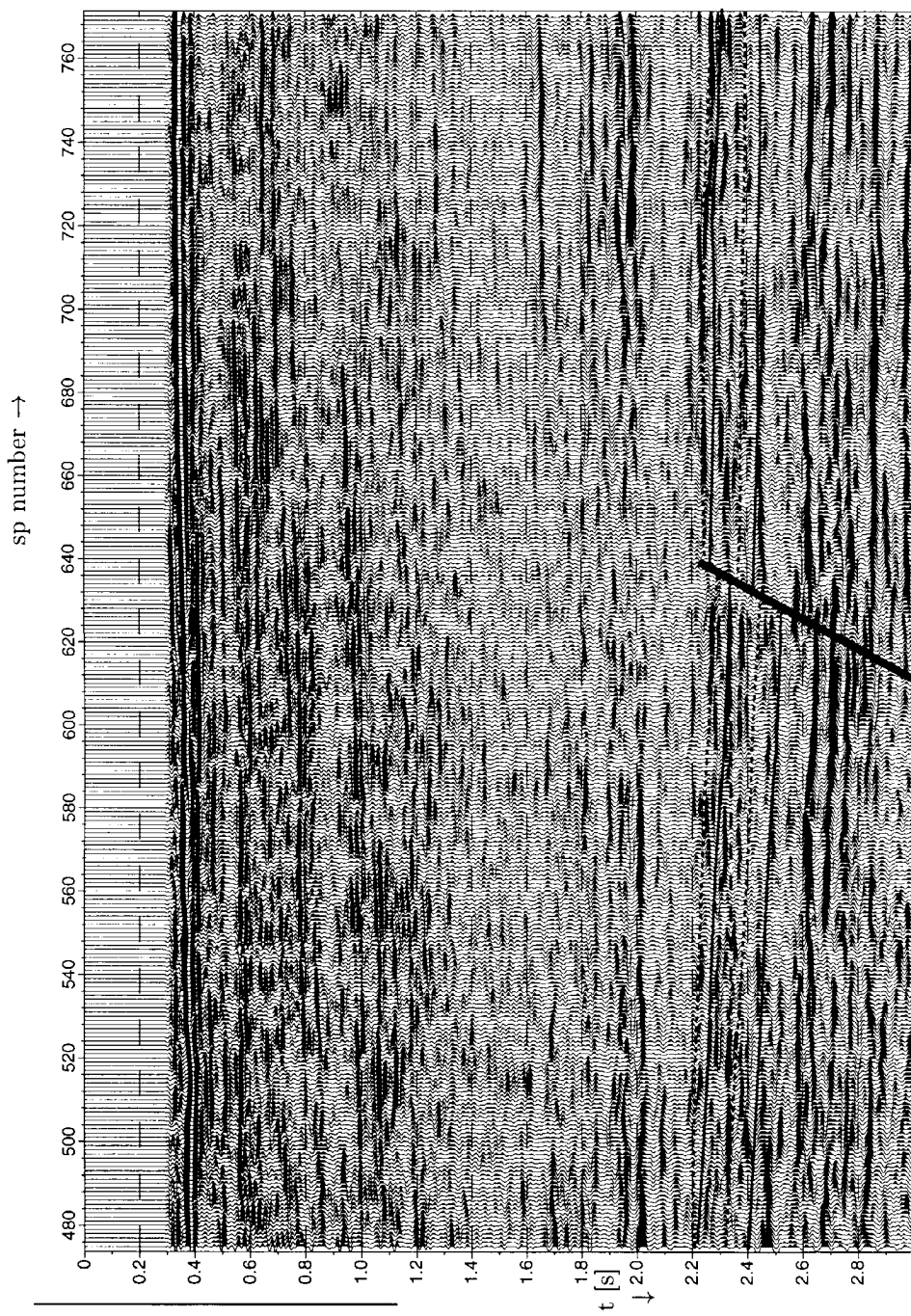


Fig. 8.6 The estimated acoustic impedance contrast section  $\Delta Z/\bar{Z}$  for the 2D marine data set using a multi-gather input.



**Fig. 8.7** The estimated P-wave velocity contrast section  $\Delta c_P / \bar{c}_P$  for the 2D marine data set using a multi-gather input.

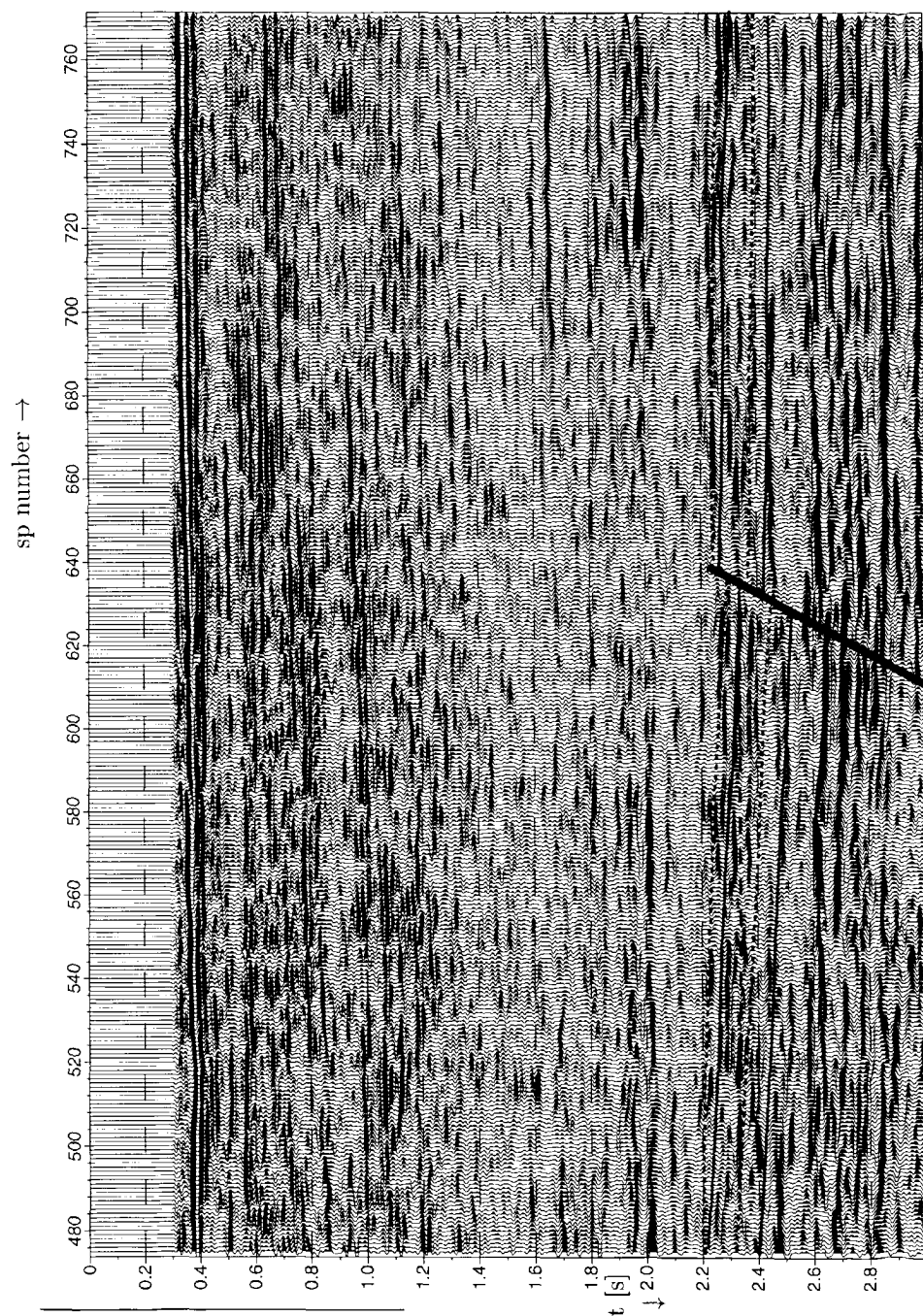


Fig. 8.8 The estimated shear modulus contrast section  $\Delta\mu/\bar{\mu}$  for the 2D marine data set a multi-gather input.

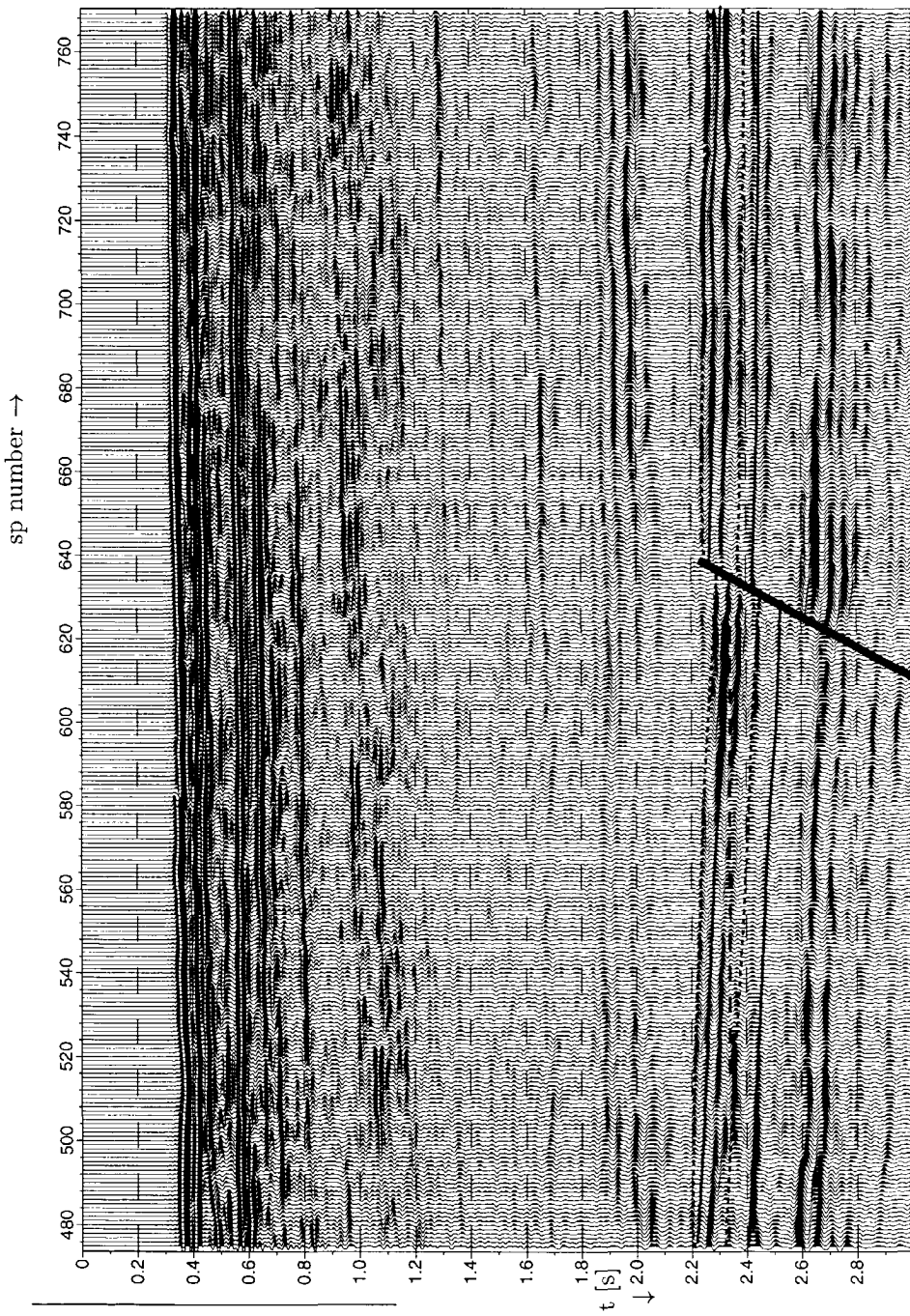


Fig. 8.9 The ZLF filtered section for a constant angle of  $30^\circ$  for the 2D marine data set.

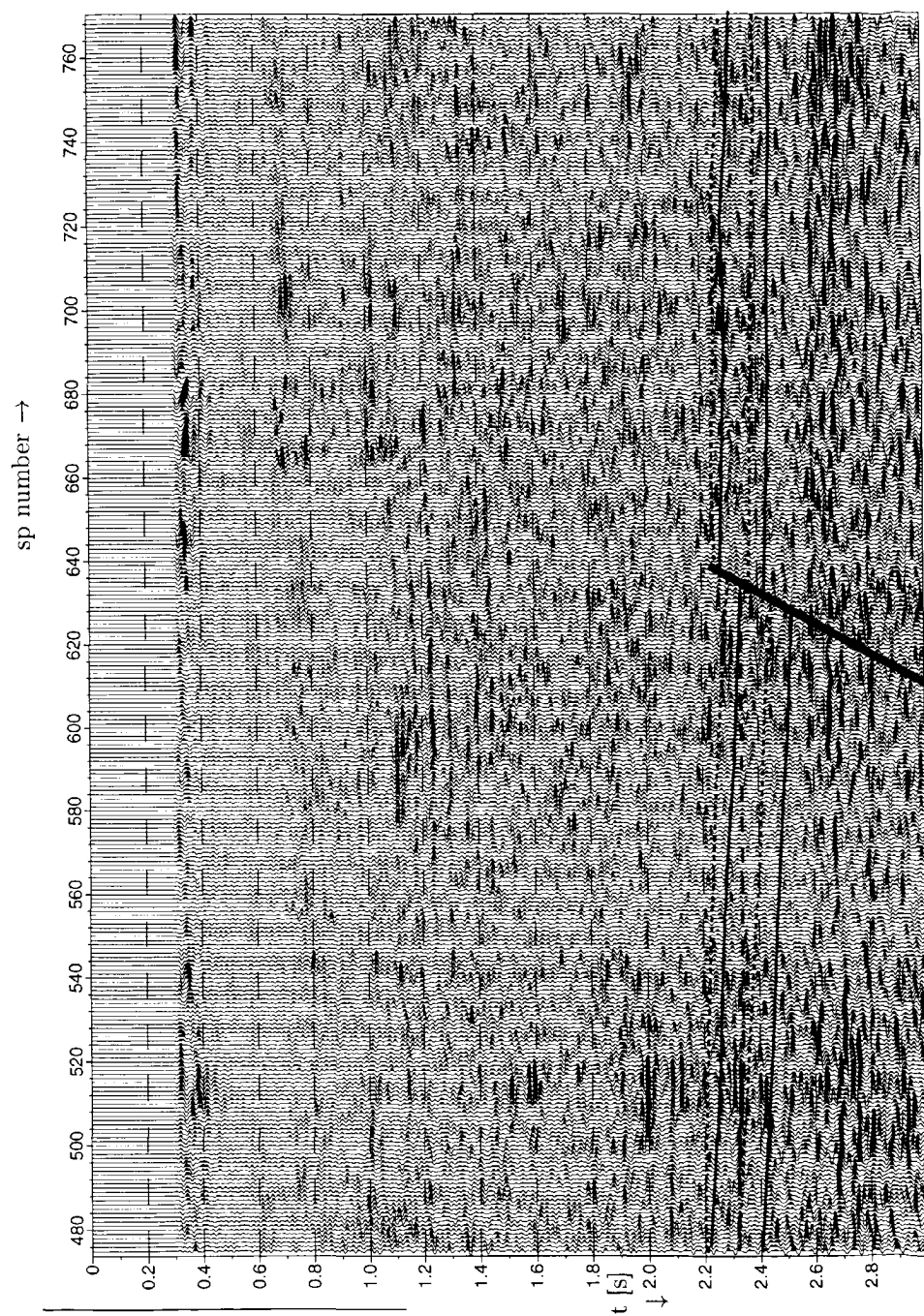


Fig. 8.10 The residue section for normal incidence for the 2D marine data set.

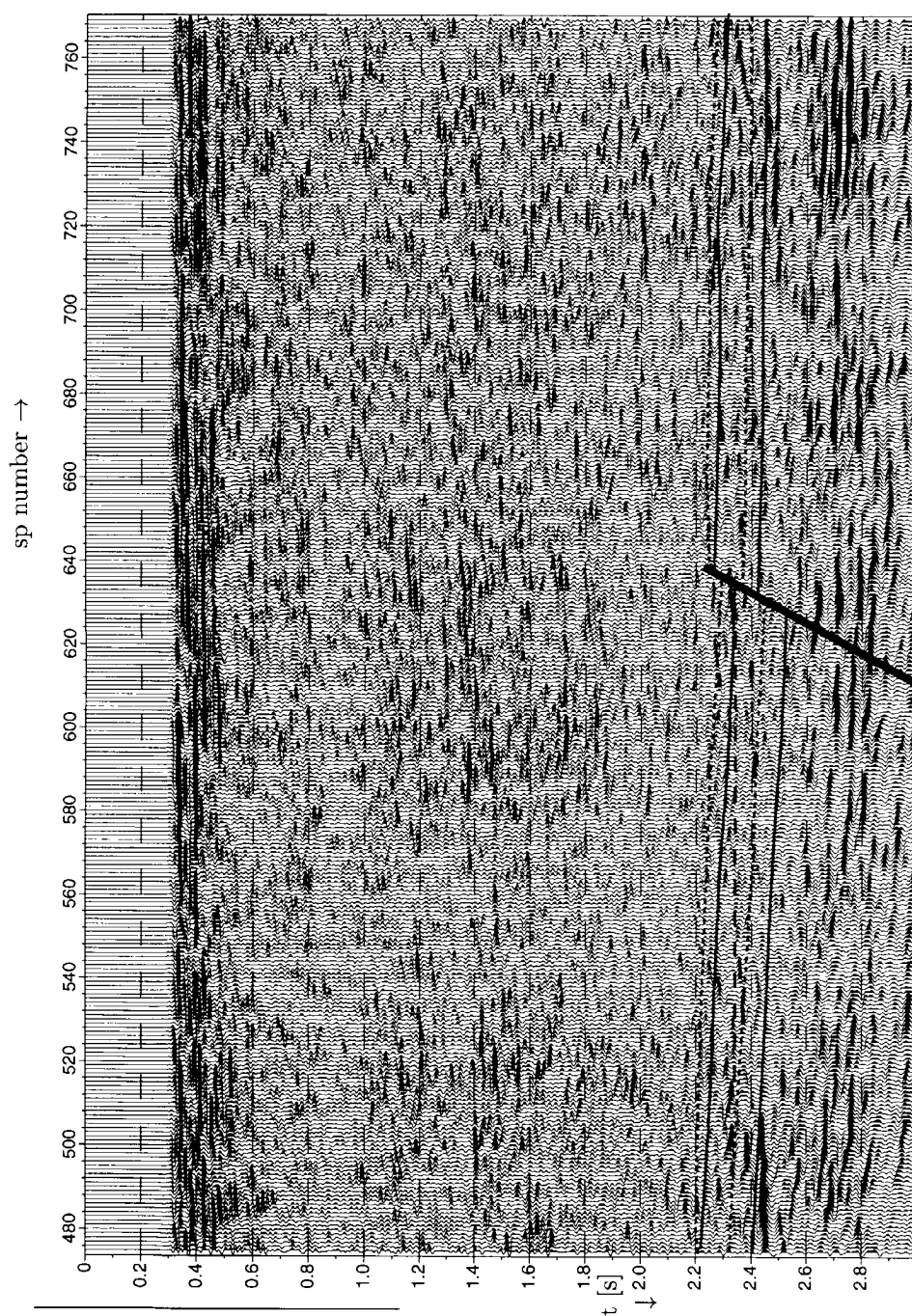
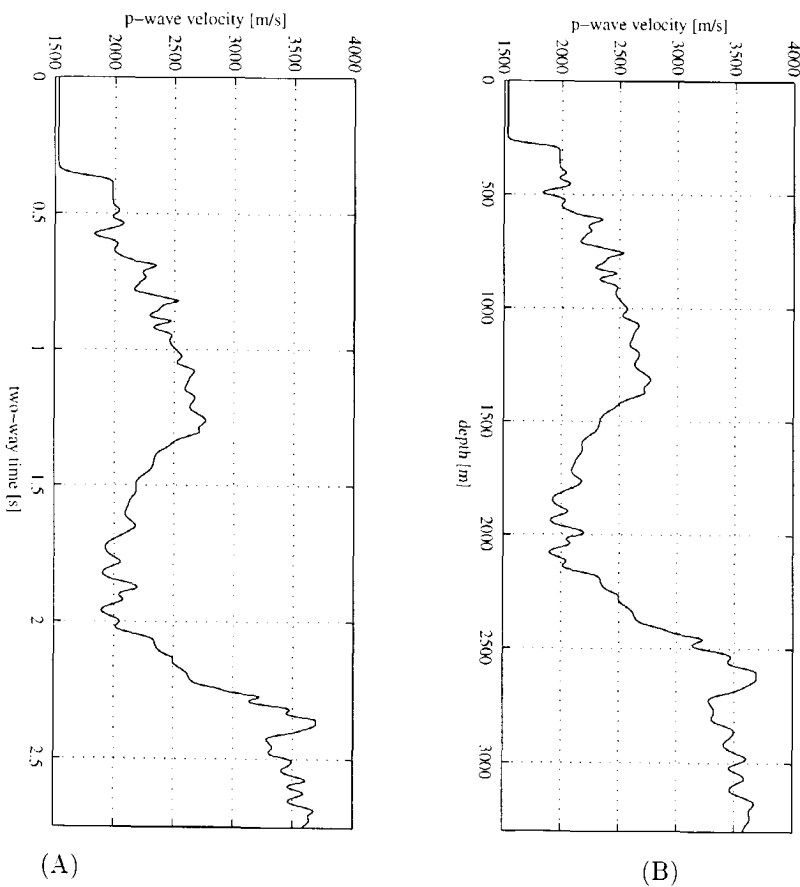
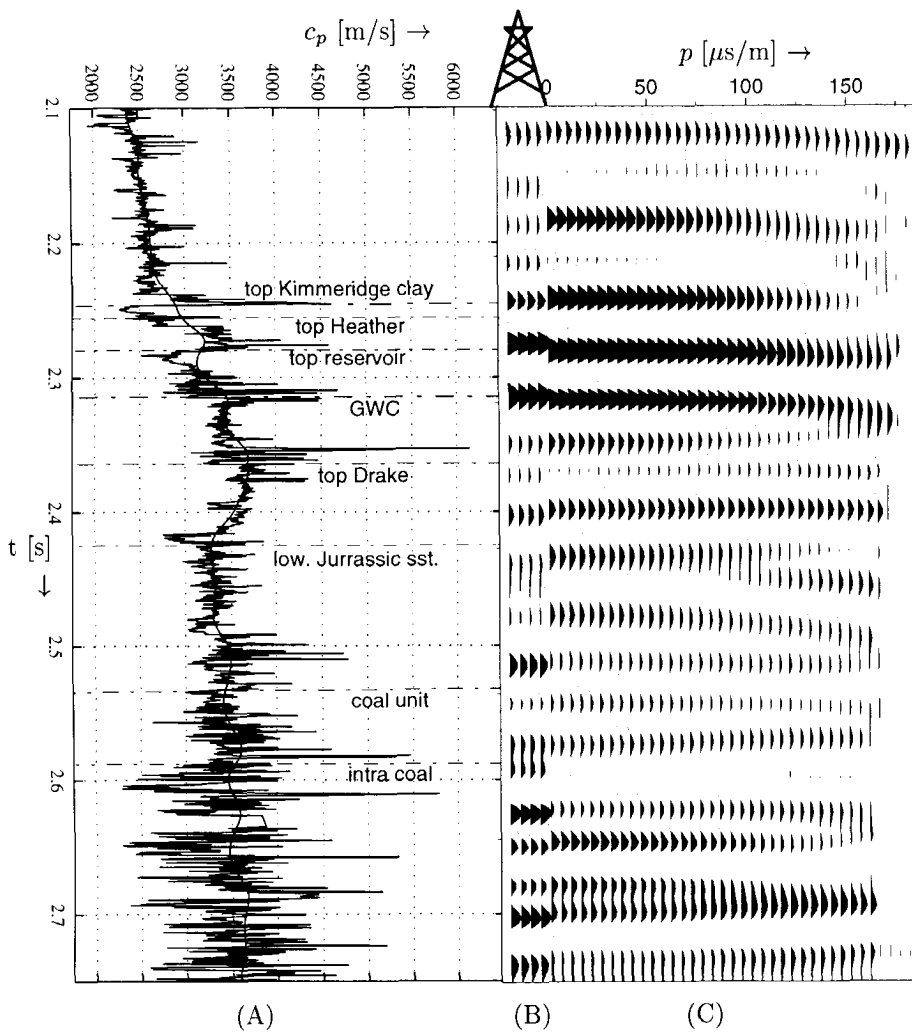


Fig. 8.11 The residue section for a constant angle of  $30^\circ$  for the 2D marine data set.

The ZLF residue section for normal incidence is shown in figure 8.10. Clearly the multiples can be recognized between shot point location 500-520 and around shot point location 600. There are not much coherent events. Figure 8.11 shows the ZLF residue section for a constant angle of  $30^0$ . Again the multiples can be recognized. In the deeper part of the data (below 2.4s) clearly coherent events can be recognized. Since these residual events are continuous through the interpret fault, they are probably (internal) multiples of layers in the upper part of the section. These events can not be described by the linearized primary PP reflection data model. Therefore the inversion result at this depth becomes unreliable.



**Fig. 8.12** The down scaled 'macro'  $\bar{c}_p$  velocity as function of two-way time (left) and depth (right) (well B). Note the difference in scale for low and high velocities in (A).



**Fig. 8.13** (A) The sonic well log, (B) the synthetic impedance contrast and (C) the ZLF gather  $\tilde{\lambda}(t)$  from the 2D marine data set with interpretation.

### 8.1.6 Modeling synthetic data at well

The measured sonic and density logs were multiplied to get an acoustic impedance log. These logs were down scaled to a range of scales in depth (Verhelst and van Wijngaarden, 1997b). From these down scaled traces a trace in time is constructed in such a way, that there is in time a constant scale (Verhelst and van Wijngaarden, 1997a). Summarizing a scale dependent depth-to-time conversion has been used in order to get the correct down scaled synthetic impedance contrast trace in time, as

also discussed in chapter 4.

In Figure 8.12 the down scaled 'macro' sonic velocity log is shown as function of two-way time and of depth. The sonic velocities are used to show the sonic log and the synthetic impedance trace as function of two-way time in Figure 8.13. This figure can be used to match the geologic interpretation on the fine log scale with the seismic scale. For a more detailed description of the down scaling and scale behaviour see Verhelst and van Wijngaarden (1997b) .

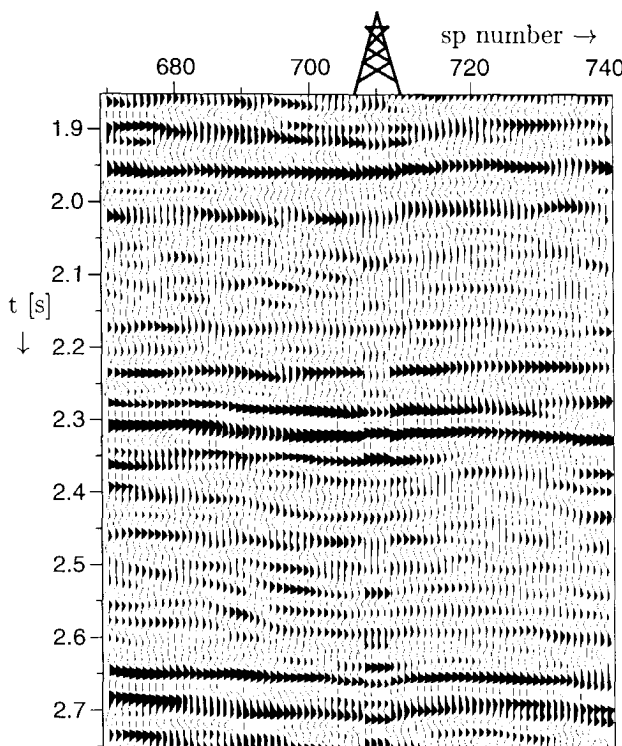


*Fig. 8.14* The estimated acoustic impedance in the target area from the marine dataset using the RC-gathers after deconvolution/filtering with the well (B) synthetic pasted in the middle.

### 8.1.7 Comparison of synthetic data and seismic data

The synthetic trace is pasted (repeated 5x) in the estimated impedance contrast sections in figure 8.14. In the seismic section we used the top of the Heather formation to position the synthetic traces in time. Using the coal layers in the lower Jurassic as a second marker.

### 8.1.8 Influence of background velocity and $Q_{lithology}$

The same RC gather from a 2D marine line as shown in figure 5.4 has been used to investigate the influence of the background velocity. First the strong reflector of the base Cretaceous is shown in the RC gather in figure 8.16A. The corresponding ZLF gather (van Wijngaarden and Berkhouwt, 1997) is shown in figure 8.16B.

The amplitude cross sections at 2.260s and 2.300s are shown in figures 8.16C and E. The estimated contrast parameters and their ratio  $Q_{lith}$  are shown in figures 8.16D and F as function of the background velocity  $\bar{c}_P$ . The background velocity is varied  $\pm 20\%$  around the measured velocity from the sonic log. Both events show decreasing contrasts with increasing background velocity. Their ratio  $Q_{lith}$  is almost constant and positive.

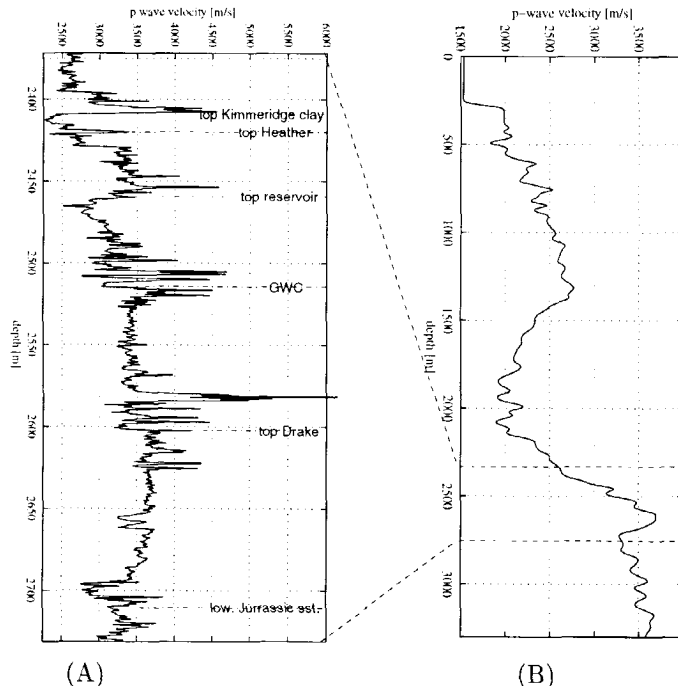


**Fig. 8.15** (A) The well log velocity  $c_P$  and (B) the down scaled 'macro'  $\bar{c}_P$  velocity as function of depth.

Note that for low background velocities in figure 8.16F the  $p$ -dependent contrasts become very large compared to the acoustic impedance contrast ( $\Delta Z/\bar{Z} = 2 \times \tilde{r}_{PP}(p = 0)$ ). Also for the smoothed well log velocity of 3175m/s the contrasts are larger than 1. Since this is unrealistic, this suggests that the used background

velocity  $\bar{c}_P$  is too low.

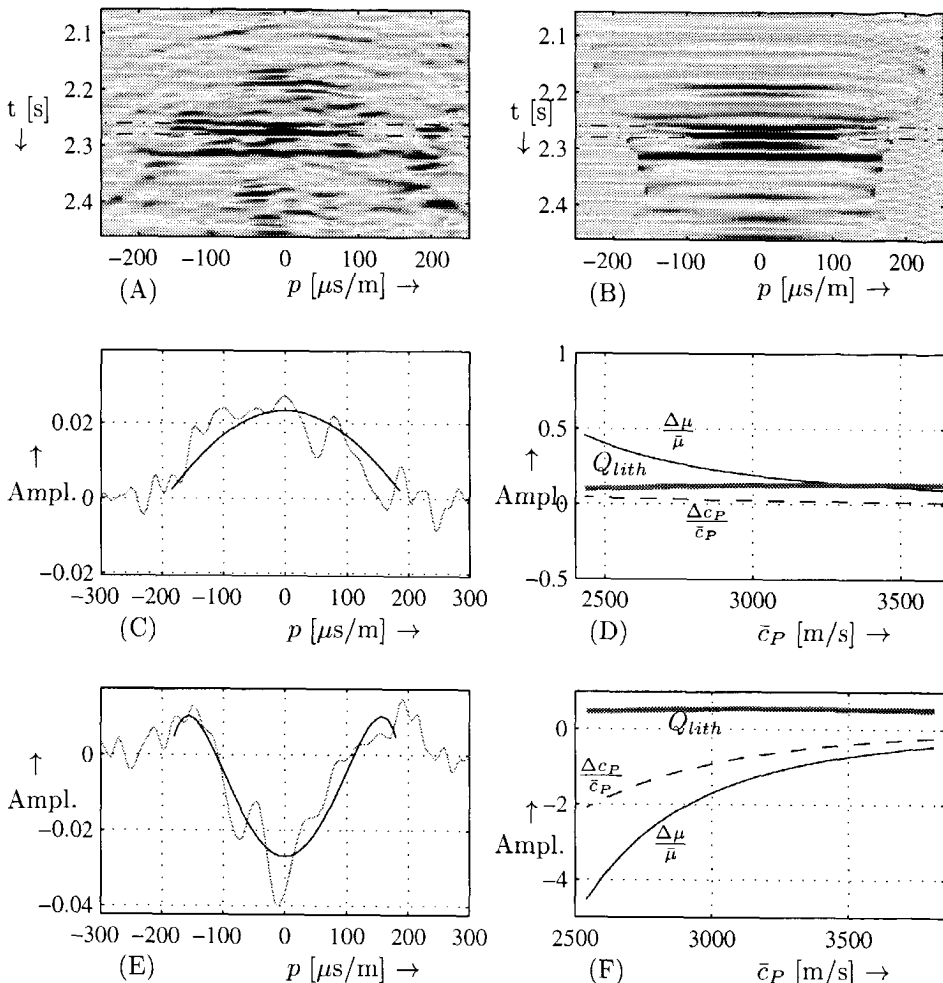


**Fig. 8.16** (A) RC gather of the marine data set (at s.p. 707) and (B) the filtered ZLF gather. (C) The AVP curves at 2.260s of the RC gather and the ZLF gather. (D) The influence of background velocity on the estimated P-velocity contrast (dashed line), shear modulus contrast (solid line) and their ratio  $Q_{\text{lith}}$  (thick gray line) at  $t=2.260$ s. (E) The AVP curves at 2.300s of the RC gather and the ZLF gather. (F) The influence of background velocity on the estimated P-velocity contrast (dashed line), shear modulus contrast (solid line) and their ratio  $Q_{\text{lith}}$  (thick gray line) at  $t=2.300$ s.

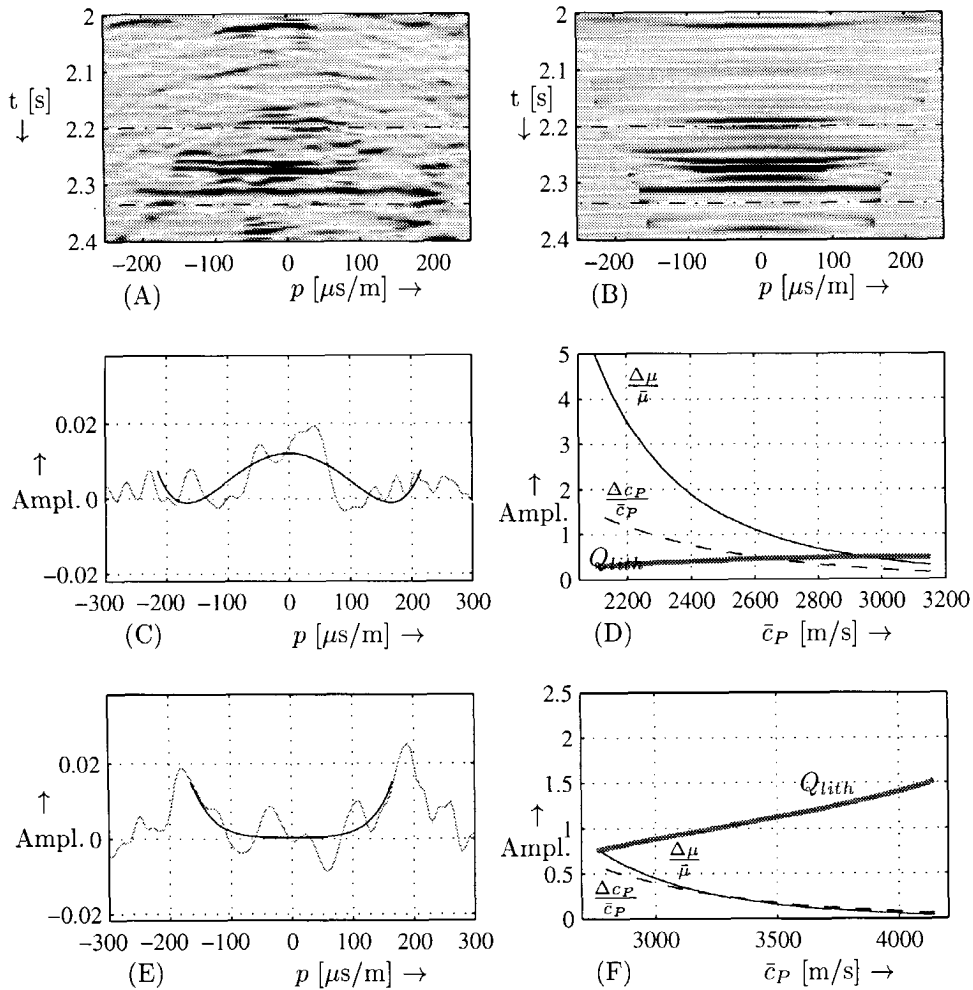


**Fig. 8.17** (A) RC gather of the marine data set (at s.p. 707) and (B) the filtered ZLF gather. (C) The AVP curves at 2.200s of the RC gather and the ZLF gather. (D) The influence of background velocity on the estimated P-velocity contrast (dashed line), shear modulus contrast (solid line) and their ratio  $Q_{lith}$  (thick gray line) at  $t=2.200$ s. (E) The AVP curves at 2.336s of the RC gather and the ZLF gather. (F) The influence of background velocity on the estimated P-velocity contrast (dashed line), shear modulus contrast (solid line) and their ratio  $Q_{lith}$  (thick gray line) at  $t=2.336$ s.

If we look at the the well log velocities at the target level and the used background velocity  $\bar{c}_P$  in figure 8.15, the local velocity around 2450m is higher than the averaged background velocity. This confirms the idea that the used background velocity should be around 3500m/s.

In figure 8.17 two other events in the same RC gather are examined. In 8.17C the AVP curves belonging to a fairly weak reflector at 2.200s are shown. The sharp decrease in amplitude at  $p=80\mu\text{s}/\text{m}$  results in rather high contrasts in figure 8.17D. Specially for low background velocities, the shear modulus contrast becomes unrealistic large. The ratio  $Q_{lith}$  shows a small increase with background velocity.

The AVP curves in figure 8.17E show the high amplitudes at large  $p$ -values in the Jurassic gas sand. Although both  $p$ -dependent contrasts decrease with increasing background velocity like the other events, their ratio  $Q_{lith}$  is much higher and shows a clear increase with increasing background velocity. This maybe used to distinguish the gas sands from the other lithotypes.

### 8.1.9 Direct Hydrocarbon Indicator

In chapter 7 the lithology indicators have been discussed. In this case study a type of anomaly indicator as described by equation 7.25 in section 7.3.2 is used. Unfortunately there is no information on the shear velocities from well log measurements for this data set. Therefore it was not possible to use cross plots between shear modulus and P-wave velocity to check wether there is a general trend between the shear modulus and the P-wave velocity. For this reason the cross plots between the acoustic impedance and P-wave velocity are used in this case study.

The cross plots for the different formations (which are indicated in the migration and well log measurements in figure 8.1 and 8.2) are shown in figure 8.19. The background trend is also indicated in these cross plots. The Kimmeridge clay and Heather formation above the reservoir show a linear relation between the P-wave velocity and acoustic impedance. The gas bearing Tomma formation and the coals deviate from this trend with a higher  $c_P/Z$  ratio. Therefore we expect that the anomaly indicator  $\bar{D}'$  between the P-wave velocity contrast and impedance contrast

$$\bar{D}'(x, t) = \frac{\Delta c_P}{\bar{c}_P}(x, t) - \bar{\Gamma}'(x, t) \frac{\Delta Z}{\bar{Z}}(x, t) \quad (8.1)$$

will highlight the gas bearing Tomma formation and the coal layers and may therefore be used as a direct hydrocarbon indicator.

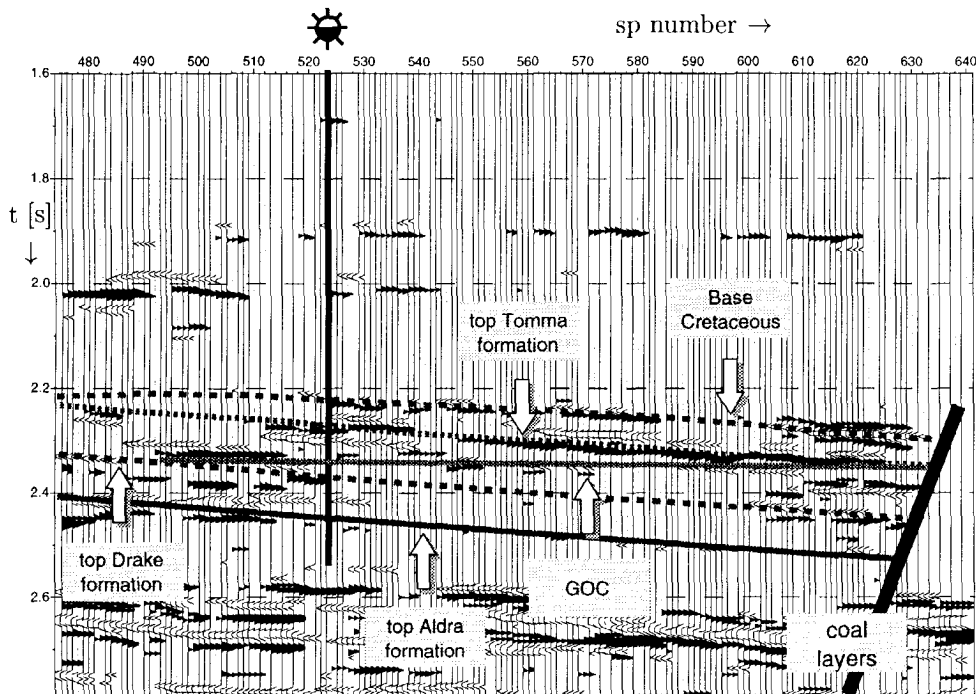


**Fig. 8.18** The Direct Hydrocarbon Indicator for the 2D marine data set, showing the target area around well A with the interpretation overlaid.

This indicator is shown in figure 8.18 for the reservoir around well A and in figure 8.20 for the whole section. As expected are the top of the Tomma formation and the coal layers clearly visible. The fact that the top of the Tomma formation between shot point locations 490 and 510 is not indicated, is probably due to the multiple problem at this lateral location (see figure 8.10 and 8.11).

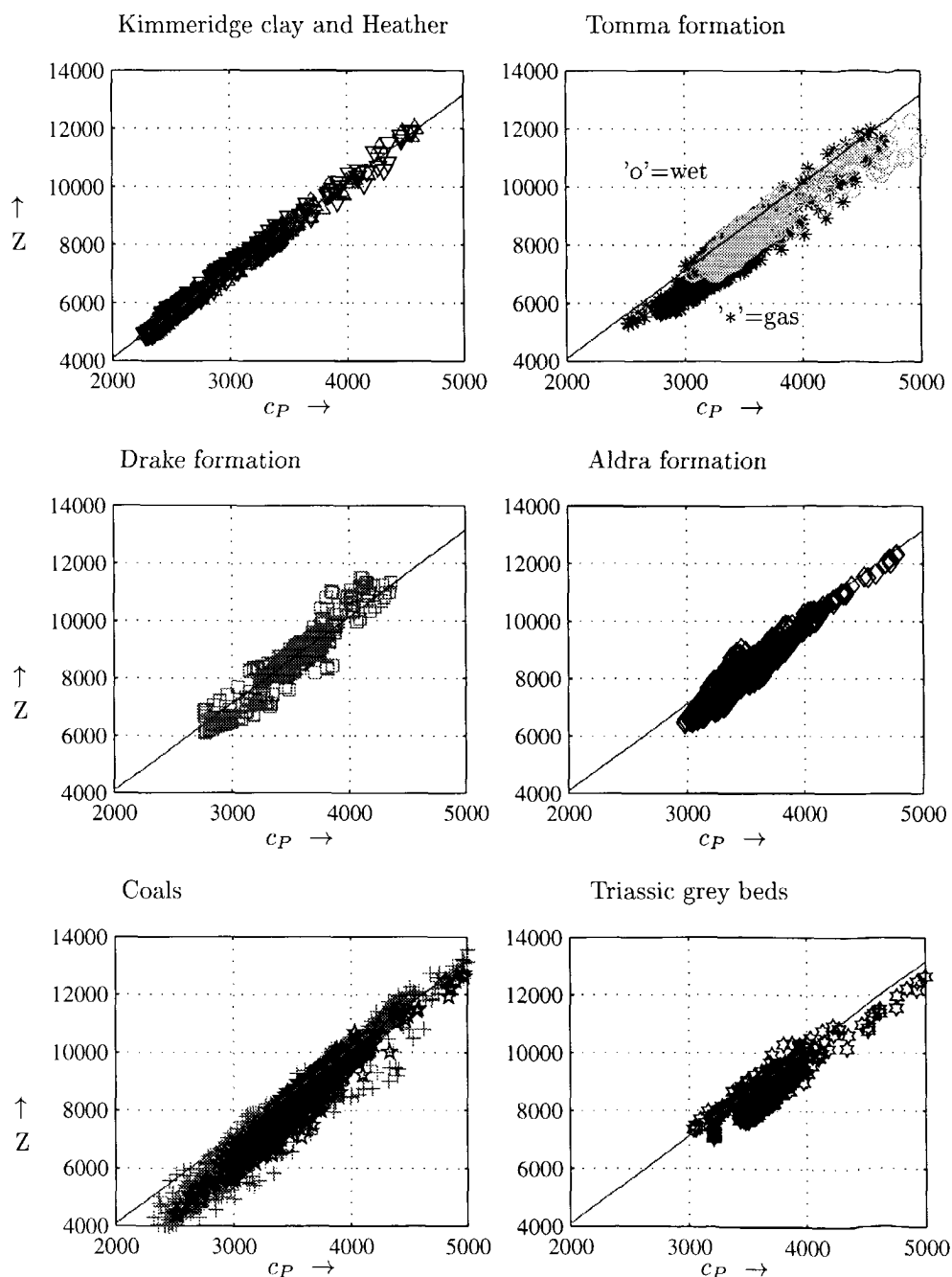


**Fig. 8.19** The cross plots of the P-wave velocity versus the acoustic impedance for the formations in the depth range 2400–3350 m.

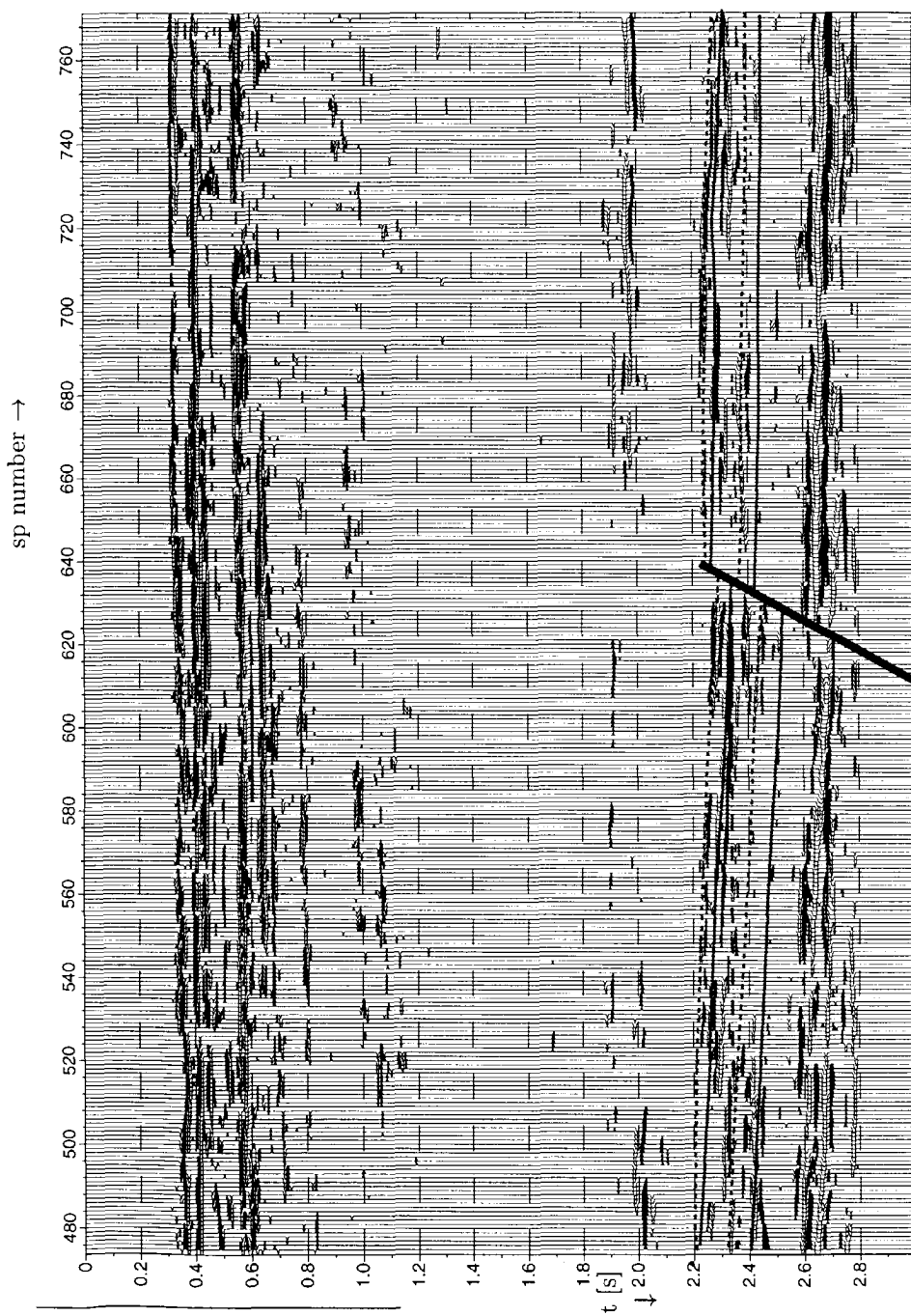


Fig. 8.20 The Direct Hydrocarbon Indicator for the 2D marine data set.

### 8.1.10 Conclusions

If we split up the angle-averaged migration into an impedance (small angles) section and a large angle section, we see that the continuity is mainly determined by the large angles. The small angle sections show a higher vertical and horizontal resolution. By splitting up the angle-dependent reflectivity in P-wave velocity, shear modulus and impedance contrasts, the interpretation of the target area is not directly improved. Especially the P-wave velocity and shear modulus contrast sections are distorted by multiple energy that is not removed in the preprocessing.

Also an accurate background velocity model is needed for the estimation of the correct values of the P-wave velocity and shear modulus contrasts. Too low velocities will introduce unrealistic high values for these contrast sections.

The ZLF process on the other hand is very robust. ZLF sections for constant angles (especially for large angles) are robust and useful for interpretation. The residue sections show clearly the quality of the preprocessing and migration. Especially remaining multiple energy is easily recognized in the residue sections.

The cross plots of the P-wave velocity and impedance from well log data show that the gas bearing Tomma formation and coal layers show a different trend than the surrounding formations. Therefore, the contrast sections for P-wave velocity and impedance can successfully be combined in a direct hydrocarbon indicator.



---

# Chapter 9

## Conclusions and remarks

In this thesis the use of seismic data for subsurface characterization is split into two steps:

1. an imaging step
2. an inversion and characterization step.

The first process deals with the imaging of the reflectivity properties of each subsurface gridpoint. The main challenges are the correct positioning of the reflecting boundaries in the subsurface (i.e. a high lateral resolution) and estimation of the correct amplitudes for the angle or  $p$ -dependent reflection functions for each subsurface gridpoint. The main conclusions related to the theoretical and practical aspects of the bifocal imaging algorithm used are drawn in the next section.

The second process deals with the inversion of the imaged reflection functions into parameters which characterize the subsurface. The purpose of this procedure is to go beyond a structural image of the subsurface and to characterize the boundaries in terms of lithology. This characterization process can either be used to determine AVP anomalies (which are often associated with gas) from a background lithology or to classify the boundaries in lithoclass transitions. The main conclusions related to the theoretical and practical aspects of the inversion and characterization processes are drawn in section 9.2.

Finally, some remarks are made for future research in section 9.3.

### **9.1 Preprocessing and imaging**

With respect to the preprocessing and the imaging processes (discussed in chapter 2) the following conclusions can be drawn:

- The preprocessing quality is important for the final result, especially the multiple elimination and the removal of the 'acquisition footprints'.

- The bifocal imaging algorithm yields the amplitude preserved image of  $p$ -dependent reflectivity (within the limits of acquisition) by means of a double focusing process.
- The bifocal imaging algorithm is an extension of the existing migration algorithm with a new 'imaging principle', which implies the selection of  $\Delta\tau=0$  in the gridpoint gather.
- The anisotropy and fine-layering effects during the wave field propagation should be incorporated in focusing operators.
- The influence of the local dip of imaged boundaries in the subsurface can be compensated for completely.
- The bifocal imaging algorithm is very well suited for imaging of mode-converted reflection data.

## 9.2 Inversion process and characterization

With respect to the inversion process and the characterization the following conclusions can be made:

- Imaged RC gathers show a decrease in frequency content with increasing  $p$ -value. This can cause a false 'apparent' AVP behaviour, which can be compensated for, as shown in chapter 4.
- The linearized Zoeppritz equations can be used for parameterization in a local inversion process using pre-critical data after compensation for non-constant lateral bandwidth within a RC gather, as shown in chapters 3 and 5.
- The converted reflections can severely deteriorate the amplitudes of the imaged mode, as shown in chapter 3.
- The background velocity is important for estimated gradients or higher order  $p$ -dependent contrast terms, as shown in chapter 5. A too low background velocity generally results in the estimation of too large  $p$ -dependent contrast terms.
- The ratio  $Q_{lith}$  as discussed in chapter 5 may be used for classification of lithologies even when an accurate background velocity model is not available.
- Each reflection mode can be inverted separately into elastic contrasts using the linearized parameterization, as shown in chapter 6.
- By cross plotting the estimated contrast parameters, relations or classifications for specific lithotypes can be found. Using these relations, deviations from the

general trend (i.e. lithotypes) can be found which are due to e.g. a different fluid fill (like gas instead of brine in a sandstone).

- The contrast sections for the different modes should be transformed to a common depth or time axis (in this thesis the two-way travel time for PP waves is used) and to the same bandwidth, before the results can be combined (which can be a problem in practical situations).
- The inversion results for the different modes can be combined to estimate P-, S-wave velocity and density contrasts. These P-, S-wave velocity and density contrasts can be directly compared with the modeled P-, S-wave and density from rock physics models and data bases.
- Residue analysis is important to check preprocessing results and the necessity for a residual move out correction of the RC gather.
- ZLF analysis is very stable and useful for computation and interpretation of specific (e.g. small and large) angle sections.

### 9.3 Recommendations for future research

A number of subjects which are discussed in this thesis are still topic of current research. The most important issues to be addressed are:

- Estimation and incorporation of anisotropy and fine-layering effects in focusing operators.
- Refinement of the residual move out correction, specially for noisy data.
- Update method for background velocity model used in the inversion process.
- Classification of lithoclass transitions using the ratio  $Q_{lith}$ .
- Extension to 3D for better imaging and interpretation possibilities of estimated contrast sections/slices.



## Bibliography

Aki, K. and Richards, P. G. (1980). *Quantitative Seismology: Theory and methods*. W.H.Freeman and Co.

Bakker, S., Wapenaar, C. P. A., and van Wijngaarden, A. J. (1995). Wave propagation in porous media. Technical report, Delft University of Technology. DELPHI, Volume VI, Chapter 13a.

Berkhout, A. J. (1982). *Imaging of acoustic energy by wave field extrapolation (2nd edition)*. Elsevier.

Berkhout, A. J. (1997a). Pushing the limits of seismic imaging, part I: Prestack migration in terms of double dynamic focusing. *Geophysics*, **62**(3), 937–953.

Berkhout, A. J. (1997b). Pushing the limits of seismic imaging, part II: Integration of prestack migration, velocity estimation and avo analysis. *Geophysics*, **62**(3), 954–969.

Berkhout, A. J., Wapenaar, C. P. A., and Verschuur, D. J. (1997). Migration of mode-converted seismic data. In *Expanded Abstracts*, pages 1595–1598, Houston. SEG, Soc. Expl. Geophys., Expanded abstracts.

Biot, M. A. (1956). Theory of propagation of elastic waves in a fluid saturated porous solid, i. low-frequency range. *J. Acoust. Soc. Am.*, **28**, 168–178.

Castagna, J. P., Batzle, M. L., and Eastwood, R. L. (1985). Relationships between compressional-wave and shear-wave velocities in clastic silicate rocks. *Geophysics*, **50**, 571–581.

Castagna, J. P., Batzle, M. L., and Kan, T. K. (1993). Rock physics - the link between rock properties and AVO response. In J. P. Castagna and M. M. Backus, editors, *Offset-dependent reflectivity - Theory and practice of AVO analysis*, pages 135–171. Soc. Expl. Geophys., Tulsa.

Crans, A. and Berkhout, A. J. (1980). Assessment of seismic amplitude anomalies. *Oil and Gas Journal*, **17**(2), 156–168.

de Bruin, C. G. M. (1992). *Linear AVO inversion by prestack depth migration*. Ph.D. thesis, Delft University of Technology.

de Haas, J. C. and Berkhouit, A. J. (1988). On the information of p-p, p-sv, sv-p and sv-sv reflections. In *58th Ann. Intern. Mtg., Soc. Expl. Geophys., Expanded Abstracts*, pages 1190–1194.

Domenico, S. M. (1976). Effect of brine-gas mixture on velocity in an unconsolidated reservoir. *Geophysics*, **41**, 882–894.

Ekern, O. F. (1987). Midgard. In A. M. Spencer, editor, *Geology of the Norwegian oil and gas fields; Norwegian Petroleum Society*, pages 403–410. Graham and Trotman, London.

Gardner, G. H. F., Gardner, L. W., and Gregory, A. R. (1974). Formation velocity and density - the diagnostic basis for stratigraphic traps. *Geophysics*, **39**, 770–780.

Gassmann, F. (1951). über die elastizität poröser medien. *Vierteljahrsschrift der Naturforschenden Gesellschaft in Zürich*, **96**, 1–23.

Herrmann, F. J. (1997). *A scaling medium representation, a discussion on well-logs, fractals and waves*. Ph.D. thesis, Delft University of Technology.

Herrmann, P. C. (1992). *Decomposition of multi-component measurements into P and S waves*. Ph.D. thesis, Delft University of Technology.

Kabir, M. M. N. (1997). *Velocity estimation of the complex subsurface using the Common Focus Point Technology*. Ph.D. thesis, Delft University of Technology.

Knott, C. G. (1899). Reflection and refraction of elastic waves with seismological applications. *Philosophical Magazine, series* **5**(48), 64–97.

Koefoed, O. (1955). On the effect of poisson's ratios of rock strata on the reflection coefficients of plane waves. *Geophysical Prospecting*, **3**, 381–387.

Kuster, G. T. and Töksoz, N. M. (1974). Velocity and attenuation of seismic waves in two-phase media i: Theoretical formulations. *Geophysics*, **39**, 607–618.

Mavko, G. M. and Nur, A. (1977). The effect of nonelliptical cracks on the compressibility of rocks. *J. Geoph. Res.*, **84**, 4769–4776.

Menke, W. (1984). *Geophysical data analysis: discrete inverse theory*. Academic Press.

Ostrander, W. J. (1982). Plane-wave reflection coefficients for gas sands at nonnormal angles of incidence. In *52th Ann. Intern. Mtg., Soc. Expl. Geophys., Expanded Abstracts*, pages 216–220.

Ostrander, W. J. (1984). Plane-wave reflection coefficients for gas sands at nonnormal angles of incidence. *Geophysics*, **49**, 1637–1648.

Rutherford, S. R. and Williams, R. H. (1989). Amplitude-versus-offset variations in gas sands. *Geophysics*, **54**, 680–688.

Simmons, J. L. and Backus, M. M. (1994). Avo modeling and the locally converted shear wave. *Geophysics*, **59**(9), 1237–1248.

Smith, G. C. and Gidlow, P. M. (1987). Weighted stacking for rock property estimation and detection of gas. *Geophys. Prosp.*, **35**(9), 993–1014.

Swan, H. W. (1993). Properties of direct AVO hydrocarbon indicators. In J. P. Castagna and M. M. Backus, editors, *Offset-dependent reflectivity - Theory and practice of AVO analysis*, pages 78–92. Soc. Expl. Geophys., Tulsa.

Thomsen, L. (1986). Weak elastic anisotropy. *Geophysics*, **51**, 1954–1966.

Thorbecke, J. (1996). CFP migration; practical aspects. Technical report, Delft University of Technology. DELPHI, Volume VII, Chapter 13.

Thorbecke, J. W. (1997). *Common Focus Point Technology*. Ph.D. thesis, Delft University of Technology.

Ursin, B. and Ekren, B. O. (1995). Robust avo analysis. *Geophysics*, **60**(2), 317–326.

van Wijngaarden, A. J. (1995). Seismic characterization. Technical report, Delft University of Technology. DELPHI, Volume VI, Chapter 13.

van Wijngaarden, A. J. and Berkhouit, A. J. (1995). Constrained linear avo inversion. In *Expanded Abstracts*, Glasgow. EAEG, Eur. Ass. of Expl. Geophys.

van Wijngaarden, A. J. and Berkhouit, A. J. (1997). Amplitude preserving imaging and characterization of angle-dependent reflection information. Technical report, Delft University of Technology. DELPHI, Volume VIII, Chapter 17.

van Wijngaarden, A. J. and Wapenaar, C. P. A. (1995). Residue analysis in linearized elastic inversion. In *65th Ann. Intern. Mtg., Soc. Expl. Geophys., Expanded Abstracts*, pages 1125–1128.

van Wijngaarden, A. J., Verschuur, E. V., and Ala'i, R. (1995). The mobil project, preliminary results of the delphi scheme. Technical report, Delft University of Technology. DELPHI, Volume VI, Chapter 15.

Verhelst, F. and van Wijngaarden, A. J. (1997a). Comparison of seismic and well-log data: reflectivity in function of scale and angle. Technical report, Delft University of Technology. DELPHI, Volume VIII, Chapter 19.

Verhelst, F. and van Wijngaarden, A. J. (1997b). Iterative search for a pre-specified scale in seismic time: a scale dependent raytracer. Technical report, Delft University of Technology. DELPHI, Volume VIII, Chapter 18.

Verschuur, D. J. (1991). *Surface-related multiple elimination, an inversion approach*. Ph.D. thesis, Delft University of Technology.

Verschuur, D. J., van Wijngaarden, A. J., and Ala'i, R. (1998). Comparison of seismic inversion methods on a single real data set, delphi stepwise approach to avo processing. In R. G. Keys and D. Foster, editors, *Comparison of Seismic Inversion Methods on a Single Real Data Set*., Soc. Expl. Geophys., Tulsa.

Wapenaar, C. P. A. and Berkhout, A. J. (1989). *Elastic wave field extrapolation*. Elsevier.

Wapenaar, C. P. A., van der Leij, T. S., and van Wijngaarden, A. J. (1996). Compensating for the effect of fine-layering. Technical report, Delft University of Technology. DELPHI, Volume VII, Chapter 23.

Wapenaar, C. P. A., van Geloven, W., Goudswaard, J., van Wijngaarden, A. J., and Dissing, F. D. (1997). Ava migration and multiscale characterization in finely layered media. *Journal of Seismic Exploration*, **6**(2/3), 181–198.

Watt, J. P., Davies, G. F., and O'Connell, R. J. (1976). The elastic properties of composite materials. *Rev. Geophys. and Space Physics*, **14**, 541–563.

Wyllie, M. R., Gardner, A. R., and Jan, L. W. (1956). Elastic wave velocities in heterogeneous and porous media. *Geophysics*, **21**(1), 41–70.

Xu, S. and White, R. E. (1995). A new velocity model for clay-sand mixtures. *Geophys. Prospl.*, **43**(1), 91–118.

Yilmaz, O. (1985). *Seismic data processing*, volume series 2. SEG.

## Author Index

Aki, K., 71, 73, 74, 101-103, 130, 140  
Ala'i, R., 66, 176

Backus, M.M., 99  
Bakker, S., 175  
Batzle, M.L., 172, 173  
Berkhout, A.J., 3, 6, 10, 11, 14, 15, 17,  
59, 175, 198  
Biot, M.A., 174

Castagna, J.P., 172, 173  
Crans, A., 175

Davies, G.F., 173  
de Bruin, C.G.M., 30, 171, 175  
de Haas, J.C., 142  
Dessing, F.D., 121  
Domenico, S.M., 172

Eastwood, R.L., 173  
Ekern, O.F., 184

Gardner, A.R., 173  
Gardner, G.H.F., 173  
Gardner, L.W., 173  
Gassmann, F., 174  
Gidlow, P.M., 140, 175  
Goudswaard, J., 121  
Gregory, A.R., 173

Herrmann, F.J., 165, 166  
Herrmann, P.C., 11, 62

Jan, L.W., 173

Kaber, M.M.N., 52  
Kan, T.K., 172, 173

Knott, C.G., 71  
Koefoed, O., 4  
Kuster, G.T., 174

Mavko, G.M., 174  
Menke, W., 127, 141

Nur, A., 174

O'Connell, R.J., 173  
Ostrander, W.J., 4, 105, 171

Richards, P.G., 71, 73, 74, 101-103, 130,  
140  
Rutherford, S.R., 5

Simmons, J.L., 99  
Smith, G.C., 140, 175  
Swan, H.W., 149

Töksoz, N.M., 174  
Thomsen, L., 173  
Thorbecke, J.W., 6, 15, 52, 53

Ursin, B., 165

Van der Leij, T.S., 105  
van Geloven, W.F.M., 121  
van Wijngaarden, A.J., 66, 105, 117, 121,  
140, 151, 175, 176, 196-198  
Verhelst, F., 117, 121, 196, 197  
Verschuur, D.J., 11, 13, 66, 176

Wapenaar, C.P.A., 17, 105, 121, 175  
Watt, J.P., 173  
White, R.E., 174  
Williams, R.H., 5

Wyllie, M.R., 173

Xu, S., 174

Yilmaz, O., 113

## Samenvatting

# **Afbeelden en karakteriseren van hoekafhankelijke seismische reflectie data\***

In de exploratie geofysica wordt seismische reflectiedata gebruikt voor het lokaliseren en evalueren van fossiele brandstofvoorraden in de ondergrond. De laatste jaren wordt de seismische methode ook gebruikt voor het monitoren van deze voorraden tijdens de produktie.

In dit proefschrift wordt een nieuwe afbeeldingstechniek geïntroduceerd die op basis van een dubbel focuseringsproces de hoekafhankelijke reflectiesterkte afbeeldt. Dit in tegenstelling tot de conventionele methode, waarbij men de twee focuseringsstappen tegelijkertijd uitvoert, en een over een hoekenbereik gemiddelde reflectiesterkte wordt berekend. De hoekafhankelijke reflectiesterkte wordt in een inversie procedure gebruikt om de gesteenten in de ondergrond te karakteriseren en de aanwezigheid van fossiele brandstoffen vast te stellen.

In hoofstuk 2 wordt de dubbele focuseringsmethode voor het afbeelden van de hoekafhankelijke reflectiesterkte beschreven. Aandacht wordt besteed aan het verwijderen van de invloed van de acquisitie methode aan het aardoppervlak en de propagatie door de ondergrond naar het af te beelden punt in de aarde. Door het opsplitsen van de afbeeldingstechniek in twee stappen, en door het uitbreiden van de tweede focuseringsstap, kan de hoekafhankelijke reflectiesterkte nauwkeurig worden afgebeeld. Tevens wordt in appendix II gedemonstreerd dat de gebruikte afbeeldingsmethode uitermate geschikt is om de zogenaamde elastische multi-mode data af te beelden. Dit wil zeggen niet alleen uitgezonden en ontvangen P-golven, maar ook conversies naar S-golven kunnen worden gebruikt.

---

\*Dutch summary of *Imaging and characterization of angle-dependent seismic reflection data*.

In hoofdstuk 3 wordt een theoretische beschrijving van de hoekafhankelijke reflectiesterkte gegeven. Daarnaast wordt numeriek de invloed van geconverteerde golven en de interferentie van dunne lagen (die een dikte hebben in de orde van de vertikale resolutie van de seismiek) gedemonstreerd en besproken.

In hoofdstuk 4 wordt de invloed van zeer dunne lagen (die duidelijk dunner zijn dan de vertikale resolutie van de seismiek) op de afgebeelde seismische reflectiesterkte besproken en de hieraan gekoppelde schijnbare hoekafhankelijke reflectiesterkte. Een methode om dit effect te compenseren wordt beschreven.

In hoofdstuk 5 wordt de lokale inversie methode besproken om de hoekafhankelijke reflectiesterkte te parametriseren. Uitgebreide aandacht wordt besteed aan de invloed van het gebruikte snelheidsveld voor de bepaling van de lokale hoek van inval en de uiteindelijke invloed op de geschatte parameters. Tevens worden de mogelijkheden van het gecombineerde gebruik van P en S-golf data besproken.

In hoofdstuk 6 wordt de nauwkeurigheid van de input data en de geschatte parameters behandeld. Dit wordt gedaan aan de hand van een residu analyse en schattingen voor de standaard deviatie van de geschatte parameters. Tevens wordt het Zoeppritz-gebaseerde lineaire filter (ZLF) geïntroduceerd. Verder worden een residuele 'moveout' correctie en een 'multi-gather' inversie besproken als methoden om het inversie resultaat te verbeteren.

In hoofdstuk 7 worden gesteente eigenschappen en hun relatie met seismische snelheden besproken. Deze relaties worden gebruikt om seismische lithologie indicatoren te definieren.

In hoofdstuk 8 worden de technieken uit de voorgaande hoofdstukken toegepast op een marine data set uit Noorwegen.

In hoofdstuk 9 worden tenslotte de conclusies en opmerkingen gepresenteerd.

## Summary

### **Imaging and characterization of angle-dependent seismic reflection data**

In exploration geophysics the seismic reflection data is used for localization and evaluation of hydrocarbon in the subsurface. During the last decade this technology is also used for monitoring the hydrocarbon reservoirs during production.

In this thesis a new method is introduced which is based on a double focusing technology for imaging of the angle-dependent reflectivity. This in contrast to the conventional imaging method, in which the two focusing steps are done simultaneously, and an angle-averaged reflectivity is estimated. The accurately imaged angle-dependent reflectivity is used in an inversion scheme to characterize the subsurface and to indicate hydrocarbon bearing rocks.

In chapter 2 the double focusing technology for imaging of the angle-dependent reflectivity is described. The influence of the acquisition at the surface and the propagation effects of the waves in the subsurface are discussed. By splitting the conventional imaging process in two parts and by extending the second focusing process, the angle-dependent reflectivity can be derived accurately. In appendix II it is demonstrated that this method is very suitable for imaging of elastic multi-mode data. This means that not only emitted and received P-waves can be used in the imaging process, but also converted S-waves.

In chapter 3 a theoretical description of the angle-dependent reflectivity function is given. Furthermore the influence of converted waves and the interference of the reflection of thin layers (with thicknesses in the order of the vertical resolution of the seismic wave field) are numerically modeled and discussed.

In chapter 4 the influence of thin-layering (with thicknesses which are clearly smaller

than the vertical resolution of the seismic wave field) on the imaged seismic reflectivity is discussed. The so-called *apparent* angle-dependent reflectivity is discussed and a method to compensate for this effect is introduced.

In chapter 5 the local inversion method for parameterization of the angle-dependent reflectivity is described. The influence of the used velocity field for determination of the local angle of incidence is extensively discussed. Furthermore the possibilities of combining P- and S-wave data is discussed.

In chapter 6 the accuracy of the input data for the inversion process and the accuracy of the estimated parameters is discussed. This is done by residue analysis and estimation of the standard deviation of the estimated parameters. Also the concept of the 'Zoeppritz-driven linear filter' (ZLF) is introduced. Finally the residual move-out correction and multi-gather inversion are discussed as technologies for improving the inversion results.

In chapter 7 rock properties and their relation with seismic velocities are discussed. These relations are used for the definition of seismic lithology indicators.

In chapter 8 the technologies described in the previous chapters are demonstrated on a marine data set from offshore Norway.

In chapter 9 the conclusions and some remarks are presented.

## Curriculum vitae

Aart-Jan van Wijngaarden was born in Dordrecht, The Netherlands, on October 7, 1967. He attended the 'Chr. Lyceum' in Dordrecht for his secundary education and received his 'VWO diploma' in 1985.

He became a student at Delft University of Technology in 1985 and received his MSc ('ir') degree in applied physics in 1992. The subject of his MSc thesis was 'modeling and inversion of surface waves' and was carried out in the laboratory for seismics and acoustics under supervision of Prof. dr. ir. A.J. Berkhout. During these years he was active in several student societies. He was member and president of the board of two sport societies and treasurer of a study trip to the USA for the society of applied physics students ('VvTP').

In 1992 he joined Geco-Prakla. He worked both in the processing and in the research department. After an introduction period within a field crew and two traineeships in Hannover (Germany) and Orpington (England) he was stationed in the Dutch office in Delft.

In 1994 he joined the DELPHI-consortium at the faculty of applied physics (Delft University of Technology) in order to pursue a PhD degree under the supervision of Prof. dr. ir. A.J. Berkhout. Within the consortium he was the contact for the TNO-NITG ('Dutch national institute for applied geoscience'). During eight consortium meetings and eight congresses and workshops of both SEG and EAGE he presented his work on seismic characterization. From 1995 to 1997 he was also a member of the faculty council.

In 1998 he joined Norsk Hydro in Bergen (Norway) as a senior geophysicist.



## Acknowledgment/Dankwoord

Although this thesis has only one author, there are many people who contributed directly or indirectly to the realization of this thesis and who I would like to acknowledge.

The sponsors of the DELPHI-consortium are gratefully acknowledged for their financial support, but also for their encouragement and discussions. Especially Paul Meldahl and Martin Landrø with Statoil, who invited me to give a course in Stavanger and to present my work in Trondheim, and Mundy Brink with Saga, who invited me to visit his office in Oslo and who provided the data set used in this thesis. Furthermore, I am obligated to Bob Keys with Mobil for organizing the AVO workshops in London and Los Angeles and providing the AVO data set. Last but not least I would like to thank Berend, Rob and Cobie from TNO-NITG for their discussions and feedback during the lunch meetings.

Aan de kant van de universiteit ben ik veel dank verschuldigd aan mijn promotor prof. Berkhout en co-promotor Kees Wapenaar voor hun gezamenlijke begeleiding en voor het verschaffen van alle mogelijkheden binnen het DELPHI consortium. Alle mede-promovendi en alle studenten van de afgelopen vier jaar wil ik bedanken voor de uitstekende tijd die ik met hen in de groep heb gehad.

De bijdragen van Jan Thorbecke verdienen een speciale vermelding hier. Niet alleen voor het op peil houden van de conditie met het wekelijkse hardlopen, maar ook voor het op peil houden van de CFP-software library ben ik je zeer dankbaar. En natuurlijk speciale dank voor Alexander Koek voor het draaiende houden van de computers op de TU en thuis. Ook de bijdragen van Frederic Verhelst waren cruciaal, niet alleen voor het uitlopen van de hele en halve marathons maar ook voor het uitlopen van de promotie. Tenslotte wil ik Riaz Ala'i bedanken voor de perfecte kwaliteit van de hoofdstukken in alle DELPHI boeken en het 'cruisen' in de VS.

Veel dank ben ik ook verontschuldigd aan de familie: mijn ouders en Karin, die mij door de jaren heen hebben gesteund in mijn bezigheden. En tenslotte Elise; jij zette de harde deadline voor het proefschrift en zorgde ervoor dat het op tijd afkwam.





